THE UNIVERSITY OF CHICAGO

ATOMIC AND MOLECULAR BEAM SCATTERING: CHARACTERIZING STRUCTURE AND DYNAMICS OF HYBRID ORGANIC-SEMICONDUCTOR INTERFACES AND INTRODUCING NOVEL ISOTOPE SEPARATION TECHNIQUES

A DISSERTATION SUBMITTED TO
THE FACULTY OF THE DIVISION OF THE PHYSICAL SCIENCES
IN CANDIDACY FOR THE DEGREE OF
DOCTOR OF PHILOSOPHY

DEPARTMENT OF CHEMISTRY

BY
KEVIN JOHN NIHILL

CHICAGO, ILLINOIS
DECEMBER 2017

The truth doesn't care

what you think

Table of Contents

List of Figures

List of Tables

Acknowledgments

Nearly all of my friends, family, and co-workers have helped me get to where I am today, whether they know it or not.

Steve Sibener brought me to UChicago with a series of phone calls, welcomed me into his group with the promise of building scientific apparatus, and helped me grow as a scientist, teacher, and presenter with countless "mentoring moments." I am truly grateful for his support inside the lab and out, and will proudly plant the Sibener flag wherever I end up.

I would also like to extend my gratitude to Ka Yee Lee and Greg Engel for taking the time to be on my dissertation committee, and to Greg especially for spending some of his academic capital to secure me a very exciting postdoctoral position at MIT.

One of the main reasons I joined the Sibener group is because of the people, all of whom made graduate school much more rewarding for me and several of whom have become close friends. Grant Langlois taught me something new on a daily basis, and was extremely patient while doing so, even while all I had in return were wisecracks; he and Traci have been excellent friends to me and Laura. Becca Thompson is a close partner in the trenches of navigating grad school and paving a way towards teaching, and also helped me further my interests in many non-lab pursuits. Bryan Wiggins is also a great friend and mentor, and I like to think that his excessive networking somehow spilled over into my own career. Gabi Avila-Bront has also been a great supporter and role model. My other group members have helped make it considerably more enjoyable to spend many long days 25 feet underground – thank you to Darren, Jeff, Ross, Sarah, Tim, Julia, Michelle, and Wenxin, among others.

Zack “Zuck” Hund, my lab partner for three years, was instrumental in showing me how the helium scattering instrument works, and helped me beyond that in furthering my academic and departmental career by giving me all his responsibilities (which worked out pretty well for both of us). Jacob Graham showed me *why* our instrument works, and undid years of blind tradition in the lab. In doing so, he made me (and to a certain extent, himself) obsolete in my own lab through automating the workday; beyond that, he taught me all about space, and ultimately not very much about the Matrix. I would also like to thank my helium lab ancestors, notably Ryan Brown for and Miriam Freedman, the latter in particular for blazing a trail from surface science to atmospheric chemistry that I look forward to following. As for the future of our lab, Ali McMillan, despite only being in our lab for a year, already feels like my superior, and I have every reason to believe she’ll go very far. Of course, none of us could have accomplished anything without Kevin “The Great” Gibson, whose selflessness in lab has always been abundantly clear, but was illustratively made manifest when he bought me beers that he had no interest in drinking.

I could not have accomplished an iota of research without the assistance of our exceptionally talented and generous staff: Helmut & Luigi, for showing me their machining chops; Dave & Gerry (R.I.P.), for fixing any electronic device without breaking a sweat; Kirk – I’m so sorry we brought you that temperature controller; John Phillips, easily the nicest man alive and among the most helpful; Melinda Moore, UChicago’s Swiss Army Knife incarnate, who has helped me in any number of ways and been a delight while doing so; Vera Dragisich, for mentoring me in the ways of the chemistry department; Mark Mendez, “Big” Mike Reedy, and Maria Jimenez for keeping the machinery running smoothly in the background.

So much of my research benefited enormously from the work done by our collaborators, all of whom are great scientists – Noah Plymale, Keith Wong, and Nate Lewis at CalTech; Cristina Díaz, Alberto Muzas, Marcos del Cueto, and Fernando Martín in Madrid; Davide Campi, Marco Bernasconi, and Giorgio Benedek in Italy. Thank you all.

I owe many tons of gratitude to the members of my class – notably Philip, Hunter, Garrett, Mark, "Real" Jon, Romit, Valentine, Jennifer, and fellow Sibener-ite Jon Raybin – all of whom owed me exactly nothing, and yet were extraordinarily selfless in getting me through my classes. I'd also like to thank the Baseliners for not swinging at the first pitch.

There are so many people that helped me reach and flourish at UChicago. At Boston College, Eben Cross was a superb mentor and friend, and I look forward to working with him down the road. Likewise, Prof. Paul Davidovits was my first chemistry mentor and, strangely, my first mentor in having a beard. Prof. Ken Metz made me love chemistry and assured me that I would one day be able to do magic.

On a more personal note, I would like to thank all of my friends and family who have always championed me and made me into a better person. Thank you to my Mom, for checking my homework every night, making me appreciate learning, and making the same joke about having incisive questions every time I publish a paper. Thank you to my Dad, for giving me the best education available, encouraging me when it felt like I couldn't make it through grad school, and openly acknowledging that you couldn't make heads or tails of anything I've ever published. Thank you to Kerry, Gwen, and Patrick, and to my grandparents and my extended family, for your undying love and support. And thank you to my new family – Bob, Mary, Sarah, Brian, Levi, and Ronan – for being so welcoming and giving, and making my life that much livelier.

Most of all, I want to thank my best friend and the love of my life, Laura Cullen Nihill. It's impossible for me to summarize in any meaningful way how much you mean to me, and the last time I tried, I ended up crying in front of all of our friends and family. You are the best wife anyone could ask for – you are the funniest, smartest, kindest, and most beautiful person I know, and I am such a better person for having found you. I am so excited to see you every day, and can't wait for everything that life has in store for us. Thank you for supporting me in following my dreams, pulling up your roots and coming with me to Boston, and being such a vocal supporter of my accomplishments. My life, my personality, my work, and my time are all dedicated to you, and they all shine brighter as a result. I will love you always.

Abstract

This thesis details a range of experiments and techniques that use the scattering of atomic beams from surfaces to both characterize a variety of interfaces and harness mass-specific scattering conditions to separate and enrich isotopic components in a mixture of gases.

Helium atom scattering has been used to characterize the surface structure and vibrational dynamics of methyl-terminated Ge(111), thereby elucidating the effects of organic termination on a rigid semiconductor interface. Helium atom scattering was employed as a surface-sensitive, non-destructive probe of the surface. By means of elastic gas-surface diffraction, this technique is capable of providing measurements of atomic spacing, step height, average atomic displacement as a function of surface temperature, gas-surface potential well depth, and surface Debye temperature. Inelastic time-of-flight studies provide highly resolved energy exchange measurements between helium atoms and collective lattice vibrations, or phonons; a collection of these measurements across a range of incident kinematic parameters allowed for a thorough mapping of low-energy phonons (e.g., the Rayleigh wave) across the surface Brillouin zone and subsequent comparison with complementary theoretical calculations.

The scattering of molecular beams – here, hydrogen and deuterium from methyl-terminated Si(111) – enables the measurement of the anisotropy of the gas-surface interaction potential through rotationally inelastic diffraction (RID), whereby incident atoms can exchange internal energy between translational and rotational modes and diffract into unique angular channels as a result. The probability of rotational excitations as a function of incident energy and angle were measured and compared with electronic structure and scattering calculations to

provide insight into the gas-surface interaction potential and hence the surface charge density distribution, revealing important details regarding the interaction of H_2 with an organic-functionalized semiconductor interface.

Aside from their use as probes for surface structure and dynamics, atomic beam sources are also demonstrated to enable the efficient separation of gaseous mixtures of isotopes by means of diffraction and differential condensation. In the former method, the kinematic conditions for elastic diffraction result in an incident beam of natural abundance neon diffracting into isotopically distinct angles, resulting in the enrichment of a desired isotope; this purification can be improved by exploiting the difference in arrival times of the two isotopes at a given final angle. In the latter method, the identical incident velocities of coexpanded isotopes lead to minor but important differences in their incident kinetic energies, and thus their probability of adsorbing on a sufficiently cold surface, resulting in preferential condensation of a given isotope that depends on the energy of the incident beam. Both of these isotope separation techniques are made possible by the narrow velocity distribution and velocity seeding effect offered only by high-Mach number supersonic beam sources.

These experiments underscore the utility of supersonically expanded atomic and molecular beam sources as both extraordinarily precise probes of surface structure and dynamics and as a means for high-throughput, non-dissociative isotopic enrichment methods.

Chapter 1

Introduction: The Versatility of Supersonic Molecular Beams

Molecular beam sources are extraordinarily interesting and useful tools – both as probes for structure and dynamics, and as means of controlling separating a gaseous mixture into its individual components. When gas molecules are forced into a small, high-pressure region, they collide with each other with such great frequency that they all attain essentially the same energy. When, by chance, some of these molecules find a tiny hole in the wall leading to a region of high vacuum, they escape the high-pressure zone with extremely narrow distributions of velocity, energy, and exit angles, and are collision-free due to the low pressure around them. To make these molecules move faster or slower, the nozzle in which they originate needs only to be heated or cooled, respectively. This seemingly simple discovery, bolstered by countless man-hours of refinement, is the driving force behind volumes of groundbreaking research and, more pertinently, to all of the experimental undertakings detailed herein.

While supersonic molecular beams were pioneered by (and owe a great deal to) scientists carrying out crossed-beam experiments, they can also be directed at a solid surface to measure fundamental details regarding its structure and dynamics. Of course, other probe particles can both achieve similar velocity distributions and be employed to precisely measure the dynamics of a crystal lattice – electrons, neutrons, and x-rays are key examples. The advantage of low-energy, neutral molecular beams is that they reflect off of the surface electron density, making this technique non-destructive, endlessly reproducible, and strictly sensitive to surface phenomena.

Due to the high velocities achieved during a supersonic expansion, molecular beams have de Broglie wavelengths on the order of surface lattice constants, meaning molecular beams will undergo quantum diffraction and reflect into discrete angular channels, enabling investigation of surface structure, vibrational dynamics, and phonon band structure. The ability to collect precise information on surface phenomena arises from the impressively narrow distribution of velocities attainable *via* a supersonic expansion, which is exceptionally narrow for beams of helium ($\Delta v/v$ <1%, FWHM; other gases struggle to get within 5x of that). The strength and versatility of helium atom scattering as an experimental technique is discussed at length in **Chapter 2**, along with the instrumentation used to carry out such experiments.

The power of helium atom scattering is exhibited in **Chapter 3**, where it is implemented to explore the surface structure of methyl-terminated Ge(111), a chemically passivated, technologically interesting interface with promising applications in high-speed circuitry and multijunction solar cells. This chapter contains measurements of surface quality and the extent of methyl termination, and also features a unique application of helium atom scattering that uses variable de Broglie wavelength scattering to precisely measure the step height of this interface.

Due to its narrow distribution of incident energies, helium atom scattering is also an unrivaled tool for measuring low-energy surface phonon modes. **Chapter 4** expounds on this capability through its focus on the vibrational dynamics and phonon band structure of CH_3-Ge(111), and demonstrates the accuracy of this technique through its comparison with density functional perturbation theory calculations, leading to a clearer understanding of the effects of organic functionalization on a semiconductor interface.

When a supersonic beam consists of molecular probes instead of atomic ones, the situation becomes more complex as rotational and vibrational degrees of freedom are

introduced. While the incident energies discussed in this work do not facilitate energy exchange between vibrational degrees of freedom, rotational modes of molecular beams can be accessed, leading to a new means of internal energy transfer upon striking a surface. Namely, when a molecule such as H_2 strikes a surface, it is capable of exchanging energy between its translational and rotational degrees of freedom, resulting in rotationally inelastic diffraction. This is the focus of **Chapter 5**, wherein hydrogen and deuterium molecules are scattered from another organic-functionalized surface, CH_3-Si(111), revealing details on the anisotropy of the gas-surface interaction potential and surface charge density. The experiments discussed in this chapter are paired with extensive computational work, resulting in the creation of an accurate potential energy surface that precisely identifies the classical turning points of the incident molecules and exposes a high degree of anisotropic character in the interaction potential at these points.

The final chapters of this thesis take advantage of a common technique in beam studies to yield an interesting and useful result. As discussed above, the most common means of changing the energy of a supersonic beam is raising or lowering the temperature of the source. However, a nifty alternative can achieve the same result: by seeding the probe gas in a lighter or heavier "carrier" gas, the frequent collisions with the carrier gas result in the probe gas being sped up or slowed down, respectively, causing it to attain roughly the same speed as the carrier gas. While this change in the velocity of the probe gas is traditionally the sole aim of such an arrangement, the act of endowing multiple components of a gaseous mixture with the same incident velocity also yields several profoundly interesting means of separating those components. When applied to a mixture of isotopes of a given element, the importance of a novel isotope separation technique cannot be understated.

When a gaseous mixture of isotopes is supersonically expanded, the seeding effect results in the all of the isotopes achieving the same velocity; however, the difference in the isotopes' masses results in isotopically unique incident energies and momenta. As predicted by the laws of quantum diffraction, this difference in incident energy results in each isotope diffracting into a distinct angular channel, allowing for the separation and enrichment of isotopes. **Chapter 6** demonstrates this effect for a beam of natural abundance neon reflecting from CH_3-Si(111), resulting in a substantial enrichment factor that can be maximized by scrutinizing the scattering conditions. Isotopic enrichment can be further improved by taking advantage temporal separation that results from the difference in flight times of two isotopes at a single reflected angle.

Lastly, **Chapter 7** embraces the incident energy difference in a supersonically co-expanded mixture of isotopes to introduce a more general isotope separation technique: differential condensation. When an atom strikes a surface, it is capable of exciting a vibrational mode by donating some of its incident kinetic energy to the surface, losing kinetic energy as a result. If the surface is sufficiently cold, it may not have enough energy to eject the incident species, resulting in the atom condensing on the surface. This process is mediated by the sticking coefficient, which is governed by, among other things, the kinetic energy of the incident particle. For two isotopes – here, the two major isotopes of argon in a natural abundance mixture – moving at the same velocity but different energies, as in a supersonic beam, this results in preferential condensation of the lighter species at low incident beam energies, and the preferential condensation of the heavier species at high incident beam energies, both of which can be used to enrich the mixture in the desired component. The techniques in **Chapters 6-7** offer interesting alternatives to the modern suite of inefficient isotope enrichment methods.

Chapter 2

Experimental Methods and Theory

This chapter provides a thorough description of the atomic scattering apparatus used to carry out the experiments detailed herein. This begins with a discussion of the atomic scattering theory and vacuum conditions that make these experiments possible and fruitful, and which are required for a full appreciation of the instrumentation and methods employed in this work. The experimental apparatus, illustrated in Figure 2-1, is then described in detail, with the primary regions of the instrument – the atomic beamline, the ultra-high vacuum (UHV) scattering chamber, and the UHV rotatable detector – discussed individually.

The research discussed in this thesis can be separated into two main types of experiments: diffraction and time-of-flight, and condensation. While both of these fields require the high-precision instrumentation described below, they fundamentally differ in their experimental approach. The theory and analytical techniques required for elastic diffraction and time-of-flight studies are required background for **Chapters 3-6**, and are the focus of this chapter. Additional theory must be considered when scattering with molecular instead of monatomic beams, as in **Chapter 5**; a separate discussion is included therein. The second class of experiments described in this work – those which use condensation as the primary experimental technique – are described in **Chapter 7**, in which they are the central focus.

Atomic Beam Scattering

Helium atom scattering is a unique experimental technique that takes advantage of low-energy, neutral, and chemically inert helium atoms to provide strictly surface-sensitive

measurements of structure and dynamics without affecting the chemical or physical composition of the surface of interest. In addition, since the classical turning point of an incident helium atom is several angstroms away from the surface atoms, the information provided by helium scattering is not derived from the bulk material. It has been applied to a variety of surfaces, including metals, semiconductors, insulators, and thin films, and has provided complementary information to other techniques such as low-energy electron diffraction (LEED), neutron scattering, and x-ray scattering, all of which sample layers beyond the surface.

Helium atom scattering was first demonstrated in 1930 in the diffraction studies carried out by Estermann and Stern from LiF and NaCl crystals.[1,2] Their experiments edified the argument for de Broglie's theory on the wavelike nature of particles; thermal helium beams range from 10 meV ($\lambda \sim 1.5$ Å) to 65 meV ($\lambda \sim 0.3$ Å), which range is similar to the wavelength of hard x-rays and the interatomic distances of crystal lattices. Combined with the fact that these relatively low energies are insufficient to allow the atoms to penetrate the surface electron density, this makes helium beams ideal for diffractive studies of surface structure.

For precise, high-resolution measurements of surface structure and dynamics, the atomic beam source must have high intensity, a narrow velocity distribution, and strong collimation. The supersonic molecular beam source utilized in these experiments fully meets these requirements, and is capable of achieving a flux greater than 10^{19} atoms sec^{-1} sr^{-1} while maintaining a velocity distribution $\Delta v/v < 1\%$ (FWHM).[3] The velocity distribution of a supersonic helium beam is significantly narrower than the velocity distributions of other probe atoms/molecules used in the research described herein (H_2, Ne, Ar); the precision requirements for those beam sources are discussed individually in their respective chapters.

Supersonic expansion of an atomic beam occurs when the following condition is met:

$$\frac{P_0}{P_b} = \left[\frac{1}{2}(\gamma+1)\right]^{\frac{\gamma}{\gamma+1}} \tag{2-1}$$

where P_0 is the stagnation pressure of the gas on the inlet side of the nozzle, P_b is the background pressure on the vacuum side of the nozzle, and γ is the specific heat ratio (C_p/C_v) of the gas ($\gamma \sim 2$ for helium). The velocity distribution is directly related to the Mach number of the expansion:

$$M = \sqrt{\frac{mv^2}{\gamma k_B T}} \tag{2-2}$$

where m is the mass of the gas atoms, v is the average gas velocity, k_B is Boltzmann's constant, and T is the parallel temperature of the beam; higher Mach numbers result in higher-quality expansions and narrower velocity distributions. The Mach number is determined by the frequency of collisions in the nozzle prior to expansion, and as such it is sensitive to the product of the backing pressure and nozzle diameter, $P_0 d$.[4] As flux increases proportionally to $P_0 d^2$, increasing the nozzle diameter d requires very high-throughput pumping in the vacuum chamber. Through implementation of high stagnation pressures and a small nozzle (15 μm diameter), the terminal Mach number in the beam source can surpass 200. Differential pumping of the beamline achieves the low background pressures required for supersonic expansion.

For a mixture of gases in the beam source – specifically one with a small fraction of heavier particles "seeded" in a larger fraction of a lighter carrier gas – the high frequency of collisions that take place in the nozzle cause the heavier particles to attain roughly the same velocity as the lighter particles, resulting in a monovelocity mixture of gases during the expansion. This seeding phenomenon is a means of increasing the velocity of a beam without

heating the nozzle source; moreover, it is a key component of the experiments carried out in **Chapters 6-7**, and is described in greater detail therein.

Ultra-High Vacuum

The surface scattering and condensation experiments described herein are possible only under ultra-high vacuum (UHV) conditions – where the background pressure is less than or equal to 10^{-9} Torr – for two predominant reasons. First, atomic scattering from surfaces requires an unobstructed path between the source and detector; the absence of gas-phase scattering can only be ensured at extremely low pressures and resultantly large mean free paths:

$$\lambda = \frac{k_B T}{1.414 P \sigma} \tag{2-3}$$

where T is the temperature, P is the background pressure, and σ is the scattering cross section; under UHV conditions, $\lambda \sim 10^5$ m. Second, molecular beam scattering requires reproducibly clean surfaces such that incident gas molecules can interact directly with the surface and not undesired contaminants. A primary source of contamination of water, which adsorbs to many surfaces below temperatures of ~160 K. This source of contamination can be mitigated by baking the chamber, resulting in background pressures on the order of 10^{-10} Torr, for which the time to form a monolayer surpasses 10^4 seconds. As such, experiments which required measurements to be taken at sample temperatures below 200 K were carried out in a sample chamber that was baked prior to scattering. A list of mean free paths and monolayer formation times is given for various backing pressures in Table 2-1.

Experimental Apparatus

Atomic Beamline

Ultra-high-purity gas (helium, H_2, D_2, neon, argon, or mixtures thereof) is controlled with a single-stage gas regulator (Matheson, M3006-677-S), operating at a backing pressure between 300-2500 psi. The purity of the gas entering the vacuum chamber is maintained by a series of in-line debris filters (Nupro). Prior to the vacuum chamber, the gas enters a custom-built elkonite (copper-tungsten alloy) nozzle capped with a 15 μm molybdenum pinhole (SPI). To enable temperature control of the nozzle (and therefore energy control of the atomic/molecular beam), the nozzle is affixed directly to the second stage of a closed-cycle helium refrigerator (Advanced Research Systems, DE-202); this refrigerator is capable of reaching temperatures as low as 25 K, as measured by a silicon diode (Lakeshore Cryotronics, DT-470-SD-13) attached to the end of the nozzle. The temperature can be adjusted using a resistive ribbon heater (Advanced Research Systems, 36 Ω) wrapped around the nozzle and controlled by a PID controller (Lakeshore Cryotronics, DRC 81C & 325) which provides a temperature stability of ±0.1 K; thermal loss from radiative heating is mitigated by wrapping the beam manifold with Mylar superinsulation.

The gas passes through the pinhole into three differentially pumped high-vacuum regions, undergoing an isenthalpic supersonic expansion as a result. The backing pressure of the gas is adjusted with the regulator to maximize the specular scattering intensity while minimizing the width of the beam (full width half max). The first stage of the beamline is pumped by an 8000 L/s diffusion oil pump (Varian, VHS-400) which has its foreline backed by a 70 m^3/h rotary vane pump (Pfeiffer, Duo65MC) and a 750 m^3/h roots blower (Pfeiffer, WKP 500AM) in series for maximum compression. After exiting the nozzle, the gaseous atoms travel only ~1 cm before

encountering a conical nickel skimmer (Beam Dynamics, Model 2), which extracts the center portion of the beam. After passing through the skimmer, the beam enters the second stage of the beamline, which is pumped with a 700 L/s diffusion oil pump (Edwards, Diffstak 160) and backed by a 70 m^3/h rotary vane pump (Pfeiffer, Duo65MC). The second differential region houses a chopper wheel used to mechanically modulate the beam, thereby providing timing resolution to scattering measurements. This 15 cm diameter wheel is mounted on a linear motion feedthrough (Huntington, VF 108) which allows three different modulation patterns to intersect the beam axis: single-shot (1% duty cycle) for time-of-flight measurements; square-wave (50% duty cycle) for diffraction and background-subtracted intensity measurements; and a pseudorandom 511-bit sequence (50% duty cycle) for cross-correlation chopping for inelastic time-of-flight.[5] A motor (Globe Motors, 75A1003-2) with specialized high-vacuum bearings (Barden Precision Bearings, SR4SSTA5) can spin the chopper wheel between 7 and 200 Hz, with chopping speed controlled by a function generator (Stanford Research Systems, DS335) that supplies AC voltage that is amplified with a stereo amplifier (Bogen, GS150). The chopper wheel contains triggering slots through which light from an LED source passes and is detected by a photon detector and converted into a TTL pulse to trigger the counting electronics (Multi-Channel Scaler). After modulation, the beam passes through the first aperture into the third beam stage; an exhaustive list of apertures and distances (measured relative to the chopper) are provided in Table 2-2. The third stage is pumped with a 135 L/s diffusion pump (Edwards, Diffstak 63) and backed by the same rotary vane pump as the second stage. Aside from providing a buffer between the second beam stage and the ultra-high vacuum scattering chamber, the third differential region also contains an in-line quadrupole mass spectrometer (Balzers, QMG 112) perpendicular to the beam line, allowing for characterization of the beam intensity

and velocity distribution prior to striking the crystal. Finally, the gas atoms pass through a gate valve into the scattering chamber.

UHV Scattering Chamber

The incident atomic/molecular beam is targeted at a sample mounted in an ultra-high vacuum scattering chamber. UHV conditions are achieved with a 2400 L/s diffusion pump (Varian, VHS-6) backed by a 12 m^3/h rotary vane pump (Pfeiffer, Duo10M), attached to the scattering chamber with a right-angle pneumatic gate valve. In order to trap oil and prevent contamination of the scattering chamber, this diffusion pump is separated from the right-angle valve by a baffle system cooled by a Freon refrigerator (Polycold PCT-200). Additional pumping is provided by a 60 L/s ion pump (Perkin-Elmer, 2106035); this pump is also in place to maintain vacuum conditions in the event the right-angle valve closes due to its interlock system with the diffusion pump. The lid of the scattering chamber is doubly differentially pumped using a series of three MoS_2-coated Teflon spring seals (Saint Gobain) to isolate the regions, allowing for rotation of the lid while maintaining ultra-high vacuum in the scattering chamber. The outer region of the lid is pumped with a 12 m^3/h rotary vane pump (Pfeiffer Duo10M) and the inner region is pumped with a 10 L/s ion pump (Gamma TiTan); the inner region can also be pumped by a sorption pump in order to initially achieve vacuum conditions.

The sample of interest is mounted on a six-axis (translation along x-, y-, and z-axes; tilt; polar; azimuth) manipulator (Vacuum Generators, HPT2), offset 5 cm from the chamber's center and resting directly above the scattering pin (which marks the geometric scattering center), with a custom-built mount and brackets. The crystal is cooled down to temperatures of ~28 K with a closed-cycle helium refrigerator (Advanced Research Systems, De-202B), the second stage of

which is connected to the sample mount with an OFHC copper bar and two copper braids. The sample mount is electrically isolated from the ground by a sapphire/indium joint between the OFCH copper bar and the copper braids. The crystal can be heated up to 850 K *via* a 0.500" resistive button heater (Heat Wave, 101137) affixed to the back of the back of the mount and powered by a power supply (HP, Harrison 6286A) externally controlled by one of two temperature controllers (Eurotherm, 818P; Lakeshore Cryotronics, 325); both temperature controllers are capable of heating/cooling the sample at a fixed ramp rate (K/s), which is necessary for precise measurements of adsorption/desorption temperatures. Depending on the temperature range required for a given set of experiments, the sample mount and thermometry devices can be installed accordingly: experiments requiring high temperatures (i.e. those described in **Chapters 3-6**) were carried out with a custom-built molybdenum mount whose temperature was monitored with two type-K thermocouples spot-welded directly to the mount and could be controlled to within ±0.1 K precision; experiments requiring low temperatures (i.e., those described in **Chapter 7**) were carried out with a custom-built copper mount whose temperature was monitored with a silicon diode (Lakeshore Cryotronics, DT-470-SD-13) and could be controlled to within ±0.05 K precision.

Additional information on the crystal and the gaseous atmosphere of the scattering chamber can gleaned from a suite of instrumentation affixed to the chamber and accessible *via* rotation of the lid. The background composition of the chamber can be characterized and monitored using a residual gas analyzer (Stanford Research Systems, 300 RGA). The quality of the crystal can be determined with several traditional surface analysis instruments, including reverse-view low-energy electron diffraction (LEED) using an integral electron gun (Princeton Research Instruments, RV-8-120). LEED can be used to collect electron diffraction spectra,

which provides the azimuthal orientation of the crystal; an example spectrum for CH_3-Si(111) is shown in Figure 2-2. Another tool for determining surface quality/composition is an Auger electron spectrometer (Phi 04-015), which uses a double-pass cylindrical mirror precision electron energy analyzer (Phi 15-255). Cleaning of certain crystals is also possible by sputtering with rare gas (typically argon) *via* another electron gun (Phi-015). The gas provided to this sputtering gun is introduced to the chamber by way of a UHV leak valve (Varian, 951-5106), which can provide pressures beginning on the 10^{-10} Torr scale. This leak valve, along with an identical leak valve terminated with a 1/8" stainless steel tube directed at the crystal, can also be used for effusively dosing gaseous species onto the crystal, as described in greater detail in **Chapter 7**.

Rotatable UHV Detector

After striking the crystal, the gas can be reflected into the ultra-high vacuum detector region, which is separated from the scattering chamber by a gate valve. The detector has several stages of differential pumping which limit the diffuse background and enable the detection of low cross-section scattering events. In order to measure the gaseous species that scatter from the crystal at a variety of final angles, the detector sits on a turntable capable of rotating ±20° about the crystal normal in the scattering plane; the detector position can be set manually or automatically with a computer-controlled motor with 0.1° precision, as measured by an optical encoder. The first stage of the chopper is pumped by 135 L/s diffusion oil pump (Edwards, Diffstak 63), which is backed by a 12 m^3/h rotary vane pump (Pfeiffer, Duo10M); this region is connected to the diffusion pump *via* a pneumatic gate valve and a liquid nitrogen-filled baffle trapping system. This region also contains another UHV leak valve (Varian, 951-5106) for calibrating and troubleshooting the detector. The second stage of the detector is pumped by a

200 L/s turbo pump (Balzers/Pfeiffer, TPU-170), which is backed by a 135 L/s diffusion oil pump (Edwards, Diffstak 63) and the same rotary vane pump as the first region of the detector. For experiments requiring increased resolution, the detector can be adjusted from a "short mode" (FWHM = 0.46°) to "long mode" (FWHM = 0.29°) by the addition of a 44.45 cm flight tube between the first and second regions; this addition causes a drop in total raw signal.

The second stage of the detector contains an axial ionizer (Extrel, 041-1) and a quadrupole mass spectrometer (QMS) rod assembly (Extrel, 7-324-9). Gaseous species are ionized *via* a heated tungsten filament, accelerated through a series of ion optics, filtered by the QMS rods, and collected with an electron multiplier (Photonis, 4816). A pneumatic gate valve connects the second stage to a liquid nitrogen-trapped 280 L/s diffusion oil pump (Edwards, Diffstak 100) for additional pumping. Pressures in the detector after baking the system can reach 7×10^{-11} Torr when both diffusion pumps are open to the detector; when the detector is not in use, the diffusion pumps are closed and pressures around 1×10^{-10} Torr are maintained by the turbo and backing pumps.

The electron multiplier converts collected ions into pulses between 10-22 mV in height and ~10 ns wide, which are sent through a 200x fast preamplifier (Ortec, VT120) to ensure full transmission to the counting electronics. After the pre-amplifier, the pulses are sent through another amplifier (Phillips Scientific, 771) and then pass through a discriminator (Phillips Scientific, 711) to remove unwanted background signal; the voltage of the discriminator can be adjusted depending on the application. The discriminator converts the raw pulses into NIM pulses with a height of 1.6 V and width of 50 ns. These NIM pulses can be measured directly, or converted into TTL pulses for counting with a multi-channel scaler or other data acquisition (DAQ) devices (National Instruments, CB-68LPR).

Data Analysis

Diffraction

Atomic and molecular beam diffraction provides a unique method for determining the size and orientation of surface unit cells, the quality of the surface, and the corrugation of the surface electronic density. Since the spot size of the atomic beam in this instrument is ~4 mm in diameter, these diffraction measurements provide a macroscopic sampling of the surface.

As discussed above, diffraction spectra are collected by setting the pre-collision chopper wheel to a square-wave pattern (50% duty cycle), where the open channel collects scattered signal and the closed channel collects background signal for modulation. For a given diffraction spectrum, the crystal is held at a fixed incident angle (θ_i) while the detector arm is rotated to measure reflectivity as a function of final scattering angle (θ_f); an illustrative schematic of atomic diffraction from CH_3-Si(111) is shown in Figure 2-3. Given the initial and final scattering angles, the parallel momentum transferred (ΔK) between the gas and surface can be calculated as follows:

$$\Delta K = k_0 \left(\sin\theta_f - \sin\theta_i \right); \tag{2-4}$$

$$k_0 = \frac{2\pi m L_{CD}}{h t_0}; \tag{2-5}$$

$$t_0 = \sqrt{\frac{m L_{CD}^2}{5 k_B T}}; \tag{2-6}$$

Where k_0 is the incident wavevector, m is the mass of the probe atom/molecule, L_{CD} is the total flight path from the chopper to the detector, h is Planck's constant, k_B is Boltzmann's constant,

and T is the temperature of the beam. For elastic diffraction to occur, the Bragg condition must hold as follows:

$$\Delta K = \overrightarrow{G_{hk}} = h\vec{b}_1 + k\vec{b}_2 , \tag{2-7}$$

where $\overrightarrow{G_{hk}}$ is the surface reciprocal lattice vector, which is composed of primitive reciprocal translation vectors $\vec{b}_1$ and $\vec{b}_2$ multiplied by diffraction indices h and k. These primitive reciprocal vectors are used to transform the reciprocal-space values into real-space values using the following orthogonality condition:

$$\vec{a}_i \bullet \vec{b}_j = 2\pi\delta_{ij} , \tag{2-8}$$

where $\vec{a}_i$ (i = 1, 2) and $\vec{b}_j$ (j = 1, 2) are the real- and reciprocal-space surface primitive unit-cell vectors, respectively, and δ_{ij} is the Kronecker delta function. Through these equations, the incident and final angles in a diffraction spectrum can be used to determine the reciprocal- and real-space lattice vectors that define the surface unit cell. Likewise, the surface quality (coherence length) can be inferred from the width of a specular peak, with smaller widths resulting from larger average domain sizes.

Helium scattering in particular is especially sensitive to surface quality, and can be used to detect steps on a given surface. This technique is utilized and described in greater detail in **Chapter 3** to determine the step height on the surface of methyl-terminated Ge(111). Specifically, the de Broglie wavelength of the incident He beam can interfere either constructively or destructively when its path length is altered as it reflects from terraces of different heights, similar to the interference of x-rays described by Bragg's law:

$$2d\sin\theta = n\lambda\,, \tag{2-9}$$

where d is the interlayer spacing, θ is the incident angle, λ is the wavelength, and n is an integer value when diffracted x-rays interfere constructively. As shown schematically in Figure 2-4, the application of Bragg's law to the diffraction of x-rays from a crystalline structure is analogous to the diffraction of helium atoms from terraces separated by a step height h, which results in constructive and destructive interference, respectively, when the following conditions are met:

$$k_0 h\cos\theta = n\pi\,; \tag{2-10}$$

$$k_0 h\cos\theta = (n+\tfrac{1}{2})\pi\,. \tag{2-11}$$

Time-of-flight

When an atomic beam strikes a surface, it is capable of undergoing an inelastic collision, resulting in the creation and/or annihilation of vibrational modes at the interface. Phonons – the collective vibrational modes of a surface – can provide important dynamical information about an interface, and so the need to precisely measure their distribution is of paramount interest. The energies of helium atoms in a supersonic beam are especially comparable to phonon energies, and their energy transfers with a given surface can be resolved with time-of-flight measurements, wherein inelastic collisions result in helium atoms arriving at the detector with faster (phonon annihilation) or slower (phonon creation) times than if they undergo elastic reflection, as illustrated in Figure 2-5. The total phonon dispersion across a surface Brillouin zone can be fully mapped out by collecting time-of-flight spectra at various kinematic conditions and azimuthal alignments, and comparing inelastic arrival times to the elastic arrival time for a set of incidence conditions.

Due to the isenthalpic nature of the supersonic expansion, the elastic time-of-flight can be predicted based on the nozzle temperature using Equation 2-6, and can be used to determine the beam energy as follows:

$$E_B = \tfrac{5}{2} k_B T \,. \tag{2-12}$$

For an inelastic event, the inelastic arrival time can be compared with the elastic arrival time to determine the final momentum of the reflected atom as follows:

$$k_f = \frac{m L_{SD}}{\hbar\left(t - t_0 \dfrac{L_{CS}}{L_{CD}} \right)}, \tag{2-13}$$

where L_{SD} is the sample-detector distance, L_{CS} is the chopper-sample distance, and L_{CD} is the chopper-detector distance. In order to quantify the energy exchanges that occur in inelastic scattering, time-of-flight spectra can be converted from the time domain to the energy domain; for this instrumental setup, the time conversion to energy exchange (ΔE) uses the following equation:

$$\Delta E = E_f - E_i = \tfrac{1}{2} m \left[\frac{L_{SD}^2}{\left(t - t_0 \dfrac{L_{CS}}{L_{CD}} \right)^2} - \frac{L_{CD}^2}{t_0^2} \right]. \tag{2-14}$$

The transformation to the energy-exchange domain does not change the area under a given inelastic peak, but the relative amplitude of an inelastic peak can change significantly due to the nonlinear relationship between t_0 and ΔE.[4] This nonlinear relationship is described by the

Jacobian of the transformation; for a distribution of intensities *f(t)* from time-of-flight and *f(ΔE)* from energy exchange, then

$$dN = f(t)dt = f(\Delta E)d\Delta E\,, \tag{2-15}$$

And the Jacobian of the transformation will become

$$\frac{dt(\Delta E)}{d\Delta E} = \frac{t^3}{mL_{SD}^2}. \tag{2-16}$$

As is evident, the amplitude of an inelastic time-of-flight peak depends on the time of its arrival and scales with the cube of time in its transformation to the energy-exchange spectrum. However, since the detector of this instrument is sensitive to number density and not particle flux, the ionization efficiency is inversely proportional to particle velocity due to slow-moving particles exhibiting a greater cross section for ionization and subsequent detection. As such, the above transformation must be given a corrective factor for the velocity, *v*, as follows:

$$f(\Delta E) = \left(\frac{t^3}{mL_{SD}^2}\right) v f(t) = \frac{t^2}{mL_{SD}}. \tag{2-17}$$

Since phonons can result from the discrete exchange of energy and parallel momentum between the surface and the probe atom, the existence and accessibility of a phonon can be determined by considering the conservation of momentum and energy. The conservation of surface-parallel momentum, as described in Equation 2-4, can be rewritten as

$$\Delta\vec{K} = \vec{K_f} - \vec{K_i}\,, \tag{2-18}$$

and can be combined with the conservation of energy law,

$$\frac{\hbar^2 k_f^2}{2m} = \frac{\hbar^2 k_i^2}{2m} + \Delta E \,, \tag{2-19}$$

to generate a scan curve, which defines the relationship between ΔE and ΔK as follows:

$$\Delta E = \frac{\left(\sin\theta_i + \frac{\Delta K}{k_0}\right)^2}{\sin^2\theta_f} - 1 \,. \tag{2-20}$$

By combining the conservation of momentum and energy, a scan curve represents the accessible energy exchanges for a given exchange in parallel momentum. As such, the intersection of a scan curve with a dispersion curve represents a kinematically accessible inelastic event – a phonon creation or annihilation – which may then be observed as an inelastic peak in a given time-of-flight spectrum.

Table 2-1

Degree of Vacuum	Pressure (Torr)	Gas Density (molecules/m^3)	Mean Free Path (m)	Time/ML (s)
Atmospheric	760	2×10^{25}	7×10^{-8}	10^{-9}
Low	1	3×10^{22}	5×10^{-5}	10^{-6}
Medium	10^{-3}	3×10^{19}	5×10^{-2}	10^{-3}
High (HV)	10^{-6}	3×10^{16}	50	1
Ultra-High (UHV)	10^{-10}	3×10^{12}	5×10^{5}	10^{4}

Pressures and instrumental conditions for varied degrees of vacuum.

Table 2-2

Aperture	Aperture Size	Distance from Chopper (Short Mode) [cm]	Distance from Chopper (Long Mode) [cm]
Nozzle	15 μm	-13.81	-13.81
Skimmer	0.5 mm	-12.81	-12.81
Chopper	Variable	0	0
Aperture 1	0.89 mm	2.66	2.66
Balzers filament	N/A	17.60	17.60
Aperture 2	1.93 mm	22.35	22.35
Sample	~4 mm	49.96	49.96
Aperture 3	4.45 mm	76.88	76.88
Aperture 4	5.56 mm	95.88	140.33
Aperture 5	5.79 mm	103.36	147.81
Ionizer entrance plate	6.35 mm	106.74	151.19
Filament	N/A	107.78	152.23

Aperture sizes and distances (measured from the chopper) in short and long detector modes.

Figure 2-1

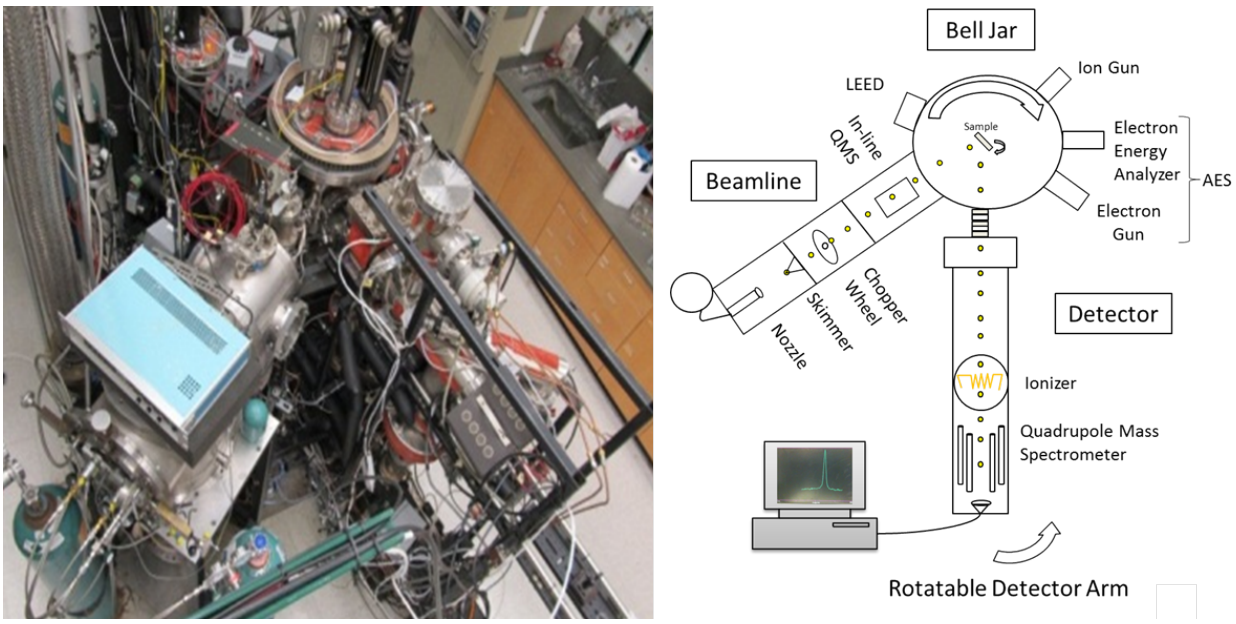

Aerial view of helium atom scattering apparatus (left) and schematic view illustrating the primary components of the apparatus (right).

Figure 2-2

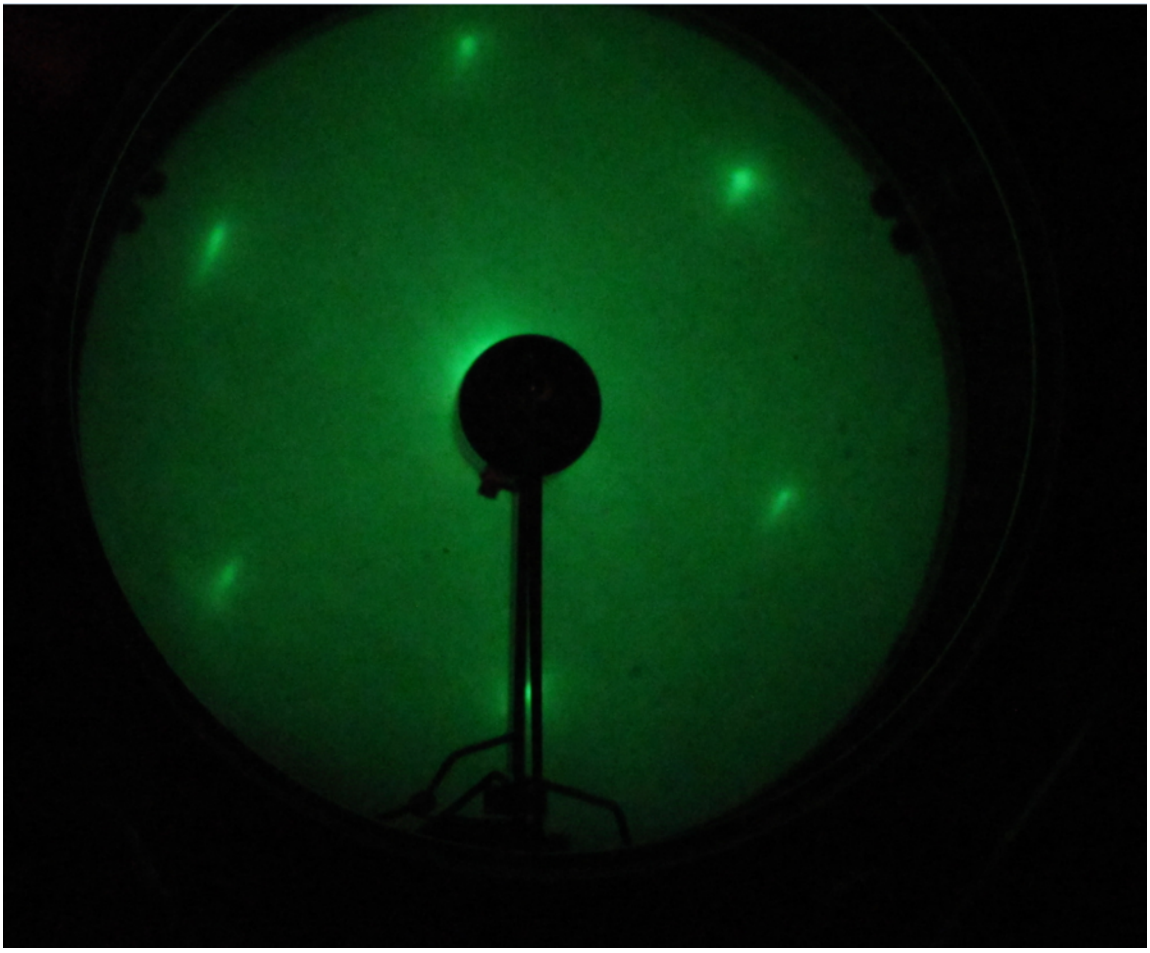

Representative LEED spectrum of CH_3-Si(111).

Figure 2-3

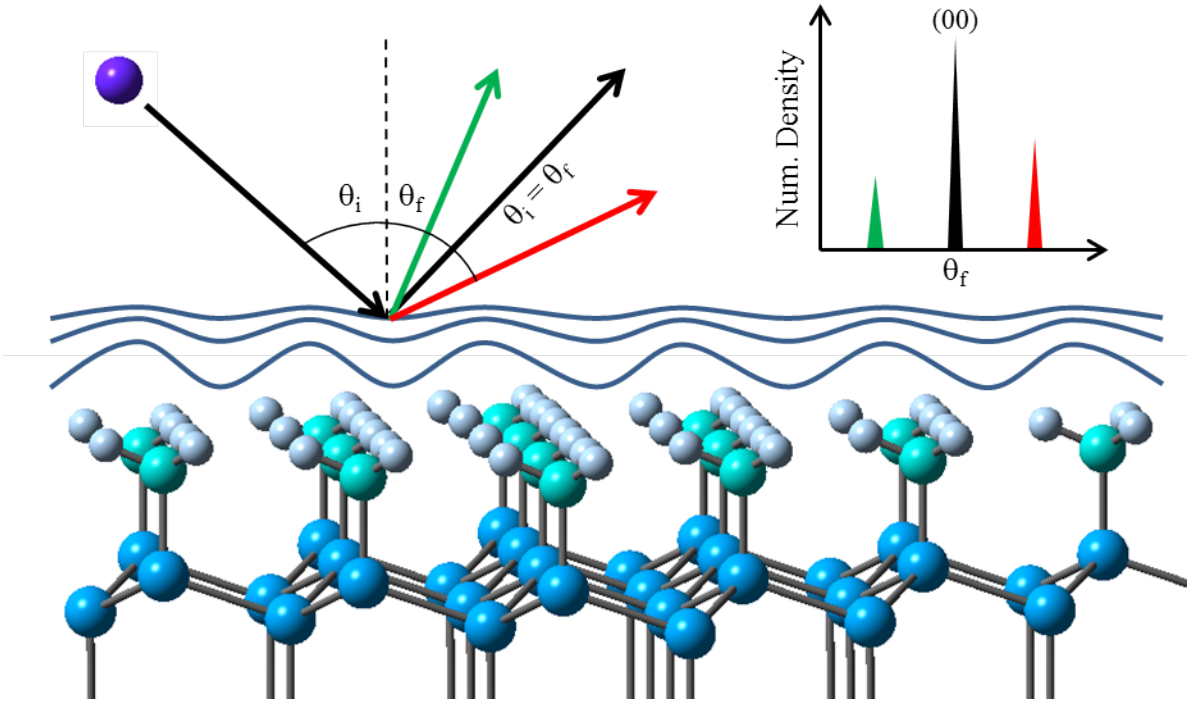

Illustration of atomic diffraction from CH_3-Si(111), with resultant diffraction spectrum.

Figure 2-4

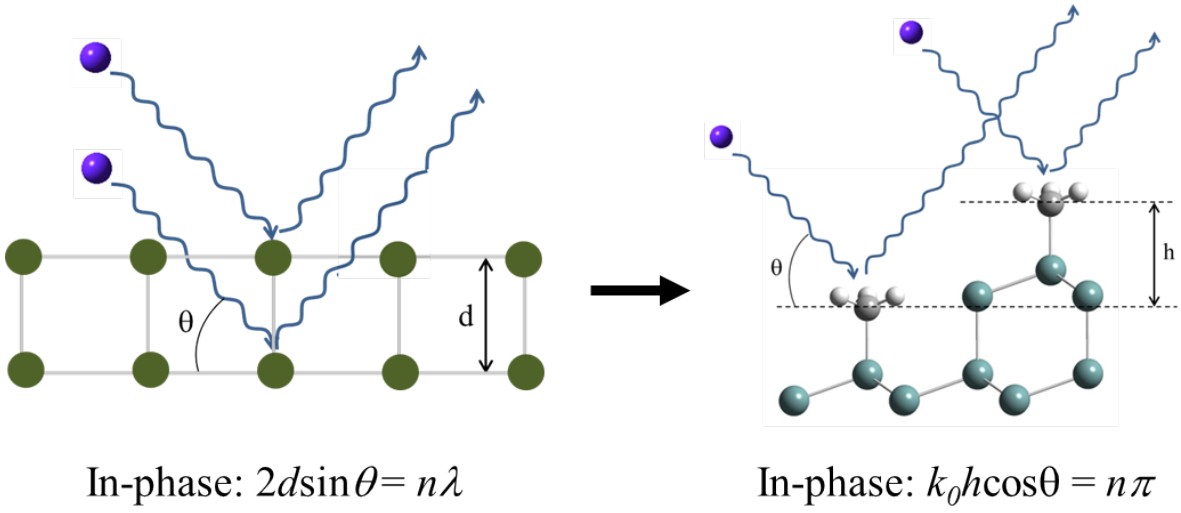

Illustration of the equivalence of applying Bragg's law for x-ray diffraction from a crystal (left) to helium diffraction from a stepped surface (right).

Figure 2-5

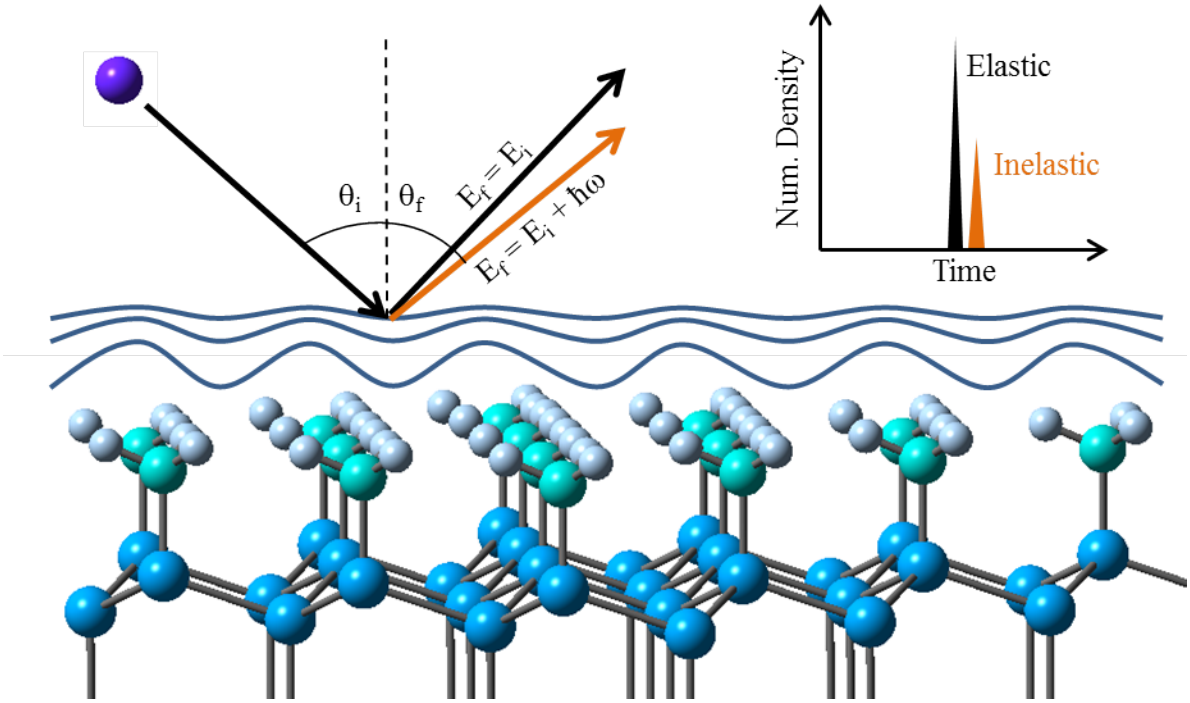

Illustration of inelastic scattering from CH_3-Si(111), with resultant time-of-flight spectrum.

Chapter 3

Atomic Surface Structure of CH_3-Ge(111) Characterized by Helium Atom Diffraction and Density Functional Theory

This chapter contains an article that was reproduced in part with permission from The Journal of Physical Chemistry C. Copyright 2015 American Chemical Society.[6]

The atomic-scale surface structure of methyl-terminated germanium (111) has been characterized by using a combination of helium atom scattering and density functional theory. High-resolution helium diffraction patterns taken along both the $<\bar{1}2\bar{1}>$ and $<01\bar{1}>$ azimuthal directions reveal a hexagonal packing arrangement with a 4.00 ± 0.02 Å lattice constant, indicating a commensurate (1x1) methyl termination of the primitive Ge(111) surface. Taking advantage of Bragg and anti-Bragg diffraction conditions, a step height of 3.28 ± 0.02 Å at the surface has been extracted using variable de Broglie wavelength specular scattering; this measurement agrees well with bulk values from CH_3-Ge(111) electronic structure calculations reported herein. Density functional theory showed that methyl termination of the Ge(111) surface induces a mild inward relaxation of 1.66% and 0.60% from bulk values for the first and second Ge-Ge bilayer spacings, respectively. The DFT-calculated rotational activation barrier of a single methyl group about the Ge-C axis on a fixed methyl-terminated Ge(111) surface was found to be approximately 55 meV, as compared to 32 meV for a methyl group on the H-Ge(111) surface, sufficient to hinder the free rotation of the methyl groups on the Ge(111) surface at room temperature. However, accurate MD simulations demonstrate that cooperative motion of neighboring methyl groups allows a fraction of the methyl groups to fully rotate on the

picosecond timescale. These experimental data in conjunction with theory provide a quantitative evaluation of the atomic-scale surface structure for this largely unexplored, yet technologically interesting, hybrid organic-semiconductor interface.

Introduction

High-quality Ge surfaces are desirable for applications in high-speed circuits and the collection of infrared radiation in multijunction solar cells due to their high hole-carrier mobility (4 times that of Si) and 0.67 eV band gap.[7–10] The high surface-state density of the GeO_x/Ge interface and the presence of unstable, water-soluble GeO_2 sites have however inhibited the commercial implementation of Ge-based technology.[11,12] Methods that passivate the Ge surface while preventing the formation of an oxide overlayer are therefore highly desirable. For example, hydrogenation of the semiconductor surface *via* chemisorption deconstructs Si(100)-(2x1) or Ge(100)-(2x1) back to their primitive (1x1) structure, creating large, atomically flat terraces of surface atoms passivated by a single layer of hydrogen. Hydrogen-termination of Si(111) and Ge(111) also deconstruct the well-known (7x7) and (2x8) clean structures for Si and Ge, respectively, and represent two of the simplest semiconductor surfaces, retaining a bulk-like structure except for mild relaxations of their outermost bilayer spacings; therefore these surfaces have attracted considerable interest with respect to elucidating their surface structure through both theory and experiment.[13–20]

Hydrogen passivation of Ge does not provide the same long-term protection against oxidation and reconstruction as seen with H-Si.[21,22] As with Si, the high quality and functionality of the hydrogen-terminated Ge surface can be used as a platform for grafting 1-alkenes to the H-Ge(111) surface to form a stable C-Ge bond.[23–27] Alkylation of the Ge surface has proven to be a robust method for creating densely packed, long-chain alkyl layers that add

resistance to oxidation and protect the electronic properties against corrosion due to moisture.[28–30] The H-Si(111) surface has been alkylated with Grignard reagents to produce functionalized Si surfaces of high perfection that exhibit correspondingly low densities of electronic defects.[31–34] Similarly, a two-step halogenation/alkylation procedure has recently been used to create chemically bonded hydrocarbon monolayers on the Ge(111) surface.[35,36] Methylation of the Ge(111) surface has the capability to form a complete monolayer, because the Ge lattice spacing is sufficiently large that the van der Waals radii of the methyl groups do not overlap extensively, resulting in a well-ordered, air-stable interface.

We describe herein a combined experimental and theoretical study of the atomic surface structure of CH_3-Ge(111). This work represents an extension of our previous studies of the structure and phonon dynamics of CH_3-Si(111) to the Ge system.[37–40] High-resolution helium atom scattering (HAS) and density functional theory (DFT) have been used to assess the surface structure, the effects of methyl termination on the Ge(111) bilayer spacings and step heights, and the extent of rotation of methyl groups on the (1x1) surface. Low-energy neutral helium atom scattering provides a nondestructive, atomic probe of structure and low-energy vibrations, with complete surface sensitivity. As will be shown herein, the methyl packing, in-plane lattice constant, and average domain size have been determined by analysis of helium diffraction patterns, including in- and out-of-phase scattering with respect to the surface normal. Due to its extremely high sensitivity to defects and exclusive surface sensitivity, a precise application of helium scattering exploiting Bragg and anti-Bragg diffraction conditions has allowed for the quantification of the CH_3-Ge(111) surface step height. Density functional theory was applied to calculate the lattice parameters, bond lengths, and bilayer spacings of CH_3-Ge(111), indicating first- and second-interlayer spacings slightly contracted from bulk values. The theoretical

approach was validated with the H-Ge(111) surface, showing significant bilayer contractions, in agreement with other previously reported experimental and theoretical results. As an additional test of our slab model, the high-energy molecular vibrational modes were calculated and showed consistency with experimental FTIR and HREELS peak assignments. The rotational dynamics of the methyl group on the fully methylated Ge(111) surface were also investigated with DFT and MD simulations. DFT suggests that the rotational barrier is sufficient to hindered the free rotation of methyl groups for a fixed surface, whereas MD simulations allowing for motion of neighboring methyl groups exhibit full rotations for some methyl groups on the picosecond timescale at room temperature.

Materials and Methods

Methyl-Ge(111) Sample Preparation

Unless otherwise noted, chemicals were obtained from Sigma-Aldrich or Fisher Scientific and were used as received. Water was obtained from a Barnstead E-Pure water purification system and had a resistivity of 18.2 MΩ-cm. 10% HF(aq) solutions were prepared by diluting 48 wt % HF (Transene). 3.0 M methylmagnesium chloride was purchased from Fisher Scientific and was used without further purification.

For scattering experiments, double-side polished, undoped Ge wafers (El-Cat Inc.) oriented within ± 0.1º of the (111) crystal plane were cut to the desired size using a diamond scribe. The samples had a resistivity > 30 Ω-cm. Immediately prior to surface modification, the samples were cleaned by rinsing sequentially with water, methanol, acetone, methanol, and water, followed by 5 min sonication in acetone and 5 min sonication in methanol. The samples were then repeatedly dipped in 10% HF(aq) for 1 min and in 30% H_2O_2(aq) for 1 min, with a

water rinse between steps. After 3 cycles of etching and oxidation, the samples were dipped in 10% HF (aq) for 1 min (a final time), rinsed with water, and dried under a stream of Ar. Cleaned Ge samples were loaded into a tube furnace that was repeatedly purged with He and pumped out before being pumped down to < 0.5 mTorr. Hydrogen termination of Ge surfaces was achieved by annealing the samples at 850 ºC for 15 min under 1 atm of H_2 at a flow rate of 500 SCCM. The samples were cooled to < 100 ºC under H_2 and were immediately transferred into a N_2-purged flushbox upon removal from the tube furnace.

H-terminated Ge(111) surfaces were loaded into an N_2 purged flushbox, rinsed with anhydrous tetrahydrofuran (THF), and then methylated in 3.0 M CH_3MgCl for 59.5 hr at 50 ºC. Methylated surfaces were then rinsed thoroughly with anhydrous THF; removed from the N_2-purged flushbox; sequentially sonicated for 10 min in THF, methanol, and water; and dried under a stream of Ar. For transport from Pasadena, CA to Chicago, IL, to minimize sample degradation, the samples were shipped under high vacuum in a sealed container.

Helium Scattering Instrumentation

An ultra-high vacuum (UHV) helium atom scattering apparatus with high energy and angular resolution was employed to measure the structure of methylated-Ge(111). The apparatus has been described previously.[41] The apparatus consists of three regions: a differentially pumped beam source, a UHV sample chamber, and a rotatable detector arm with a total flight path of 1.5230 m (chopper-to-crystal distance of 0.4996 m, crystal-to-ionizer distance of 1.0234 m).

Helium was expanded through a 15 μm nozzle source, which was cooled by a closed-cycle helium refrigerator, to generate a nearly monochromatic ($\Delta v/v \leq 1\%$, FWHM) supersonic neutral helium beam. A mechanical chopper modulated the helium beam in the first

differentially pumped region of the beam line with a 50% duty cycle. The beam was collimated into a 4 mm spot on the crystal surface, which was housed in the UHV surface-scattering chamber (base pressure 3 x 10^{-10} Torr). The CH_3-Ge(111) crystals were mounted onto a six-axis manipulator that could be positioned precisely to control the incident angle, θ_i, the azimuthal angle, ϕ, and the tilt, χ, with respect to the scattering plane. Sample temperatures ranging from 30 K – 900 K were achieved using a button heater and a second closed-cycle helium refrigerator. Reflected atoms entered a triply differentially pumped rotatable detector arm, were ionized *via* electron bombardment, and then filtered using a quadrupole mass spectrometer.

The beam energies in these experiments ranged from 17 to 67 meV (incident wave vector, k_i = 5.7–11.3 $Å^{-1}$), and the surface temperatures generally ranged from 140 to 200 K. At the start of each set of experiments, the sample was first flashed to 650 K to remove trace adsorbates from the surface, and then quenched to the sample temperature that was used during data acquisition. Previous work has demonstrated that similar methyl surface moieties are stable at these temperatures; the stability of the surfaces investigated was confirmed by highly sensitive helium reflectivity measurements as described herein. Diffraction patterns were recorded by aligning the crystal at a given incident angle, θ_i, and then using a computer-controlled motor to scan the detector through the final angle, θ_f.

Density Functional Theory Computational Details

The structural properties of the H-Ge(111) and CH_3-Ge(111) surfaces were calculated using density functional theory, as implemented in the QUANTUM-ESPRESSO package[42] using a norm-conserving pseudopotential for Ge and ultrasoft pseudopotentials[43] for C and H. Both the local-density approximation[44] (LDA) and the generalized gradient Perdew-Burke-Ernzerhof

approximation[45] (PBE) for the exchange-correlation energy functional were used. The electronic wave functions were expanded in plane waves up to a 28 Ry energy cut-off and a 280 Ry charge density cutoff. We optimized the bulk geometry by integrating the Brillouin zone over a 6x6x6 Monkhorst-Pack mesh.[46] The resulting equilibrium lattice parameters were a = 5.62 Å for the LDA and a = 5.77 Å for PBE, in good agreement with an experimental value of a = 5.657 Å.[47] The surface was modeled with a slab geometry and periodic boundary conditions (PBC); the slabs were composed of 18 germanium atom layers with methyl groups adsorbed on both sides, which were separated by a 12 Å-wide vacuum gap. The surface Brillouin zone (SBZ) was sampled over a Monkhorst-Pack grid of 6x6x1 k-points.[46] Atomic positions were relaxed until the forces were below a $5 \cdot 10^{-5}$ a.u. threshold. The vibrational frequencies at the Gamma point were calculated by diagonalizing the dynamical matrix calculated within the density functional perturbation theory (DFPT).[48]

To analyze the motion of the methyl groups at room temperature, in particular to verify the possibility of a free rotation, *ab-initio* Born-Oppenheimer molecular dynamics calculations were performed in an NVE ensemble with an average temperature of 300 K using the CP2K suite of programs[49] with a time step of 1.5 fs. In CP2K simulations Kohn-Sham (KS) orbitals were expanded on a triple-zeta-valence plus polarization (TZVP) Gaussian-type basis set, while the charge density was expanded in a plane-wave basis set with a cut-off of 240 Ry, to efficiently solve the Poisson equation within periodic boundary conditions using the Quickstep scheme.[49] Brillouin zone integration was restricted to the 4x4 and 5x5 supercell Gamma point. CP2K simulations were performed only for with the PBE functional and using Godecker-Teter-Hutter (GTH) pseudopotentials.[50,51]

Results and Discussion

Helium Diffraction

Figure 3-1 shows diffraction scans taken for CH_3-Ge(111) aligned on both the $\langle \bar{1}2\bar{1} \rangle$ (black) and $\langle 01\bar{1} \rangle$ (red) azimuthal directions, vertically offset for clarity. These angular distributions are plots of the reflected helium intensity as a function of the surface parallel momentum transfer, ΔK. Both distributions were taken with the same incident beam energy, E_i = 44 meV (k_i = 9.2 Å^{-1}), and crystal temperature, T_s = 140 K. The arrangement of the diffraction peaks is given by the periodicity of the surface, so knowledge of the azimuthal symmetry and the spacings of the diffraction peaks allows for the determination of the surface unit cell parameters. Elastic diffraction peaks arise when the kinematic condition for Bragg diffraction for in-plane scattering is met, as given by

$$\Delta\vec{K} = \vec{K_f} - \vec{K_i} = \vec{k_f}\sin\theta_f - \vec{k_i}\sin\theta_i = \vec{G_{mn}} \tag{3-1}$$

where

$$\vec{G_{mn}} = m\vec{b_1} + n\vec{b_2} \tag{3-2}$$

and

$$\vec{b_1} = 2\pi \frac{\vec{a_2} \times \hat{z}}{\vec{a_1} \bullet \left(\vec{a_2} \times \hat{z}\right)} \tag{3-3}$$

where $\vec{K_f}$ and $\vec{K_i}$ are the surface parallel components of the helium wavevectors, θ_i and θ_f are the initial and final scattering angles, $\vec{G_{mn}}$ is the surface reciprocal lattice vector, m and n are the

diffraction indices, $\vec{b}_1$ and $\vec{b}_2$ are the reciprocal lattice vectors, $\vec{a}_1$ and $\vec{a}_2$ are the primitive real space lattice vectors, and $\hat{z}$ is the surface normal unit vector. The spacings between specular (ΔK = 0 Å^{-1}) and the first-order diffraction peaks observed at ΔK = 1.82 Å^{-1} and 3.14 Å^{-1} for the $\langle \bar{1}2\bar{1} \rangle$ and $\langle 01\bar{1} \rangle$ alignments, respectively, correspond to a real space lattice constant of 4.00 ± 0.02 Å for the hexagonal close-packed arrangement of the CH_3-Ge(111) surface. This value is in excellent agreement with the known spacing (4.00 Å) for the native Ge(111) surface;[52] hence the data are fully consistent with the formation of a (1x1) commensurate monolayer of methyl groups on the Ge(111) surface, as visualized in the inset of Figure 3-1.

To a first approximation, the helium beam is scattered coherently within domains of length l_c; this coherence length is the approximate size of the atomically flat terraces of CH_3-Ge(111), separated by domain boundaries or other structural defects**.** The widths of the helium diffraction peaks are used to obtain the coherence length of CH_3-Ge(111), with narrower diffraction peaks corresponding to larger domain sizes. It has been shown previously[53] that the measured specular width, $\Delta\theta_{exp}$, is a convolution of the instrument function broadening, $\Delta\theta_{inst}$, and the domain size broadening, $\Delta\theta_w$. The measured broadening therefore allows measurement of the domain size using

$$\Delta\theta_{\exp}^2 = \Delta\theta_w^2 + \Delta\theta_{inst}^2 \tag{3-4}$$

$$l_c = \frac{5.54}{\Delta\theta_w k_i \cos\theta_f}. \tag{3-5}$$

The coherence length measurements were taken in-phase, with a low beam energy of ~16.5 meV to minimize the diffuse elastic and surface defect contributions (see below) to the linewidth.

High resolution was obtained using a crystal-to-ionizer distance of 1.0234 m, allowing for a narrow acceptance angle of 0.29° (~0.02 $Å^{-1}$) and measurements of domain sizes up to ~900 Å. The average measured width of the specular peaks, FWHM = 0.46°, provides a coherence length of ~170 Å for CH_3-Ge(111); thus, the average domain spans over nearly 50 methyl groups in a given direction. The mean terrace size of CH_3-Ge(111) is half of what has been measured in prior work for an analogous surface, CH_3-Si(111), which is consistent with the lower helium reflectivity for CH_3-Ge(111) relative to CH_3-Si(111).[37]

Normalized helium diffraction spectra taken from both CH_3-Ge(111) and CH_3-Si(111) are shown in Figure 3-2. The larger ΔK spacing observed in the CH_3-Si(111) diffraction pattern is a function of its smaller real space lattice constant (3.82 Å). The relative intensities between the specular and first-order diffraction peaks are similar for the CH_3-Ge(111) and CH_3-Si(111) surfaces. These low-energy helium scattering potentials are directly related to the surface electron densities,[54] which we expect to be similar for two semiconductor crystals terminated with the same commensurate methyl layer. One notable difference between the two diffraction patterns was the appearance of broad shoulders, or "wings," on the CH_3-Ge(111) specular diffraction peak; this broadening of the diffraction profile provides information on how defects decorate the CH_3-Ge(111) surface.

Surface imperfections like point defects, steps, domains, facets, and superstructures produce characteristic modifications to the elastic intensity and can therefore be qualitatively identified by visual inspection of the helium diffraction spectra. These static defects cause deviations from the ideal diffraction pattern to include splitting or broadening of peaks, streaks, or background.[55] Not all intensity is scattered elastically; excitations of phonons, plasmons, or electronic band transitions are all considered dynamic defects. Phonons have been shown to play

a major role in the scattering and vibrational dynamics of methylated semiconductor surfaces;[39] and an extensive characterization of phonons spanning the surface Brillouin zone for CH_3-Ge(111) will be discussed separately.[56] Multi-phonon scattering causes the uniform background while single-phonon excitations contribute significantly to the wings of the specular peak.[57,58] The broadening due to phonon excitations is dependent on energy and this contribution can be reduced by lowering the incident beam energy used for CH_3-Ge(111) diffraction (Figure 3-2, inset). However, the intensity decay and narrowing of the diffraction lineshape is not strictly a monotonic function of decreasing beam energy, but instead shows characteristic oscillations that are only possible for stepped structures.[59] Unlike regular step arrays, randomly distributed steps do not cause diffraction peak splitting, instead they only cause peak broadening around a sharp central spike, consistent with the behavior observed herein.[60,61] By exploiting the kinematic conditions, which include the beam energy and scattering angles, the role of randomly distributed steps on the surface can be investigated further *via* coherent and incoherent scattering from terraces at differing heights.

The stepped nature of the surface was surveyed by scattering under both in-phase (Bragg) and out-of-phase (anti-Bragg) helium diffraction conditions. Helium atoms are not able to penetrate the surface and scatter from bulk layers, differences in their path lengths arise due to the presence of steps on the surface. The in-phase diffraction conditions correspond to constructive interference of the de Broglie waves of helium atoms specularly scattered from adjacent terraces, separated by steps, satisfying

$$k_i h\left(\cos\theta_i + \cos\theta_f\right) = 2k_i h\cos\theta_i = 2n\pi\,, \tag{3-6}$$

where h is the step height and n is an integer value. Similarly, the out-of-phase conditions

$$k_i h\left(\cos\theta_i + \cos\theta_f\right) = 2k_i h\cos\theta_i = (2n+1)\pi \tag{3-7}$$

correspond to destructive interference between helium atoms. With known scattering conditions, these expressions allow for a unique determination of the step height of the CH_3-Ge(111) surface.

Figure 3-3(a) shows three examples of our drift spectra, which show the relative intensity of a specularly-scattered helium beam as a function of the surface-perpendicular component of the incident wavevector, $k_{perpendicular}$. Specifically, the specular intensity was monitored at three different incident angles while the temperature of the beam nozzle source was allowed to slowly drift from room temperature to 100 K over the course of ~ 1 hr. These runs were also repeated while undergoing a controlled drift from 100 K up to room temperature, and no significant difference was observed between the two data sets. The temperature reading from a diode attached directly to the nozzle source was calibrated against the actual helium beam energy by use of a series of time-of-flight runs over the range of nozzle temperatures.

Peaks and dips in the drift spectra arise from coherent and incoherent scattering accessed by varying the beam energy, or the incident angle (Figure 3-3(b)), of the incoming helium atoms. The peak maxima and minima in our drift spectra (Figure 3-3(a)) correspond to the different in-(n) and out-of-phase (n + 0.5) scattering conditions, respectively. Figure 3-3(c) shows diffraction spectra for the n =7 and n = 7.5 conditions. The drift spectra taken at three different incident angles exhibited the same k_{perp} peak maxima and minima, within experimental error. The baselines of the scattered intensities have been normalized to account for changes associated with Debye-Waller effects and a changing helium beam flux over the temperature range of data collection. The step height was extracted from each peak maximum and minimum, and these

values were then averaged. The experimental data yield a calculated step height of 3.28 ± 0.02 Å. This value, within the precision of these measurements, is equivalent to the (111) interlayer spacing of 3.27 Å known for the ideal, unrelaxed diamond-lattice configuration of Ge(111).[15,18] Electronic structure calculations reported herein are in agreement with this experimentally measured CH_3-Ge(111) step height and will be used to provide further insight into substrate relaxations not extractable from scattering measurements.

Model Calculations

To complement our scattering results, a slab model of the (1x1) methyl-terminated Ge(111) interface was generated and investigated using density functional theory. Two approximations were used to calculate the crystal structure, with the equilibrium lattice parameters a = 5.62 Å for the LDA and a = 5.77 Å for the PBE approximation. In the optimized CH_3-Ge(111) structure, the calculated bond lengths for C-H and C-Ge were 1.102 Å and 1.974 Å, respectively, for the LDA functional (surface lattice constant = 3.972 Å) while 1.098 Å and 2.008 Å were obtained within the PBE approximation (surface lattice constant = 4.076 Å). Additionally, the dihedral angle for H-C-Ge-Ge, which defines the rotation of the surface methyl groups about the Ge-C axis, was found to be 41.9° (LDA) and 41.3° (PBE), both of which are slightly larger than the value of 37.7º calculated for the analogous CH_3-Si(111) surface.[49] In addition to the crystal lattice constants and adlayer bond lengths, additional structural parameters, such as the Ge-Ge bilayer spacings, which play a major role in the interfacial charge density, have also been calculated. The first (d_{12}) and second (d_{23}) Ge bilayer spacings sum together to produce the surface step height ($d_{step} = d_{12} + d_{23}$), as visualized in Figure 3-4, and also measured *via* helium scattering.

As an initial test of our CH_3-Ge(111) slab surface, the molecular vibrational modes of the adsorbed methyl groups were calculated using density functional perturbation theory at the Γ-point. The frequencies of the six high-energy molecular modes, including the methyl stretching, deformation, and rocking are presented in Table 3-1, *via* both the LDA and PBE approximation. The calculated frequencies are compared with experimentally observed peaks from Wong *et al.*[63] as measured using Fourier transform infrared spectroscopy (FTIR) and high-resolution electron energy loss spectroscopy (HREELS). Overall, the consistency observed between our calculated frequencies and both the FTIR and HREELS data provide further validation of our model of the CH_3-Ge(111) interface.

The effects of an adlayer, such as hydrogen, on the atomic structure and spacings of Ge and Si semiconductors have been observed with both experiment and theory.[13–20] We report herein the first investigation into the structural changes of the Ge(111) interface due to methyl termination. As a consistency check, the model and calculations have also been applied to H-Ge(111)-(1x1). Table 3-2 shows the first and second bilayer spacings, along with the Ge-H bond length. A significant inward contraction of d_{12} was obtained, which agrees with theory[15,19] and experiment.[18] A smaller inward contraction was obtained for d_{23} relative to ideal Ge(111) bulk values. Inward relaxations are commonly found on the outermost layers of bare surfaces, whereas hydrogen would be expected to saturate the dangling bonds and remove this relaxation. Instead, the contraction of the bilayer spacing has been explained by Kaxiras,[15] who argues that an electronegativity difference between Ge and H induces a dipole moment, which would be partially cancelled by a charge transfer from the Ge-H bond into the Ge-Ge back bond. This charge transfer would strengthen and shorten the back bond, causing the outer Ge layer to contract towards the bulk. As a result of the inward contraction of both the first and second

bilayer, the calculations indicate an overall contraction of 0.057 Å (PBE) and 0.053 Å (LDA) in the H-Ge(111) step height from a bulk value of 3.328 Å. These results are in excellent agreement with previous quantitative low-energy electron diffraction results which determined an overall step height contraction of 0.05 Å due to the hydrogen termination of the Ge(111) surface.[18]

Having successfully modeled the H-Ge(111) interface, the structural effects of terminating the Ge(111) surface with methyl groups were then investigated. Table 3-2 lists the lattice parameters, Ge-C bond lengths, and bilayer spacings for the ideal bulk and methyl-terminated Ge(111), respectively, using the PBE and LDA approximations. The interlayer spacings of the ideal truncated bulk Ge(111) result in a step height of 3.244 Å (LDA) and 3.328 Å (PBE); the experimental value of 3.28 Å reported above lies between these two values, demonstrating agreement with the modeled surface. An inward contraction of the first and second Ge bilayers due to functionalization is obtained from the calculations for CH_3-Ge(111), the magnitude of the contraction for the first Ge bilayer was 2.23% (LDA) and 1.66% (PBE), with respect to the ideal truncated bulk values. The second bilayer was calculated to contract 0.51% (LDA) and 0.60% (PBE), which is nearly identical to what was calculated for H-Ge(111). These first and second bilayer contractions, relative to H-Ge(111), suggest minimal electronic charge transfer between the outermost Ge atoms and the adsorbed methyl groups.

The rotational character of the methyl groups on the Ge(111) surface was investigated to investigate whether the surface methyl groups were locked, hindered, or freely rotating. The rotational barrier was calculated by employing a 2x2 supercell with the same slab configuration used for the structural properties, but with a 3x3x1 k-point sampling. Two extreme cases were considered: a) a fully methylated surface in which only one methyl group was rotated and the

position of the neighboring groups was fixed, and b) an isolated methyl group on an otherwise hydrogen-terminated Ge(111) surface. These approximations can provide both upper and lower boundaries for the rotational barrier of the real system, wherein all of the methyl groups are free to rearrange to compensate for the steric interactions due to rotations of neighboring methyl groups.

Figure 3-5 shows the energy profiles of both rotational barriers as a function of the methyl rotation angle with respect to its equilibrium position. The rotational activation barrier for the methylated Ge(111) surface with fixed neighbors was calculated to be ~55 meV, with the highest energy measured at a 60 degree rotation from equilibrium. Sum frequency generation (SFG) experiments[64] and DFT calculations[40] proposed a hindered rotation of the analogous methylated Si(111) surface, with Brown *et al.*[40] calculating a rotational barrier of 112 meV, arising predominately from the close packing of neighboring methyl groups. The helium diffraction data described above indicate that the methyl spacing for CH_3-Ge(111) is larger than CH_3-Si(111), which is consistent with a significant lowering of the calculated rotational activation barrier from 112 meV for CH_3-Si(111) to 55 meV for CH_3-Ge(111). Even with a larger lattice spacing, the steric interactions from neighboring methyl groups on CH_3-Ge(111) still play a role in the rotational barrier. By replacing the neighboring methyl groups with hydrogens, the rotational barrier decreased further, from 55 to 32 meV. The lower-bound activation barrier of 32 meV for an isolated methyl group surrounded by H-Ge(111) presents a notable corrugation in the rotational potential for this model system as compared to kT (25.7 meV at room temperature). These DFT calculations therefore suggest that the free rotation of the methyl groups on the CH_3-Ge(111) surface is hindered at room temperature.

As mentioned above, concerted motion of neighboring methyl groups might bring the rotational barrier closer to the lower bound given by the model system specified by an isolated methyl group on a hydrogen-terminated Ge(111) surface. To investigate this possibility, DFT molecular dynamics (MD) simulations were performed using the CP2k suite of programs.[49] Two slab models were considered, with a 4x4 or 5x5 surface supercell that contained respectively 16 or 25 methyl groups grafted on both surfaces of a 6-layer slab of Ge. After equilibration at 300 K, the rotational dynamics were analyzed over a 1.3 ps interval. Figure 3-6 shows snapshots of the largest model in the initial (ordered) and final configurations. In the larger model, five methyl groups out of 25 underwent one or several (up to five) complete rotations in 1.3 ps. These results suggest that although most methyl groups undergo hindered rotation, cooperative motion allows for some methyl groups to perform complete rotations on the picosecond time scale at room temperature.

Conclusions

A combined experimental/theoretical approach using low-energy helium diffraction data and density functional theory has been used to characterize the atomic surface structure of methyl-terminated Ge(111). Helium diffraction patterns for two primary azimuths showed that methyl termination of the Ge(111) surface creates a (1x1) hexagonally packed adlayer, preserving the native, unreconstructed structure of the Ge(111) crystal. The diffraction peaks indicated the presence of large domains of CH_3-Ge(111), while also revealing the presence of atomic steps. Drift spectra, which measure diffraction intensity as a function of the helium perpendicular wavevector, utilize data obtained under Bragg and anti-Bragg scattering conditions to experimentally determine the surface step height. Density functional theory yielded an optimized structure of CH_3-Ge(111). Bulk spacings were in quantitative agreement with the step

height measured from scattering, and organic functionalization of the surface resulted in small inward relaxations of the first and second Ge(111) bilayers with respect to bulk Ge(111). The close proximity of neighboring methyl groups results in a rotational activation barrier that is sufficient to hinder the free rotation of methyl groups on the fixed CH_3-Ge(111) surface at room temperature. However, cooperative motion of neighboring methyl groups allows for few of the methyl groups to undergo complete rotations on a picosecond timescale. Hence, a detailed investigation of this hybrid organic-semiconductor surface, using scattering and calculations, has revealed the effects of methylation on the atomic structure, interlayer spacings, and rotational character of the methyl groups decorating Ge(111).

Table 3-1

Mode	PBE	LDA	transmission FTIR[a]	HREELS[a]
M1 (CH_3 asymmetric stretch)	3052	3030	2928, 2906	2910 [b]
M2 (CH_3 symmetric stretch)	2956	2923	2956, 2860	2910 [b]
M3 (CH_3 asymmetric deformation)	1404	1366	- [c]	1411
M4 (CH_3 symmetric deformation)	1200	1187	1234	1234
M5 (CH_3 internal rocking)	731	739	762	780
M6 (Ge-C stretch)	530	557	- [d]	568

Frequencies (cm^{-1}) at the Γ-point for the high energy modes of CH_3-Ge(111).

[a] *Reference*[63]
[b] *Symmetric and asymmetric C-H stretches unresolved by HREELS*
[c] *Not IR active*
[d] *Not visible above noise*

Table 3-2

	PBE			LDA		
	ideal bulk	**H-**	**CH_3-**	**ideal bulk**	**H-**	**CH_3-**
lattice parameter	4.0764			3.97245		
d_{Ge-H} (d_{Ge-C})	-	1.56211	2.00879	-	1.54231	1.97400
d_{12}	0.82925	0.78689	0.81547	0.80947	0.76918	0.79141
$\Delta d_{12}/d_{bulk}$	-	-5.10%	-1.66%	-	-4.97%	-2.23%
d_{23}	2.49917	2.48423	2.48410	2.43403	2.42157	2.42158
$\Delta d_{23}/d_{bulk}$	-	-0.60%	-0.60%	-	-0.52%	-0.51%

Structural parameters of terminated Ge(111) using the PBE and LDA approximations.

Figure 3-1

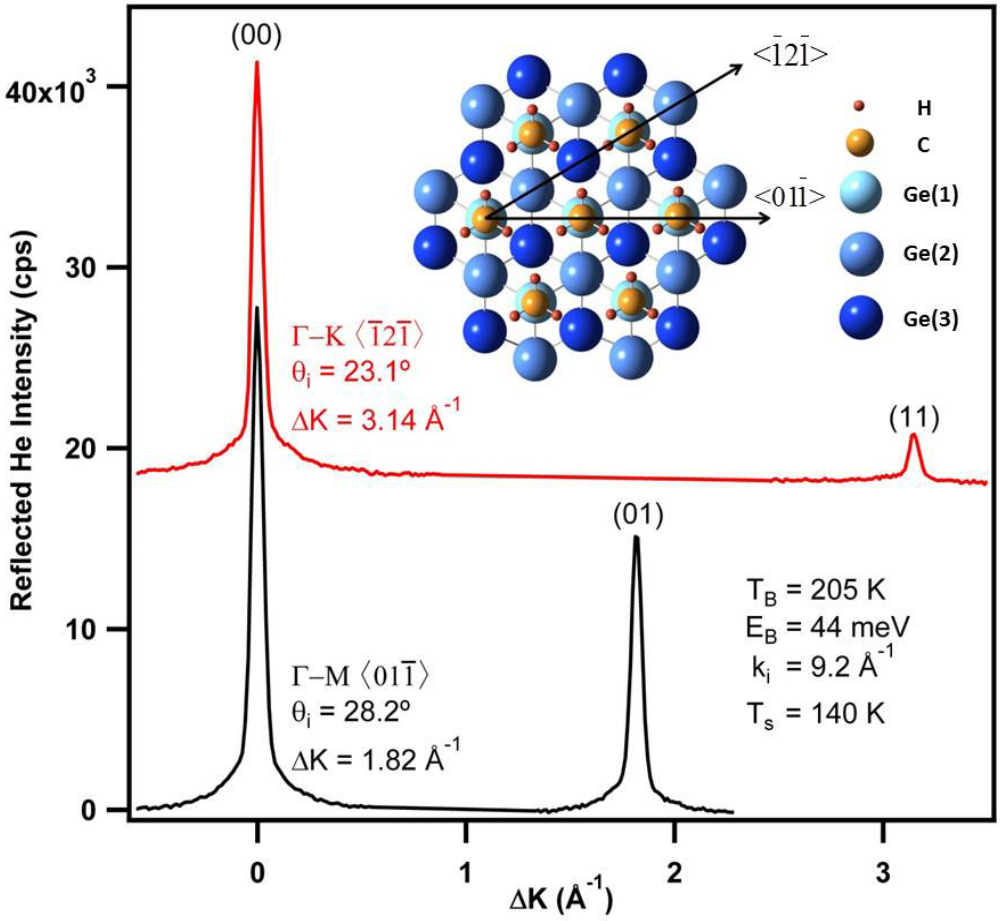

Helium diffraction scans for the CH_3-Ge(111) surface showing specular and first-order diffraction peaks along the <$01\bar{1}$> (top) and <$\bar{1}2\bar{1}$> (bottom) azimuths (traces vertically offset for clarity); inset displays a top view of CH_3-Ge(111) surface labeled with corresponding azimuthal orientations.

Figure 3-2

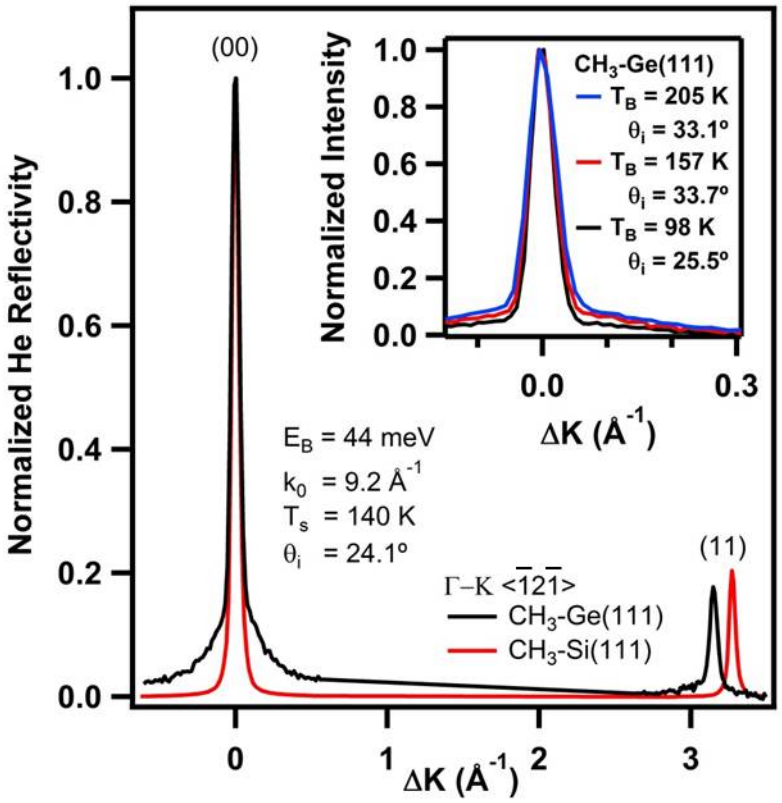

Comparison of helium diffraction data on CH_3-Ge(111) (black) and CH_3-Si(111) (red) along the <$\bar{1}2\bar{1}$> azimuth; inset demonstrates diminishing phonon contribution to "wings" of the same in-phase specular diffraction peak of CH_3-Ge(111) as a function of decreasing beam energy.

Figure 3-3

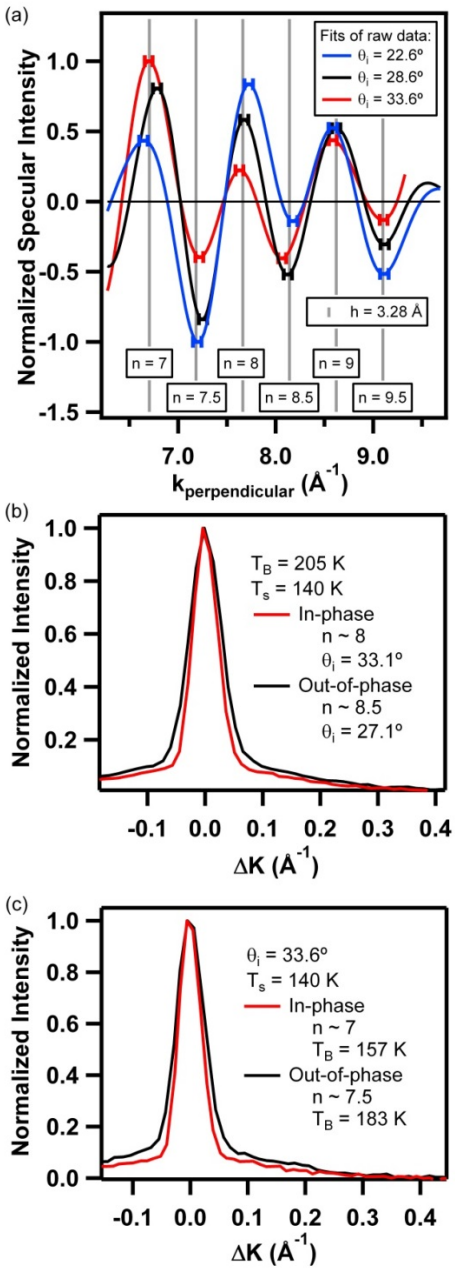

(a) Normalized intensity of multi-peak fits to drift spectra at three different incident angles on the CH_3-Ge(111) surface; vertical lines depict n-values for Bragg (integer) and anti-Bragg (non-integer) scattering; below, comparison of in- and out-of-phase specular diffraction peaks by varying (b) beam temperature, and (c) incident angle.

Figure 3-4

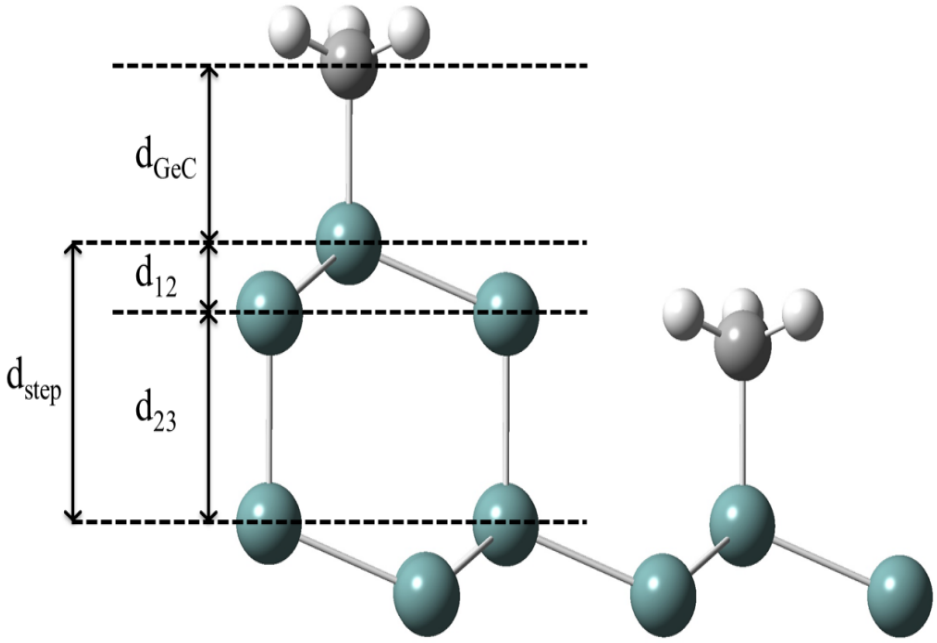

Lateral view of the CH_3-Ge(111) lattice exhibiting a single step along the $<\bar{1}2\bar{1}>$ orientation; d_{12} and d_{23} define the first and second bilayer spacings, respectively.

Figure 3-5

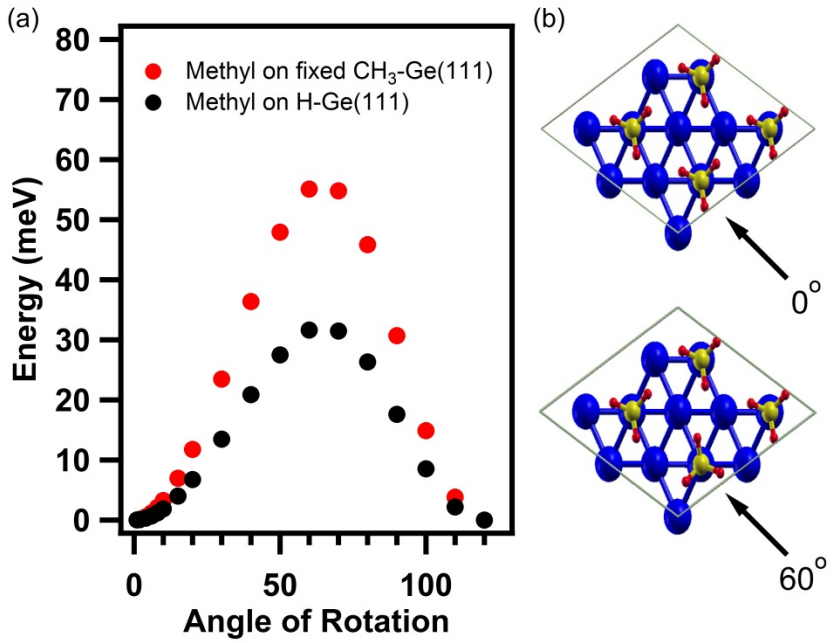

The change in potential energy as a function of the rotation of a surface methyl group from its equilibrium conformation, for a rotationally-fixed methylated Ge(111) surface (red) and an isolated methyl group residing on a H-Ge(111) surface (black), calculated using the PBE approximation for the exchange-correlation functional; (b) top view of CH_3-Ge(111) showing the surface methyl group in its equilibrium rotational conformation (top) and highest-energy rotational conformation (bottom).

Figure 3-6

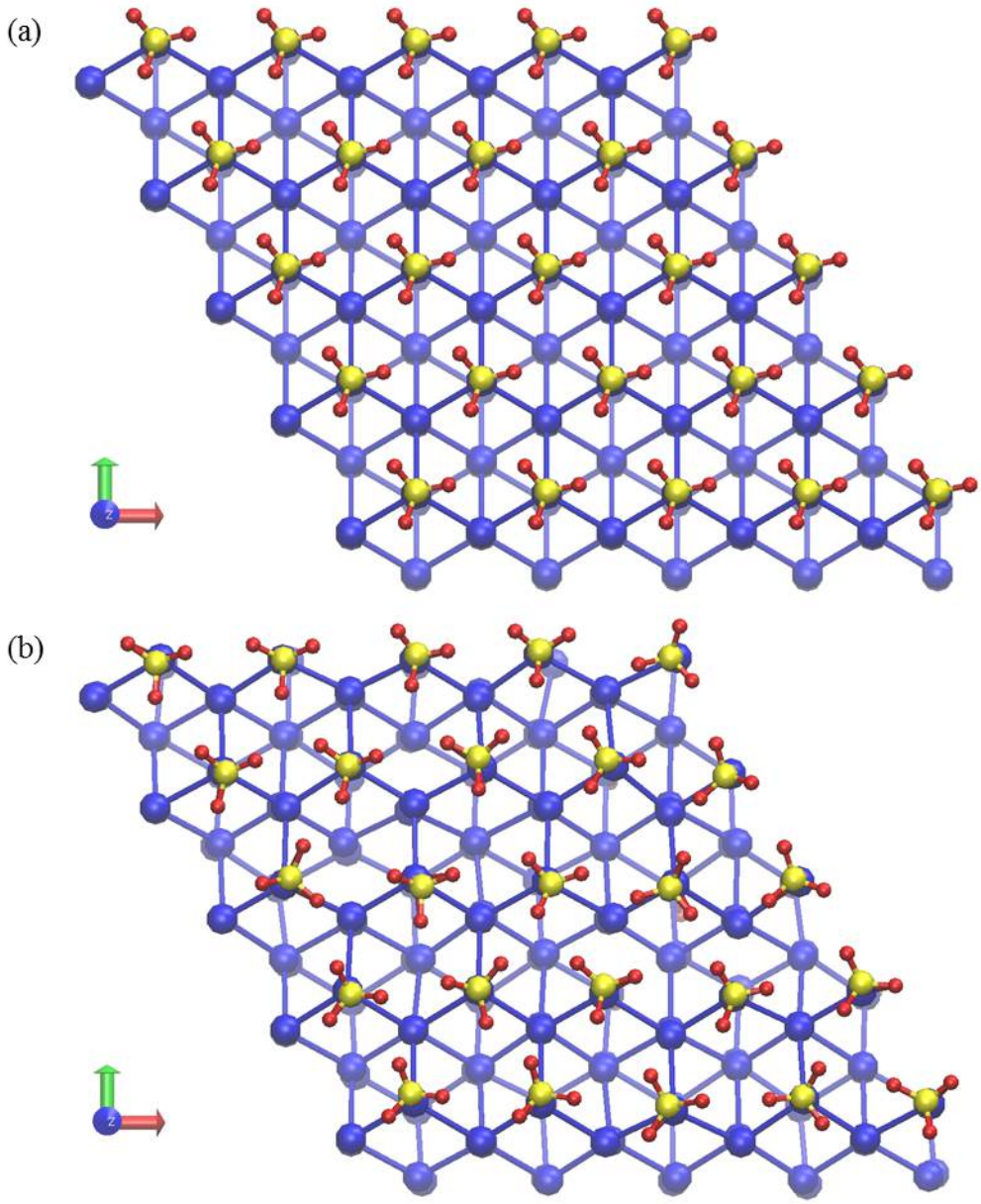

Snapshot of the 5x5 surface supercell (a) before and (b) after a molecular dynamics simulation 1.3 ps long at 300 K. Five methyl groups out of 25 undergo one or more complete rotations due to the cooperative motion of the neighboring CH_3 groups.

Chapter 4

Vibrational Dynamics and Band Structure of Methyl-terminated Ge(111)

A combined synthesis, experiment, and theory approach, using elastic and inelastic helium atom scattering along with *ab initio* density functional perturbation theory, has been used to investigate the vibrational dynamics and band structure of a recently synthesized organic-functionalized semiconductor interface. Specifically, the thermal properties and lattice dynamics of the underlying Ge(111) semiconductor crystal in the presence of a commensurate (1x1) methyl adlayer were defined for atomically flat methylated Ge(111) surfaces. The mean-square atomic displacements were evaluated by analysis of the thermal attenuation of the elastic He diffraction intensities using the Debye-Waller model, revealing an interface with hybrid characteristics. The methyl adlayer vibrational modes coupled with the Ge(111) substrate, resulting in significantly softer in-plane motion relative to rigid motion in the surface normal. Inelastic helium time-of-flight measurements revealed the excitations of the Rayleigh wave across the surface Brillouin zone, and such measurements were in agreement with the dispersion curves that were produced using density functional perturbation theory. The dispersion relations for H-Ge(111) indicated that a deviation in energy and lineshape for the Rayleigh wave was present along the nearest-neighbor direction. The effects of mass loading, as determined by calculations for CD_3-Ge(111), as well as by force constants, were less significant than the hybridization between the Rayleigh wave and methyl adlayer librations. The presence of

mutually similar hybridization effects for CH_3-Ge(111) and CH_3-Si(111) surfaces extends the understanding of the relationship between the vibrational dynamics and the band structure of various semiconductor surfaces that have been functionalized with organic overlayers.

Introduction

Crystalline semiconductors, including silicon and germanium, have played a crucial role in the electronics industry since the development of the transistor at Bell Laboratories in 1947. These materials also exhibit many properties that allow them to play a critical role in solar electricity generation.[65] Until recently, stable SiO_2 sites have allowed Si to become the semiconductor material of choice for field-effect devices, but now materials with larger dielectric constants are replacing SiO_2 (due to the relatively large Si/SiO_2 leakage current at the nanometer scale). Specifically, Ge has a 0.67 eV band gap and is thus an attractive option for the collection of infrared radiation in multijunction solar cells.[9,10] Additionally, the higher electron and hole mobilities (4 times larger than silicon) and lower processing temperatures of Ge relative to Si make Ge a desirable alternative for use in high-speed circuits as well as in metal-oxide-semiconductor field-effect transistors (MOSFETs).[66,67] However, a limiting factor that precludes facile fabrication of Ge-based devices is the rapid oxidation of the Ge surface that leads to water-soluble germanium oxides. Hence, to enable new opportunities for device applications, chemical control of the surface and interface properties is necessary to prevent oxidation and maintain the surface ordering of Ge crystals.

To minimize free energy, clean Ge(111) surfaces prepared under vacuum undergo reconstruction from a diamond cubic lattice structure to a c(2x8) surface configuration.[68] However, chemical passivation of the Ge(111) surface via hydrogenation, bromination, or

alkylation leads to a reconstruction of Ge(111) that retains the native (1x1) unit cell. Hydrogen or bromine atoms can passivate all of the dangling bonds above the surface Ge atoms, providing enhanced stability against surface oxidation relative to clean Ge.[21,69,70] The hydrogenated surface is sufficiently inert towards oxidation that H-Ge(111) can act as a reactive precursor for subsequent surface reactions, such as alkylation.[30] For example, hydrogenated Ge(111) surfaces have been methylated using a two-step halogenation/alkylation process, creating well-ordered, air-stable surfaces with excellent electrical properties.[36,71] Recently, highly ordered, atomically flat CH_3-Ge(111)-(1x1) surfaces have been prepared, resulting in improved chemical and electrical passivation.[63]

Several standard surface analytical techniques have revealed the chemical composition, surface structure, surface conductance, and methyl vibrational modes of methylated Ge(111) surfaces.[6,36,63,71] X-ray photoelectron spectroscopy (XPS) indicates that the two-step halogenation/methylation process provides complete termination of the Ge surface sites by methyl groups.[36,63,71] The vibrational modes of CH_3-Ge(111) have been investigated by use of transmission infrared spectroscopy (TIRS), high-resolution electron-energy loss spectroscopy (HREELS), and density functional perturbation theory (DFPT).[6,36,63] Low-energy electron diffraction (LEED) indicates the formation of a hexagonal unit cell, whereas atomic force microscopy (AFM), scanning tunneling microscopy (STM), and helium atom diffraction all yield evidence for an atomic spacing of ~ 4.0 Å, confirming the (1x1) surface structure of CH_3-Ge(111).[6,63] Additionally, methylated germanane (a single-layer crystal of germanium terminated with hydrogen) has recently been synthesized, and X-ray diffraction data indicate a hexagonal spacing with a lattice constant of a = 3.96 Å.[72] Despite extensive structural characterization, the dynamics of CH_3-Ge(111) remain largely unexplored, whereas the

dynamics of a surface analog, CH_3-Si(111), have been thoroughly studied both experimentally[38–40,64,73,74] and theoretically.[40,75,76]

We describe herein the comprehensive characterization of the dynamical properties of CH_3-Ge(111), to provide a foundation for understanding the thermal properties, energy accommodation at the interface, and vibrational band structure of such surfaces. Specifically, a combined scattering and theoretical study has been performed to characterize the vibrational dynamics and phonon band structure of this organic-functionalized Ge(111) interface. The vibrational features of methyl-terminated Ge(111) surfaces influence the thermal properties as well as the ability of the surface to accommodate energy. High-resolution helium atom scattering (HAS) and *ab initio* density functional perturbation theory (DFPT) have been used herein to study the effects of methylation on the surface thermal motion and phonon band structure of the CH_3-Ge(111) surface. Extremely surface sensitive low-energy neutral helium diffraction measurements have been used to define the interfacial structure, gas-surface interaction potentials, and the temperature-dependent mean-square displacements both normal and parallel to the methylated surface. The phonon evolution of the Rayleigh wave across the surface Brillouin zone for two high-symmetry azimuthal alignments has been experimentally recorded because inelastic scattering of helium atoms, which is important in characterizing physical quantities such as the specific heat, thermal expansion coefficients, and electron-phonon interactions of a material,[77] is due to phonon (e.g. Rayleigh wave) excitations. These scattering measurements are found to be in agreement with the calculated phonon dispersions produced *via* density functional perturbation theory. DFPT was also used to generate the vibrational band structure for H-Ge(111) and CD_3-Ge(111), and these surfaces provided a comparison to CH_3-Ge(111) to elucidate the effects of mass loading, force constants, and adlayer vibrations. As seen

previously for CH_3-Si(111) surfaces, the hybridization with organic adlayer librations is the major influence that dictates the energy and lineshape of the surface phonon dispersions.

Methods

The hydrogenation and subsequent alkylation of Ge(111) using a one-step alkylation from a H-Ge(111) precursor[6] disproportionately etches the surface and yields a surface with a significant concentration of randomly distributed steps. The surfaces investigated herein were therefore instead prepared using a two-step halogenation-alkylation that produces atomically flat, methyl-terminated Ge(111) surfaces.[63] Briefly, a thoroughly cleaned and rinsed Ge(111) wafer was hydrogenated by exposure to a flow of H_2 at 850 ºC and atmospheric pressure. The sample was then cooled to below 100 ºC. The resulting H-Ge(111) surface was brominated for 1 min at 50 ºC in neat CCl_3Br that contained a small amount of benzoyl peroxide. The sample was rinsed with anhydrous tetrahydrofuran (THF) and then methylated in $(CH_3)_2Mg$/THF/1,4-dioxane for 5 min at 50 ºC. For shipment from Pasadena, CA to Chicago, IL, the CH_3-Ge(111) surfaces were placed under high vacuum *via* turbo pumping prior to shipping. Upon receipt, the samples were immediately loaded into the ultra-high vacuum sample chamber, with limited exposure to atmosphere in the interim.

Data were collected using an ultra-high vacuum (UHV) helium atom scattering apparatus that provided high angular and energy resolution; this instrument and the range of its parameters have been thoroughly described elsewhere.[78] The crystal-to-ionizer distance was however shortened from 1.0234 m to 0.5705 m, which when added to a constant chopper-to-crystal distance of 0.4996 m, produced a total flight path of 1.0701 m (shortened from a total distance of 1.5230 m for the long mode). Inelastic helium time-of-flight experiments (described below) were performed with the detector in both configurations, providing greater angular resolution in

the long mode whereas greater intensity was produced in the short mode.

To collect the scattering data, helium gas was supersonically expanded into a series of differentially pumped chambers. The He was then scattered from a CH_3-Ge(111) crystal that had been mounted on a six-axis manipulator and temperature controlled with cryostatic cooling and a button heater; ionized by electron bombardment, and then filtered through a quadrupole mass spectrometer (QMS) before striking an electron multiplier. Prior to entering the sample chamber, the beam was mechanically modulated by a chopper wheel. For the elastic diffraction data that were used for Debye-Waller analysis the beam was chopped with a 50% duty cycle for modulated detection. For collection of inelastic data, time-of-flight spectra were collected by chopping the beam with either a 50% duty cycle for cross-correlation analysis,[5] which used a pseudorandom 511 bit sequence of openings in the chopped wheel to increase signal-to-noise, or by use of a 1% duty cycle for a single-slit pattern. For single-shot time-of-flight runs, composite spectra were often produced to increase the signal-to-noise, by adding multiple spectra taken under identical incidence conditions. The temperature of the sample was flashed to 450 K between runs to eliminate unwanted surface adsorbates.

The dynamical properties of the H-Ge(111), CH_3-Ge(111), CD_3-Ge(111) surfaces were calculated using density functional perturbation theory, as implemented in the QUANTUM-ESPRESSO package[42] using a norm-conserving pseudopotential for Ge, ultrasoft pseudopotentials[43] for C and H, and the Perdew-Burke-Ernzerhof (PBE) approximation[45] for the exchange-correlation energy functional. The electronic wavefunctions were expanded in plane waves up to a 28 Ry energy cut-off and a 280 Ry charge-density cutoff. The surfaces were modeled with a slab geometry and periodic boundary conditions (PBC), and the slabs were composed of 18 germanium atom layers with hydrogen or methyl groups adsorbed on both sides,

which were separated by a 12 Å-wide vacuum gap.[6] The surface Brillouin zone (SBZ) was sampled over a Monkhorst-Pack grid of 6x6x1 k-points.[46] The atomic positions were relaxed until the forces were below a $5 \cdot 10^{-5}$ a.u. threshold. The dynamical matrix was calculated on a 6x6x1 q-point mesh for the SBZ. The Fourier transform of the dynamical matrices on a discrete uniform mesh in the SBZ provided the real-space interatomic force constants that allowed calculation of the dispersions relations.

Results and Discussion

Vibrational dynamics

He diffraction of CH_3-Ge(111) surfaces has previously indicated the presence of a hexagonally packed methyl adlayer with a (1x1) methyl termination of the Ge(111) lattice.[6] Figure 4-1 shows diffraction spectra that include first-, second- and zeroth-order diffraction peaks for the high-symmetry $\langle \bar{1}2\bar{1} \rangle$ and $\langle 0\bar{1}\bar{1} \rangle$ azimuthal alignments. These alignments and their corresponding diffraction peaks were used for the experiments reported on herein.

The diffraction patterns show the helium reflectivity as a function of the parallel momentum transfer,

$$\Delta\vec{K} = \vec{k_i}\left(\sin\theta_f - \sin\theta_i\right), \tag{4-1}$$

where $\vec{k_i}$ is the incident helium beam wavevector, and θ_i and θ_f are the initial and final scattering angles, respectively. The ΔK spacing of 1.82 $Å^{-1}$ observed between the diffraction peaks for the $\langle \bar{1}2\bar{1} \rangle$ alignment (Figure 4-1) is consistent with a 4.00 Å real-space lattice constant, confirming the presence of a hexagonally packed (1x1) methyl adlayer. Figure 4-1(c) shows a proposed top-

view model of the CH_3-Ge(111) surface. The sharp and large diffraction peak intensities, along with a minimal diffuse background, suggest the formation of a low-defect surface with long-range ordering. These large intensities are required to extract information on the surface dynamics *via* thermal attenuation measurements.

The thermal attenuation of the diffraction peaks provides information on the vibrational dynamics of the surface, because the diffraction peak intensity decays with increasing sample temperature as the vibrational amplitude of the surface oscillators increases, resulting in inelastic scattering of the impinging helium atoms.[79] The surface temperature, T_s, of CH_3-Ge(111) was varied (T_s = 200 – 500 K) at five different incident beam angles between diffraction scans, to calculate the Debye-Waller factor, $W(T_s)$. The observed diffraction peak intensity, I, is exponentially dependent on the Debye-Waller factor, such that

$$I = I_0 e^{-2W(T_s)}, \tag{4-2}$$

where I_0 is the peak intensity at a theoretical surface temperature of 0 K. The Debye-Waller factor is comprised of four components: the normal and parallel momentum transfers during the scattering process, Δk_z and ΔK, respectively, and their associated mean-square displacements (MSD) of the crystal atoms, $\left\langle u_z^2 \right\rangle$ and $\left\langle u_{\|}^2 \right\rangle$,

$$2W(T_s) = \Delta k_z^2 \left\langle u_z^2 \right\rangle + \Delta K^2 \left\langle u_{\|}^2 \right\rangle \tag{4-3}$$

where

$$\Delta\overrightarrow{k_z} = \overrightarrow{k_i}\left[\left(\cos^2\theta_i + \tfrac{D}{E_i}\right)^{1/2} + \left(\cos^2\theta_f + \tfrac{D}{E_i}\right)^{1/2}\right]; \tag{4-4}$$

here, the D/E_i term accounts for acceleration of a He atom with energy E_i as the atom enters the attractive portion of the gas-surface potential well having a depth D.[80] When only the thermal attenuation of the specular ($\theta_i = \theta_f$) peak (Figure 4-2(a)) is observed, the parallel momentum transfer to the surface is assumed to be zero, allowing simplification of Equations (4-3) and (4-4) to yield:

$$2W(T_s) = \Delta k_z^2 \left\langle u_z^2 \right\rangle \tag{4-5}$$

$$\Delta\overrightarrow{k_z} = 2\overrightarrow{k_i}\left[\left(\cos^2\theta_i + \tfrac{D}{E_i}\right)^{1/2}\right] \tag{4-6}$$

According to Equation (4-2), plotting the natural log of $I(T_s)/I_0$ as a function of the surface temperature should result in a linear relationship. Figure 4-2(b) shows linear decays of the total peak area with respect to increases in the surface temperature, confirming that the Debye-Waller model held for the experimental range of surface temperatures in this system. Each diffraction pattern was recorded with a 44 meV helium beam and was repeated three separate times at five different incident angles (θ_i = 22.1°, 26.1°, 29.1°, 32.6°, 36.1°). Taking the derivative of Equation (4-5) with respect to the surface temperature reveals the surface temperature-dependence of the Debye-Waller factor,

$$\sigma = -\frac{d(2W)}{dT_s} = -\left[\Delta k_z^2 \frac{d\left\langle u_z^2 \right\rangle}{dT_s}\right]. \tag{4-7}$$

The expression for the exchange of perpendicular momentum (Equation (4-6)) can then be inserted to produce the desired relationship:

$$\sigma = 4k_i^2 \frac{d\left\langle u_z^2 \right\rangle}{dT_s}\left[\cos^2\theta_i + \frac{D}{E_i}\right], \tag{4-8}$$

such that a linear fit of the Debye-Waller decay, σ, versus $cos^2\theta_i$ can be used to determine the temperature dependent mean-square displacement and potential well depth from the slope and y-intercept, respectively of the data.

Figure 4-3 shows the angular dependence of the Debye-Waller factor for the CH_3-Ge(111) surface.[74] A linear fit to the specular data yielded a slope of -0.0145 K^{-1} and an intercept of 0.0041. Given k_i = 9.2 $Å^{-1}$, $d\left\langle u_z^2 \right\rangle / dT_s$ is (4.3 ± 0.2) x 10^{-5} $Å^2K^{-1}$ for the CH_3-Ge(111)-(1x1) surface. For comparison, a previous He diffraction study identified a perpendicular MSD of ~1.5 x 10^{-5} $Å^2K^{-1}$ (based on extrapolation of their diffraction data) for Ge(111)-c(2x8).[81] The perpendicular MSD of the CH_3-Ge(111)-(1x1) surface shows a significant deviation from that of Ge(111)-c(2x8), which is consistent with the decreased effective surface mass (72 amu for Ge, now 15 amu for CH_3) and an increase in the surface Debye temperature, as discussed in detail below. In the harmonic limit of the Debye-Waller model, the MSD is inversely proportional to the effective surface mass as well as to the square of the Debye temperature. The mass reduction by a factor of five thus overwhelms a less than doubled surface Debye temperature, accounting for an increase in the perpendicular MSD. Additionally, Ohkuma and Nakamura[82] have shown that surface reconstruction of diamond-structure crystals can suppress the perpendicular MSD, causing an even larger deviation between the two values. As shown by Figure 4-3, the perpendicular MSD for CH_3-Ge(111) is approximately four times larger than that of (1.0 ±0.1) x 10^{-5} $Å^2K^{-1}$ for CH_3-Si(111).[37] This deviation arises from the lesser effective mass reduction (28 amu for Si, now 15 amu for CH_3), with a similarly large increase in its Debye temperature. Hence, methyl-termination of Si(111)

instead results in a decrease of the perpendicular MSD relative to the bulk value for Si(111)-(7x7). Although functionalization of both surfaces causes a decrease in their effective masses to different degrees, the still-present perpendicular stiffness of both methyl-terminated surfaces is associated with the rigidity of their directional, sp^3-hybrid Si/Ge-C covalent bonds.

Due to the large slope observed for CH_3-Ge(111) (Figure 4-3), the y-intercept extracted from the linear fit does not provide a realistic value for the He potential well depth. This arises from the inability of such Debye-Waller measurements to properly account for the low-temperature librational dynamics of the system. A well depth of ~7.5 meV has been measured for similarly functionalized CH_3-Si(111)[37] and H-Si(111) surfaces.[83] The He scattering potential is a function of the surface electron density,[54] which we expect to be similar for CH_3-Ge, so a well depth of 7.5 meV has been assumed herein. By inserting the parallel momentum component from Equation (4-3) into Equation (4-7), the parallel MSD can be calculated and separated from the perpendicular MSD component. Figure 4-4 shows representative thermal attenuation diffraction spectra for two non-specular diffraction peaks. The temperature-dependent decay in the areas of these peaks was compared with similar spectra that measured other first- and second-order peaks at a range of surface temperatures, and provided an average parallel MSD of $(2.2 \pm 1.6) \times 10^{-3}$ $Å^2K^{-1}$. The parallel MSD was found to be nearly two orders of magnitude larger than the perpendicular MSD of $(4.3 \pm 0.2) \times 10^{-5}$ $Å^2K^{-1}$ measured herein for CH_3-Ge(111). Recent theoretical studies on methyl-terminated semiconductor surfaces have proposed couplings between methyl bending vibrational modes and the underlying lattice waves, thereby significantly increasing the surface thermal motion in the parallel direction, as observed here.[75,76] These larger parallel MSDs suggest that the surface shares librational characteristics

with not only the previously studied methyl silicon system but also with other organic overlayers on metals.[84]

For a classical harmonic oscillator, the Debye-Waller model can also be expressed as

$$W(T_s) = \frac{12m\left[E_i \cos^2\theta_i + D\right]T_s}{M_{eff} k_B \Theta_D^2}, \tag{4-9}$$

where m is the mass of the incident helium atom, M_{eff} is the effective surface mass, k_B is Boltzmann's constant, and Θ_D is the surface Debye temperature. The Debye temperature of the CH_3-Ge(111) surface is calculated to be 689 ± 20 K (479 cm^{-1}), given that the effective mass that a helium atom collides with decreases from 72 amu for Ge(111) to 15 amu for CH_3-Ge(111), and the estimated potential well depth is 7.5 meV. This value is significantly larger than the value of ~360-374 K that has been measured for the Debye temperature of bulk Ge(111).[85,86] Additionally, RHEED measurements give an effective surface Debye temperature of 96 K for clean c(2x8)-Ge(111) surfaces, which was proposed to be due to the weakening of the harmonic force constant of the interlayer potential.[87] Therefore, instead of producing a softer Ge(111) surface, methyl termination imposes a greater rigidity, as indicated by a nearly doubled Debye temperature for the surface. This rigidity can be explained by the coupling of impinging helium atoms to the vibrational modes of the terminated methyl groups. The calculated surface Debye temperature (479 ± 14 cm^{-1}) is in accord with the Ge-C stretching mode frequency for CH_3-Ge(111) measured with HREELS[63] (568 cm^{-1}) and DFT[6] (530 cm^{-1}), as well as in accord with IR data for methylgermane[88] (601.6 cm^{-1}). By terminating the Ge(111) lattice with methyl groups, the collisional dynamics have changed such that helium atoms strongly interact with localized molecular modes rather than just interacting with low-energy phonons that originate from the lattice.

Phonon band structure

The vibrational motion and band structure of surface groups can be additionally characterized by use of inelastic helium atom scattering, which involves the transfer of both energy and momentum between an impinging He atom and the surface. The extreme sensitivity of HAS to sagittal displacement (shear vertical motion of surface atoms) allows for strongly resolved measurements of the Rayleigh wave, which is the lowest-energy surface acoustic mode that vibrates in the sagittal plane. The relatively short wavelength and small penetration of the Rayleigh wave make it especially sensitive to interatomic forces at the surface; hence measurement of the Rayleigh wave provides insight into the interaction of the surface methyl groups with the underlying germanium lattice. Hence, inelastic helium atom scattering was used to map out the surface phonon dispersion curves for CH_3-Ge(111) along both the $\langle \bar{1}2\bar{1} \rangle$, Γ-M, and $\langle 01\bar{1} \rangle$, Γ-K, primary azimuthal directions across the surface Brillouin zone (SBZ).

The inelastic scattering data were extracted from a series of time-of-flight spectra taken over a large range of kinematic conditions. Figure 4-5 shows representative composite inelastic single-shot time-of-flight spectra that were recorded at seven different final scattering angles for the same beam energy and sample temperature. Each spectrum exhibited a large diffuse elastic peak, as well as two sharp inelastic peaks on either side, indicating single-phonon interactions with the Rayleigh wave. Each of these peaks was located atop a broad inelastic background formed by multiple-phonon excitations, which is consistent with expectations based on the soft nature of the surface, as indicated by the Debye-Waller experiments detailed above.

The time-of-flight spectra readily provide the energy and parallel momentum that is exchanged with the surface in an inelastic scattering process. The flight times of elastic and

single-phonon creation and annihilation peak maxima were determined by least-squares fitting the data with multiple Gaussian peaks, with the multiphonon background subtracted, to leave a fairly flat residual. The fitted flight times were then referenced to the length of the flight path from the crystal to the detector, to calculate the associated energy exchanges with the surface. The conservations of energy and surface parallel momentum for single-phonon interactions:

$$\vec{k_f}^2 = \vec{k_i}^2 \frac{2m}{\hbar^2}\hbar\omega(\vec{Q}) \tag{4-10}$$

$$\vec{K_f} = \vec{K_i} + \vec{G_{mn}} + \vec{Q} \tag{4-11}$$

where $\hbar\omega(\vec{Q})$ is the energy of a phonon with wavevector $\vec{Q}$ and frequency ω ($\omega < 0$ indicates creation of a phonon, $\omega > 0$ an annihilation), were then combined to yield an expression that describes the functional form of a scan curve:

$$\frac{\hbar\omega(Q)}{E_i} = \frac{\sin^2\theta_i}{\sin^2\theta_f}\left(1 + \frac{\Delta K}{K_i}\right) - 1 . \tag{4-12}$$

Scan curves calculate the allowed exchange of surface parallel momentum as a function of the known phonon energy and kinematic parameters, and delineate the possible single-phonon events that may be observed experimentally. Such data are presented in the inset of Figure 4-5 as colored bands that correspond to the conditions of their respective time-of-flight spectra.

The experimental data in the Figure 4-5 inset agrees very well with the dispersion curves provided by the DFPT calculations, and shows a clear dispersion of the Rayleigh wave across the $\langle\bar{1}2\bar{1}\rangle$ region of the SBZ. The increasing temporal distance between the elastic and inelastic creation peaks in the time-of-flight spectra results from a greater exchange of momentum and

energy with the surface, causing the phonon data to disperse away from the zone center ($\bar{\Gamma}$-point) in the dispersion curve. Moreover, the increase in surface parallel momentum and energy exchange causes the intensity of the Rayleigh wave peak to decrease considerably, as has been demonstrated elsewhere.[89] Conversely, the annihilation time-of-flight peaks initially moved away from the elastic peak, but then dispersed back towards the elastic peak (beginning at θ_i = 24.6°) as the phonons crossed over the $\bar{M}$-point ($|\Delta K|$ = 0.907 Å^{-1}) in the dispersion curve. These inelastic transitions involving *umklapp* phonons are expected for surfaces with high corrugation, as reported elsewhere.[90] These *umklapp* phonons are folded into the irreducible surface Brillouin zone along with the entire inelastic data set, as shown in Figure 4-6.

Density functional perturbation theory was used to calculate the vibrational band structure for CH_3-Ge(111). The absolute energies of all experimental single-phonon processes are displayed on the reduced dispersion curves in Figure 4-6, which has been color-coded to represent the total degree of sagittal polarization at the surface. A large degree of the sagittal vibrational motion clearly arises from the Rayleigh wave, the lowest-energy dispersion curve. Within experimental error (less than 0.5 meV), the large amount of experimental inelastic data agrees with the theoretical dispersion curves, clearly mapping out the Rayleigh wave across the SBZ, along with a few higher-energy modes. The inability to completely map out the Rayleigh wave in the $\overline{\Gamma K}$ and $\overline{KM}$ regions is explained by a lower degree of sagittal displacement. Additionally, the low-energy Rayleigh wave is difficult to experimentally resolve from the significant bulk band excitations and multiphonon contributions introduced by the aforementioned corrugation and relative softness of the surface.[91] Likewise, single phonons occurring at higher-energy areas of strong sagittal displacement (such as at the $\bar{K}$-point, ~12 and 14 meV) require higher beam energies to excite, but are washed out by the simultaneous

excitation of multiple lower-energy modes, as higher beam energies increase the Weare parameter beyond the threshold of single-phonon domination.[92]

The Debye-Waller measurements reported above indicate a considerably softer surface for CH_3-Ge(111) relative to CH_3-Si(111), an analog hybrid organic-semiconductor interface. The relative softness of CH_3-Ge(111) is reflected in the overall lower energy of the Rayleigh wave, in that the calculated energies at the $\overline{M}$- and $\overline{K}$-point are 7.3 and 9.6 meV, respectively, for CH_3-Ge(111), whereas these values are approximately twice as large for CH_3-Si(111), at 13.3 and 17.9 meV.[75] As detailed elsewhere,[91] the Rayleigh wave can be reproduced fairly accurately by a force constant model for a single atomic layer with nearest- and next-nearest-neighbor interactions. This disparity in the Rayleigh wave energies should therefore be reflected in the force constants of the two surfaces. Wei and Chou[93] created an 8x8 supercell and used the Hellmann-Feynman theorem to calculate the transverse force constants for surface atoms of bare Ge(111) (-1.937 dyn/cm) and Si(111) (-2.193 dyn/cm), which strengthens this hypothesis of softening. Additionally, Han *et al.*[94] noted that the largest phonon energy in Ge (38 meV) is only about 60% of that in Si (64 meV), which matches well with the relative Rayleigh wave zone-edge energies of these two methyl-terminated interfaces.

Phonon dispersions for clean Ge(111) have been measured experimentally[68,95,96] and theoretically.[93] Clean Ge(111) reconstructs rapidly, which causes distortions of the dispersion curves;[97] however, at high temperature Ge(111) recovers the (1x1) structure such that the Rayleigh wave dispersion curves measured by HAS at 1000 K[96] can be directly compared with the present data for CH_3-Ge(111) at low temperatures. There is a surprising agreement between the Rayleigh wave data in both cases, indicating that the anharmonic softening expected for the clean Ge(111) at high temperature is comparable to that due to the mass loading effect of the

methyl adlayer at low temperatures. To better understand the relationship between organic functionalization and the vibrational band structure of germanium, the results for CH_3-Ge(111) have been compared with H-Ge(111)-(1x1). In the case of H-Ge(111), surface atoms preserve the ideal tetrahedral configuration of the unreconstructed (1x1) surface, which ought to exhibit dynamics similar to those of the clean (1x1) semiconductor surface,[98] such that adlayer interactions do not significantly affect the vibrational characteristics of the semiconductor lattice. In the absence of measurements of the surface phonon relations for hydrogen-terminated germanium, the vibrational band structure for H-Ge(111)-(1x1) has been constructed in this work by use of DFPT. Figure 4-7 compares the low-energy vibrational band structure of H-Ge(111) and CH_3-Ge(111), with the color scale indicating the relative sagittal displacement of their respective 1st layer Ge atoms.

Although the Rayleigh wave frequency is nearly identical for both terminated surfaces at the $\overline{M}$ point, methylation of the Ge(111) surface produces a noticeable increase in the Rayleigh wave energy along the $\overline{\Gamma K}$ azimuth near the zone edge ($\overline{K}$ point). This deviation can be attributed to three sources: changes in the local force constants, mass-loading effects, and/or hybridization between lattice and adlayer vibrations. Methyl termination results in the addition of only 0.04 electrons to the Ge-Ge bonds in the first two layers with respect to clean Ge(111)-(1x1). Comparison of H-Ge(111) and CH_3-Ge(111) surfaces display similar Ge lattice charge densities, as seen with DFPT; as a result, the force constants for CH_3-Ge(111) are only 2.5% and 2.2% weaker in-plane and out-of-plane, respectively, than H-Ge(111). Modifications of the local force constants due to methyl termination are therefore not primarily responsible for the increase in phonon energy observed for CH_3-Ge(111). Additionally, the DFPT-calculated displacement fields did not display a linear sagittal polarization at the $\overline{M}$ point, which would be expected for a

Rayleigh wave associated with an ideal fcc surface.[77] Our previous work on methyl-terminated Si(111) showed that the deviation in the shape and energy of the Rayleigh wave for CH_3-Si(111) from H-Si(111) was a result of hybridization of the Si(111) lattice waves with methyl adlayer rocking librations.[75] This mechanism can hence be formally extended to the Ge(111) system, where the rocking libration of the terminated methyl group (characterized by a slight distortion of the internal C-H bonds and the bending of the C-Ge bond with an energy of 13.1 meV at the $\bar{\Gamma}$ point) has coupled with the lattice waves near the zone edge to induce an observable deviation of the Rayleigh wave along the $\overline{\Gamma K}$ alignment. The hybridization is slightly weaker for Ge(111) than Si(111), because the hybridization in CH_3-Si(111) caused an increase of nearly 2 meV at the $\bar{K}$ point for the Rayleigh wave, whereas the hybridization for CH_3-Ge(111) only resulted in an increase of about 1.5 meV relative to H-Ge(111). This weaker hybridization is attributed to the lower energy of the CH_3-Ge(111) Rayleigh wave, causing an increased energy difference between the methyl vibrational modes and the Rayleigh wave.

To account for mass-loading contributions of the terminal methyl groups to the underlying lattice wave dispersions, DFPT was used to produce the vibrational band structure for CD_3-Ge(111), a simple isotopic analog of CH_3-Ge(111). Experimental comparisons with the theory data for CD_3-Ge(111) have not yet been performed due to difficulties in synthesizing high-quality crystals with near-complete CD_3 termination, thereby prohibiting resolved inelastic helium scattering measurements. Figure 4-8 compares the vibrational band structure for CH_3-Ge(111) and CD_3-Ge(111), with the color scale representing the relative sagittal displacement of the C atoms in each system. The Rayleigh wave frequency should scale as $C^{1/2}M_{eff}^{-1/2}$, where C is the interatomic force constant and M_{eff} is the effective mass. For the Rayleigh wave, the effective mass can be taken as the mass of a single germanium atom with a single methyl group.

This approach is taken from the comparison between data for CD_3- and CH_3-Si(111) surfaces, where the increased mass (43 amu for CH_3-Ge, 46 amu for CD_3-Si) resulted in an energy decrease of 17.9 to 17.3 meV for CD_3-Si(111). Applying the same approach here, the smaller deviation in mass (87 amu for CH_3-Ge, 90 amu for CD_3-Ge) becomes negligible, suggesting a decrease in the Rayleigh wave frequency of only ~0.16 meV. Figure 4-8 consistently provides evidence for this rather small decrease in the Rayleigh wave energy, demonstrating that mass-loading effects play a minimal role in determining the energies of the Rayleigh wave dispersion for CH_3-Ge(111). One notable difference in the band structure for CH_3-Si(111) vs CD_3-Si(111) is the presence of a mode crossing between the Rayleigh wave and a hindered methyl rotation. The crossing is absent for CD_3-Ge(111), due to the much lower energy of its Rayleigh wave compared to CD_3-Si(111), while the hindered rotational mode is only slightly decreased (13.8 meV for CD_3-Ge(111) and 20.8 meV for CD_3-Si(111)) due to the larger Ge lattice constant and therefore reduced interaction between neighboring methyl groups. Overall, analysis of the H-Ge(111), CH_3-Ge(111), and CD_3-Ge(111) band structures indicates that hybridization of modes is the primary influence in determining the Rayleigh wave dispersion, with mass loading and force changes contributing negligibly. This phenomenon has now been extended from CH_3-Si(111) to CH_3-Ge(111), and is likely present for other organically functionalized group IV semiconductors.

Conclusions

This combined experimental and theoretical effort has revealed the vibrational dynamics and band structure of the atomically flat CH_3-Ge(111) interface. The attenuated intensities of helium atom diffraction peaks at a variety of incidence angles were exponentially dependent on increasing surface temperature, allowing for the application of the Debye-Waller model to this

hybrid organic-semiconductor interface. This approach allowed for a precise estimation of the surface Debye temperature as well as an estimation of the temperature-dependent atomic displacements of the surface methyl groups in both the surface-normal and -parallel directions, which indicated a transition in the regime of surface motion enforced by the methyl adlayer. Inelastic helium scattering measurements were complemented with high-level density functional perturbation theory calculations, showing agreement in the mapping of the phonon dispersion of the Rayleigh wave across the surface Brillouin zone. The minimal effects of mass loading on the lattice waves were resolved by producing the vibrational band structure for an isotopically substituted surface, CD_3-Ge(111). Comparing the surface phonon dispersions of CH_3-Ge(111) and H-Ge(111) aided in the identification of hybridization of methyl adlayer librations with the Rayleigh wave as the dominant factor in shaping the Rayleigh wave dispersion, which agrees with similar effects observed for CH_3-Si(111). The results collectively strengthen the understanding of the relationship between the nature of the organic functionalization and the vibrational dynamics and phonon band structure of Ge(111), and can be applied to other group IV semiconductors as well.

Figure 4-1

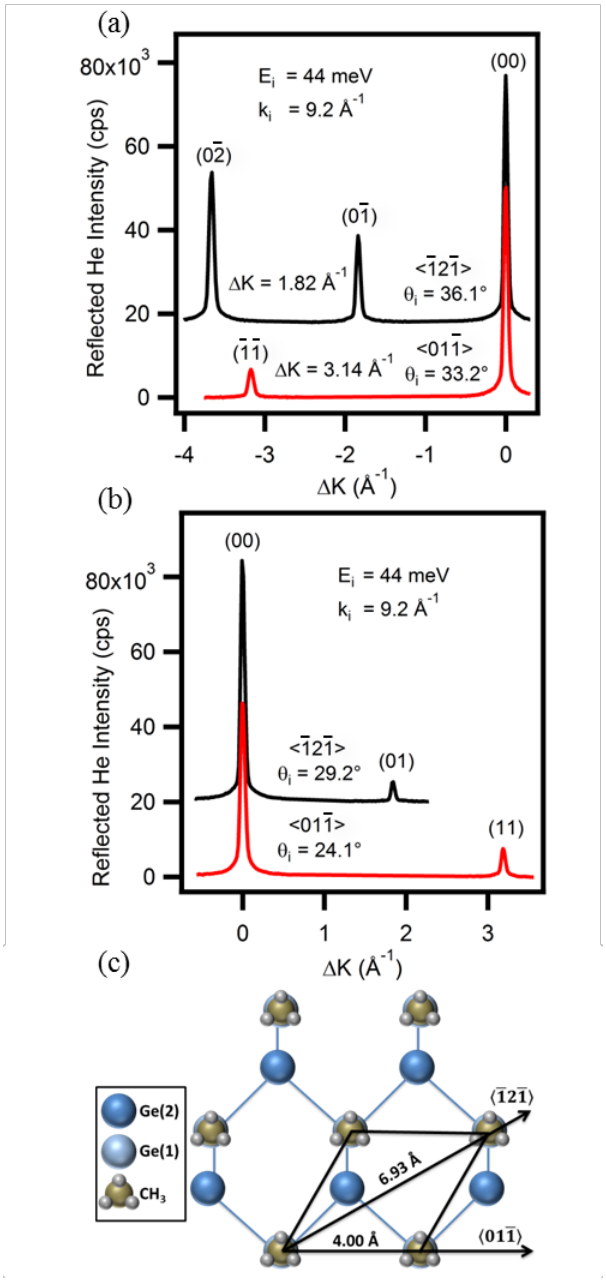

(a) He diffraction spectra showing the back-scattered (negative) diffraction peaks along both primary azimuthal alignments with corresponding peak spacings; (b) diffraction spectra showing the forward-scattered (positive) diffraction peaks along both azimuthal alignments; (c) top-view model of the CH_3-Ge(111) surface with real lattice spacings.

Figure 4-2

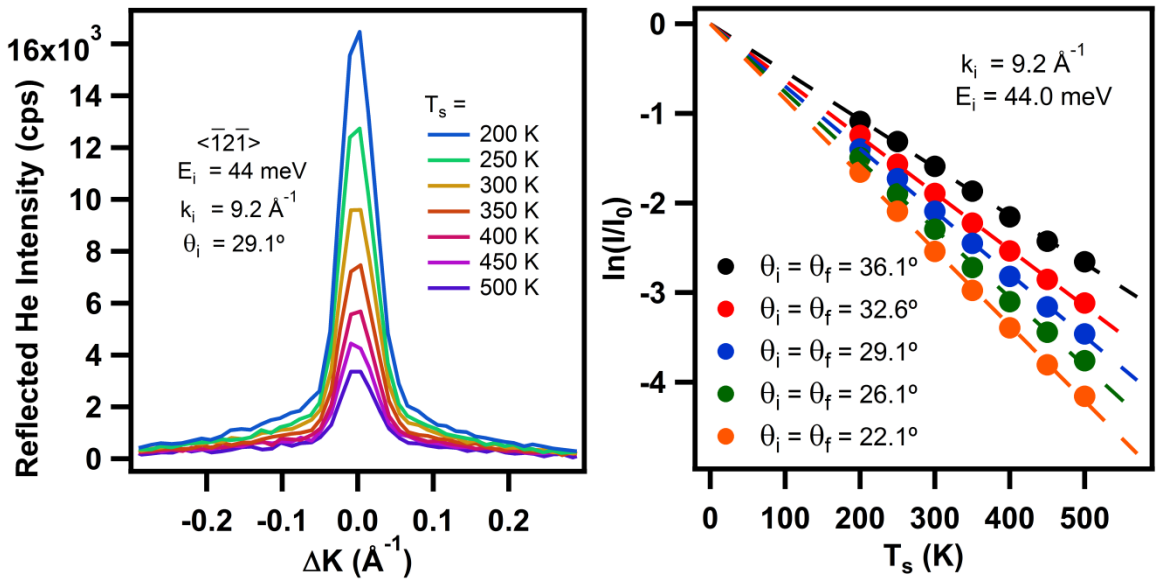

(a) Decay of the specular ($\theta_i = \theta_f$) diffraction peak as a function of CH_3-Ge(111) surface temperature, plotted vs. parallel component of momentum exchange; (b) natural log of specular decay with respect to total intensity for five different incidence angles; data exhibits a linear decrease with increasing sample temperature, and a greater rate of signal decay for a more normal incidence angle.

Figure 4-3

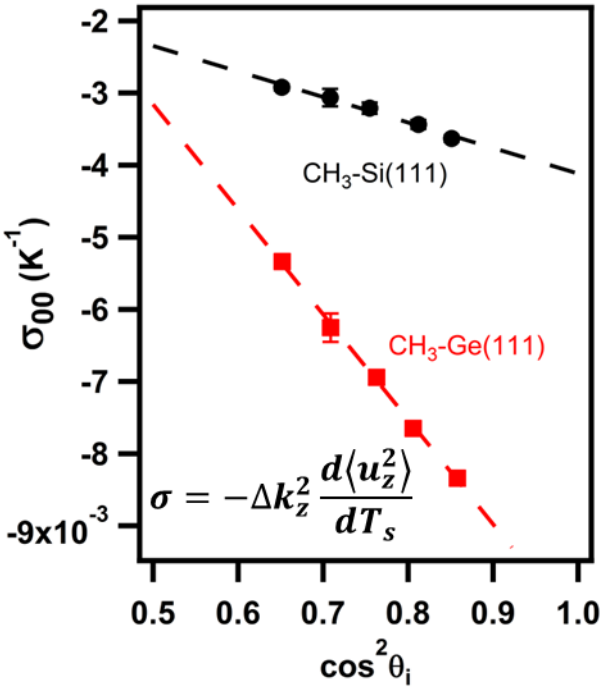

Decay rate of specular intensity as a function of the squared cosine of the incidence angle, showing a greater dependence on angle for CH_3-Ge(111) as compared with CH_3-Si(111), indicating a softer interface. Error bars represent standard deviations from independent measurements repeated three times for each point.

Figure 4-4

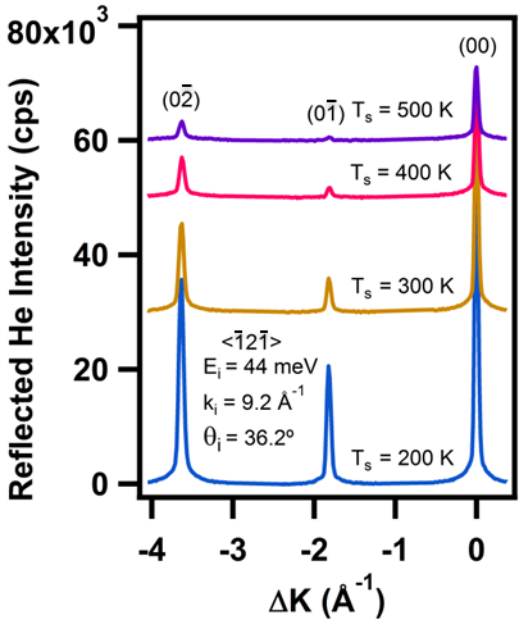

Decay of the specular and first- and second-order diffraction peaks for the same incidence energy.

Experiment file: Figure 4-4 (120214).pxp

Raw data file: 120214.D01; 120214.D03; 120214.D05; 120214.D07

Figure 4-5

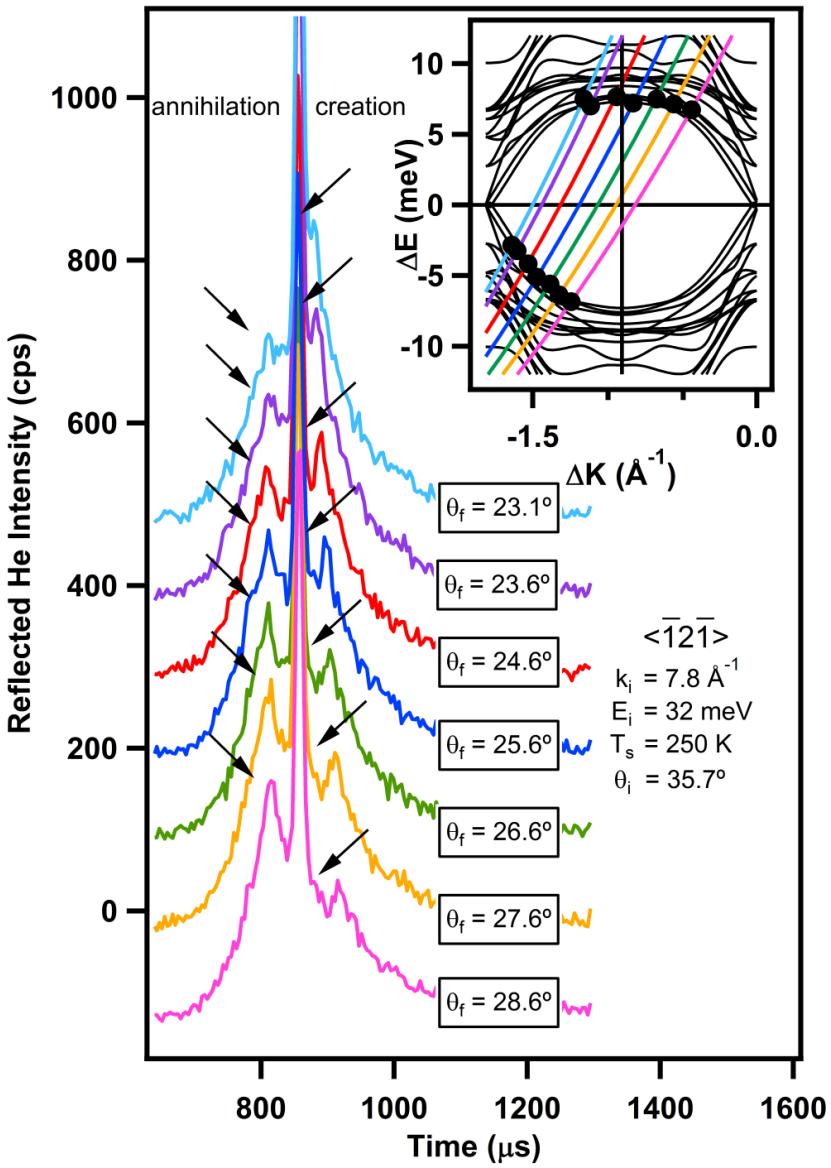

Inelastic time-of-flight spectra of several final scattering angles (θ_f), offset vertically for clarity; arrows indicate single-phonon annihilation and creation peaks, corresponding to the black dots in the dispersion curve (inset), which themselves fall on color-coded scan curves for each spectrum.

Experiment file: Figure 4-5.pxp

Raw data file: 032715.004; 032715.006; 032715.007; 040215.002; 040215.004; 040215.006

Figure 4-6

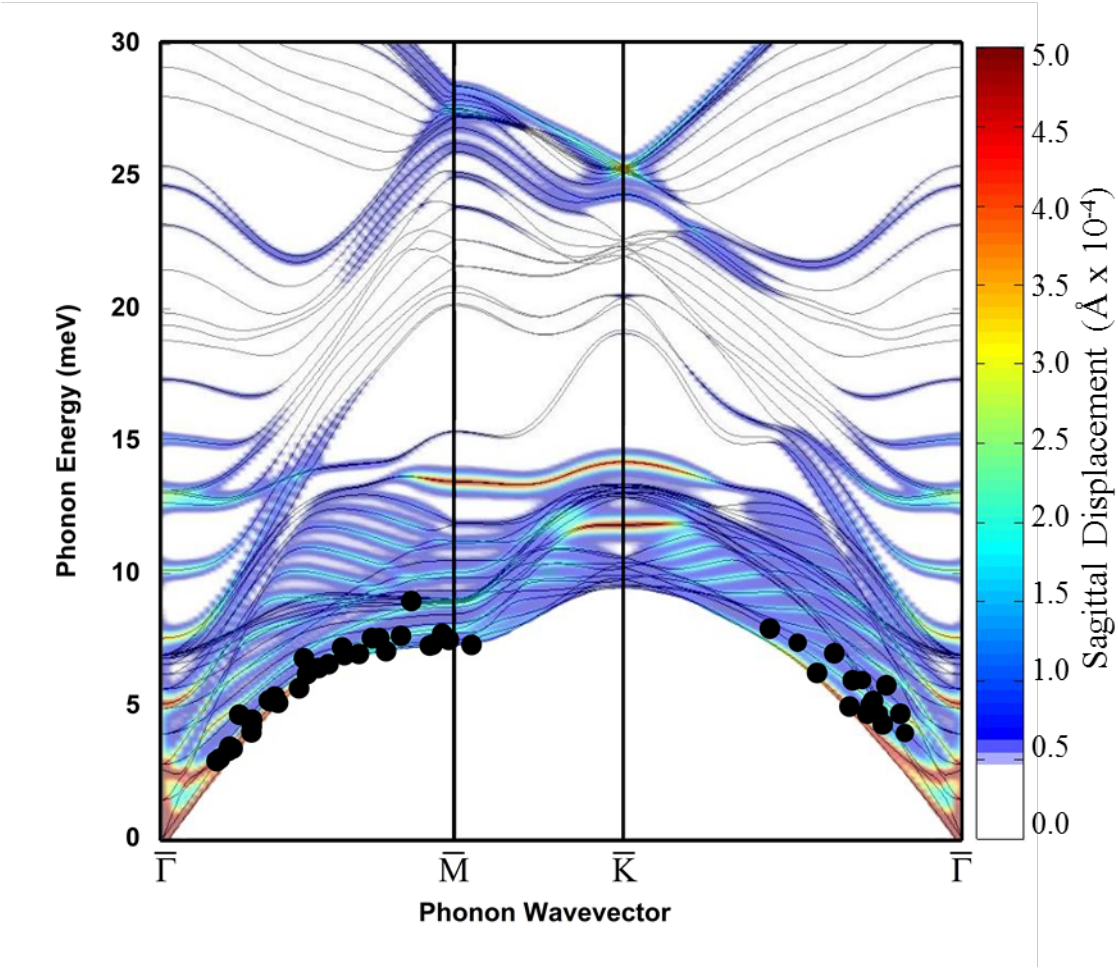

Dispersion curves (lines) of CH_3-Ge(111) as determined by DFPT calculations, overlaid with HAS single phonon data collected in the same manner as in Fig. 3; total sagittal displacement of the CH_3 group is indicated by color bar.

Figure 4-7

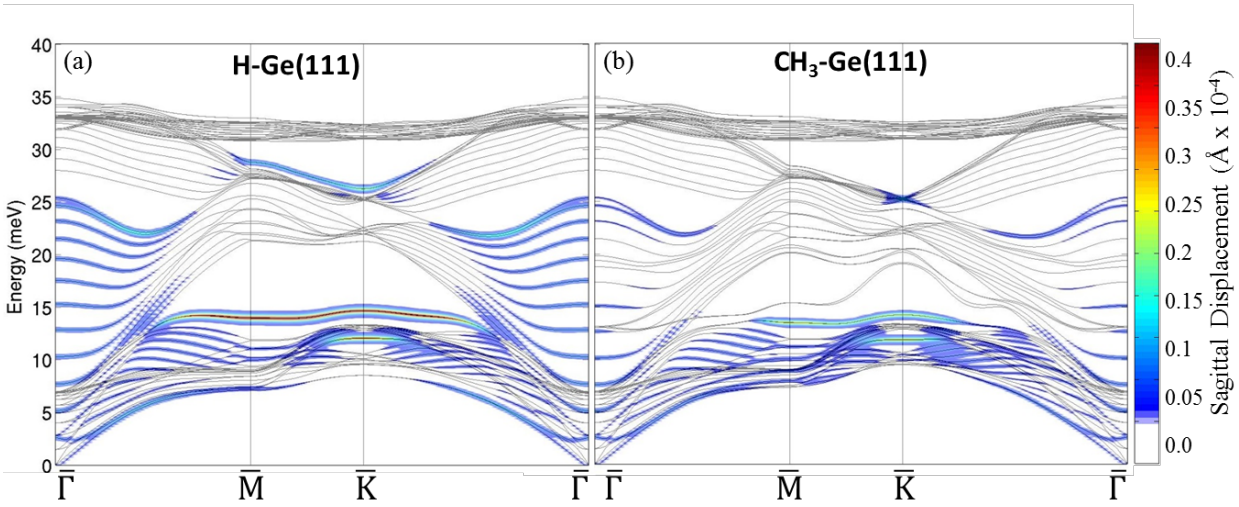

Dispersion curves of (a) H-Ge(111) and (b) CH_3-Ge(111) as determined by DFPT calculations; relative sagittal displacements of 1st layer Ge atoms indicated by color bar.

Figure 4-8

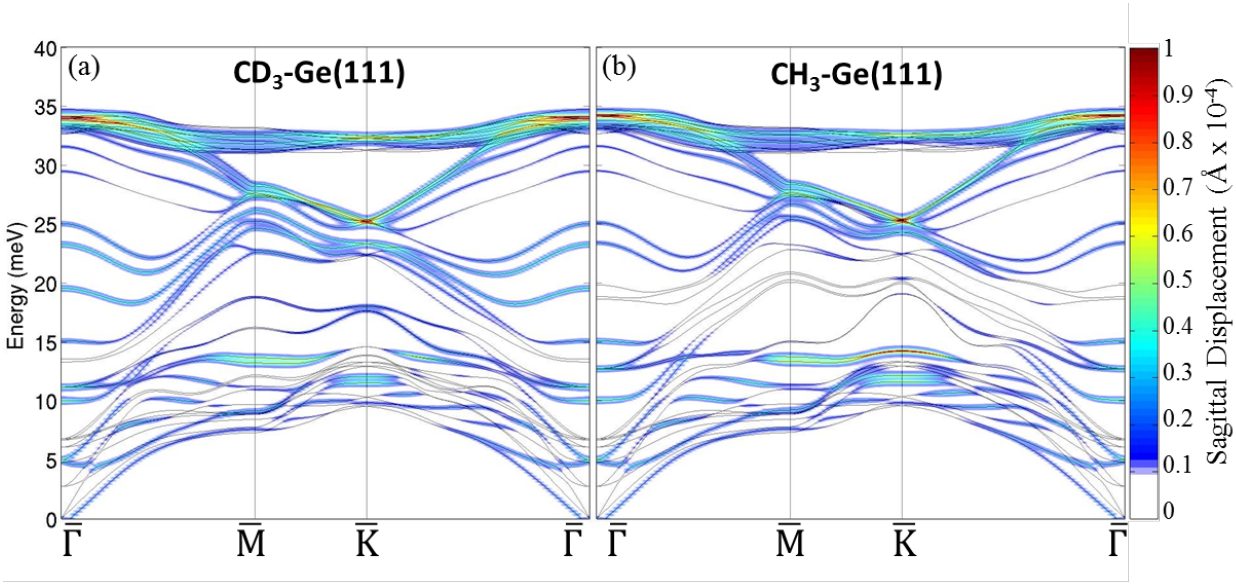

Dispersion curves of (a) CD_3-Ge(111) and (b) CH_3-Ge(111) as determined by DFPT calculations; relative sagittal displacements of C atoms indicated by color bar.

Chapter 5

Experimental and Theoretical Study of Rotationally Inelastic Diffraction of $H_2(D_2)$ from Methyl-terminated Si(111)

This chapter contains an article that was reproduced in part with permission from The Journal of Chemical Physics. Copyright 2016 American Institute of Physics.[99]

Fundamental details concerning the interaction between H_2 and CH_3-Si(111) have been elucidated by the combination of diffractive scattering experiments and electronic structure and scattering calculations. Rotationally inelastic diffraction (RID) of H_2 and D_2 from this model hydrocarbon-decorated semiconductor interface has been confirmed for the first time *via* both time-of-flight and diffraction measurements, with modest $j = 0 \rightarrow 2$ RID intensities for H_2 compared to the strong RID features observed for D_2 over a large range of kinematic scattering conditions along two high-symmetry azimuthal directions. The Debye-Waller model was applied to the thermal attenuation of diffraction peaks, allowing for precise determination of the RID probabilities by accounting for incoherent motion of the CH_3-Si(111) surface atoms. The probabilities of rotationally inelastic diffraction of H_2 and D_2 have been quantitatively evaluated as a function of beam energy and scattering angle, and have been compared with complementary electronic structure and scattering calculations to provide insight into the interaction potential between H_2 (D_2) and hence the surface charge density distribution. Specifically, a six-dimensional potential energy surface (PES), describing the electronic structure of the $H_2(D_2)$/CH_3-Si(111) system, has been computed based on interpolation of density functional theory (DFT) energies. Quantum and classical dynamics simulations have allowed for an assessment of the accuracy of the PES, and subsequently for identification of the features of the

PES that serve as classical turning points. A close scrutiny of the PES reveals the highly anisotropic character of the interaction potential at these turning points. This combination of experiment and theory provides new and important details about the interaction of H_2 with a hybrid organic-semiconductor interface, which can be used to further investigate energy flow in technologically relevant systems.

Introduction

This study details the first rotationally inelastic diffraction of molecular hydrogen from a hybrid organic-semiconductor interface, bolstering the understanding of technologically relevant systems, such as fuel cells and biosensing electronics, where the interaction of H_2 with the surface charge density distribution of these materials is of paramount interest.[100–106] The nature of gas interactions at solid surfaces has been thoroughly examined through characterizations of chemisorption for a variety of interfaces, providing a strong basis for understanding the processes involved in surface chemical reactions.[107] While a traditional route for understanding molecular chemisorption is monitoring the fraction of molecules that stick to a given surface,[108] it has been theoretically demonstrated and experimentally proven that diffraction of molecules from a surface can provide complementary and precise information regarding the gas-surface interaction potential.[109,110] Diffraction patterns of diatomic molecules in particular have highlighted the role of rotational degrees of freedom in the chemisorption process, indicating a direct effect on dissociative probabilities and revealing fundamental details concerning the interaction of gases with surface charge densities.[107,111]

Methyl-terminated Si(111) features a complete (1x1) methyl termination of its underlying lattice, endowing this surface with improved interfacial electronic properties and surface

passivation, and establishing it as a model system for the understanding of organic-functionalized systems. This interface has been thoroughly characterized by many experimental and theoretical techniques: the surface structure and extent of methyl termination have been surveyed by elastic helium atom scattering,[37,40,75] scanning tunneling microscopy,[70,112] and synchrotron-based x-ray photoelectron spectroscopy (XPS),[113] and the vibrational dynamics were studied *via* high-resolution electron energy loss spectroscopy,[114] transmission infrared spectroscopy,[73,115] and inelastic helium atom scattering in conjunction with density functional perturbation theory.[40,75] This study employs rotationally inelastic diffraction and accompanying scattering calculations to further explore the surface charge density of CH_3-Si(111) and probes the interaction potential with H_2, broadening the understanding of the anisotropic features of this system. This potential anisotropy can serve a fundamental role in dissociative chemisorption for thin-film systems.

Rotationally inelastic diffraction (RID), whereby diatomic molecules impinging upon a surface convert translational energy into rotational energy (or *vice versa*) and are scattered into unique angular channels, was first reported in experiments involving diffraction of H_2 from MgO and LiF in the 1930s.[116–118] Since then, this technique has seen improvements through gains in angular resolution that have allowed a more precise investigation of the RID peaks.[119,120] High angular resolution and a wide range of incident energies have enabled the widespread use of RID, with the goal of investigating the gas-surface potential for a variety of systems.[116,120–123] These studies have provided a wealth of information not only on the nature of interfacial dynamics, but also on the theory that has been developed to study them.[116,117,124,125]

The dependence of diatomic diffraction on molecular orientation processes makes theoretical modeling of the interaction a distinctly more complicated task than for monatomic

systems such as He,[121] because the rotational transitions that occur at the surface are highly sensitive not only to the anisotropy of the interactions, but also to the corrugation of the gas-surface interaction potential and the coupling of these two factors.[117] However, a number of combined theoretical and experimental studies have already attempted to understand better the effect of parallel momentum transfer on elastic[126–128] and rotationally inelastic diffraction.[116,129] State-of-the-art theoretical models have shown some limitations, for example, in accurately reproducing the intensities of RID peaks relative to their elastic counterparts. However, they have proven very useful in reproducing general trends,[110,124,125,130,131] which are the result of the main features characterizing the underlying potential energy surfaces, such as the corrugation and the anisotropy.

This paper presents the first rotationally inelastic diffraction measurements on an organic-functionalized semiconductor. In contrast to the various metal and alloy surfaces that have been characterized *via* RID, CH_3-Si(111) represents a new soft-film, *i.e.*, low Debye temperature system for experimental studies. High-resolution rotationally inelastic diffraction of H_2 and D_2 has been employed to study the anisotropy of the CH_3-Si(111) surface *via* comparison with quantum dynamics simulations. The low-energy molecular diffraction measurements performed herein are primarily surface-sensitive, revealing information on the structure, charge density, and interfacial properties of the surface and its interactions with impinging molecules. This low incident energy permits a valid use of the rigid rotor assumption and energetically forbids vibrational excitations at the energies used.[121] Rotationally inelastic diffraction spectra for H_2 and D_2 are compared, demonstrating much greater rotational excitation probabilities for D_2. Measurements of experimental RID excitations relative to elastic scattering events are examined as a function of incident angle and beam energy. The precision of these rotational

probabilities is improved by employing the Debye-Waller model to account for the attenuation of diffraction peak intensities as a function of increasing surface temperature. Experimentally measured RID probabilities indicate a greater likelihood, not unexpectedly, of rotational excitation for higher beam energies, but show no significant dependence on incident angle. The potential energy surface (PES) of the $H_2(D_2)/CH_3$-Si(111) system has been modeled by interpolation of a density functional theory (DFT) energies data set, and used to study rotationally inelastic scattering and to simulate RID probabilities by means of quasi-classical and quantum dynamics. Quantum dynamics simulations have been used to assess the accuracy of the PES through a direct comparison with experimental results, whereas quasi-classical trajectories have been used to track down the aspects of the molecule-surface PES that lead to rotational excitation. These classical turning points show both large corrugation and high anisotropy for the interaction, as revealed by a thorough survey of the polar angular dependence of the PES landscape on these regions.

Methods

Methyl-Si Sample Preparation

All chemicals were used as received. Water (≥18.2 MΩ cm) was obtained from a Barnstead Nanopure system. Czochralski-grown n-Si wafers (Virginia Semiconductor, Fredericksburg, VA), 381 ± 25 μm thick, were double-side polished, doped with phosphorus to a resistivity of 1 Ω cm, and oriented to within 0.1° of the (111) crystal plane. CH_3-Si(111) surfaces were prepared according to a published procedure.[132] The wafers were cut into 1 cm x 3 cm pieces and rinsed sequentially with water, methanol (≥99.8%, EMD), acetone (≥99.5%, BDH), methanol, and water. Organic contaminants were removed and the surfaces were

oxidized by immersing the wafers in a freshly prepared piranha solution (1:3 v/v of 30% H_2O_2(aq) (EMD): 18 M H_2SO_4 (EMD)) at 90 – 95 °C for 10 min. The piranha solution was drained and the wafers were rinsed with copious amounts of water. Atomically flat H-terminated surfaces were prepared[133] by immersing the cleaned wafers in buffered HF(aq) (Transene Co. Inc., Danvers, MA) for 18 s, rinsing with water, and immediately placing the wafers in an Ar-purged solution of NH_4F(aq) (40%, Transene Co. Inc.) for 9 min. The wafers were agitated periodically to remove bubbles that formed on the surface. The Si samples were removed from the NH_4F(aq) solution, rinsed with water, and dried under a stream of N_2.

The Si wafers were chlorinated inside a N_2-purged glove box with <10 ppm O_2. A saturated solution of PCl_5 (99.998% metal basis, Alfa Aesar) in chlorobenzene (anhydrous, ≥99.8%, Sigma-Aldrich) was preheated with an initiating amount (<1 mg/mL) of benzoyl peroxide (≥98%, Sigma-Aldrich). The wafers were rinsed with chlorobenzene and reacted in the PCl_5 solution at 90 ± 2 °C for 45 min. The reaction solution was drained and the wafers were rinsed with copious amounts of chlorobenzene, followed by tetrahydrofuran (THF, anhydrous, inhibitor-free, ≥99.9%, Sigma-Aldrich).

The Cl-terminated surfaces were alkylated in a 1.0 – 3.0 M solution of CH_3MgCl (Sigma-Aldrich or Fisher Scientific) in THF. The reaction was heated to 50 ± 2 °C for >12 h. The reaction solution was drained and the wafers were rinsed with THF, submerged in THF, and removed from the N_2-purged glove box. The samples were sonicated sequentially for 10 min in each of THF, methanol, and water. The wafers were broken into 1 cm^2 pieces, dried under a stream of N_2, and sealed under Ar for shipment from Pasadena, CA to Chicago, IL. X-ray photoelectron spectroscopy (XPS) indicated that the surfaces were fully terminated with Si-C bonds, and that there was no detectable surface oxidation.

H_2 and D_2 Diffraction Techniques

To measure the elastic and rotationally inelastic diffraction peaks, these experiments required the use of an energy- and momentum-resolved ultra-high vacuum (UHV) scattering apparatus. This instrument has been described in full-detail elsewhere;[41] in brief, this apparatus consists of three primary sections: a differentially pumped beam-source manifold, a UHV crystal chamber, and a rotatable mass spectrometer detector. For beam generation, high pressures (800 to 2000 psi) of ultra-high purity gases (He, H_2, D_2) are expanded through a 15 μm diameter nozzle source that is cooled by a closed-cycle helium refrigerator to generate an intense and nearly monoenergetic ($\Delta v/v \leq 1\%$ for He, 10% for H_2, D_2) supersonic neutral atomic beam. The beam energy is dependent on the nozzle temperature, which can be adjusted for beam energies in the range of 35 – 90 meV. For diffraction and time-of-flight measurements, a mechanical chopper was used to modulate the beam prior to collision with a duty cycle of 50%. For collection of time-of-flight data, the beam is modulated with a pseudorandom chopping sequence for cross-correlation analysis.[5] Collimation of the beam occurs through a series of apertures, resulting in a 4 mm spot size on the crystal (chopper-to-crystal distance = 0.4996 m) in the UHV scattering chamber (base pressure 3×10^{-10} Torr). The crystal was mounted onto a six-axis manipulator which can be positioned precisely to control the incident angle, θ_i, the azimuth, φ, and the tilt, χ, with respect to the scattering plane. Post-collision, the atoms travel along a 1.0234 m (crystal-ionizer distance) triply-differentially pumped rotatable detector arm, with an angular resolution of 0.29° FWHM, after which they are ionized by electron bombardment. The ions then pass through a quadrupole filter where they are mass-selected before being collected by an electron multiplier. Angular distributions were obtained by scanning the detector at 0.1° computer-controlled increments while holding the incident angle at a fixed value.

The rotational experiments are carried out with n-H_2 or n-D_2 molecular beams, with varied stagnation pressures. The rotational populations of H_2 and D_2 were not measured directly, but instead were calculated based on previous theoretical and experimental results. Generally, the ratio of ortho- to para-$H_2(D_2)$ is determined by the source temperature, and subsequent ortho–para conversion does not occur during the expansion.[134] The occupation of rotational states follows a near Boltzmann distribution within the respective ortho/para families, and can be characterized by an effective rotational temperature, T_R, which can be expressed with an empirical fit[135] for n-D_2 as

$$\log\left(\frac{T_R}{T_0}\right) = -0.401 \cdot \log\left[P_0 d \cdot \frac{T_{ref}}{T_0}\right] + 0.16\,, \tag{5-1}$$

where the reference temperature, T_{ref}, is 298 K, T_0 is the beam temperature, and $P_0 d$ is the stagnation pressure times the nozzle diameter, given in units of Torr·cm. The beam energies, rotational temperatures, and corresponding rotational populations for the experiments performed herein are given in Table 5-1. In cases where high-translational-energy D_2 beams were created by seeding in a 1:1 mixture of H_2 and D_2, the rotational populations of the D_2 molecules were calculated using the measured nozzle temperature instead of the temperature derived from time-of-flight analysis, allowing for a more precise determination of these data points. All experiments reported herein used incident energies below 120 meV for D_2, such that over 99% of the impinging D_2 molecules are in their vibrational ground states. Additionally, vibrational excitations can be ignored due to the large inter-level spacing for D_2 molecules (~380 meV).[136]

Theoretical Modeling

Theoretical analysis of the $H_2(D_2)/CH_3$-Si(111) system has been performed within the Born-Oppenheimer static surface approximation (BOSSA). The Born-Oppenheimer approximation is justified by the different time scales associated with the motion of nuclei and electrons. The surface static approximation is justified by the mass mismatch between the surface-terminating CH_3 layer and the H_2 and D_2 projectiles (although low recoil effects could be expected). Furthermore, experimental results have been extrapolated to a surface temperature of 0 K *via* the Debye-Waller correction, which allows a direct comparison between experimental measurements and SSA theoretical results. Working within this framework, a six-dimensional (6D) PES is first computed, and then is included in the nuclear Hamiltonian to perform dynamics simulations.

Electronic Structure Calculations

The 6D PES, for which the degrees of freedom are illustrated in Figure 5-1, has been computed by interpolation of a density functional theory energy data set. To perform the DFT periodic calculations, the plane-wave-based code VASP (Vienna *ab initio* Simulation Package)[137,138] has been used. In these calculations, the exchange-correlation energy of the electrons has been described using the generalized gradient approximation (GGA); in applying the GGA, the Perdew-Burke-Ernzerhof (PBE) functional[45] has been used. Additionally, the ion cores have been described using the PAW (projector augmented-wave) method.[139]

The $H_2(D_2)/CH_3$-Si(111) system has been modeled using a five-layer slab and a 2x2 hexagonal surface unit cell, as shown in Figure 5-1. The size of the unit cell has been chosen to mitigate interaction between molecules in adjacent cells, which are present in the calculations

due to the use of periodic boundary conditions (PBC). To avoid artifacts caused by the use of PBC in the *z* direction, a vacuum layer of 21 Å has been set. A 7x7x1 Monkhorst-Pack grid of k-points was used to sample the Brillouin zone.[46] The cutoff energy for the plane-wave basis has been set to 650 eV. The lattice bulk parameter has been optimized, finding a value of a = 5.48 Å, which agrees well with the known experimental value (5.431 Å).[47] The surface interlayer distances have also been relaxed until the forces were below a 1 meV/Å threshold.

Modified Shepard Interpolation Method

To build the continuous 6D PES, $V_{6D}(X,Y,Z,r,\Theta,\varphi)$, representing the ground electronic state structure of the $H_2(D_2)$-CH_3/Si(111) system, this work makes use of the modified Shepard (MS) interpolation method, originally developed by Collins *et al.*[140,141] to study gas-phase reactions, and later adapted to study reactive scattering of molecules from surfaces.[142–145] Specifically, a recent implementation of the MS method,[146] which includes strict plane group symmetry and translational periodicity, is utilized herein. In the MS method the interpolated PES is described by a weighted series of Taylor expansions centered on a number of DFT energy data points, N. These data points are sampled throughout the configuration space of the system. Thus, the global PES at any configuration $\vec{Q}$ is given by:

$$V(\vec{Q}) = \sum_{i=1}^{N} \sum\nolimits_{g \in G_{CNP} \times G_{PG}} w_{(g \circ i)}(\vec{Q}) S_{(g \circ i)}(\vec{Q}), \tag{5-2}$$

where w is a weighting function, G_{CNP} and G_{PG} are the molecular permutation and plane symmetry groups, and S is the Taylor series expansion of the PES in the vicinity of the geometry of data point $(g \circ i)$, which denotes that the quantity for data point i has been transformed according to the symmetry operation $g \in G_{CNP} \times G_{PG}$. Note that $\vec{Q}$ in Equation (5-2) does not

represent the set of Cartesian coordinates used to compute the DFT energy points, but a set of redundant internal coordinates relative to them through the Wilson B matrix.[146] The Taylor series expansion used here is expressed as:

$$S_i\vec{Q} = E(i) + \Delta E(i)^T \Delta\varsigma(i) + \tfrac{1}{2}\Delta\varsigma(i)^T F(i)\Delta\varsigma(i), \tag{5-3}$$

where *E(i)* is the energy at the data point geometry *i*, $\Delta E(i)$ is the vector of first derivatives at data point *i* with respect to elements of $\varsigma(i)$, which are local coordinates resulting from a linear combination of the redundant internal coordinates $\vec{Q}$, *F(i)* is the matrix of second derivatives at data point *i* with respect to elements of $\varsigma(i)$, and $\Delta\varsigma(i)$ is the displacement of the point $\vec{Q}$ from the data point geometry $\vec{Q}(i)$ in $\varsigma(i)$ coordinates.

It is important to note that the MS method uses a non-homogeneous sampling of the configuration space, so that more DFT energy points are used in the dynamically relevant regions. These regions are selected by using classical dynamics through a feedback process, hereafter called the GROW process. The first step begins with an initial basic version of the PES, defined in this case by only 50 DFT energy points. Then a small batch of classical trajectories is run on this basic PES, and from these trajectories new geometries are selected and added to the PES, thereby augmenting it. The new geometries are chosen according to two different criteria:[147] either new energy data points are added to the region most frequently visited by the trajectories, or they are added to regions suspected to be the most inaccurate ones. Periodically, a larger batch of trajectories is run and used to compute some observables, which in this case are the rotational excitation probabilities. If the probabilities change significantly with the number of DFT data points added to the PES, the procedure goes back to the second step of running a small batch of trajectories. If the probabilities do not change significantly, the PES is

considered converged, as illustrated in Figure 5-2. At this point, it should be pointed out that in order to properly sample the dynamical regions relevant to this analysis, the incident conditions of the classical trajectories are selected to correspond to the experimental conditions.

Quasi-classical Dynamics

Quasi-classical dynamics – *i.e.*, classical dynamics including the zero point energy of the molecule – have been used to both grow and scrutinize the PES. To compute quasi-classical trajectories, the classical equations of motion are solved using the velocity-Verlet algorithm.[148] For each initial energy (E_i) and incident angle (θ_i), the classical scattering probability is calculated as an average over the molecular initial conditions, *i.e.* over the internal coordinates and conjugated momenta. The initial molecular conditions are sampled using a Monte Carlo method. To ensure low statistical error, approximately 2.5 x 10^4 trajectories are computed for each set of initial conditions (E_i, θ_i). In these calculations, a molecule is considered reflected (and the integration ends) whenever the final distance between the molecule and the surface, z_f, becomes equal to initial distance, z_i, with the molecular velocity vector pointing towards the vacuum. To analyze rotational excitation upon scattering using classical dynamics, it must be taken into account that the classical angular momentum (L) follows a continuous distribution. Therefore, to analyze rotational excitations, the continuous representation is transformed into a discrete one.[149,150] This transformation is performed, in general, by evaluating the closest integer that satisfies

$$j = \frac{1}{2}\left[-1+\left(1+\frac{4L^2}{\hbar^2}\right)^{1/2}\right]. \tag{5-4}$$

However, quantum selection rules for homonuclear diatomic molecules only allow rotational transitions for which $\Delta j = \pm 2$. Therefore, to obtain D_2 rotational excitation probabilities, the initial rotational state of the molecule is considered, and only the closest even or odd integers that satisfy Equation (5-4) are evaluated.

Quantum Dynamics

Diffraction probabilities are computed herein by solving the time-dependent Schrödinger (TDS) equation of the nuclear Hamiltonian using the Multi-Configuration Time-Dependent Hartree (MCTDH) method[151,152] which has already been successfully used to study diffraction of atomic projectiles,[153] as well as reactive scattering of molecular projectiles.[154–156] In the MCTDH method, the nuclear wavefunction is written as a sum of products of single-particle functions (SPFs). In this particular case, each SPF (χ) combines up to two degrees of freedom, and so the nuclear function of this system can be written as:

$$\Phi(Q,t) = \sum_{h=1}^{N_{x,y}} \sum_{k=1}^{N_z} \sum_{l=1}^{N_{\Theta,\varphi}} C_{hkl}(t)\chi_h(x,y;t)\chi_k(z;t)\chi_l(\Theta,\varphi;t), \tag{5-5}$$

where Q represents the set of nuclear coordinates, and ($N_{x,y}$,N_z,$N_{\Theta,\varphi}$) represents the number of SPFs used to describe each mode. The SPFs are in turn represented by linear combinations of time-independent primitive basis functions. In order to reduce the computational effort, and taking advantage of the lack of reactivity of D_2/CH_3-Si(111) in the energy range considered here, five-dimensional (5D) calculations have been performed, in which the atom-atom distance has been kept frozen at the equilibrium D_2 gas-phase distance (see Table 5-2 for calculation parameters). Within the MCTDH framework, the equations of motion for both the expansion coefficients and the SPFs are derived from the Dirac-Frenkel variational principle, which leads to

a set of coupled equations. In general, solving this coupled-equation system requires less computational effort than standard time-dependent wave packet propagation (TDWP) methods,[157] because the number of SPFs needed is smaller than the number of time-independent basis functions used in the standard TDWP methods. To obtain elastic and inelastic diffraction probabilities, a flux analysis is carried out with the aid of a complex absorbing potential located in the non-interaction z region.[158]

Finally, it should be noted that to take full advantage of the MCTDH formalism, the multidimensional non-separable PES has to be rewritten as a linear combination of products of one- or two-dimensional functions. This transformation can be performed using the POTFIT algorithm, which is based on the approximation theorem of Schmidt,[159] provided with the Heidelberg MCTDH package. Thus, the multi-dimensional PES is rewritten as:

$$V(Q) \approx V_{approx} = \sum_{j=1}^{m_{x,y}} \sum_{k=1}^{m_z} \sum_{l=1}^{m_{\Theta,\varphi}} c_{jkl} \zeta_j^{(x,y)}(x,y) \zeta_k^{(z)}(z) \zeta_l^{(\Theta,\varphi)}(\Theta,\varphi), \tag{5-6}$$

where $\zeta_j^{(u)}$ is the j^{th} one- or two-dimensional function used to describe the single particle mode u (the so-called natural potential). These functions are the ones used to expand the SPFs, which are represented in a primitive grid of points. The expansion coefficients c_{jkl} are determined by the overlap between the multi-dimensional PES and the natural potentials (see Table 5-3 for representative parameters for PES refits).

Results and Discussion

H_2 and D_2 Diffraction from CH_3-Si(111)

Angular distributions of H_2 scattered from CH_3-Si(111) are shown in Figure 5-3 along the high-symmetry $\langle \bar{1}2\bar{1} \rangle$ $\left(\bar{\Gamma} - \bar{\mathrm{M}}\right)$ and $\langle 01\bar{1} \rangle$ $\left(\bar{\Gamma} - \bar{\mathrm{K}}\right)$ azimuthal alignments; both diffraction spectra were taken under identical conditions, with a room temperature beam (E_i = 81.4 meV) and cold surface temperature (T_s = 140 K). The zeroth-order specular ($\theta_i = \theta_f$) diffraction peak and elastic first-order diffraction peaks are clearly resolved here; the relatively large first-order diffraction peak intensities compared to specular indicate a significant corrugation of the gas-surface potential. Elastic diffraction peaks arise when the kinematic condition for Bragg diffraction for in-plane scattering is satisfied, such that

$$\Delta\vec{K} = \vec{k_i}\left(\sin\theta_f - \sin\theta_i\right) = \overrightarrow{G_{mn}}, \tag{5-7}$$

where $\Delta\vec{K}$ is the change in the surface-parallel component of the H_2 wavevector, $\vec{k_i}$, θ_i and θ_f are the initial and final scattering angles relative to the surface normal, and $\overrightarrow{G_{mn}}$ is the surface reciprocal lattice vector. Information on the surface geometry and lattice constant can be determined by analyzing the spacing between diffraction peaks; the spacings between specular $(\Delta\vec{K} = 0)$ and first-order diffraction peaks are $\Delta\vec{K}$ = 1.90 Å^{-1} and 3.29 Å^{-1} along $\langle \bar{1}2\bar{1} \rangle$ and $\langle 01\bar{1} \rangle$, respectively, corresponding to a hexagonally-packed methyl adlayer with a real-space lattice constant of 3.82 Å. This value is in excellent agreement with previous helium diffraction measurements from this methyl-terminated Si(111) surface,[74] with both identifying a (1x1) commensurate monolayer of methyl groups on Si(111).

Unlike with helium diffraction, when a H_2 or D_2 molecule scatters from the surface, it is capable of exchanging energy between its internal rotational and translational degrees of freedom; this exchange must still conserve total energy, such that

$$E_f - E_i = \frac{\hbar^2 k_f^2}{2m} - \frac{\hbar^2 k_i^2}{2m} = \Delta E_{\text{int}}^{rot} . \tag{5-8}$$

Here, $\hbar$ is the reduced Planck constant, m is the mass of H_2 or D_2, E_i and E_f are the initial and final kinetic energy of the projectile, respectively, and $\Delta E_{\text{int}}^{rot}$ is the energy exchanged between rotational and translational modes, which equals a difference between the molecule's rotational energy levels as determined by the rigid rotor model; note that symmetry constraints within the hydrogen molecule impose a rotational selection rule of $\Delta j = \pm 2$. This phenomenon of internal energy exchange results in RID peaks scattered at distinct angles from their parent elastic diffraction peaks, such that

$$\theta_f^{RID} = \arcsin\left[\frac{k_i \sin\theta_i - \overrightarrow{G_{mn}}}{\left(k_i^2 - \frac{2m}{\hbar^2}\Delta E_{\text{int}}^{rot}\right)^{1/2}} \right]. \tag{5-9}$$

Figure 5-4(a) shows a diffraction spectrum for H_2 scattering from CH_3-Si(111), which includes a small peak associated with the specular $j = 0 \rightarrow 2$ rotational excitation; note that RID peaks are labeled using the (j_i,j_f,m,n) notation, whereas elastic diffraction peaks are labeled with the (mn) notation. By positioning the rotatable detector arm at the final scattering angle of this RID peak, time-of-flight measurements can be used to confirm the inelastic scattering of the hydrogen molecules. A cross-correlation time-of-flight spectrum taken at the same conditions as this peak is shown in Figure 5-4(b); a diffuse elastic and rotationally inelastic hydrogen peak are observed to be fully resolved from one another. The flight time separation between the elastic and

inelastic peak can be used to calculate the energy exchange as a result of inelastic scattering from the surface (Figure 5-4(b), inset). The RID peak shown in Figure 5-4(b) arrived at a longer time than the elastic peak, indicating a loss in energy and velocity of the H_2 molecules; specifically, the calculated energy agrees well with the expected value of 45.4 meV for a $j = 0 \rightarrow 2$ rotational excitation for an incident H_2 molecule.

In order to obtain highly resolved elastic and inelastic diffraction peaks in this range of relatively low beam energies, the surface probe was switched from H_2 to D_2. The predominant advantage in using D_2 is that the energy required to transition between rotational states is half that of H_2 (D_2: $j = 0 \rightarrow 2$, 22.7 meV), as predicted by the rigid rotor model, leading to a greater probability of rotational excitation. In addition, the combination of nuclear spin states for each of the nuclei in H_2 and D_2 leads to the formation of ortho (symmetric) and para (antisymmetric) spin isomers, which pair with a set of rotational states to maintain the antisymmetry of the molecule as a whole. The degeneracy of these spin states causes only ~25% of n-H_2 molecules to be in the $j = 0$ state, whereas ~66% of n-D_2 molecules are in the rotational ground state.

The utility of D_2 as a surface probe is demonstrated in Figure 5-5(a), in which a diffraction spectrum for a room temperature D_2 beam from CH_3-Si(111) shows several high-intensity elastic and RID peaks. The resolution of inelastic peaks in D_2 spectra allows for precise measurements of rotationally inelastic transition probabilities; specifically, the rotational excitations can be measured as a function of scattering angle or beam energy, as seen in Figure 5-5(b).

As the setup of this instrument does not allow for direct measurement of the absolute incident beam flux, the probabilities of rotationally inelastic diffraction are evaluated describing

them as ratios of inelastic to elastic diffraction intensities.[119,121,122] This ratio enables the number density measured by the detector to be effectively converted into flux by accounting for the change in beam velocity that results from transferring energy between translational and rotational degrees of freedom. In addition, this approach obtains accurate values by accounting for the influences of instrumental broadening, finite crystal temperature, energy spread of the beam, and the initial rotational distributions of the incident beam.

Specifically, to relate a RID peak to its parent elastic peak, the following expression is used:

$$r\left(j_i, j_f, m, n\right) = \frac{I\left(j_i, j_f, m, n\right)}{I(mn)n(j_i)} \sqrt{\frac{E_i + \Delta E_{\text{int}}^{rot}}{E_i}} \exp\left[2W_{j_i, j_f, m, n} - 2W_{mn}\right]; \tag{5-10}$$

In this expression, $I(j_i,j_f,m,n)$ and $I(mn)$ are the peak-area integrated intensities of D_2 molecules scattered from a crystal of finite surface temperature T_s. The square root term corrects for the velocity difference between elastic and rotationally inelastic scattering events, as discussed above.[122] Additionally, the rotational distributions of the impinging atoms are accounted for with $n(j_i)$. By using this ratio rather than a pure probability, the effects of surface defects and beam geometry are eliminated and experimental error associated with evaluation of the Debye-Waller factor, $W(T_s)$, is mitigated.

Attenuation of diffraction intensity due to thermal motion at the CH_3-Si(111) surface is accounted for *via* the Debye-Waller factor, which can be approximated in the semi-classical limit of a quantum-mechanical description of inelastic scattering as

$$W(T_s) = \frac{12m\left[E_i \cos^2\theta_i + D\right]T_s}{M_{eff} k_B \Theta_D^2} \tag{5-11}$$

for the specular peak, where D is the attractive well depth for a gas-surface interaction potential, M_{eff} is the effective surface mass that a given H_2 or D_2 molecule interacts with (assumed here to be 15 amu), k_B is Boltzmann's constant, and Θ_D is the surface Debye temperature.[80,134] The attenuated intensities of RID peaks are corrected using the Debye-Waller factor associated with their parent diffraction peaks, which is a reasonable assumption based on the small parallel momentum transfer associated with the (0,2,0,0) and $(0,2,0,\bar{1})$ peaks.[149,160]

The Debye-Waller factor can be quantified by relating the intensity of a peak to its ideal intensity for a lattice at 0 K, I_0, such that

$$I = I_0 e^{-2W(T_s)}. \tag{5-12}$$

As such, the natural log of I/I_0 versus T_s produces a linear decay, from which the Debye-Waller factor for a given system can be extracted. Figure 5-6(a) shows the thermal attenuation of the specular peak at a given set of incident conditions over surface temperatures ranging from 140 to 350 K; the inset of this figure exhibits the linear decay which provides the Debye-Waller factor for the H_2/CH_3-Si(111) system. This exponential factor is derived from the normal and parallel momentum transfers during the scattering process (Δk_z and ΔK, respectively) and the associated mean-square displacements (MSD) of the crystal atoms ($\langle u_z^2 \rangle$ and $\langle u_\parallel^2 \rangle$), such that

$$2W(T_s) = \Delta k_z^2 \langle u_z^2 \rangle + \Delta K^2 \langle u_\parallel^2 \rangle. \tag{5-13}$$

For the specular peak,

$$\Delta\vec{k_z} = 2\vec{k_i}\left[\left(\cos^2\theta_i + \tfrac{D}{E_i}\right)^{1/2}\right]. \tag{5-14}$$

The perpendicular MSD and the well depth (D) of the gas-surface interaction potential can therefore be determined by plotting the derivative $d2W(T_s)/dT_s$ versus $cos^2\theta_i$ and extracting the slope and y-intercept, respectively.[56,74] Figure 5-6(b) shows diffraction decay rates at several angles, and the inset demonstrates the angular dependence of the Debye-Waller factor that provides a perpendicular MSD of (1.85±0.30) x 10^{-5} $Å^2K^{-1}$. Analogous data for the He/CH_3-Si(111) system is also shown in this figure, and its comparable slope provides a perpendicular MSD of (1.0±0.1) x 10^{-5} $Å^2K^{-1}$, just slightly below what is measured for the H_2 system.[74] The difference in y-intercepts indicates a higher potential well depth for H_2 (D = 32 ± 9 meV) than for He (D = 7.5 ± 2.6 meV), as expected based on the higher degree of polarizability for H_2. Equation (5-11) uses these well depths to provide a surface Debye temperature of 723 K (503 cm^{-1}) for the H_2 system, which is considerably lower than 983 K (683 cm^{-1}) measured *via* He diffraction. While the surface Debye temperature measured for H_2/CH_3-Si(111) differs from He, both molecules seem to interact with a vibrational mode of the methyl adlayer: either Si-C bending (507 cm^{-1}) or Si-C stretching (683 cm^{-1}).[161]

Figure 5-7 shows plots of r(0,2,0,0) and r(0,2,0,$\bar{1}$) for D_2 on CH_3-Si(111) as a function of beam energy, as calculated *via* Equation (5-10) with Debye-Waller corrections. There is a clear increase in rotational excitation probability with increasing beam energy, which is expected due to higher-energy incident molecules penetrating further into the surface charge density, thereby increasing the corrugation of the gas-surface interaction potential and the resultant torque on the non-spherical molecule. The dependence of rotational excitation probability on incident angle is weaker, with a more normal incident angle eliciting slightly more rotational probability for the first-order RID peak, and no apparent trend in angular dependence for the specular RID peak.

Theoretical Analysis

Quantum and classical dynamics simulations have been carried out with the goal of more accurately interpreting experimental measurements. First, to assess the accuracy of the theoretical tools employed herein, in particular the interpolated PES, quantum dynamics simulations have been compared with experimental measurements obtained at several representative sets of initial conditions (Figure 5-8). To perform this comparison, the quantum simulations consider the initial rotational distribution of the molecular beam (Table 5-1). Overall, a good agreement is observed between both sets of data; in particular, the theoretical and experimental spectra exhibit an increase in the rotational excitation probability as the incident energy increases. These results indicate that the calculated PES is accurate enough to perform the required analysis.

In Figure 5-7, quantum ratios r(0,2,0,0) and r(0,2,0,$\bar{1}$) (dashed lines) are compared with the experimental ones; it should be noted that theoretical probabilities for a fixed incident energy were within 1 degree of the experimental scattering angle. The theoretical results generally agree with the increase in rotational excitation probability as a function of incident energy. Slight disagreement between theory and experiment is observed at higher beam energies, which is likely due to the strong corrugation of this system, as well as the use of a frozen-surface model for the PES, which becomes a less reasonable approximation when the energy of incident D_2 molecules nears the rotational barrier of the methyl group (~100 meV for a surface temperature of 0 K).[40]

Having established the accuracy of the PES, a quasi-classical dynamics analysis can be performed on the regions of the PES that determine the characteristics of the diffraction spectra.

To establish the validity of the classical analysis, quantum and classical total elastic and rotational excitation probabilities have been compared. Figure 5-9 displays the elastic and rotational excitation probabilities for H_2 (classical results only) and D_2 (quantum and classical results) as a function of the beam energy, along the $\left(\overline{\Gamma}-\overline{\mathrm{M}}\right)$ direction, for three different incident angles. Several notable features are evident in this figure: (a) in the case of H_2, rotational excitation stays below 5% over the entire energy range investigated; (b) for D_2, quantum and classical simulations yield rather similar results – the classical rotational excitation probability fluctuates around 20-25%, whereas the quantum probability is slightly higher (30-35%). These results agree with the experimental results reported above, which show the presence of large RID in the diffraction spectra of D_2, whereas negligible RID has been observed for H_2 in diffraction spectra. This qualitative agreement between classical and quantum rotational excitation probabilities justifies further analysis of the systems using classical trajectories calculations, especially for incidence energies below 90 meV, beyond which point classic and quantum rotational excitation probabilities begin exhibiting different trends.

Classical trajectories have revealed that most molecules are scattered at a classical turning point around 2 Å from the plane formed by the H atoms in the methyl groups, with a molecular bond length around 0.78 Å. Given that these values are almost independent of θ_i and E_i within the range of experimental incident conditions, the characteristics of the potential have been analyzed at these (z, r) values. Figure 5-10 illustrates the one-dimensional (1D) potential energy profile along both the $\left(\overline{\Gamma}-\overline{\mathrm{M}}\right)$ and $\left(\overline{\Gamma}-\overline{\mathrm{K}}\right)$ azimuthal directions. One important feature of the PES that can be observed in Figure 5-10 is that the corrugation of the potential due to H atoms is very small compared to that due to C atoms, as the only indication of the presence of H

atoms is the small shoulder seen between the hill and the valley. Another interesting feature that can be extracted is that the projectiles are guided towards the hollow and bridge sites. It is clear that molecules with incident energies below 90 meV cannot adiabatically approach the top site or surrounding sites, and therefore most of the molecules are scattered from the hollow and bridge sites. This behavior is also corroborated by analysis of classical trajectories, which indicates that the molecules are scattered far from the top site after being efficiently steered towards the hollow and bridge sites.

Finally, Figure 5-10 also reveals a marked anisotropy of the potential in the classical turning point regions. For a closer inspection of the potential anisotropy, Figure 5-11 displays the relative potential energy as a function of the molecular orientation angle, Θ, at several z-distances from the surface. The anisotropy of the potential is observed to increase rapidly when the molecule approaches the surface, except in the case of the top site, which molecules do not sample, as discussed above. This rapid increase in the corrugation around the classical turning points is responsible for the substantial rotational excitation found in this system. It is noted that insubstantial differences are obtained for the trajectories followed by H_2 and D_2 molecules, when similar incident molecular velocities are considered. It can thus be concluded that the anisotropy experienced by both isotopes is similar, and therefore that the different rotational excitation observed is only due to the differences in rotational level spacing (~45 meV for H_2, ~22 meV for D_2).

Further insight into the nature of the PES can be extracted from Figure 5-12, which shows a series of 2D xy-cuts for several (Θ,φ) orientations. In these plots, z and r values have been chosen according to the average values at the classical turning points revealed by a classical trajectory analysis, as discussed above. This figure indicates strong corrugation in the PES, and

shows that the molecular projectile feels, although rather weakly, the H atoms that belong to the CH_3 groups.

Conclusions

The diffraction of H_2 and D_2 molecular beams from CH_3-Si(111) was complemented by electronic structure and scattering calculations to investigate the nature of the interaction potential and surface charge density for a technologically relevant organic-functionalized semiconductor interface. Time-of-flight measurements confirmed the presence of rotationally inelastic diffraction for both H_2 and D_2 on this surface, and diffraction measurements demonstrated a stronger probability of rotational excitation for D_2 as compared with H_2, as expected based on the lower energy required for an internal exchange of rotational energy. The probabilities of these $j = 0 \rightarrow 2$ rotational transitions were quantitatively evaluated as a function of beam energy and scattering angle, accounting for the thermal attenuation caused by incoherent motion at the CH_3-Si(111) surface by implementing the Debye-Waller model. The interaction potential between H_2 (D_2) and the surface charge density was then examined *via* the combination of these experimental results and quantum and quasi-classical dynamics simulations carried out on a continuous potential energy surface for $H_2(D_2)/CH_3$-Si(111) constructed by interpolation of density functional theory energies. Both experimental and theoretical data show high rotational excitation probabilities that increase with incident energy and which are weakly dependent upon incident angle, for the angle range investigated here. Additionally, dynamics calculations have identified the classical turning point regions (2 Å over hollow and bridge sites), and close scrutiny of these regions reveals a large anisotropy in the potential as a function of molecular orientation, which increases rapidly when the molecule approaches these regions and is responsible for the large rotational excitation observed experimentally. Overall, this work has

revealed important details regarding the interaction of molecular hydrogen with a model hydrocarbon-decorated interface, which are important for fuel cells and next-generation energy systems.

Table 5-1

D_2 beam parameters, rotational temperatures, and corresponding rotational populations.

T_0 (K)	**E_B (meV)**	**T_R (K)**	**n(j=0)**	**n(j=1)**	**n(j=2)**
184	55.5	46.7	0.654	0.333	0.013
231	69.9	61.3	0.620	0.332	0.047
234	70.6	64.9	0.610	0.332	0.057
289	87.3	68.2	0.598	0.331	0.069
307	105.4	95.5	0.498	0.324	0.168
356	107.3	94.1	0.503	0.325	0.163

Table 5-2

Parameters used in the 5D(x,y,z,Θ,ϕ) MCTDH calculations.

Initial wave packet	
Width, Δz_0 (Å)	0.9
Position, z_0 (Å)	14.74
Momentum, k_{z0} (au)	[4.96, 6.61]
Primitive grid parameters	
Type x,y	FFT DVR
x,y-range (Å)	[0, 7.75]
$M_{x,y}$	65
Type z	FFT DVR
z-range (Å)	[-2.66, 15.33]
M_z	200
Type Θ,ϕ	Legendre DVR
$M_{\Theta\phi}$	20x17
SPF basis	
$N_{x,y}$	65
N_z	17
$N_{\Theta,\phi}$	17
Complex absorbing potential	
z-range (Å)	[5.62, 15.33]
Strength (au)	$6x10^{-4}$

Table 5-3

Parameters used to represent the PES in a suitable form for the MCTDH equations of motion using POTFIT. Δ_{rms}^{rw}, Δ_{rms}^{w} represent the root-mean-square error on all grid points and on relevant grid points, respectively. max(ε^r), max(ε) represent the maximum error on all grid points and on relevant grid points, respectively.

Natural potential basis	
m_z	20
$m_{x,y}$	Contr.
$m_{\theta,\phi}$	20
Relevant region of the fit	
z(Å)	> -0.66
V(eV)	< 3
r(Å)	0.767
V_{max}(eV)	20
POTFIT accuracy	
N_{iter}	3
Δ_{rms}^{rw} , Δ_{rms}^{w} (meV)	3.1, 4.4
max(ε^r), max(ε) (meV)	150, 226

Figure 5-1

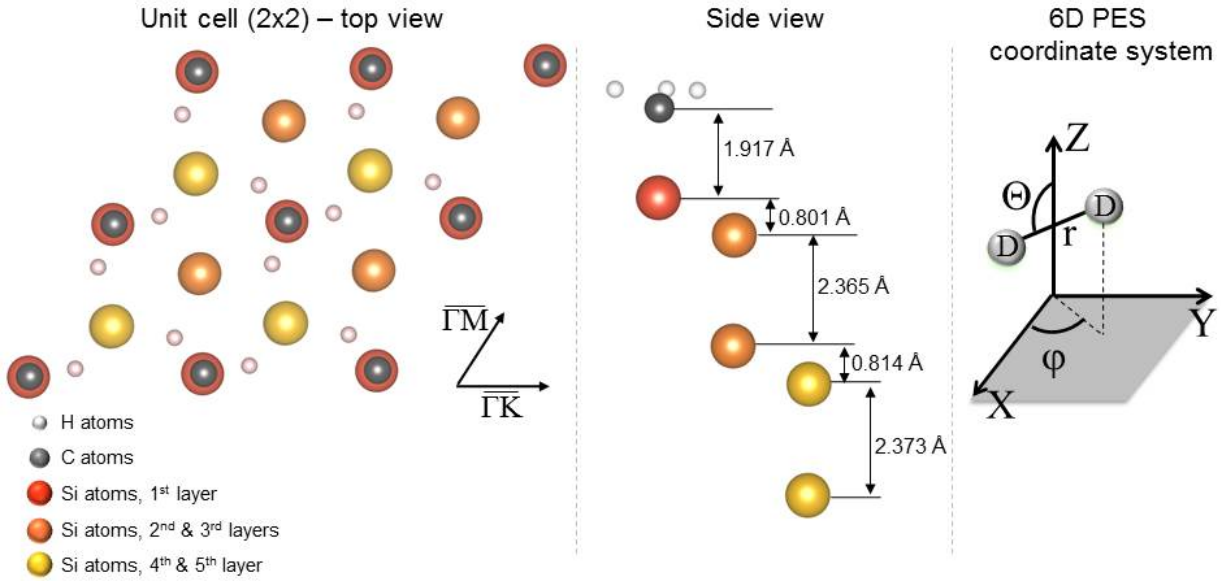

Schematic representation of the CH_3-Si(111) unit cell used, viewed from above (left panel) and the side (center panel). Right panel shows the degrees of freedom included in the PES.

Figure 5-2

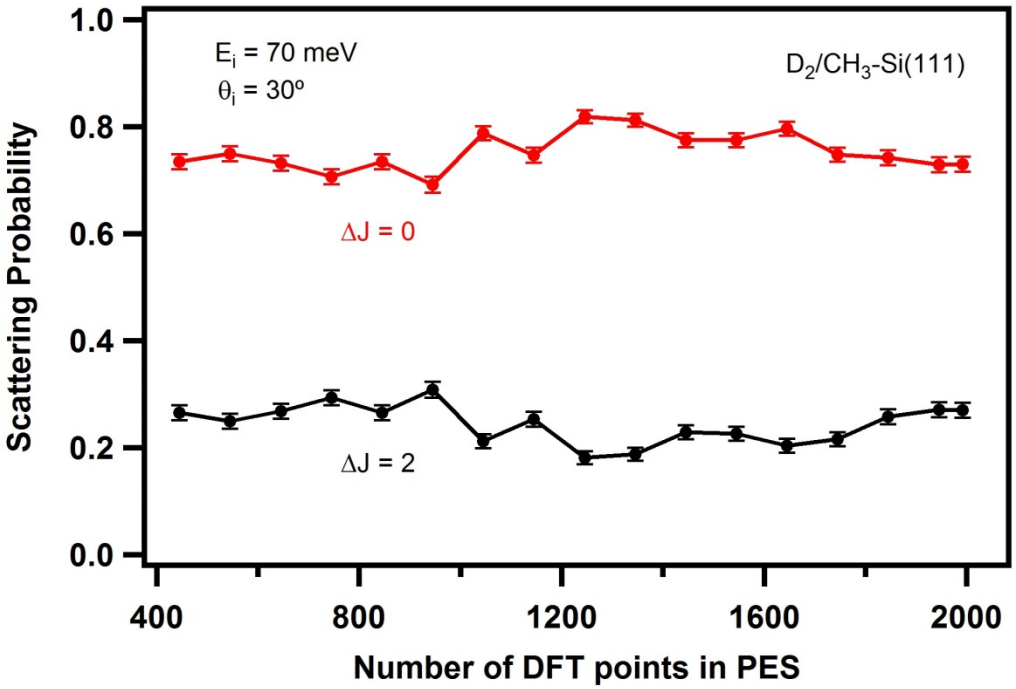

Elastic and inelastic scattering probabilities as a function of the number of DFT points added to the PES data set.

Figure 5-3

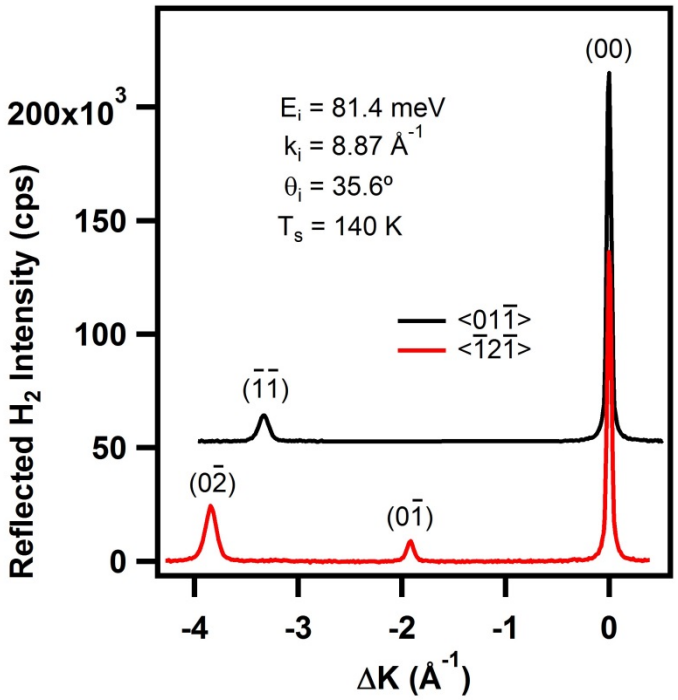

Representative diffraction spectra for H_2 on CH_3-Si(111) along two principal symmetry axes, $\langle 01\bar{1}\rangle$ (black) and $\langle \bar{1}2\bar{1}\rangle$ (red), as a function of parallel momentum exchange.

Experiment file: Figure 5-3.pxp

Raw data file: 052413.D01; 052713.D01

Figure 5-4

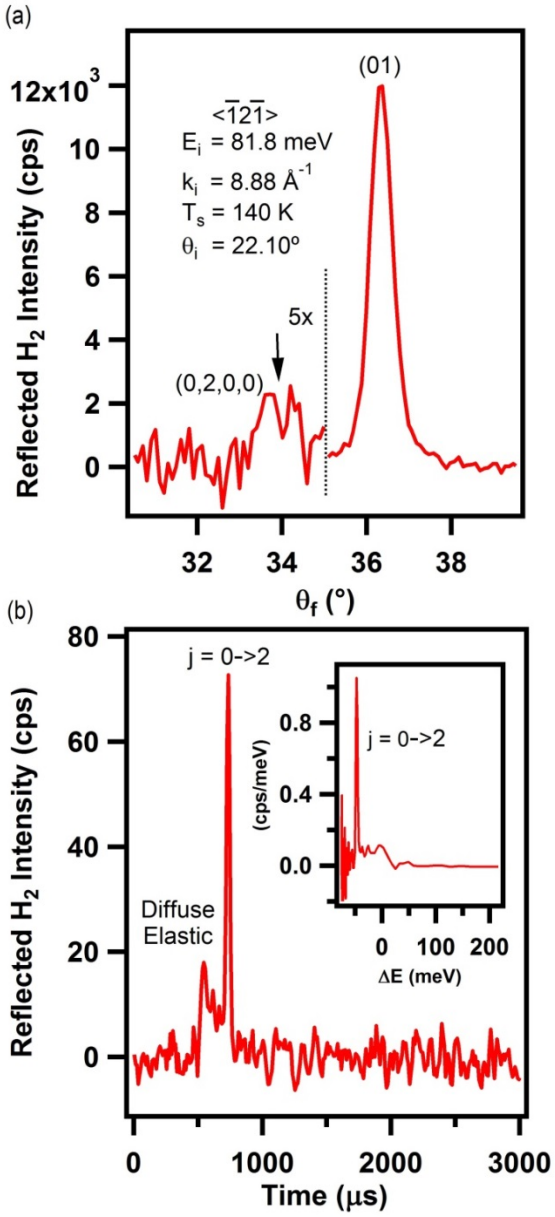

(a) H_2 diffraction spectrum with magnified bump attributed to (0,2,0,0) rotationally inelastic diffraction; (b) Corresponding time-of-flight spectrum and energy-exchange spectrum (inset) measured at position indicated by the arrow in (a), demonstrating $j = 0 \rightarrow 2$ inelastic transition.

Experiment file: Figure 5-4.pxp

Raw data file: 060613.D01; 061013.003

Figure 5-5

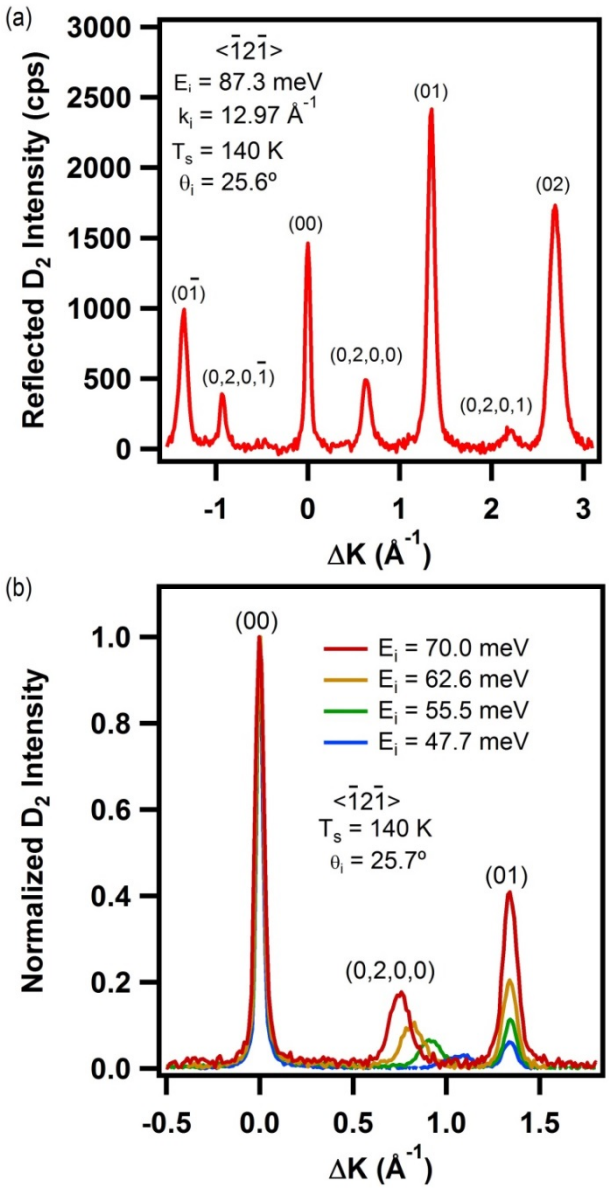

(a) Representative diffraction spectrum for D_2 on CH_3-Si(111), featuring high-intensity elastic and rotationally inelastic diffraction peaks; (b) D_2 diffraction spectra normalized to specular intensity demonstrate effect of incident energy on location of RID peak, as well as relative intensity of RID and elastic diffraction peaks (number density, not yet flux corrected).

Experiment file: Figure 5-5.pxp

Raw data file: 061813.D01; 062413.D01; 062513.D02; 062513.D03; 062513.D04

Figure 5-6

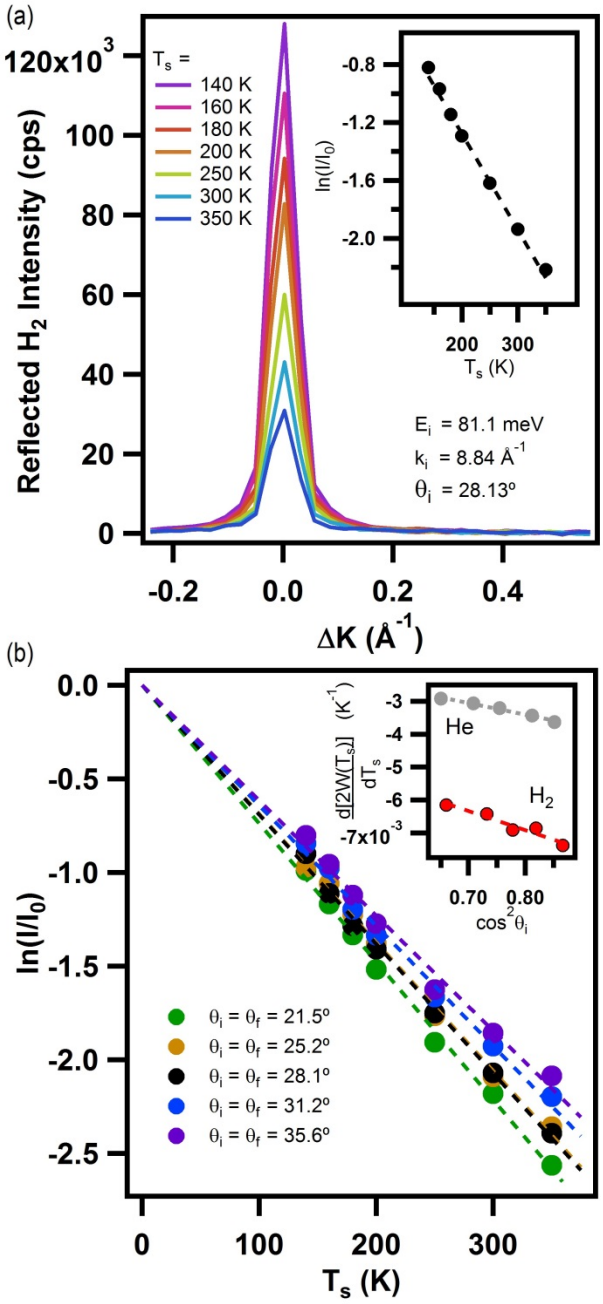

(a) Decay of specular ($\theta_i = \theta_f$) peak intensity as a function of CH_3-Si(111) surface temperature, plotted vs. parallel momentum exchange; natural log of intensity decay vs. sample temperature (inset) confirms application of Debye-Waller formalism. (b) Intensity decays for five incident angles (including that of panel (a)), with the slopes of these decays plotted against the square of the cosine of the incident angle (inset), as compared to the same conditions for He diffraction.

Figure 5-7

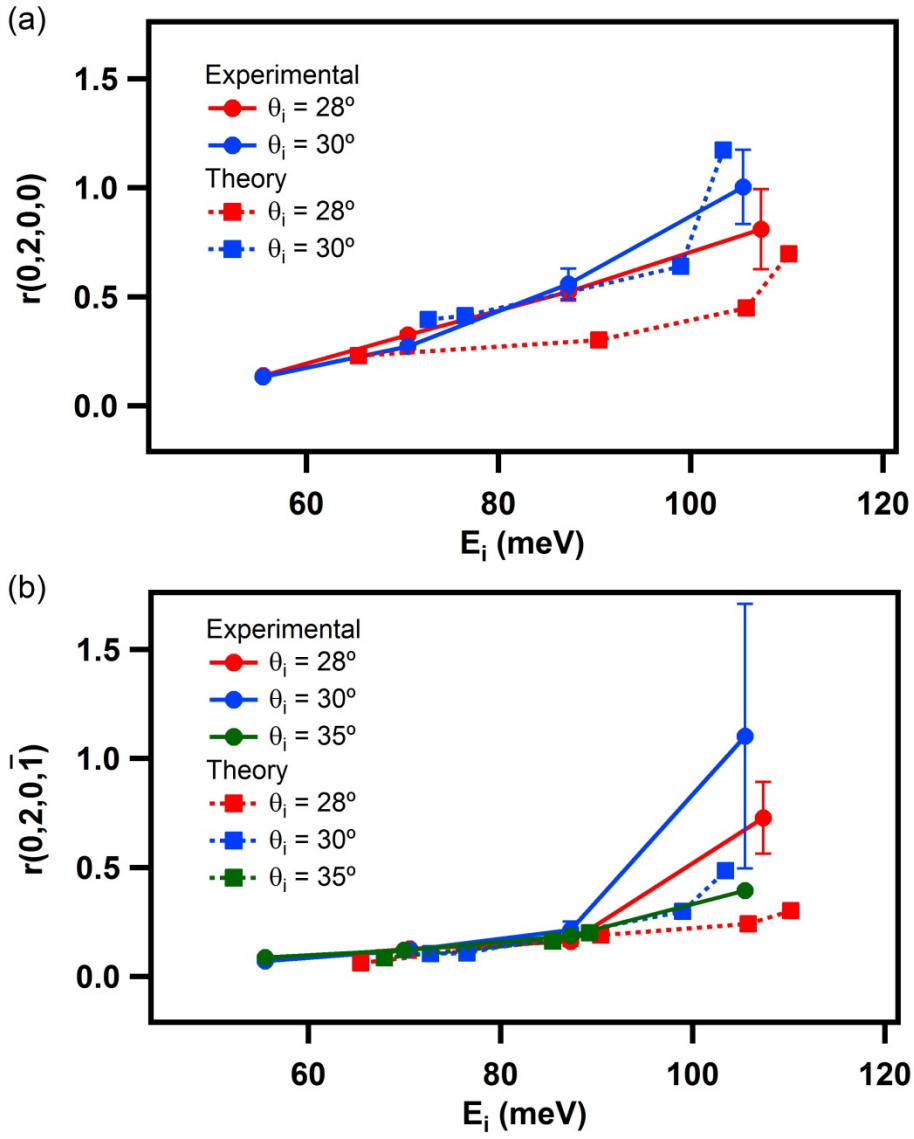

Rotational probabilities for the $j = 0 \rightarrow 2$ transition for experiment (solid) and theory (dashed) data as a function of beam energy and incident angle for (a) specular and (b) first-order diffraction peaks.

Figure 5-8

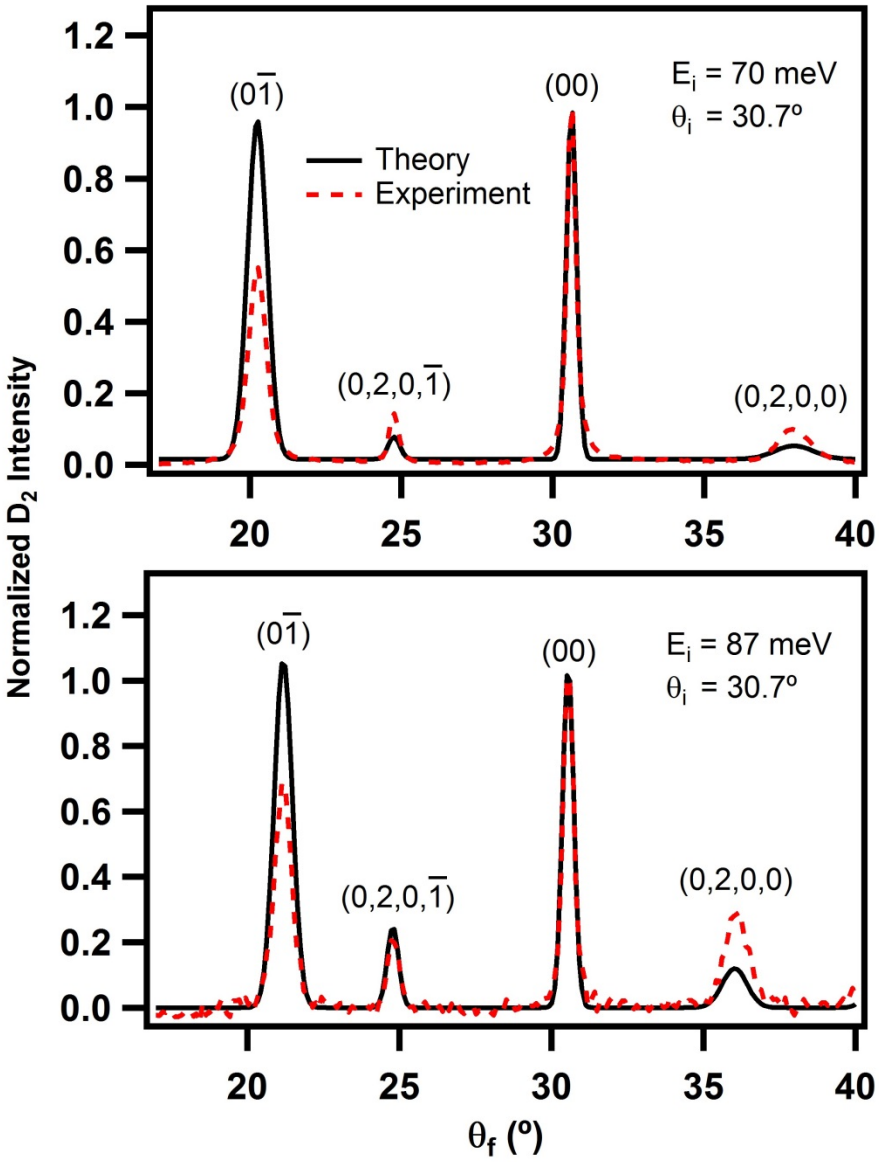

Comparison of experimental (red dashed line) and simulated diffraction spectra (black solid line) for two representative sets of incident conditions.

Figure 5-9

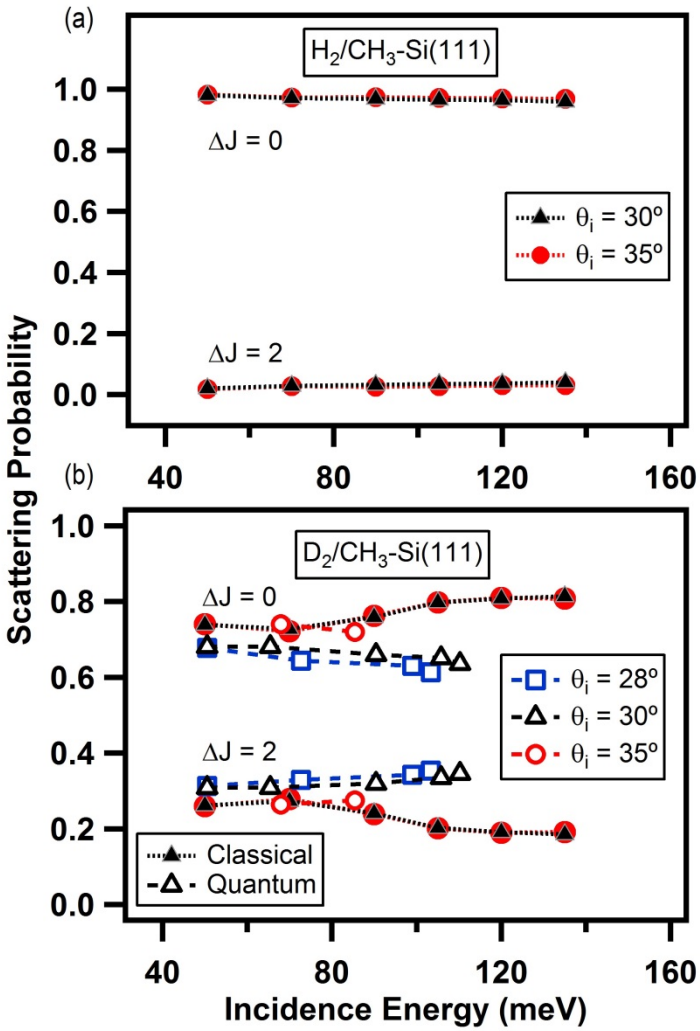

Quantum (open symbols) and classical (solid symbols) elastic ($\Delta J = 0$) and rotational excitation ($\Delta J = 2$) probabilities as a function of the incident energy along the $\bar{\Gamma}$-$\bar{M}$ azimuthal direction, for several incidence angles.

Figure 5-10

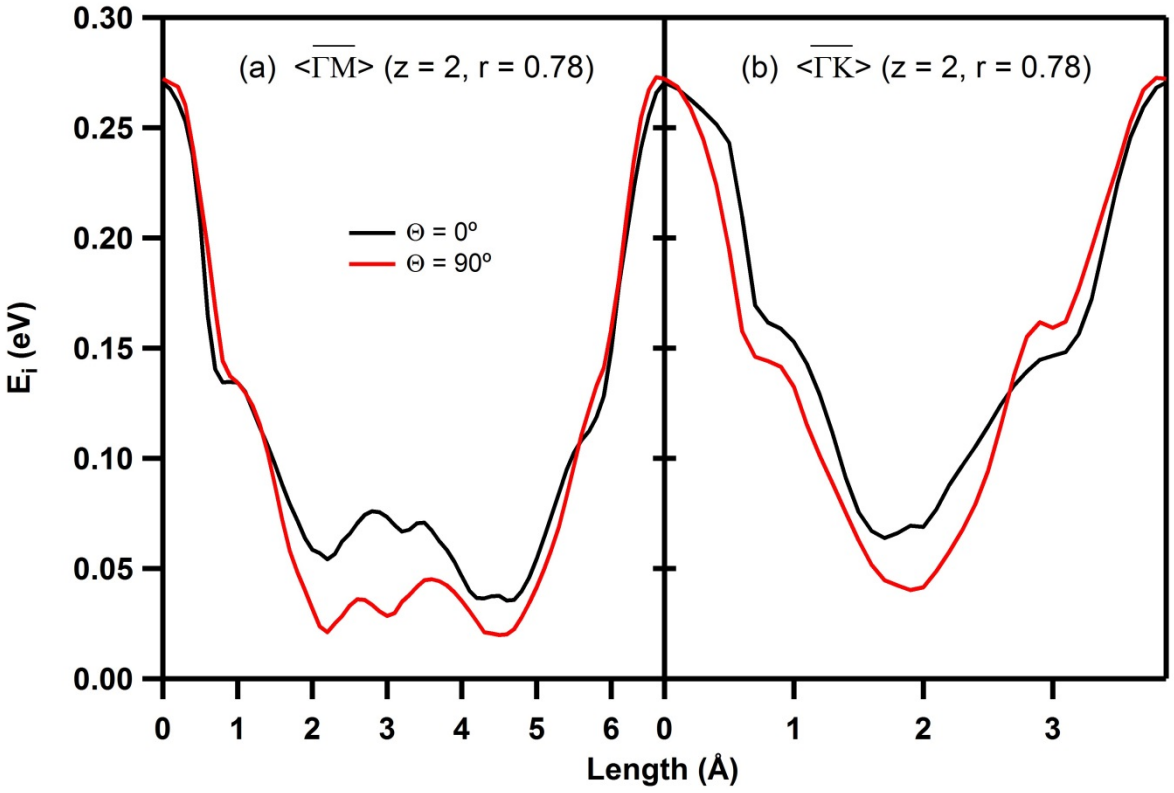

1D potential energy surfaces along the high-symmetry directions $\overline{\Gamma}$-$\overline{K}$ and $\overline{\Gamma}$-$\overline{M}$, with z = 2 Å and r = 0.78 Å, for molecules approaching with surface-parallel (Θ = 90°, red lines) and perpendicular (Θ = 0°, black lines) orientations (cf. Figure 5-1).

Figure 5-11

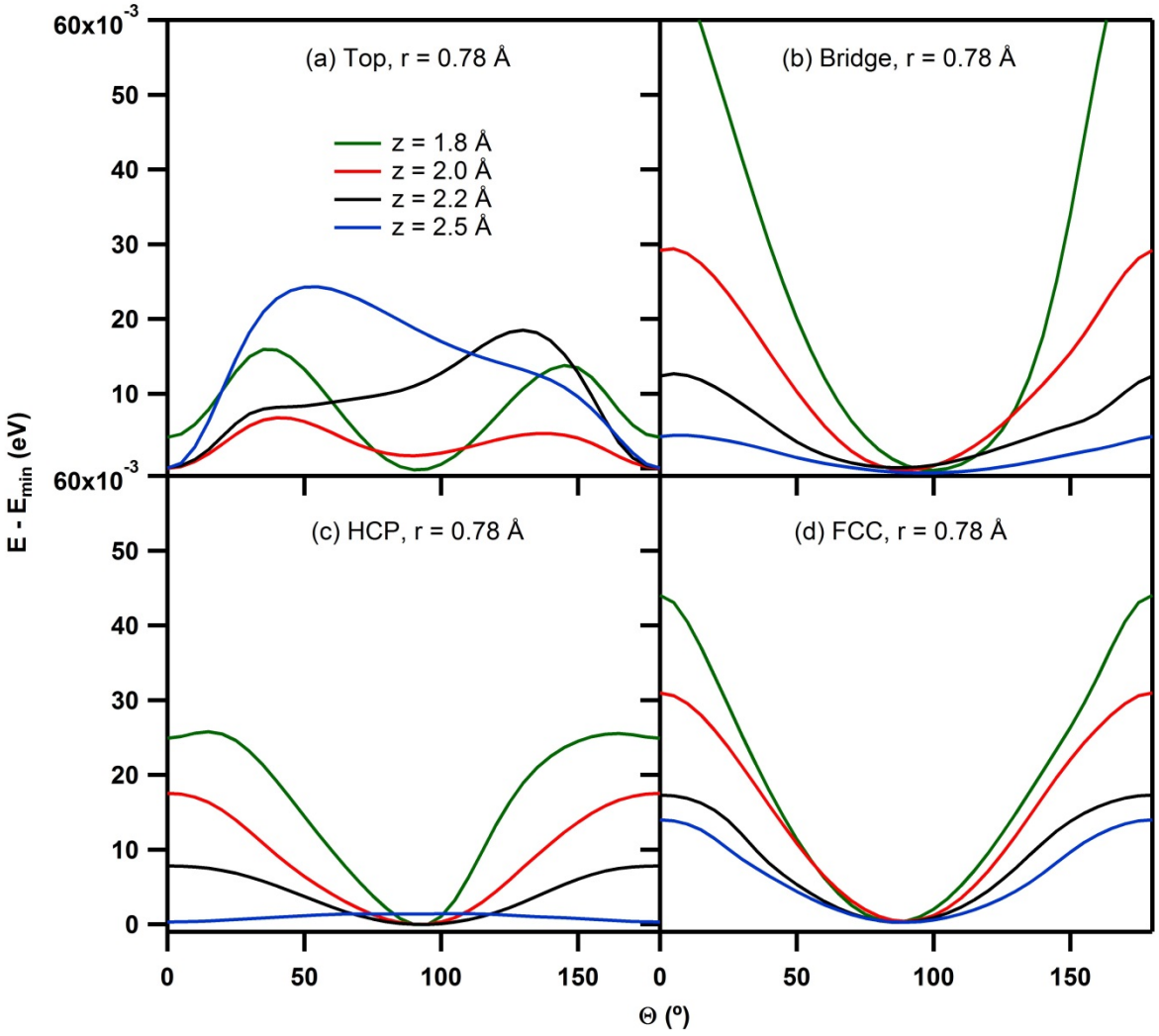

Relative 1D potential energy surfaces as a function of molecular orientation angle (Θ) for four high-symmetry sites at several z values (r = 0.78 Å); E_{min} represents the energy of the system when H_2 is in its equilibrium configuration far from the surface.

Figure 5-12

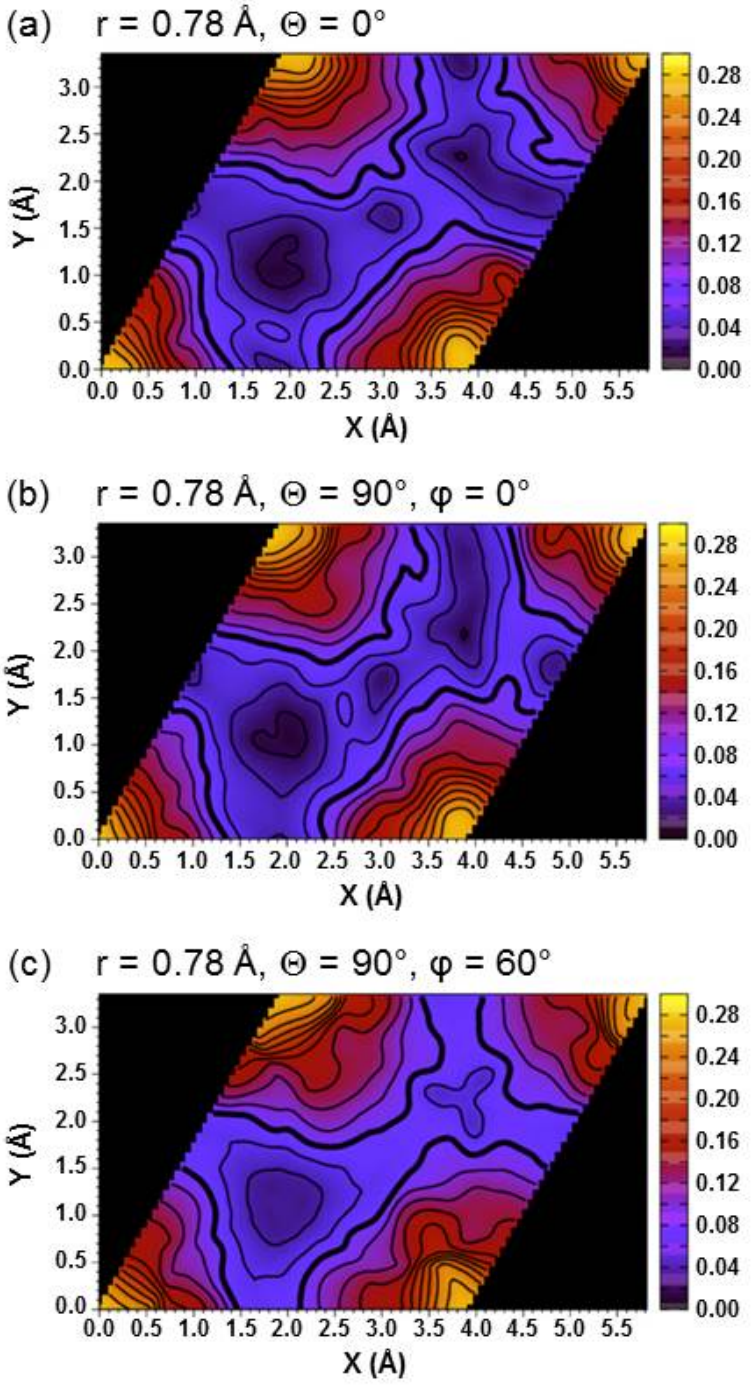

2D xy-cuts of the potential energy surface with z = 2 Å. Bold line corresponds to 0.08 eV, and the spacing between the contour levels is 0.02 eV.

Chapter 6

Separation of Isotopes in Space and Time by Gas-Surface Atomic Diffraction

The separation of isotopes in space and time by gas-surface atomic diffraction is presented as a new means for isotopic enrichment. A supersonic beam of natural abundance neon is scattered from a periodic surface of methyl-terminated silicon, with the ^{20}Ne and ^{22}Ne isotopes scattering into unique diffraction channels. Under the experimental conditions presented in this chapter, a single pass yields an enrichment factor 3.50 ± 0.30 for the less abundant isotope, ^{22}Ne, with extension to multiple passes easily envisioned. The velocity distribution of the incident beam is demonstrated to be the determining factor in the degree of separation between the isotopes' diffraction peaks. In cases where there is incomplete angular separation, the difference in arrival times of the two isotopes at a given scattered angle can be exploited to achieve complete temporal separation of the isotopes. This study explores the novel application of supersonic molecular beam studies as a viable candidate for separation of isotopes without the need for ionization or laser excitation.

Introduction

Proposals for separating and enriching isotopes came about almost immediately after isotopes were discovered. In 1919, Lindemann and Aston examined a vast array of possible methods including fractional distillation, chemical separation, gaseous diffusion, and

gravitational and centrifugal separation, along with separation of positive ions with electric and magnetic fields.[163] Their early analysis concluded that isotopes "must be separable in principle though possibly not in practice." The Manhattan Project in the 1940s ushered in large-scale practical implementation of many of these techniques. Fractional distillation, gaseous diffusion, and magnetic sector mass spectrometers (calutrons) were all used on an industrial scale to enrich ^{235}U.[164,165] Today, isotope separation and enrichment underpins advanced technologies in a wide variety of fields, including isotopic labeling in life science, the use of radioisotopes in medicine, and a variety of energy systems. Microelectronics may also begin to utilize isotopic enrichment as highly enriched ^{28}Si wafers have markedly increased thermal conductivity[166] and electron transport characteristics[167] over natural abundance silicon wafers. Gaseous diffusion, distillation, and gas centrifuges exhibit small isotopic separation effects that are overcome through large-scale installations where many separation steps are performed in sequence. Alternatively, a variety of laser-based techniques exist[168] that are capable of separating isotopes to a much higher degree, but require ionization or excitation of the target isotope; illustrative examples include techniques such as atomic vapor laser isotope separation (AVLIS)[169] and magnetically activated and guided isotope separation (MAGIS).[170]

A rather unexplored isotope separation technique is supersonic beam diffraction. Among isotope separation methods, supersonic beam diffraction has the unique combination of being a nonionizing and non-dissociative process that can achieve high separation effects. This high degree of separation is only achievable *via* the narrow velocity distribution of a supersonic beam, which translates into a narrow angular distribution that is scattered from a highly periodic surface. While effusive beam sources have been used for atomic and molecular diffraction since pioneering experiments in the 1930s, a very small percentage of the beam flux is within a few

percent of the mean beam velocity,[171] preventing any meaningful degree of isotopic purification by atomic diffraction. In contrast, the advent of supersonic nozzle sources with high Mach numbers affords considerably narrower velocity distributions – here, as low as $\Delta v/v = 6.4\%$. Such narrow velocity distributions, when coupled with a high-quality, high Debye temperature surface, make separation of atomic isotopes *via* atomic diffraction feasible.

Previous work by Boato *et al.* suggested the existence of isotopically unique diffraction channels for neon scattering from LiF(001), but was unable to resolve this feature.[172] Here, the separation of the ^{20}Ne and ^{22}Ne isotopes *via* atomic diffraction is observed for the first time when a neon beam with a natural abundance of each isotope is scattered from a methyl-terminated Si(111) surface as shown schematically in Figure 6-1(a). When paired with the extreme resolution and sensitivity of the isotopically specific scattered angle with respect to the mass differences of the incident atoms, diffraction experiments offer a promising isotope separation technique.

Methods

The ultrahigh vacuum (UHV) scattering apparatus required for this experiment is illustrated in Figure 6-1(b), and has been described in greater detail elsewhere.[41] Briefly, it is comprised of three primary sections: a differentially pumped beam source, a UHV chamber that houses the crystal, and a rotatable mass spectrometer detector. A natural abundance (90.48% ^{20}Ne and 9.25% ^{22}Ne) neon beam with a narrow energy distribution is generated by supersonically expanding ultrahigh purity Ne gas through a 15 μm diameter nozzle source that is cooled by a closed-cycle helium refrigerator. The incident energy distribution of this beam is measured with an in-line mass spectrometer and is minimized to $\Delta v/v = 6.4\%$ by adjusting the

backing pressure of Ne. Similarly, the beam energy, which is determined by the nozzle temperature, is optimized to 50 K (E_B ~10 meV) in order to minimize the incident energy while avoiding the formation of clusters. For diffraction and time-of-flight measurements, a precollision chopper is used to modulate the beam with a duty cycle of 50%; the time-of-flight measurements are performed by modulating the beam with a pseudorandom chopping sequence for cross-correlation analysis.[5] The spatial profile of the beam is minimized by collimation through a series of apertures, resulting in a 4 mm spot size on the crystal (chopper-to-crystal distance = 0.4996 m). From this spot size, pressure rise in the scattering chamber, and the pumping speed, an incident flux of ~10^{14} $cm^{-2}s^{-1}$ was determined. After the collision with the surface, which is mounted on a six-axis manipulator in order to control the incidence angle (θ_i), azimuth (φ), and tilt (χ) of the crystal, the neon atoms travel along a 0.5782 m (crystal-to-ionizer distance) triply differentially pumped rotatable detector arm with an angular resolution of 0.29° FWHM, are ionized by electron bombardment, which is sensitive to number density, and then pass through a quadrupole mass spectrometer (QMS) before striking an electron multiplier. The QMS is adjusted to selectively filter either the ^{20}Ne or ^{22}Ne isotope. The angular distributions for diffraction scans are obtained by scanning the detector at 0.1° increments over a range of 35°, all while holding the incident angle at a fixed value. Between scattering experiments, the temperature of the crystal was flashed to 200 K to eliminate unwanted surface adsorbates and maximize elastic scattered intensity.

The crystal used for this experiment, CH_3-Si(111), was created by the Lewis group at the California Institute of Technology,[132] and shipped under argon to the University of Chicago for the neon scattering experiments. This crystal was chosen for its small surface atom spacing (3.82 Å), high surface Debye temperature (983 K) which limits diffusive scattering, and high

quality and long-range periodicity achieved in the synthesis of the crystal, which is described in greater detail elsewhere.[74,99,112]

Results and Discussion

When molecules elastically scatter from a surface, they can undergo a discrete exchange of parallel momentum ΔK with the surface, as governed by the equation

$$\Delta K = k_i \left(\sin\theta_f - \sin\theta_i \right), \tag{6-1}$$

where k_i is the incident wave vector of the beam, and θ_i and θ_f are, respectively, the incident and final scattered angles of the molecular beam as measured from the surface normal. This condition for elastic diffraction is met when the change in parallel momentum is equal to a sum of the reciprocal lattice vectors b_i according to the equation

$$\Delta K = h\vec{b_1} + k\vec{b_2}. \tag{6-2}$$

As is evident from Equation (6-1), the angular location of a diffraction peak is determined in part by its incident wave vector (k_i), which in turn is dependent on the velocity of the incident beam.

For an elastic gas-surface interaction, the incident velocity distribution of the molecular beam can be transformed into a theoretical angular distribution of the scattered beam through the implementation of equation (6-1). Figure 6-2 shows the predicted angular distribution of Ne scattered from CH_3-Si(111) for both a supersonic molecular beam ($\Delta v/v = 6.4\%$) and an effusive beam using a Maxwell-Boltzmann distribution at a temperature of 55 K. The separation of the isotopes is nearly complete with the supersonic nozzle source, whereas the effusive source is incapable of any significant degree of isotope purification using this method.

Experimental angular scans of the (11) diffraction peak for ^{20}Ne and ^{22}Ne are shown in Figure 6-3. These diffraction spectra were recorded using a naturally abundant supersonic neon beam with both isotopes having the same average velocity and velocity distribution. These spectra illustrate the high degree of angular separation between the respective isotopes' (11) diffraction peaks and thus the feasibility of separating isotopes *via* supersonic beam diffraction. The natural abundance of the neon beam (90.48% ^{20}Ne and 9.25% ^{22}Ne) accounts for the nearly order of magnitude intensity difference for the maximum of each isotope's (11) diffraction peak. For this particular experimental condition, one can assess the efficacy of this isotopic enrichment method. As the angular resolution of the instrument is 0.67°, each point on the spectra can represent a collector with this acceptance angle. For the case of enriching the major ^{20}Ne component, the collector can be placed at the maximum of the ^{20}Ne (11) diffraction peak (θ_f = 47.5°) shown in Figure 6-3, which sits on top of a small incoherent background and the tail of the ^{22}Ne diffraction peak. The collected signal after scattering provides a ^{20}Ne abundance of 97.3% ± 3.0%, as compared to the original abundance of ^{20}Ne (90.48%), thus yielding an enrichment factor of 1.08 ± 0.03 (this represents 1σ error). Similarly, for the minor ^{22}Ne component, the collector can be placed at the maximum of the ^{22}Ne (11) diffraction peak (θ_f = 45.1°) shown in Figure 6-3, which sits on top of a small incoherent background and the tail of the ^{20}Ne diffraction peak. The collected signal after scattering provides a ^{22}Ne abundance of 32.4% ± 2.8%, as compared to the original abundance of ^{22}Ne (9.25%), thus yielding an enrichment factor of 3.50 ± 0.30. Note that these enrichment factors can be improved further by lowering the temperature of the substrate to near but above the adsorption limit, ~7 K for neon, which minimizes incoherent scattering from Debye-Waller effects for given incident kinematics.

The large but still incomplete spatial separation of the isotopes' diffraction peaks is primarily due to the width of these features. To emphasize this point, Figure 6-4 shows helium and neon scattering from CH_3-Si(111), with the width of the diffraction peaks for these species resulting from the convolution of the instrument function, surface quality, and their incident velocity distributions. The narrower angular distribution for He results from its considerably narrower incident velocity distribution ($\Delta v/v = 0.8\%$) as compared to that of Ne ($\Delta v/v = 6.4\%$), indicating that improvement of the beam quality will result in even greater angular separation than the data shown in Figure 6-3. While a common method for narrowing the velocity distribution is seeding the beam with a light gas (e.g., He, H_2),[4,99,173] the increased average velocity of this mixture would bring the angular positions of the diffraction peaks closer together, limiting the degree of separation, as predicted by equation (6-1). We note that this can be compensated for by cooling the nozzle of the seeded beam to regain the increased reciprocal-space distance between diffraction peaks while maintaining a narrow incident velocity distribution. An additional solution would be the addition of an in-line precollision velocity selector that would directly lead to more complete angular separation of the two isotopes.[174]

Velocity selection techniques can also be implemented after the atoms collide with the surface. For a given θ_f at which there is angular overlap between the ^{20}Ne and ^{22}Ne nonzeroth-order diffraction peaks, the two isotopes will necessarily have different velocities, as required by equation (6-1). This is demonstrated in Figure 6-5, which shows time-of-flight spectra for both isotopes at the midway point between their (11) diffraction peak maxima. The pronounced difference in arrival time between the two isotopes opens up the possibility for complete isotope separation mediated by velocity selection techniques.

The practical throughput of diffractive isotope separation can be maximized by thoughtful consideration of the incident parameters and the choice of diffracting surface. As established by equation (6-1), the total number of angles at which atoms scatter from a surface depends upon the incident wavevector of the atomic beam (k_i) and the spacing between diffraction peaks (ΔK), which is in turn dependent on the real-space distance between atoms at the surface. The incident flux of an atomic beam can be concentrated into a smaller number of accessible diffraction channels by lowering the incident wave vector/beam velocity (e.g., by nozzle cooling or seeding in a heavier gas such as xenon) or increasing the angular spread between diffraction peaks by choosing a surface with a smaller lattice parameter, such as graphite (lattice constant = 2.46 Å). We have also observed in other studies the coupling of neon with diffractive bound state resonances for this system. The resulting change in diffraction probabilities due to this phenomenon may hold additional promise for further enhancements in isotope separation.

The choice of surface can also affect the relative flux scattered into various diffraction channels. Higher ratios of scattered intensity between nonzeroth-order diffraction and specular peaks have been demonstrated to be correlated with increased surface corrugation.[172,175–177] Additionally, the amount of flux that is scattered diffusely from a surface is strongly affected by the surface stiffness, which is quantified by the surface Debye temperature.[74,178] When gases diffract from surfaces with high Debye temperatures, less of the incident flux is scattered into diffuse elastic channels due to the Debye-Waller effect than for soft surfaces, resulting in a more directed channeling of the incident beam into coherent diffraction peaks. Further improvement can be realized by minimizing the surface temperature (while remaining above the physisorption limit) and thus mitigating Debye-Waller effects arising from the thermal motion of the

substrate.[179,180] In sum, the judicious selection of a well-ordered, highly perfected surface with a relatively high Debye temperature, small lattice constant, and inertness to a specific isotope or isotopologue, opens this diffractive isotope separation method to a larger class of atoms and molecules.

A practical implementation of this enrichment process would necessitate some collection scheme for the enriched product. In principle, the desired isotope can be collected with a strategically positioned cold surface where a single diffraction channel will strike and condense. Alternatively, a strategically placed aperture that admits one diffraction channel would also be a straightforward means to collect the reflected isotope from only one of the diffraction channels; this could be extended to an array of apertures placed to collect numerous higher-order (and out-of-plane) diffraction channels. Furthermore, this isotope separation technique is also amenable to recycling the diffracted beam through recompression and/or staging the diffraction process until a desired isotopic enrichment level is reached.

Conclusions

The angular and temporal separation effects of supersonic molecular beam diffraction provide a promising isotope enrichment method that does not require ionization or laser excitation of the target isotope. The necessity of a supersonic expansion for this technique is demonstrated, and as a proof of concept natural abundance neon has been shown to diffract into separate, isotopically dependent diffraction lab frame angles, yielding for the set of experimental conditions used herein an enrichment factor of 1.08 ± 0.03 for the major ^{20}Ne component and 3.50 ± 0.30 for the minor ^{22}Ne component in a single pass, with extension to multiple passes easily envisioned. The incomplete separation of isotopes exhibited in this work demonstrates the need for scrupulous consideration of the experimental setup to achieve maximum separation and

throughput, with the velocity spread of the incident beam serving as the determining factor for separation. As atomic diffraction has been observed for species with masses as high as 40 amu,[181] this isotope separation technique is applicable to a wide range of coexpanded atoms and molecules. In sum, using a combination of a supersonic molecular beam and a well-ordered, corrugated surface with a small lattice spacing and high level of structural perfection, we have successfully demonstrated novel and efficacious routes to isotopic enrichment and separation in space and time based on gas-surface diffraction.

Figure 6-1

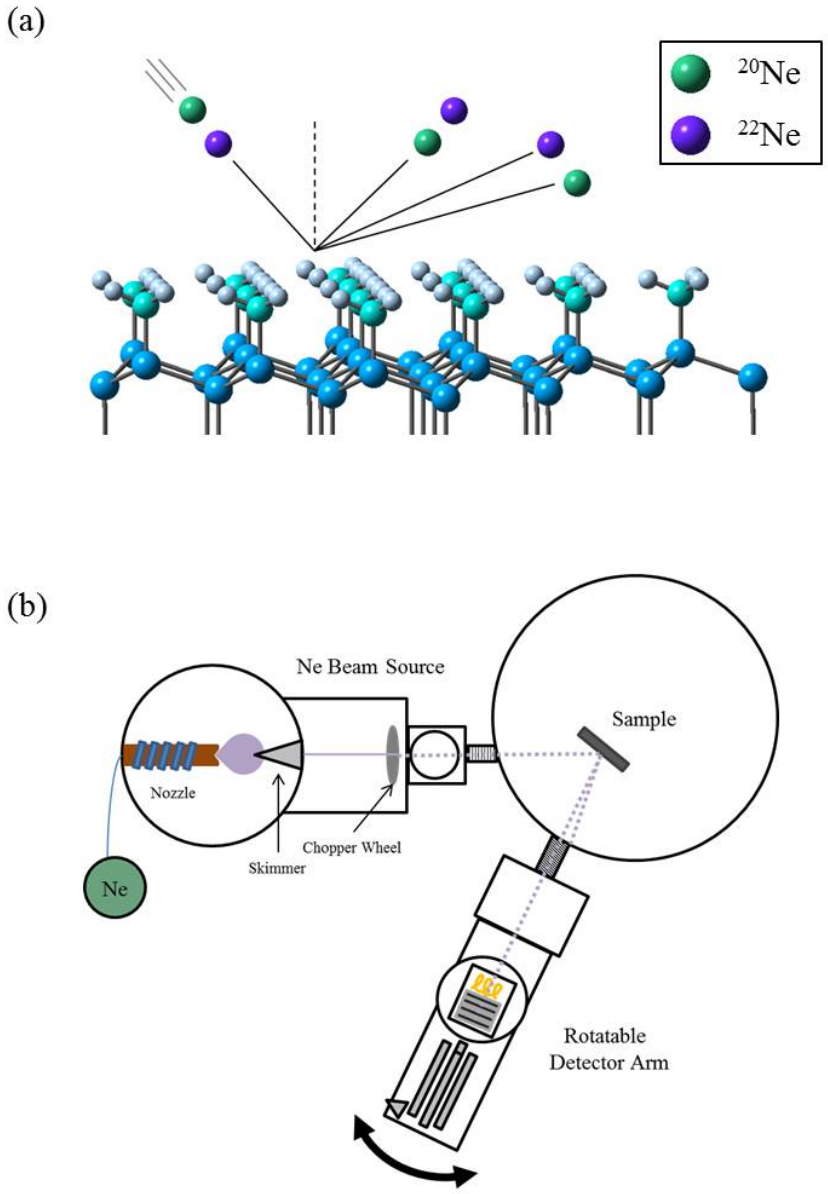

(a) Illustration of a monoenergetic beam of ^{20}Ne and ^{22}Ne diffracting from CH_3-Si(111) into spatially well-separated final scattering angles; (b) schematic of the ultrahigh vacuum surface scattering instrument employed in this experiment; key components are a high-Mach number, triply differentially pumped molecular beam source with variable temperature nozzle, a UHV scattering chamber with a full suite of diagnostics (not shown), and a high sensitivity triply differentially pumped detector with a high degree of collimation, that can rotate to detect a range of final scattering angles while maintaining constant incident kinematic conditions.

Figure 6-2

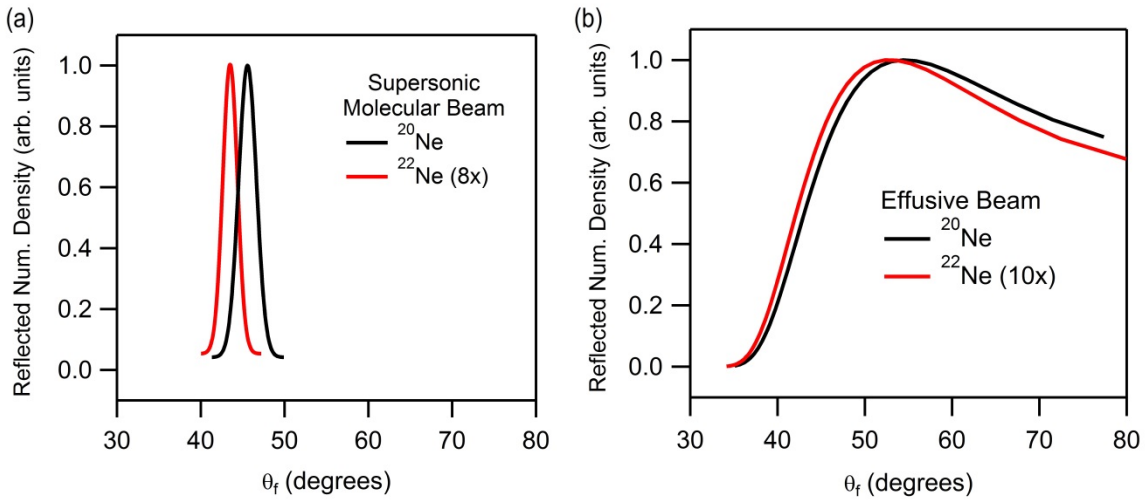

(a) Demonstration of angular separation for supersonic molecular beam diffraction from an ideal grating for the conditions reported herein; (b) lack of angular separation for an effusive source under identical incident conditions; $T_B = 55$ *K,* $\theta_i = 25.2°$.

Figure 6-3

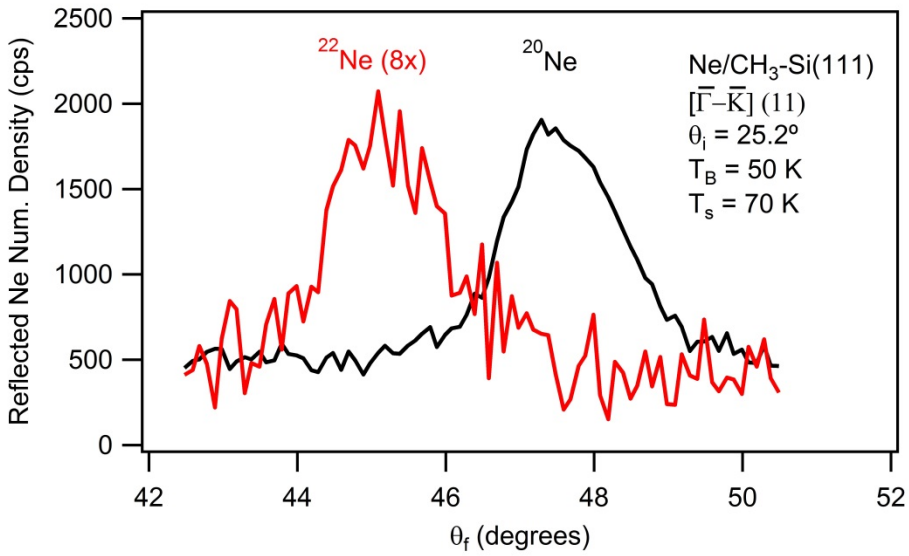

Nearly complete angular separation of (11) diffraction peaks for ^{20}Ne (black) and ^{22}Ne (red) diffracted from CH_3-Si(111). Further purification of the major ^{20}Ne component or separation and enrichment of the minor ^{22}Ne component can be realized through experimental considerations as discussed in the text.

Figure 6-4

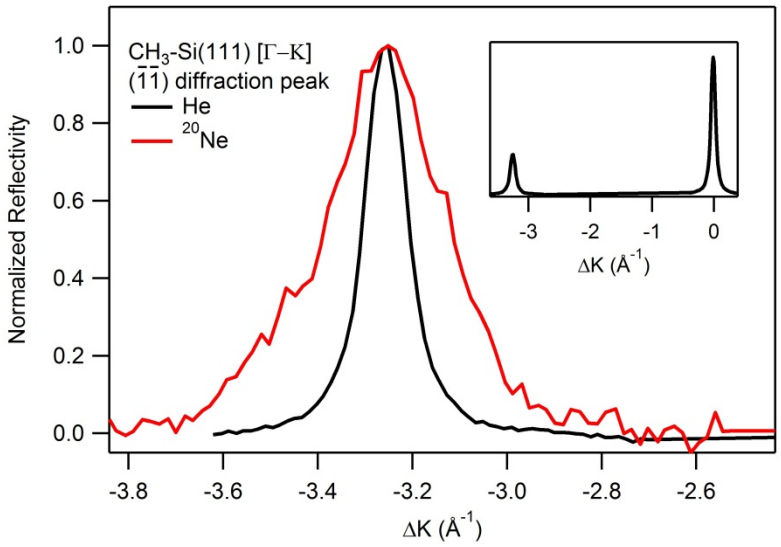

*(**11**) diffraction peak for helium (black) and ^{20}Ne (red) scattering from CH_3-Si(111). Note that the width of these peaks is a consequence of the convolution of the instrument function, surface quality, and their incident velocity distributions. The He diffraction peak has a significantly narrower angular distribution than the Ne peak, due to the narrower velocity distribution of the He beam used ($\Delta v/v$ = 0.8%) as compared to that for the Ne beam ($\Delta v/v$ = 6.4%). Potential further improvement in angular separation, as compared to the data shown in Figure 3, can be realized by additional narrowing of the beam's incident velocity distribution. Inset: wide angular range diffraction scan for He/CH_3-Si(111), demonstrating the high quality of the substrate used in these experiments.*

Figure 6-5

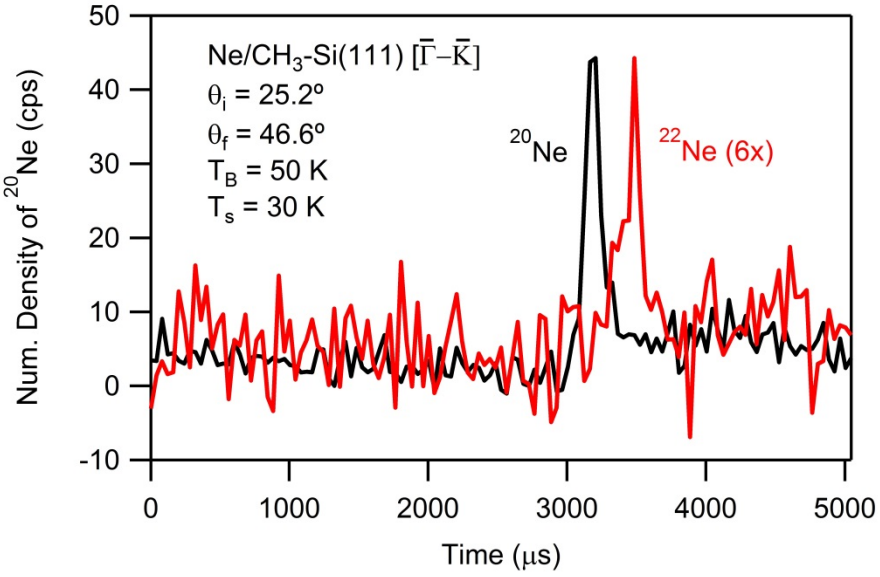

Time-of-flight spectra for ^{20}Ne (black) and ^{22}Ne (red) at the midpoint between the maxima of the ^{20}Ne and ^{22}Ne (11) diffraction peaks as shown in Figure 3, providing a route for temporal separation of the isotopes.

Chapter 7

Isotope Enrichment *via* Differential Condensation and Reflection of Isotopes during Supersonic Beam Gas-Surface Scattering

Isotopic enrichment through the condensation of supersonic beams is proposed and quantified. This enrichment is a product of the high sensitivity of physisorption to incident kinetic energy and the distinct kinetic energies of isotopes in a supersonic beam. As a test case, temperature-programmed desorption (TPD) of an amorphous argon condensate grown at 29 K using a room-temperature supersonic beam of pure Ar displays an enrichment of ^{36}Ar relative to ^{40}Ar by a factor of 1.052 ± 0.011, as compared to the incident abundance. This work was extended by increasing the velocity of the incident beam and thus lowering the sticking coefficient, where less enrichment of ^{36}Ar is observed in the condensate, ultimately resulting in an inversion of this phenomenon whereby ^{40}Ar is shown to condense preferentially to ^{36}Ar. These results inform the fundamental understanding of physisorption processes and may lead to new isotope enrichment techniques.

Introduction

Current isotope enrichment techniques display a range of complexity, throughput, and selectivity. These techniques include the straightforward but inefficient gaseous diffusion as well as complex and highly selective laser excitation schemes.[164,168,170] Although new laser techniques such as MAGIS hold promise at being both highly selective and energy efficient,[169] modern isotope enrichment is largely performed by calutrons.[182,183] While applicable to the separation of essentially every stable isotope, calutrons suffer from many of the same problems encountered when they were first developed in the 1930s – namely throughput and energy

consumption.[165] This leads to an increased desire for novel isotope enrichment schemes. Here, we propose and demonstrate isotope enrichment through differential condensation and reflection of isotopes in a supersonic molecular beam, which holds the promise of widespread applicability in separating supersonically expanded gaseous mixtures.

The probability of an incident gas particle condensing on a surface is quantified by its sticking coefficient, *S*, which is governed by the kinetic energy of the incident particle,[184] the temperature of the surface, the surface-particle binding energy, and the energy transfer between the particle and the surface as described by the energy accommodation coefficient.[185] After a particle exchanges energy with the surface, physisorption will occur if its kinetic energy is lower than its binding energy to the surface. Decades of experimental and theoretical effort have gone into understanding this surface phenomenon. Although electronic excitations of the surface mediate sticking under some conditions,[186] generally energy transfer occurs between a gas particle's kinetic energy and the substrate's phonons, or collective vibrations. A natural consequence is that a surface with more phonon modes available to excite (i.e., a colder surface) has a greater ability to condense an impinging gas particle, just as a particle with less kinetic energy is more likely to be condensed.

The energy of an incident beam can be controlled by means of a supersonic expansion, which produces an intense beam with narrow velocity and energy distributions. When a mixture of gases undergoes a supersonic expansion, the seeding effect results in the averaging of velocities: for the simple case of a trace, lighter-mass species coexpanding with a dominant, heavier-mass species, the lighter species is slowed to the velocity of the heavier species. This experiment realizes this scenario through the expansion of natural-abundance argon; ^{40}Ar and ^{36}Ar have 99.604% and 0.334% natural abundances, respectively. Due to matching velocities

from the seeding effect, the lighter ^{36}Ar will have less kinetic energy than ^{40}Ar and, as we demonstrate, will condense preferentially relative to ^{40}Ar upon striking a sufficiently cold surface, as depicted schematically in Figure 7-1(a).

Methods

Isotopic ratios of reflected and condensed argon were measured using an ultra-high vacuum (UHV) scattering apparatus, illustrated in Figure 7-1(b). The instrument has been thoroughly described elsewhere.[41] Briefly, it is composed of three sections: a differentially-pumped supersonic beam source containing a chopper for timing resolution and an in-line mass spectrometer for incident beam analysis; a scattering chamber that houses the substrate – which is mounted on a six-axis manipulator that can be temperature-controlled between 27-750 K – and an effusive doser situated ~1 cm from and directed at the substrate; and a triply differentially pumped rotatable quadrupole mass spectrometer (QMS) that is capable of rapidly switching between mass filter settings, allowing for effectively simultaneous measurements of reflected or desorbed isotopes.

To examine the effects of incident energy on the sticking coefficient and the resultant preferential adsorption of ^{36}Ar over ^{40}Ar, three beam energies were used in this experiment. The lowest-energy beam was created through supersonic expansion of pure argon through a room-temperature nozzle (beam energy = 68 meV for ^{40}Ar and 61 meV for ^{36}Ar); a more energetic beam was created through expansion of a 10% argon in helium mixture at room temperature, which boasts greater incident energies (254 meV for ^{40}Ar and 229 meV for ^{36}Ar) due to the aforementioned seeding effect, and the most energetic beam resulted from the expansion of helium-seeded argon through a nozzle heated to 650 K (562 meV for ^{40}Ar and 506 meV for ^{36}Ar). Figure 7-2(a) shows the velocities of ^{40}Ar in each of these beams as measured by time-of-

flight experiments carried out prior to collision with the surface. Further, Figure 7-2(b) compares the velocity distributions of ^{36}Ar and ^{40}Ar in the room-temperature Ar beam to demonstrate the nearly identical velocities that lead to isotopically unique incident energies.

Results and Discussion

The sticking coefficients at these beam energies were measured by directing a modulated beam of a given energy at the substrate and monitoring the incoherently reflected signal at temperatures above and below the sticking temperature (~32 K) with a residual gas analyzer (RGA). After subtracting the instrument background *via* mechanical chopping of the beam with a 50% duty cycle, we compared the reflected argon signals at 29 K and 160 K, the latter temperature being above the adsorption temperature of both argon and other unwanted contaminants. Through this process, we measured sticking coefficients of 0.985 ± 0.002 for the pure Ar beam, 0.965 ± 0.005 for the room-temperature helium-seeded beam, and 0.878 ± 0.010 for the 650 K helium-seeded beam. Figure 7-3 shows a plot of sticking coefficient versus incident energy, demonstrating an exponential relationship that can be exploited to choose a desired enrichment factor through the techniques discussed below.

The detector used for these experiments cannot measure the incident beam compositions directly due to instrumental geometry constraints. Instead, the ratio of isotopes ($^{36}Ar/^{40}Ar$) in the incident beams were determined by measuring the argon reflected from the crystal at a surface temperature of 200 K, well above the adsorption temperature of argon (~32 K) and other unwanted contaminants. The incident beam was modulated with mechanical chopping (50% duty cycle) to account for instrumental background, and the reflected beam was collected while switching between mass filter settings at a rate of 0.1 Hz. We measured an incident ratio of $^{36}Ar/^{40}Ar$ = 0.00338 ± 0.00001 for the pure Ar beam, 0.00354 ± 0.00002 for the room-

temperature helium-seeded beam, and 0.00325 ± 0.00002 for the 650 K helium-seeded beam. The difference in incident ratio between the two room-temperature beams is attributed to a mass-focusing effect, whereby the heavier components of a molecular beam are more concentrated towards the center-line, causing the lighter components to be diminished after passing through a skimmer.[4] This effect is expected to be more pronounced for a pure beam, since the loss of the lighter helium atoms in the seeded beam do not affect the $^{36}Ar/^{40}Ar$ ratio.

It is important to note that, while the unique kinetic energies of the incident species could result in isotope separation through scattering into isotopically unique diffraction angles,[162] this phenomenon is not observed for this experiment. Due to the large mass of the incident argon, the distribution of reflected angles is lobular in nature and scattering does not exhibit distinct diffraction peaks. This is demonstrated in Figure 7-4, in which the $^{36}Ar/^{40}Ar$ ratio for a pure argon beam reflecting from the crystal surface above the adsorption temperature is linear across a range of final angles, indicating that measurements taken at one reflected angle reveal the overall behavior of this system.

For a sticking coefficient $S < 1$, the isotope-specific kinetic energies in the incident beam should cause the preferential condensation of ^{36}Ar over ^{40}Ar. Experimental measurement of the condensate's composition is possible through temperature-programmed desorption (TPD), in which the surface is held below the adsorption temperature and dosed with a supersonic Ar beam. The surface is then heated at a fixed rate while the mass spectrometer switches between the two masses of interest at a rate of 10 Hz. The representative TPD spectra in Figure 7-5 confirm the expected depletion of ^{40}Ar in the condensate, with $^{36}Ar/^{40}Ar$ ratios of 0.00356 ± 0.00004 for the pure Ar beam, 0.00363 ± 0.00003 for the room-temperature helium-seeded beam, and 0.00324 ± 0.00000 for the 650 K helium-seeded beam. When compared with the

incident beam composition reported above, this yields enrichment factors for ^{36}Ar of 1.052 ± 0.011, 1.025 ± 0.010, and 0.997 ± 0.005, respectively. As shown in Figure 7-6, this ratio indicates the preferential adsorption of ^{36}Ar on the substrate when dosed with a supersonic molecular beam at low incident energies, but this trend exhibits an inversion at high energies. Forthcoming measurements of the ratio of the reflected beam below the condensation temperature will be instrumental in confirming and understanding this phenomenon.

To prove that this differential condensation effect relies on the identical velocities achieved with seeded supersonic beams, an analogous TPD experiment was carried out using an effusive source pointed directly at the substrate. Once the surface temperature is cooled below the sticking temperature, an argon mixture (from the same gas cylinder as above) is dosed effusively onto the surface, followed by surface heating at a fixed rate while rapidly switching between masses on the mass spectrometer. The sample TPD spectra in Figure 7-7 can be used to calculate a mass focusing enrichment factor of 1.07 ± 0.01 for pure argon (results from the argon/helium mixture are forthcoming).

Conclusions

Isotope enrichment by means of differential condensation and reflection of coexpanded isotopes in supersonic molecular beams offers a promising alternative to the inefficient enrichment processes that currently dominate this space and provides greater insight into the nature of physisorption. We have proven the practicality and efficacy of this approach, which is possible when a supersonically expanded mixture of isotopes is directed toward a substrate at a sufficiently low temperature for adsorption. Additionally, we have demonstrated the dependence of enrichment on the sticking coefficient, which in turn is governed by the kinetic energy of the incident beam. Measurements of the composition of the condensate show enrichment in the

lighter species at low incident energies, and enrichment in the heavier species at higher incident energies. Upcoming changes to our mass-filtering electronics will improve the quality of the measurements recorded above, and will enable the precise measurement of reflected beam composition below the condensation temperature, where instability in mass filtering leads to insurmountable difficulties in collecting a meaningful flux of ^{36}Ar. These additional experiments, along with forthcoming measurements at a wider range of incident beam energies and computational modeling of energy transfer at the gas-surface interface, will help to elucidate the nature of this preferential condensation phenomenon. Because this process requires only the creation of a supersonic beam and the use of a surface that is inert to the given beam, it promises to be applicable to a large range of isotopes and molecular isotopologues, with varied enrichment factors tunable through incident kinetic energy.

Figure 7-1

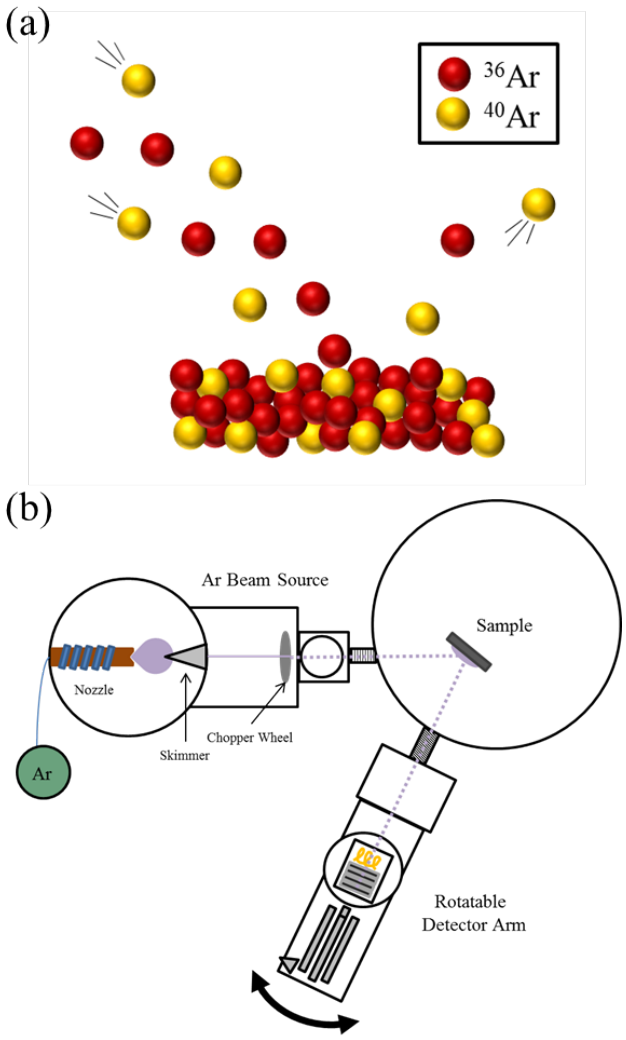

(a) Illustration of a monoenergetic beam of ^{36}Ar and ^{40}Ar striking a surface of amorphous argon; (b) schematic of the ultra-high vacuum surface scattering instrument employed in this experiment; key components are described in the text.

Figure 7-2

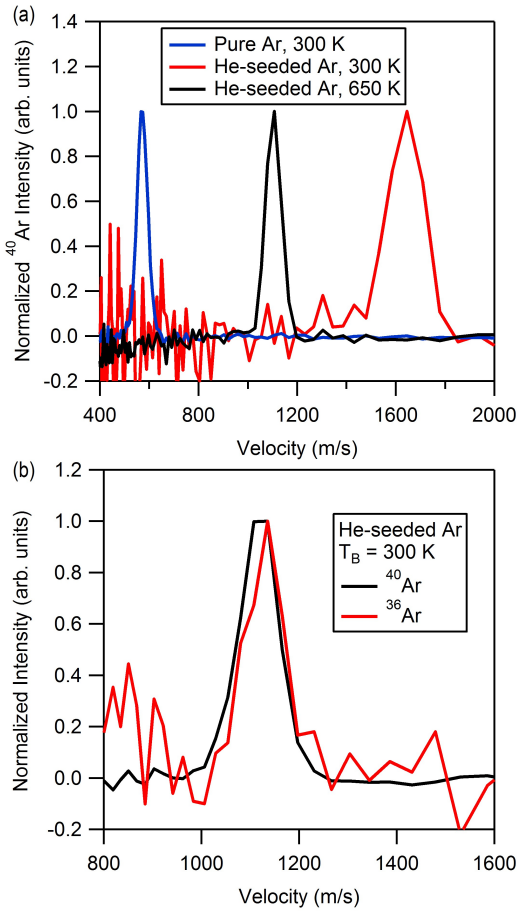

(a) Background-subtracted incident velocity distributions of ^{40}Ar for room-temperature pure argon (blue), room-temperature helium-seeded argon (black), and 650 K helium-seeded argon beams (red); (b) incident velocity distributions of ^{40}Ar (black) and ^{36}Ar (red) in a room temperature beam of pure Ar.

Figure 7-3

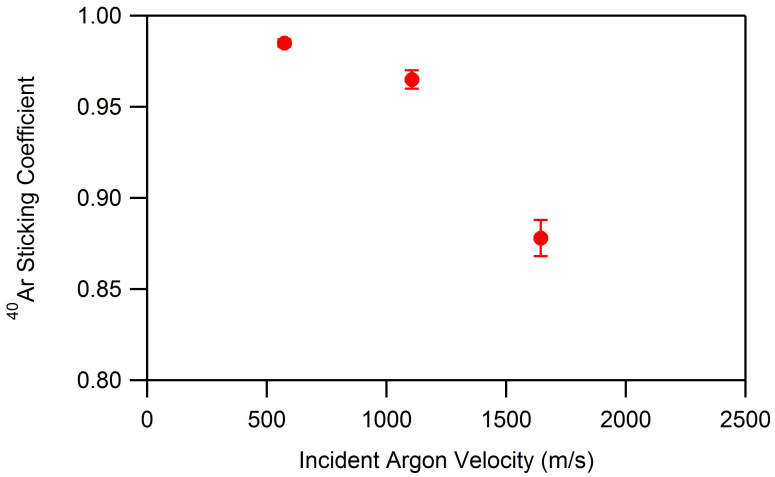

Measured sticking coefficient of ^{40}Ar as a function of incident velocity. This relationship can be exploited by changing the energy of the incident beam and selectively tuning the enrichment factor through the techniques discussed below.

Figure 7-4

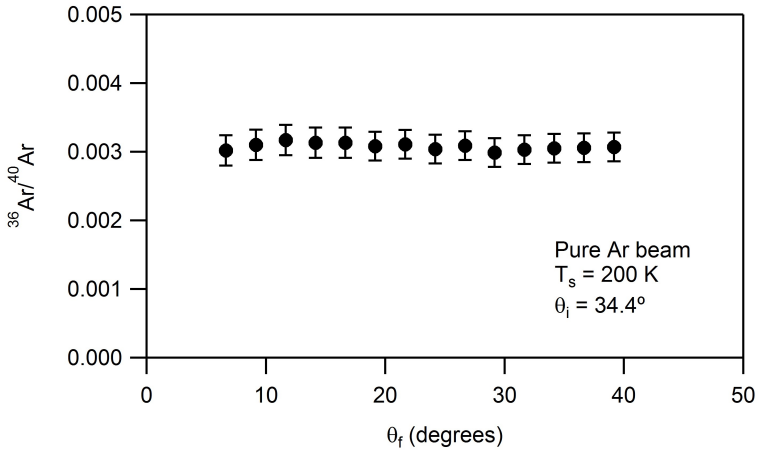

$^{36}Ar/^{40}Ar$ isotope ratio for a pure argon beam reflecting from CH_3-Si(111) at T_s = 200 K (above the adsorption temperature) as a function of reflected angle, demonstrating that measurements taken at one final angle are representative of the complete set of reflected angles. The difference in initial ratio between beam energies, and from the literature ratio, is attributed to a mass-focusing effect that leads to enrichment of the heavier species and depletion of the lighter species.

Figure 7-5

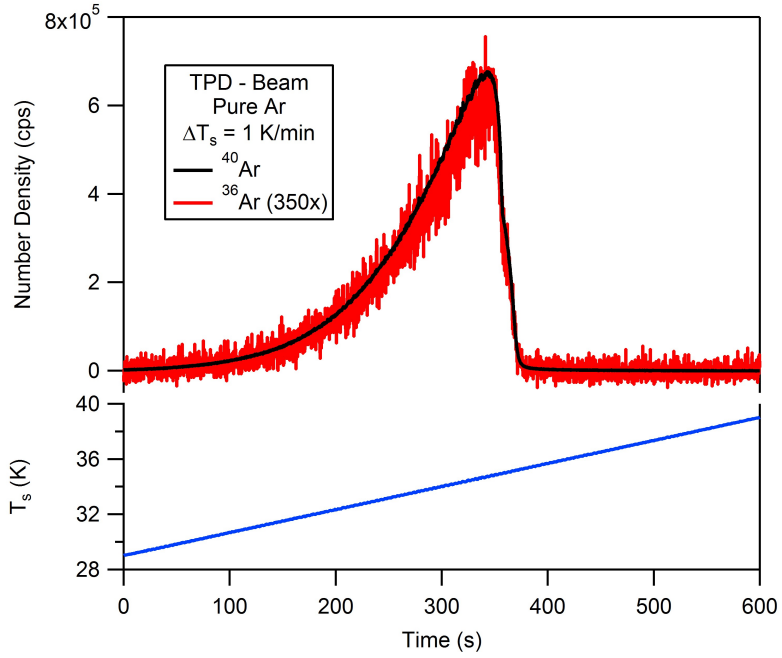

Representative temperature-programmed desorption (TPD) spectra for ^{40}Ar (black) and ^{36}Ar (red) for a pure argon beam dosed on a cold surface. The data from this figure are used to determine the $^{36}Ar/^{40}Ar$ isotope ratios of the condensate, as depicted in Figure 7-6.

Figure 7-6

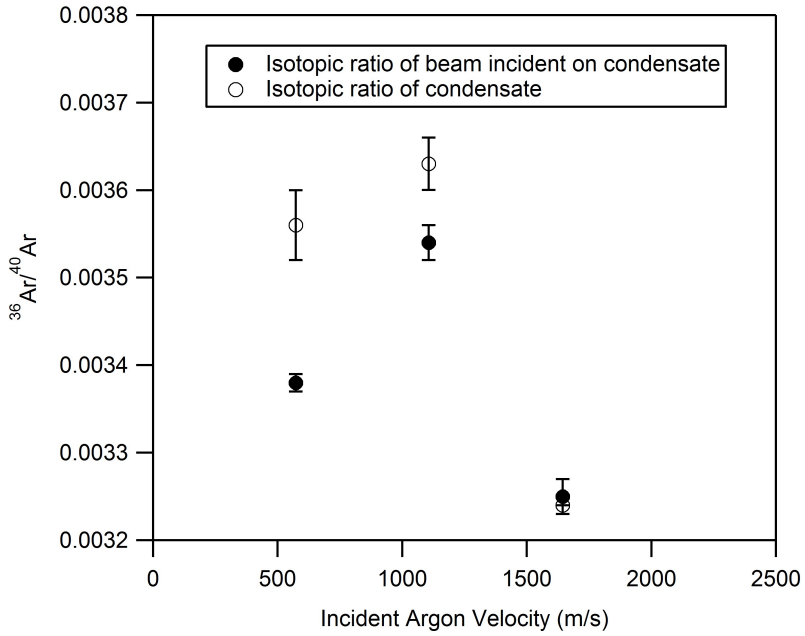

$^{36}Ar/^{40}Ar$ isotope ratio after desorption from a surface of amorphous argon as a function of incident beam velocity. This is the first demonstration of isotope enrichment due to preferential condensation from supersonic molecular beams, showing preferential adsorption of the lighter isotope at low incident energies and preferential adsorption of the heavier isotope at higher incident energies.

Figure 7-7

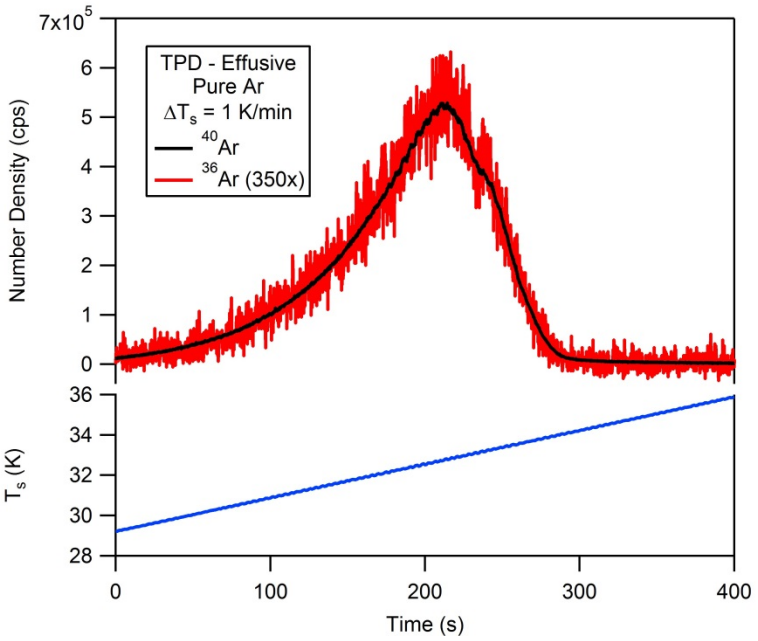

Representative temperature-programmed desorption (TPD) spectra for ^{40}Ar (black) and ^{36}Ar (red) for a mixture of pure argon effusively dosed onto CH_3-Si(111). The data from this figure are compared with the data from Figure 7-5 to determine the extent of isotope enrichment that results from the mass-focusing effect in the supersonic expansion of the incident beam.

Appendix

Raw Data Referenced in All Figures

The following contains figures showing the raw data as collected for figures used throughout the preceding chapters. The naming scheme for each figure follows the following convention: '**A**', followed by the chapter where the data appears in a figure (*i.e.* '**2**'), followed by a dash and the number of the raw data figure in the order it appears in the appendix (*i.e.* '**-1**' for the first, '**-2**' for the second, etc.). This number **does not necessarily correspond** to the associated figure's number in the thesis.

In all cases, the figure(s) in which the raw data appear is indicated in the appendix figure's caption.

Figure A3-1

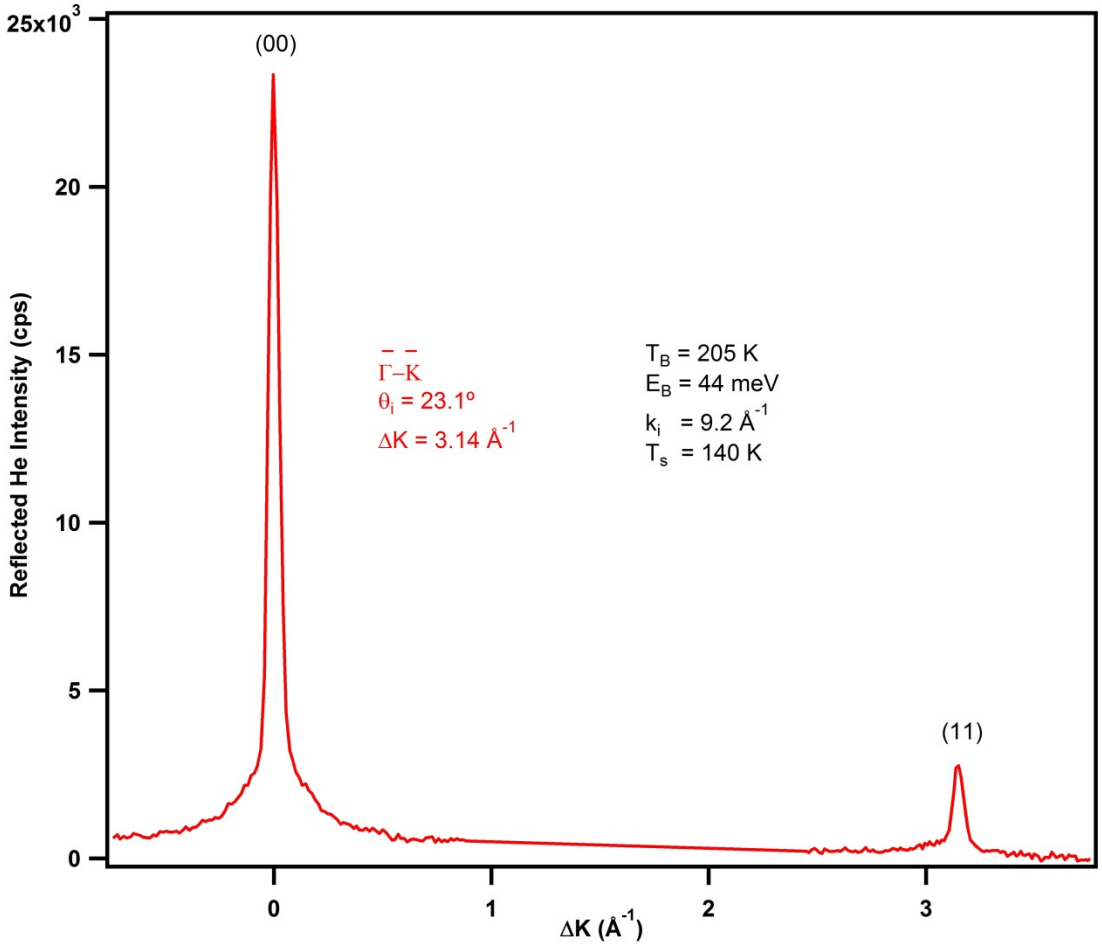

Raw He/CH_3-Ge(111) diffraction spectrum (Γ–K) used to create **Figure 3-1.**

Experiment file: Figure A3-1 (091814_D01).pxp

Raw data file: 091814.D01

Figure A3-2

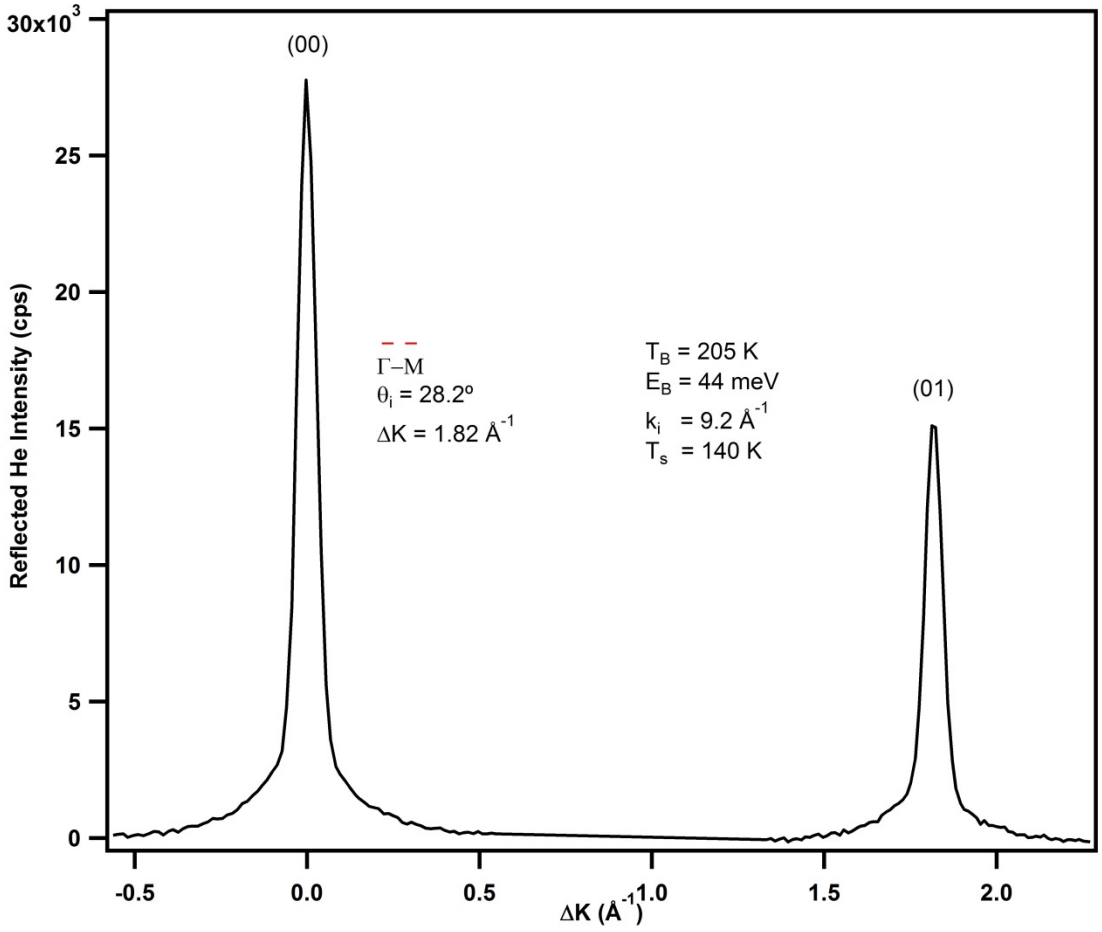

Raw He/CH_3-Ge(111) diffraction spectrum (Γ–M) used to create **Figure 3-1.**

Experiment file: Figure A3-2 (090514_D01).pxp

Raw data file: 090514.D01

Figure A3-3

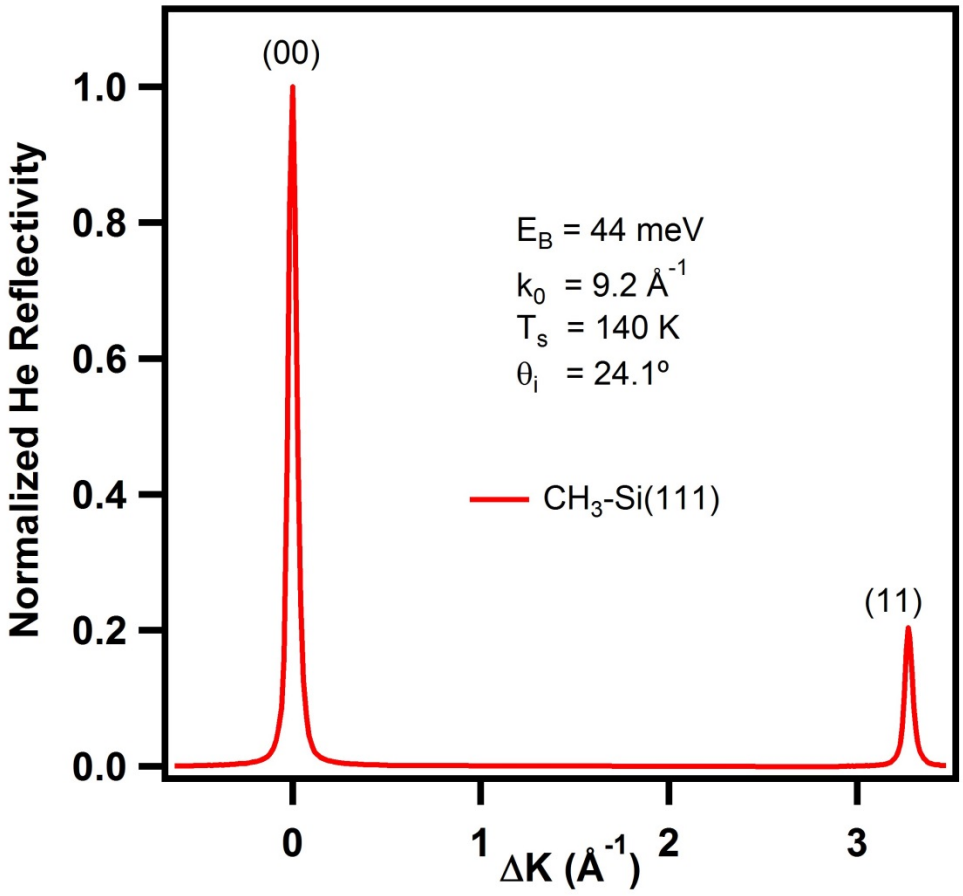

Normalized He/CH_3-Si(111) diffraction spectrum (Γ–K) used to create **Figure 3-2.**

Experiment file: Figure A3-3 (012214_D01).pxp

Raw data file: 012214.D01

Figure A3-4

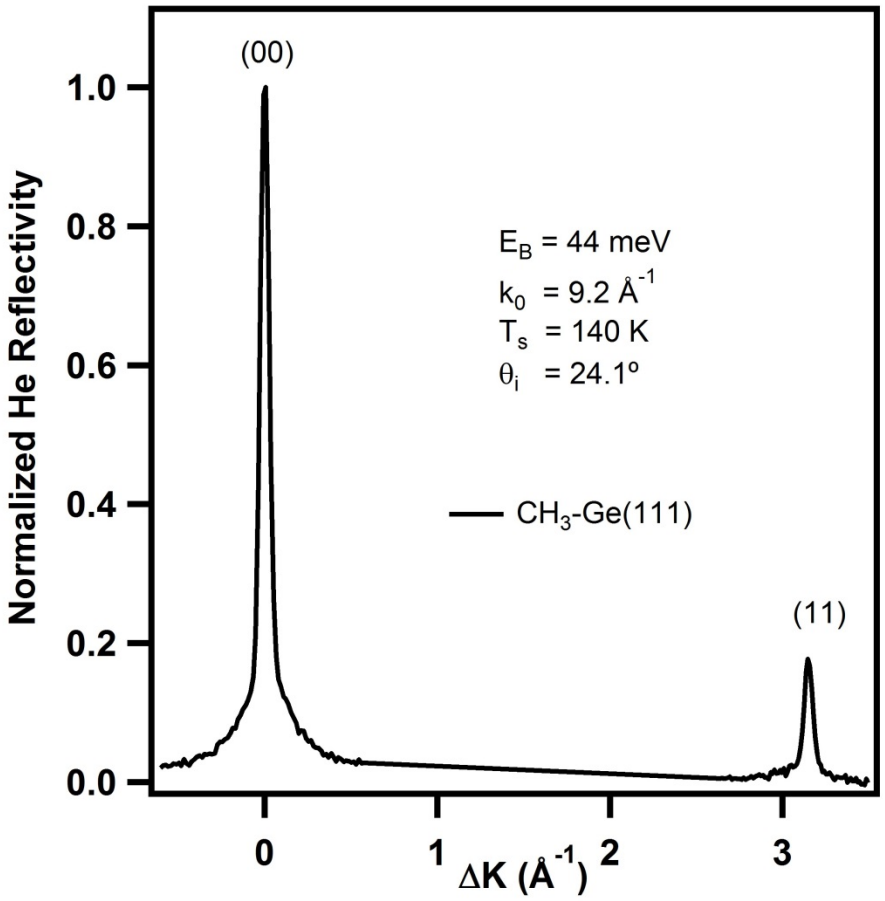

Normalized He/CH_3-Ge(111) diffraction spectrum (Γ–K) used to create **Figure 3-2.**

Experiment file: Figure A3-4 (092214_D03).pxp

Raw data file: 092214.D03

Figure A3-5

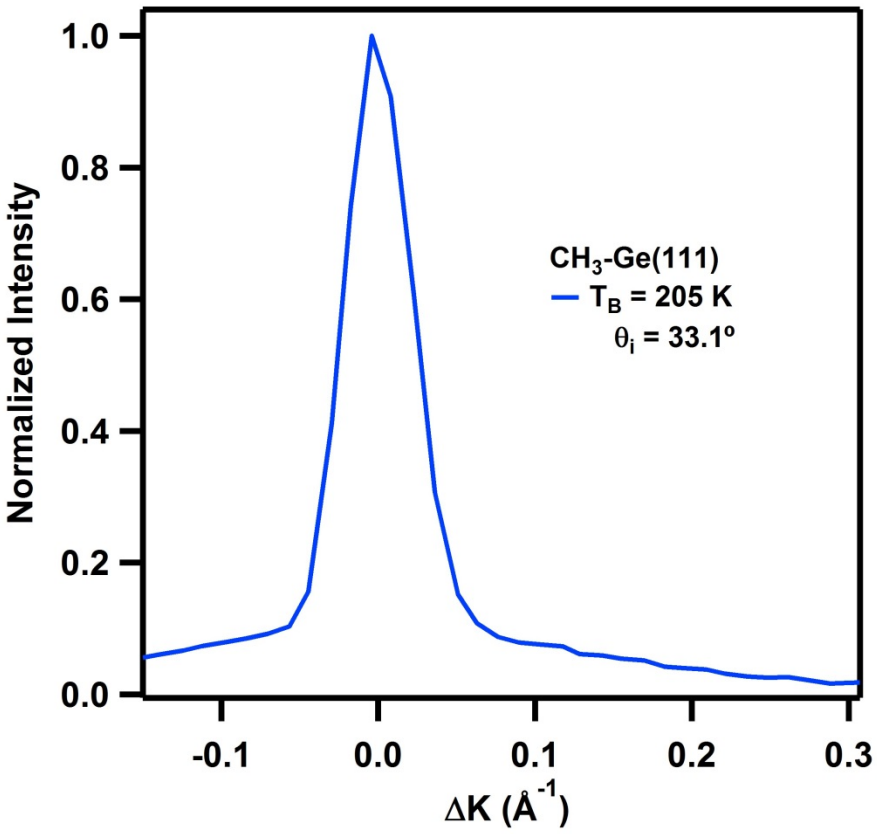

Normalized He/CH_3-Ge(111) diffraction spectrum (Γ–K) used in the inset of **Figure 3-2.**

Experiment file: Figure A3-5 (092214_D06).pxp

Raw data file: 092214.D06

Figure A3-6

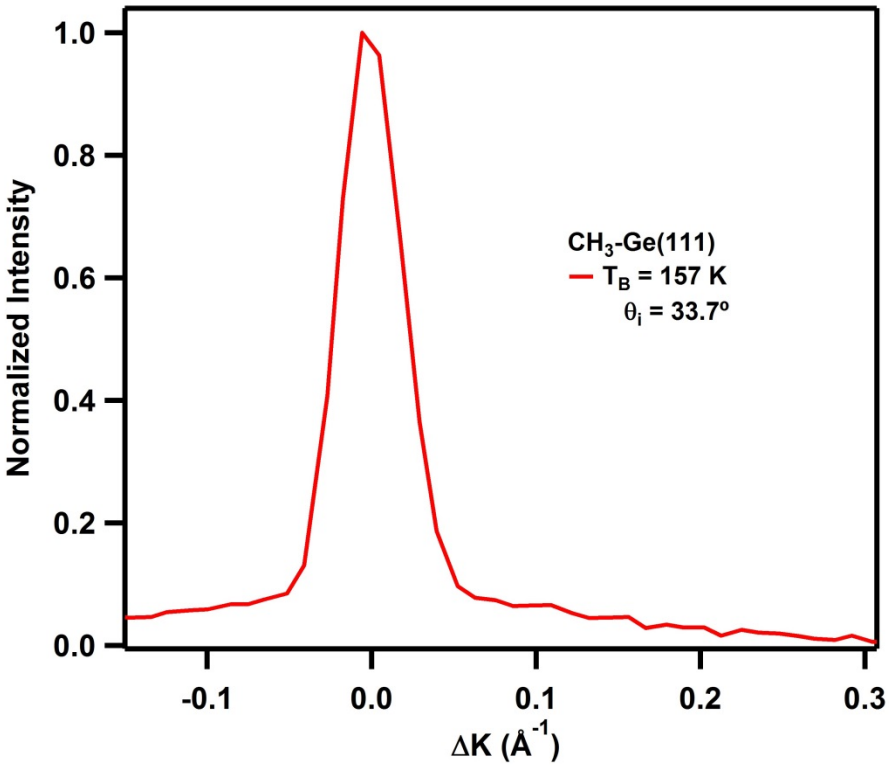

Normalized He/CH_3-Ge(111) diffraction spectrum (Γ–K) used in the inset of **Figure 3-2.**

Experiment file: Figure A3-6 (091914_D01).pxp

Raw data file: 091914.D01

Figure A3-7

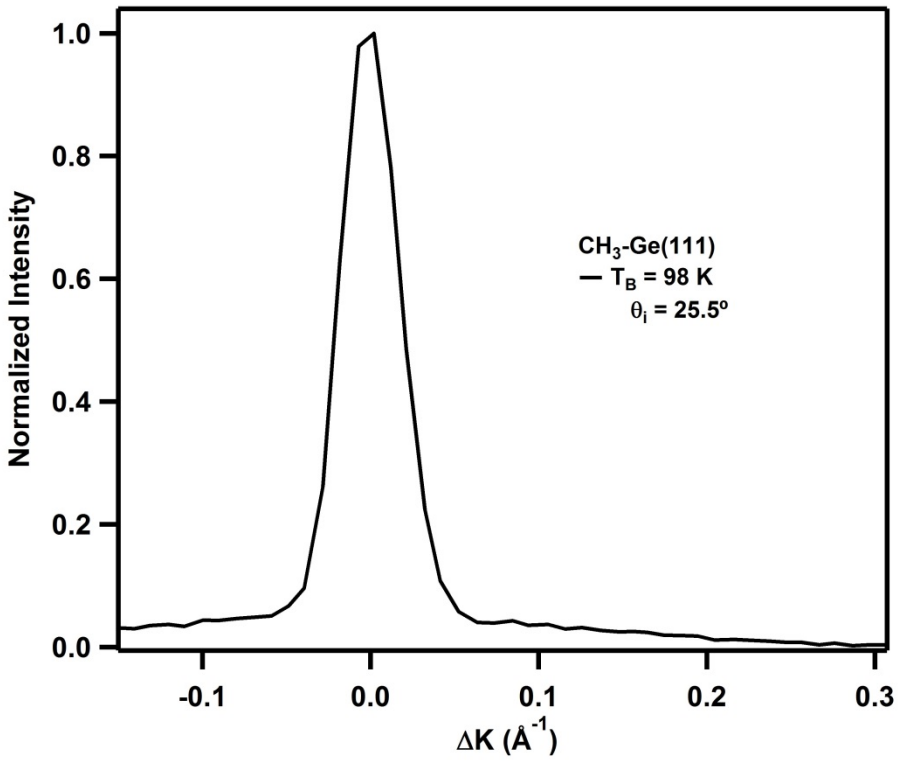

Normalized He/CH_3-Ge(111) diffraction spectrum (Γ–K) used in the inset of **Figure 3-2.**

Experiment file: Figure A3-7 (091714_D07).pxp

Raw data file: 091714.D07

Figure A3-8

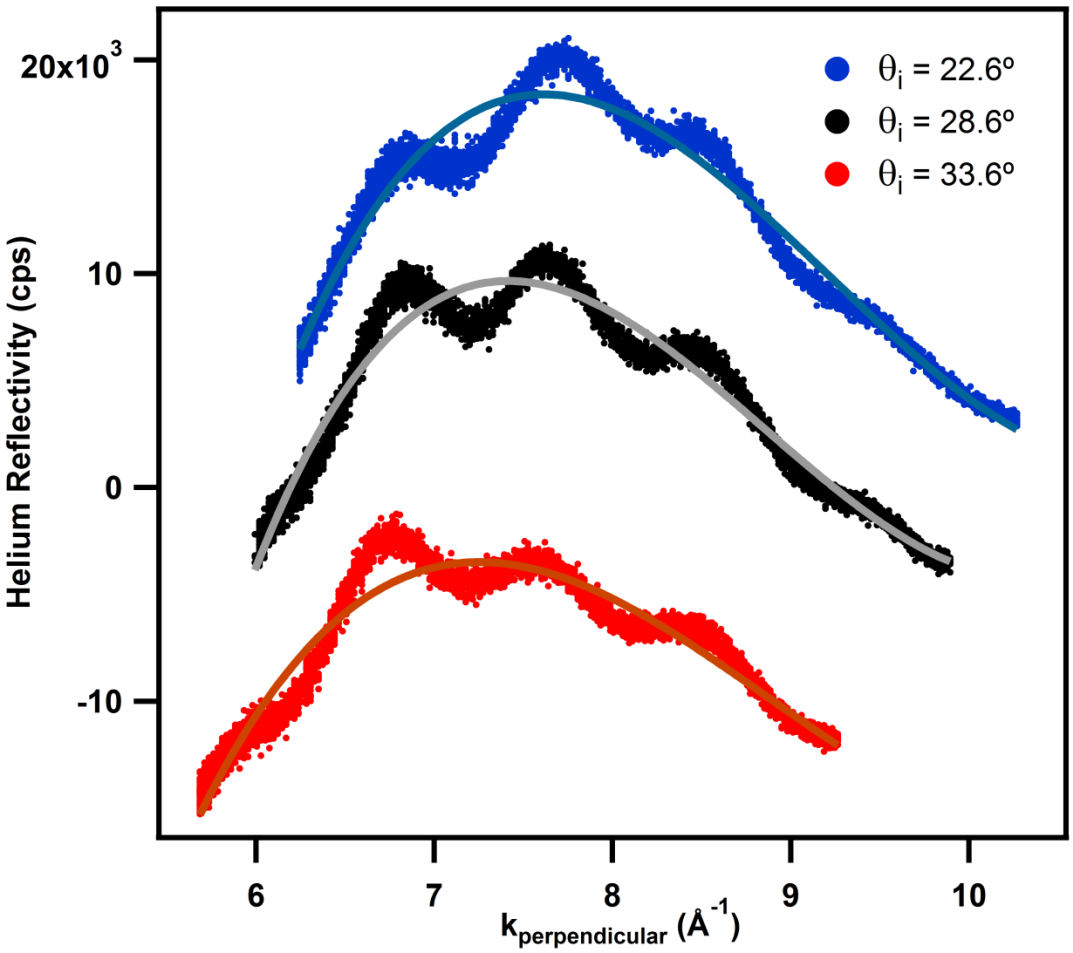

Raw He/CH_3-Ge(111) drift spectra at three different incident angles, offset on the y-axis for ease of viewing, with fits (solid lines) used for background subtraction; fits are subtracted to create the residual traces in **Figure 3-3(a).**

Experiment file: Figure A3-8 (091914).pxp

Raw data file: 091914.001; 091914.003; 091914.005

Figure A3-9

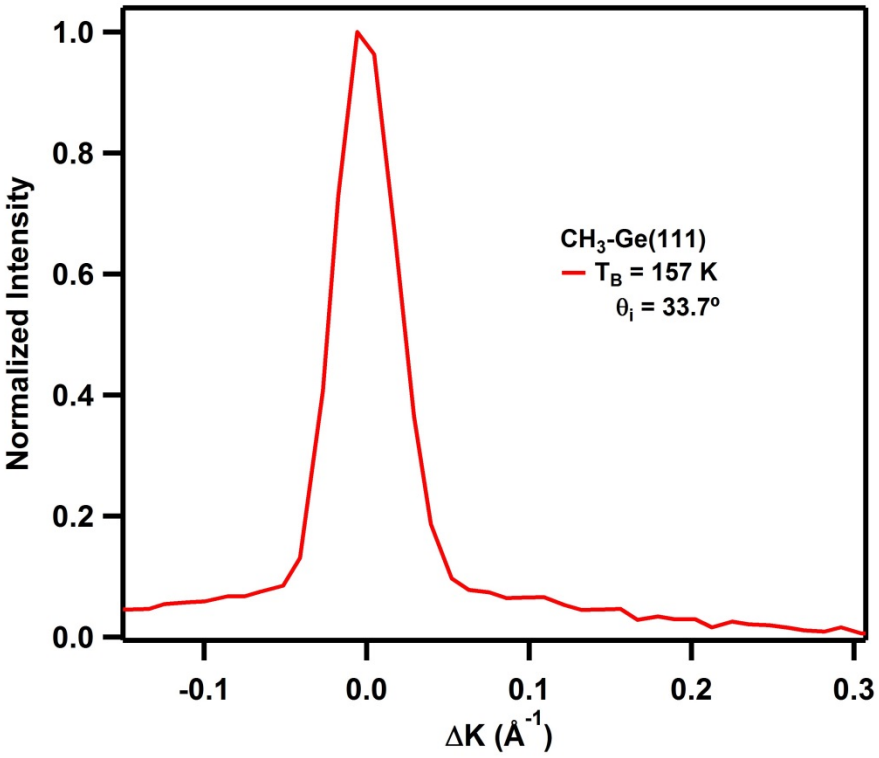

Normalized He/CH_3-Ge(111) diffraction spectrum (Γ–K) used in **Figure 3-3(c).**

Experiment file: Figure A3-9 (091914_D01).pxp

Raw data file: 091914.D01

Figure A3-10

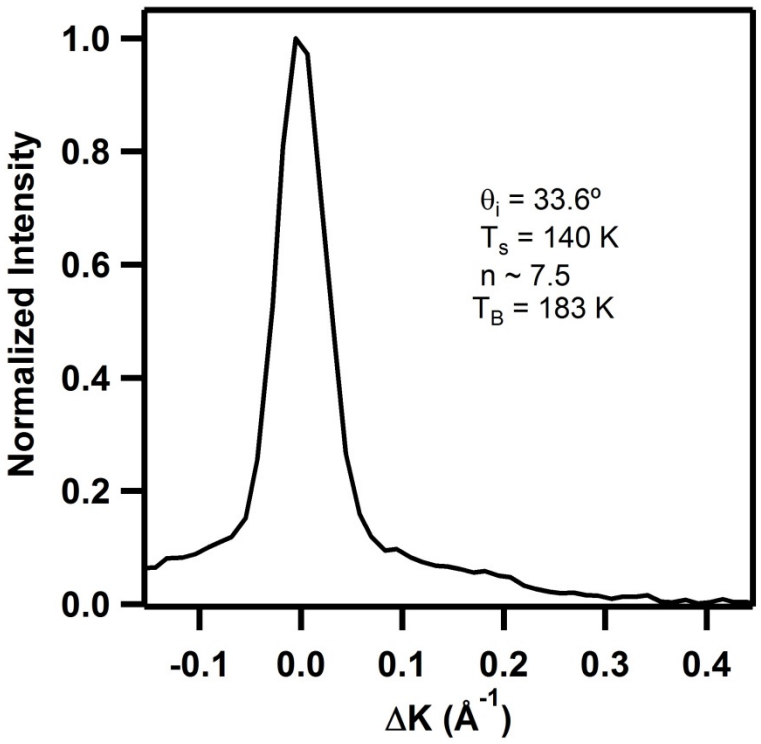

Normalized He/CH_3-Ge(111) diffraction spectrum (Γ–K) used in **Figure 3-3(c).**

Experiment file: Figure A3-10 (091914_D02).pxp

Raw data file: 091914.D02

Figure A3-11

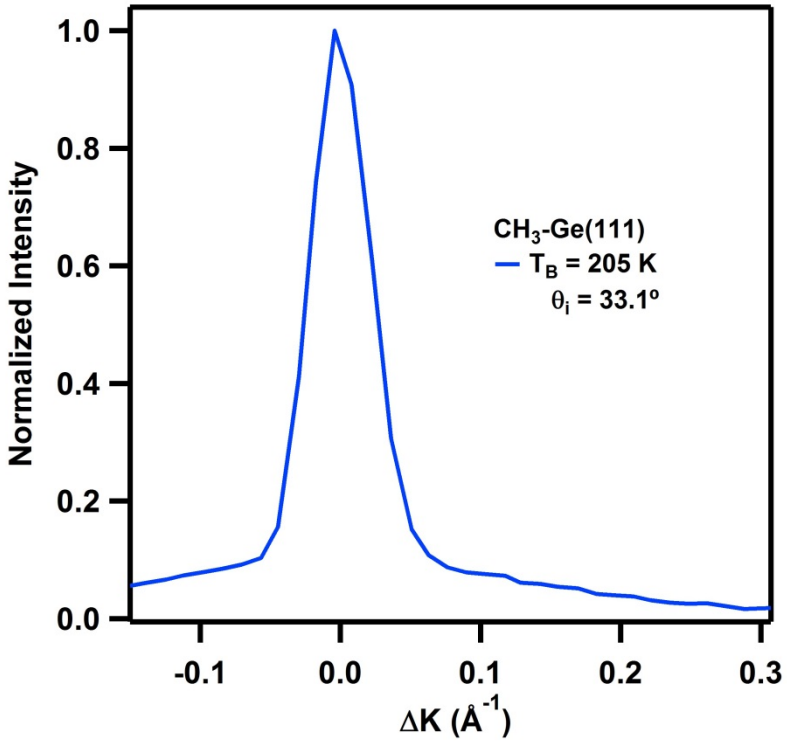

Normalized He/CH_3-Ge(111) diffraction spectrum (Γ–K) used in **Figure 3-3(b).**

Experiment file: Figure A3-11 (092214_D06).pxp

Raw data file: 092214.D06

Figure A3-12

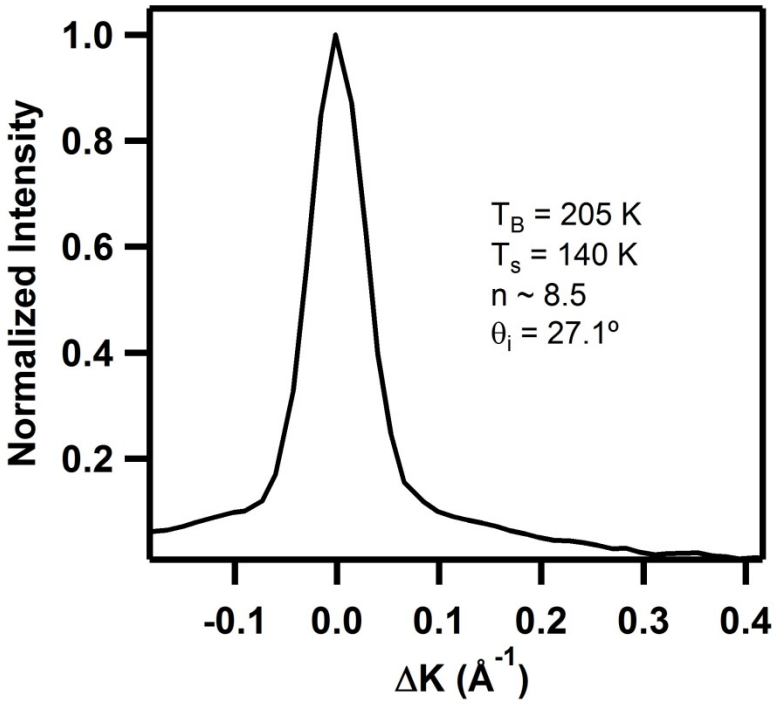

Normalized He/CH_3-Ge(111) diffraction spectrum (Γ–K) used in **Figure 3-3(b).**

Experiment file: Figure A3-12 (092214_D07).pxp

Raw data file: 092214.D07

Figure A4-1

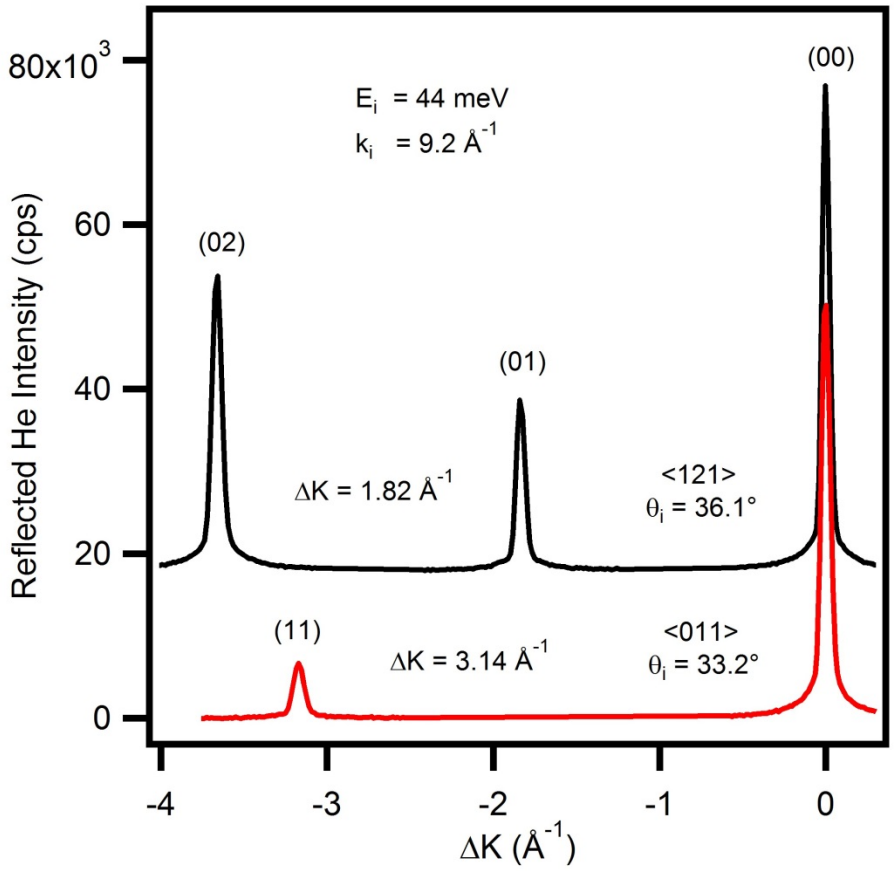

Raw diffraction spectra of He/CH_3-Ge(111) back-scattered on Γ-M (top, black) and Γ-K (bottom, red) azimuthal alignments used in **Figure 4-1(a).**

Experiment file: Figure A4-1.pxp

Raw data file: 120214.D01; 111214.D01

Figure A4-2

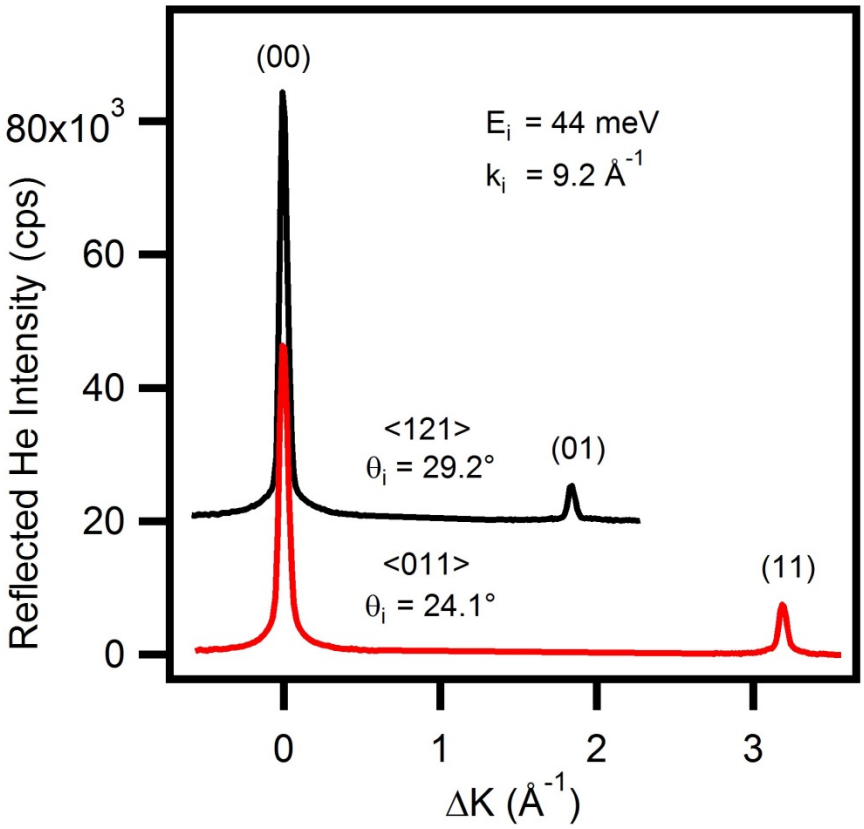

Raw diffraction spectra of He/CH_3-Ge(111) forward-scattered on Γ-M (top, black) and Γ-K (bottom, red) azimuthal alignments used in **Figure 4-1(b).**

Experiment file: Figure A4-2.pxp

Raw data file: 120514.D01; 111214.D02

Figure A4-3

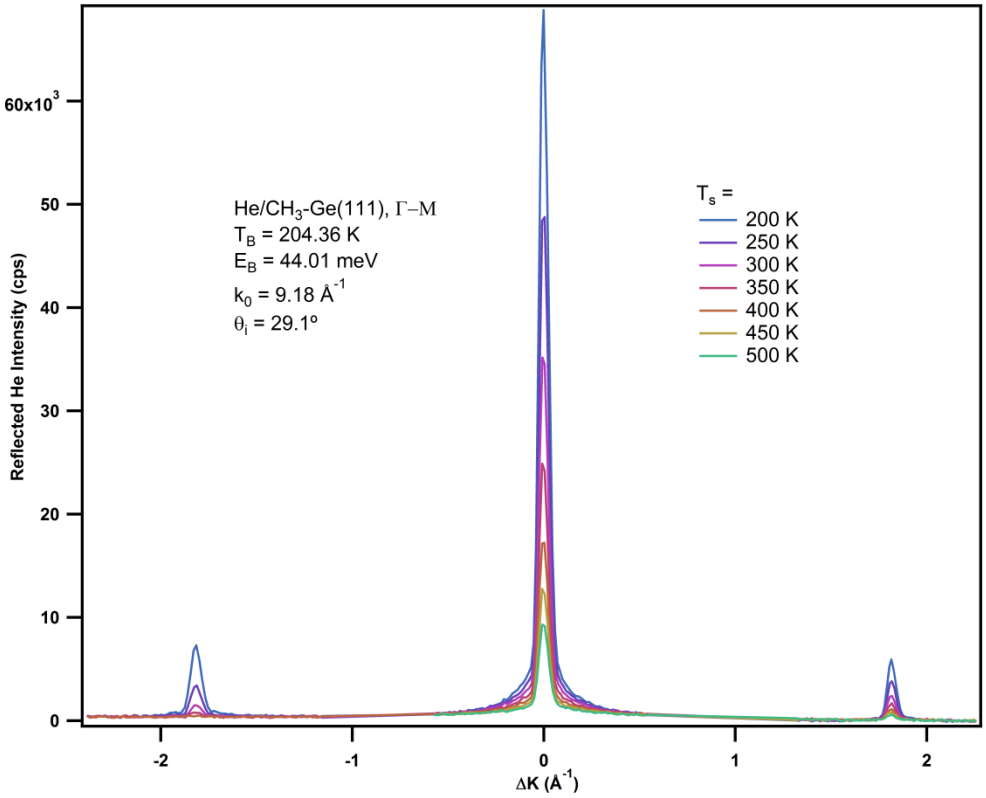

Raw He/CH_3-Ge(111) Debye-Waller diffraction spectra (Γ-M) taken at θ_i = 29.1°. Peaks are integrated to determine area, and the natural log of these areas are displayed in **Figure 4-2(b).**

Experiment file: Figure A4-3 (120314).pxp

Raw data file: 120314.D01; 120314.D02; 120314.D03; 120314.D04; 120314.D05; 120314.D06; 120314.D07

Figure A4-4

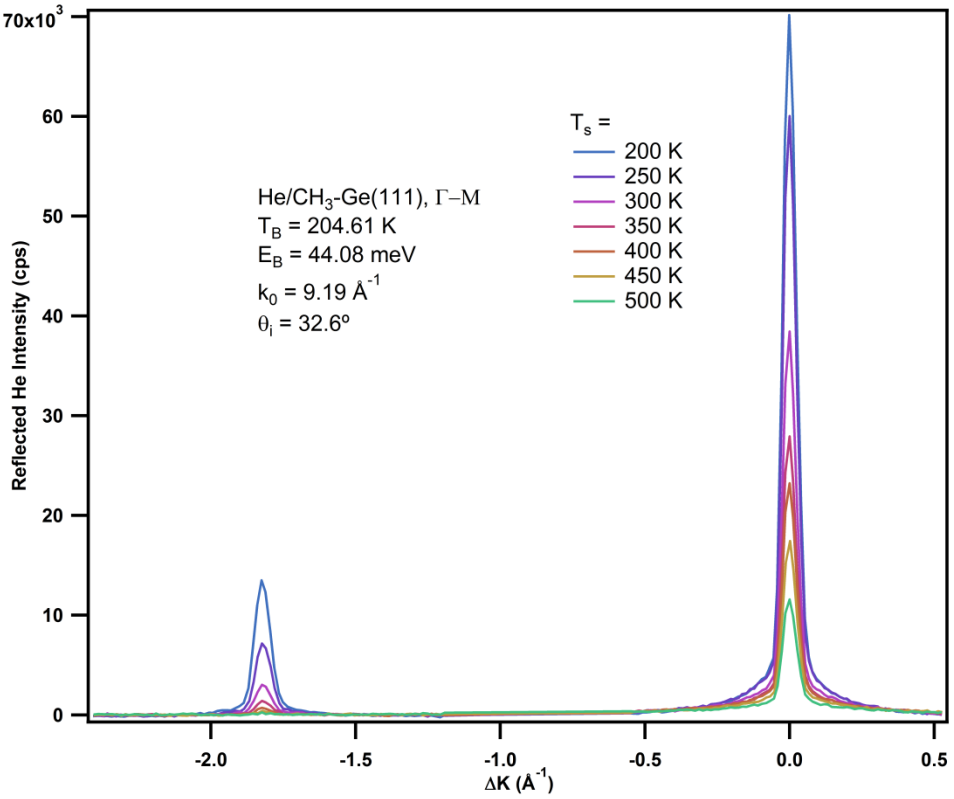

Raw He/CH_3-Ge(111) Debye-Waller diffraction spectra (Γ-M) taken at θ_i = 32.6°. Peaks are integrated to determine area, and the natural log of these areas are displayed in **Figure 4-2(b).**

Experiment file: Figure A4-4 (120214).pxp

Raw data file: 120214.D08; 120214.D09; 120214.D10; 120214.D11; 120214.D12; 120214.D13; 120214.D14

Figure A4-5

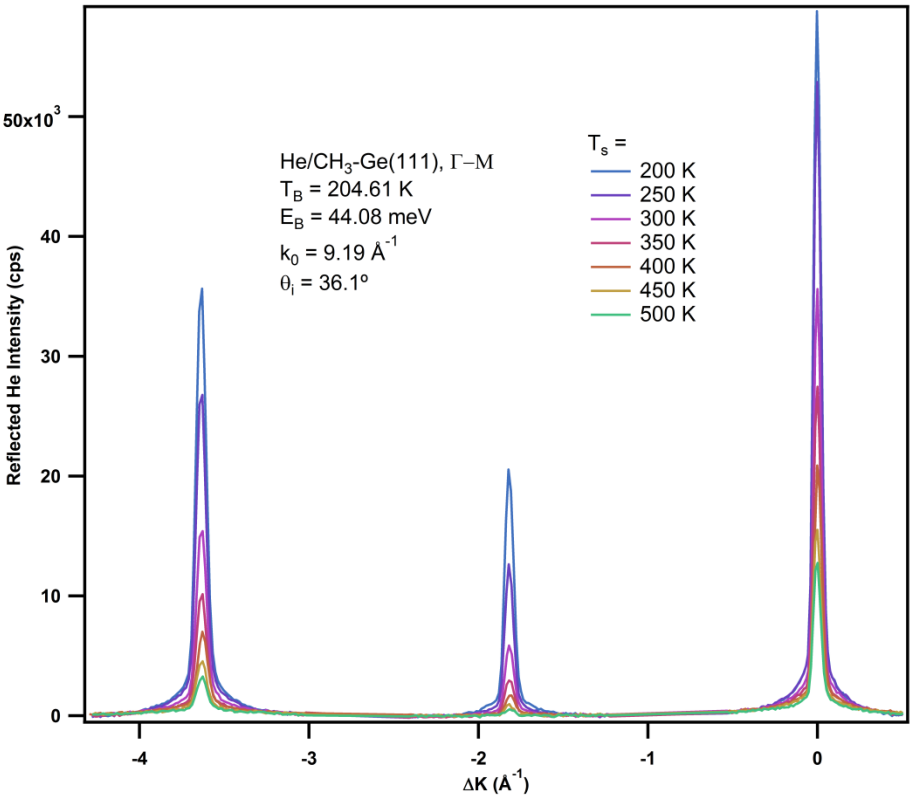

Raw He/CH_3-Ge(111) Debye-Waller diffraction spectra (Γ-M) taken at θ_i = 36.1°. Peaks are integrated to determine area, and the natural log of these areas are displayed in **Figure 4-2(b).**

Experiment file: Figure A4-5 (120214).pxp

Raw data file: 120214.D01; 120214.D02; 120214.D03; 120214.D04; 120214.D05; 120214.D06; 120214.D07

Figure A4-6

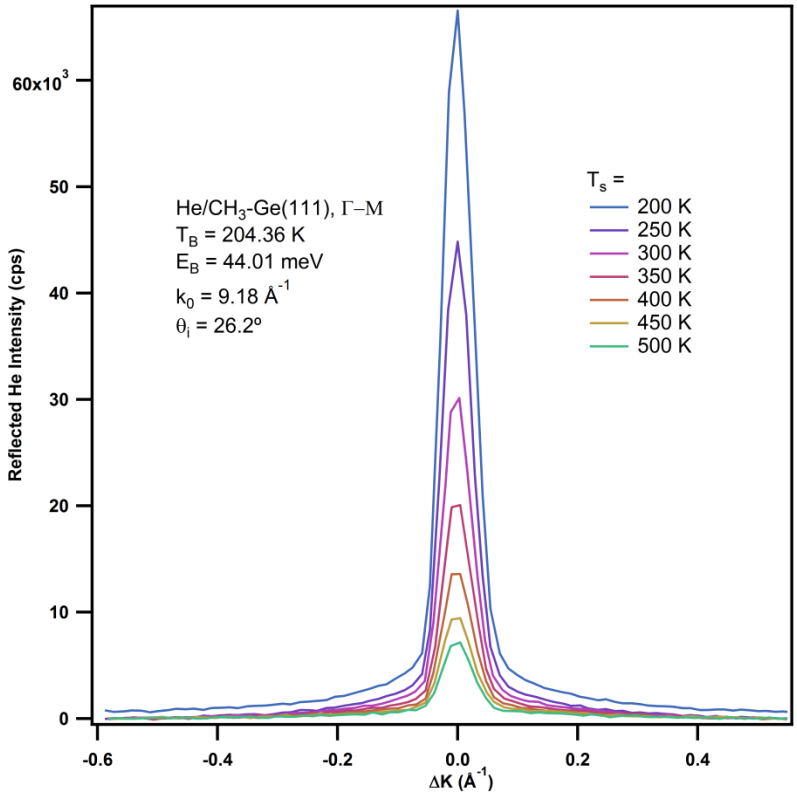

Raw He/CH_3-Ge(111) Debye-Waller diffraction spectra (Γ-M) taken at θ_i = 26.2°. Peaks are integrated to determine area, and the natural log of these areas are displayed in **Figure 4-2(b).**

Experiment file: Figure A4-6 (120314).pxp

Raw data file: 120314.D08; 120314.D09; 120314.D10; 120314.D11; 120314.D12; 120314.D13; 120314.D14

Figure A4-7

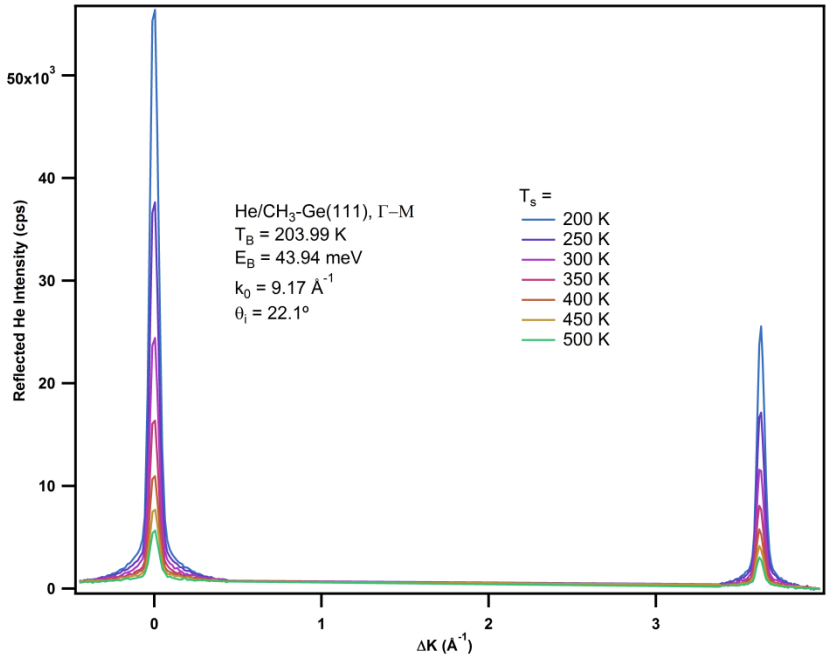

Raw He/CH_3-Ge(111) Debye-Waller diffraction spectra (Γ-M) taken at θ_i = 22.1°. Peaks are integrated to determine area, and the natural log of these areas are displayed in **Figure 4-2(b).**

Experiment file: Figure A4-7 (120414).pxp

Raw data file: 120414.D01; 120414.D02; 120414.D03; 120414.D04; 120414.D05; 120414.D06; 120414.D07

Figure A4-8

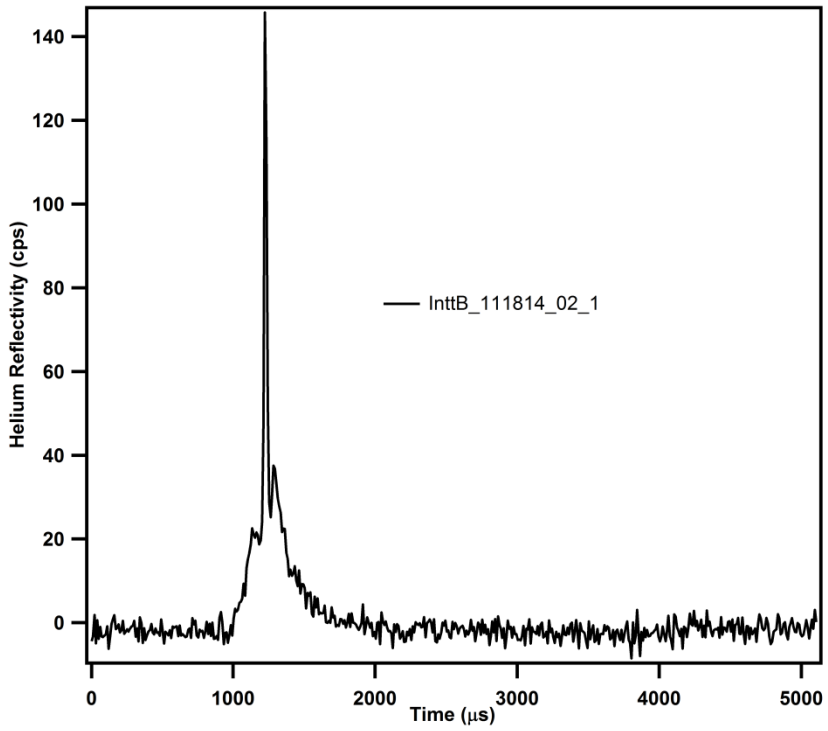

Raw He/CH_3-Ge(111) inelastic time-of-flight spectrum which contributes an experimental phonon point to the final dispersion curves in **Figure 4-6**. *Cross-correlation spectrum taken in long mode with a 150 K beam, 140 K surface temperature, Γ–M alignment, 35.2° incident angle, and 24.2° final angle.*

Experiment file: Figure 4-6.pxp

Raw data file: 111814.002

Figure A4-9

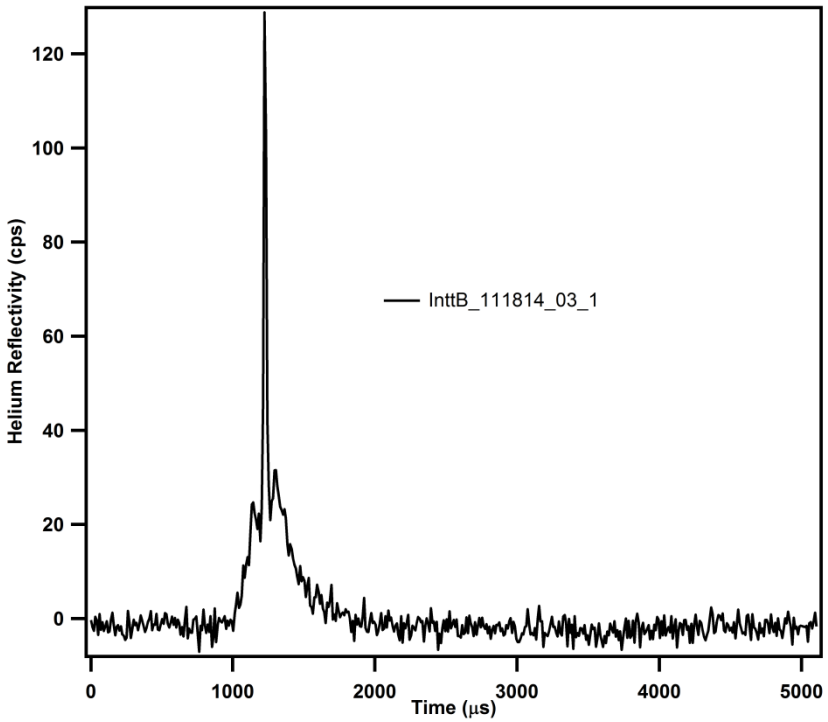

Raw He/CH_3-Ge(111) inelastic time-of-flight spectrum which contributes an experimental phonon point to the final dispersion curves in **Figure 4-6**. *Cross-correlation spectrum taken in long mode with a 150 K beam, 140 K surface temperature, Γ–M alignment, 35.2° incident angle, and 25.2° final angle.*

Experiment file: Figure 4-6.pxp

Raw data file: 111814.003

Figure A4-10

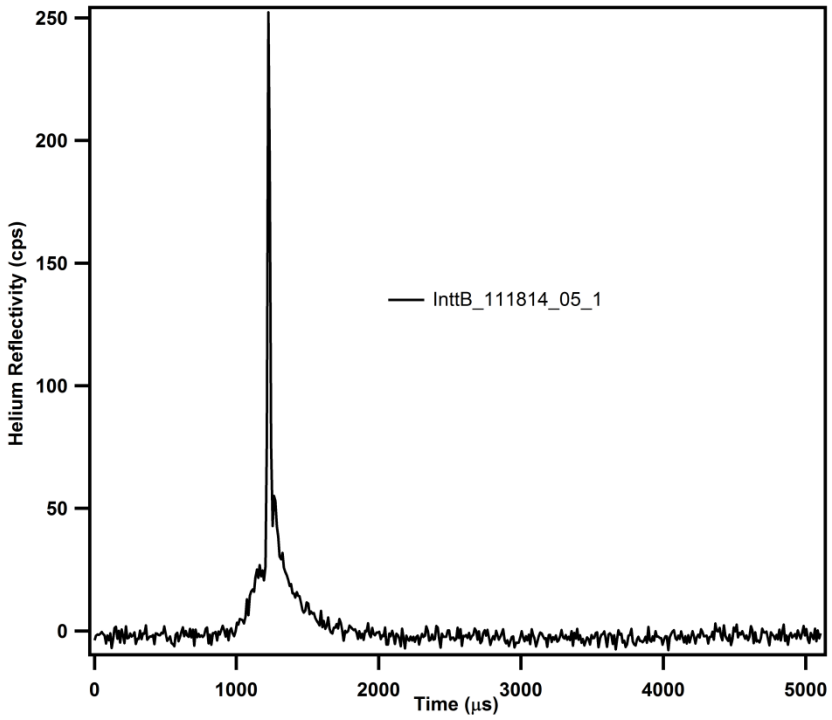

Raw He/CH_3-Ge(111) inelastic time-of-flight spectrum which contributes an experimental phonon point to the final dispersion curves in **Figure 4-6**. *Cross-correlation spectrum taken in long mode with a 150 K beam, 140 K surface temperature, Γ–M alignment, 35.2° incident angle, and 22.7° final angle.*

Experiment file: Figure 4-6.pxp

Raw data file: 111814.005

Figure A4-11

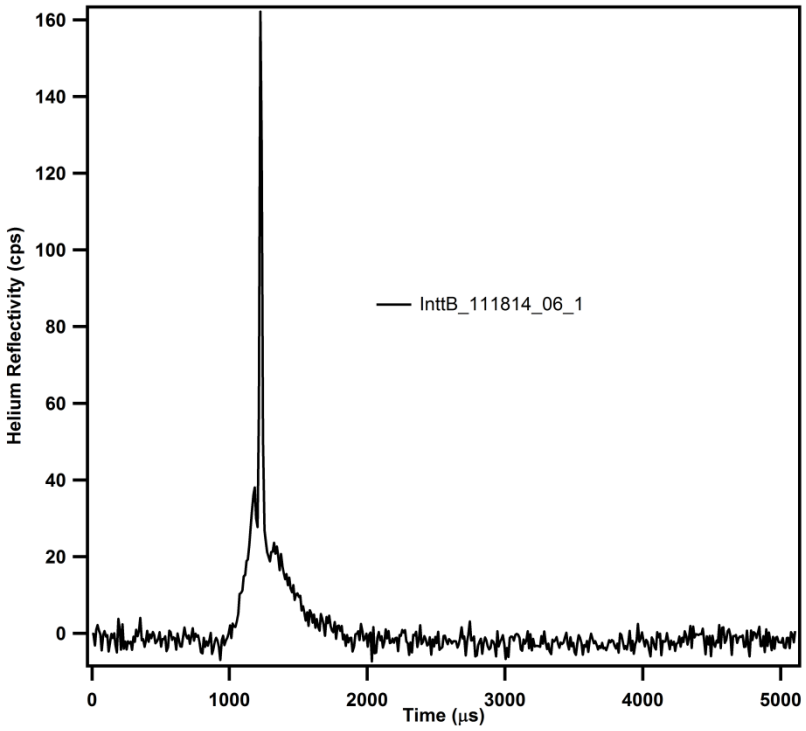

Raw He/CH_3-Ge(111) inelastic time-of-flight spectrum which contributes an experimental phonon point to the final dispersion curves in **Figure 4-6**. *Cross-correlation spectrum taken in long mode with a 150 K beam, 140 K surface temperature, Γ–M alignment, 35.2° incident angle, and 17.2° final angle.*

Experiment file: Figure 4-6.pxp

Raw data file: 111814.006

Figure A4-12

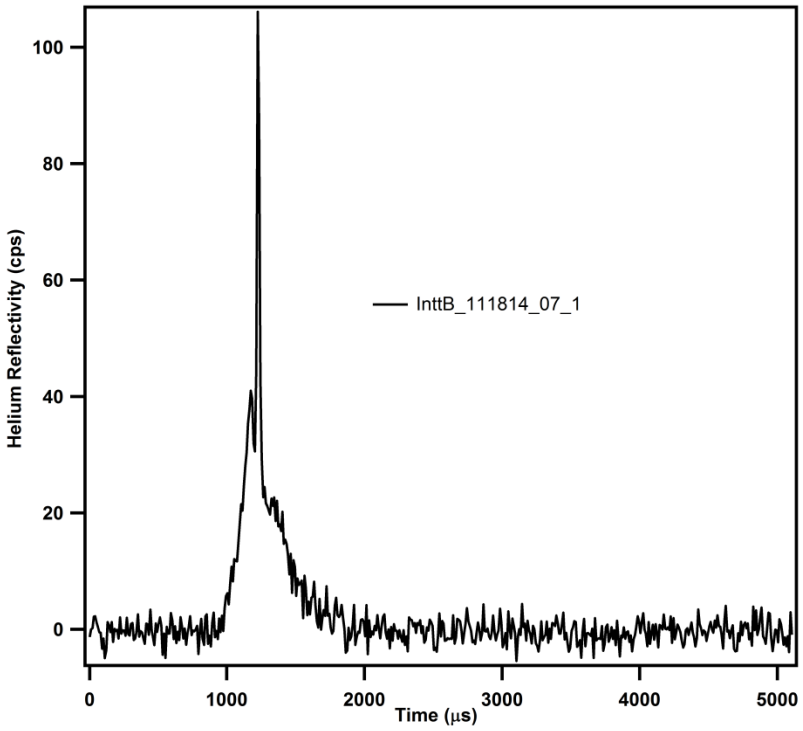

Raw He/CH_3-Ge(111) inelastic time-of-flight spectrum which contributes an experimental phonon point to the final dispersion curves in **Figure 4-6**. *Cross-correlation spectrum taken in long mode with a 150 K beam, 140 K surface temperature, Γ–M alignment, 35.2° incident angle, and 17.2° final angle.*

Experiment file: Figure 4-6.pxp

Raw data file: 111814.007

Figure A4-13

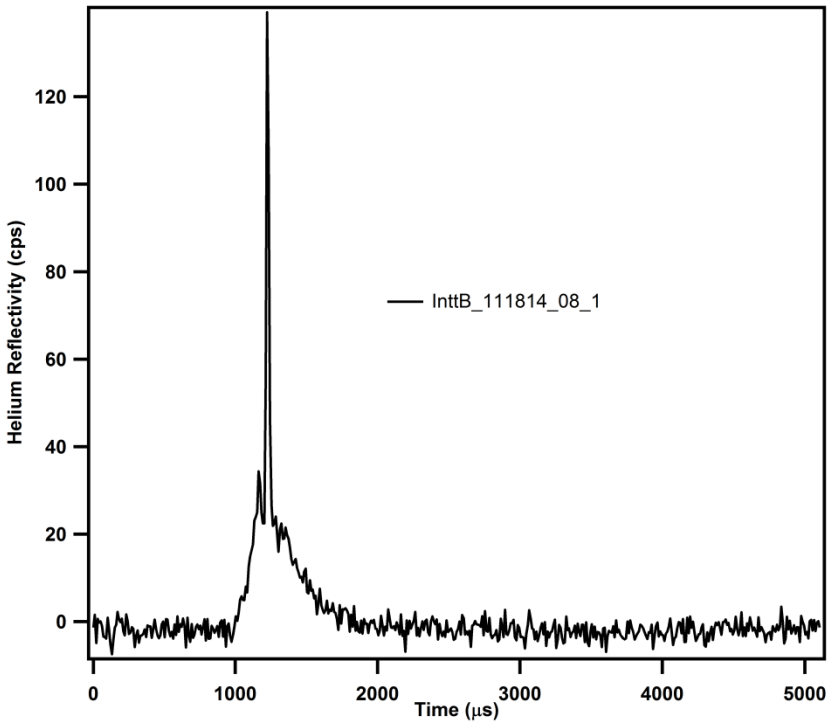

Raw He/CH_3-Ge(111) inelastic time-of-flight spectrum which contributes an experimental phonon point to the final dispersion curves in **Figure 4-6**. *Cross-correlation spectrum taken in long mode with a 150 K beam, 140 K surface temperature, Γ–M alignment, 35.2° incident angle, and 16.2° final angle.*

Experiment file: Figure 4-6.pxp

Raw data file: 111814.008

Figure A4-14

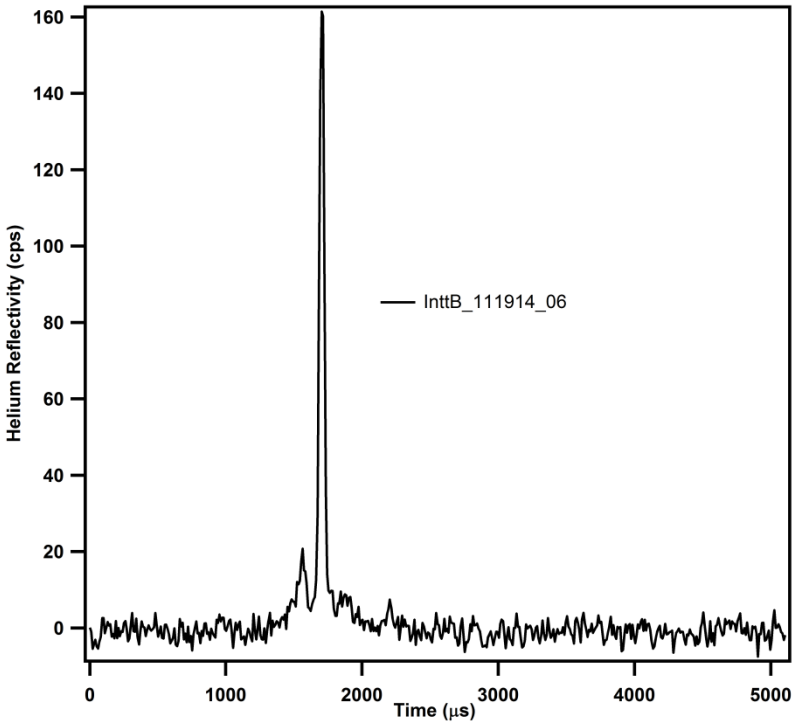

Raw He/CH_3-Ge(111) inelastic time-of-flight spectrum which contributes an experimental phonon point to the final dispersion curves in **Figure 4-6**. *Cross-correlation spectrum taken in long mode with a 80 K beam, 140 K surface temperature, Γ–M alignment, 32.2° incident angle, and 13.7° final angle.*

Experiment file: Figure 4-6.pxp

Raw data file: 111914.006

Figure A4-15

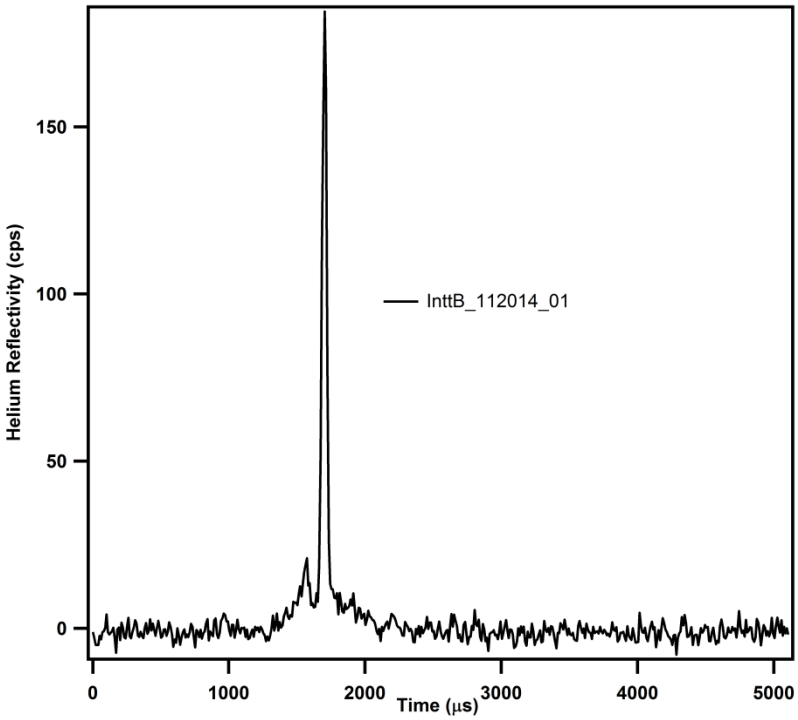

Raw He/CH_3-Ge(111) inelastic time-of-flight spectrum which contributes an experimental phonon point to the final dispersion curves in **Figure 4-6**. *Cross-correlation spectrum taken in long mode with a 80 K beam, 140 K surface temperature, Γ–M alignment, 32.2° incident angle, and 13.7° final angle.*

Experiment file: Figure 4-6.pxp

Raw data file: 112014.001

Figure A4-16

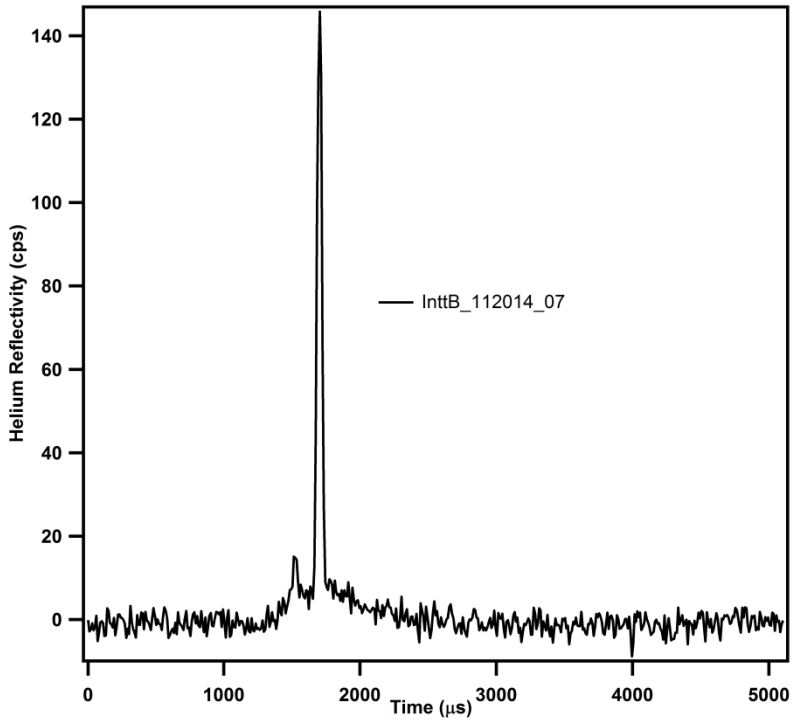

Raw He/CH_3-Ge(111) inelastic time-of-flight spectrum which contributes an experimental phonon point to the final dispersion curves in **Figure 4-6**. *Cross-correlation spectrum taken in long mode with a 80 K beam, 140 K surface temperature, Γ–M alignment, 32.2° incident angle, and 14.2° final angle.*

Experiment file: Figure 4-6.pxp

Raw data file: 112014.007

Figure A4-17

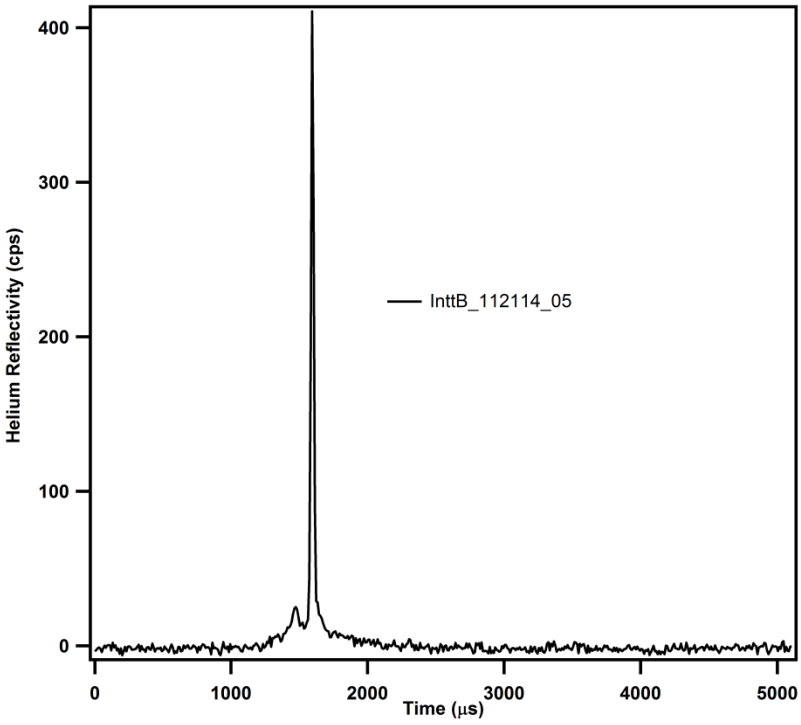

Raw He/CH_3-Ge(111) inelastic time-of-flight spectrum which contributes an experimental phonon point to the final dispersion curves in **Figure 4-6**. *Cross-correlation spectrum taken in long mode with a 90 K beam, 140 K surface temperature, Γ–M alignment, 32.2° incident angle, and 14.7° final angle.*

Experiment file: Figure 4-6.pxp

Raw data file: 112114.005

Figure A4-18

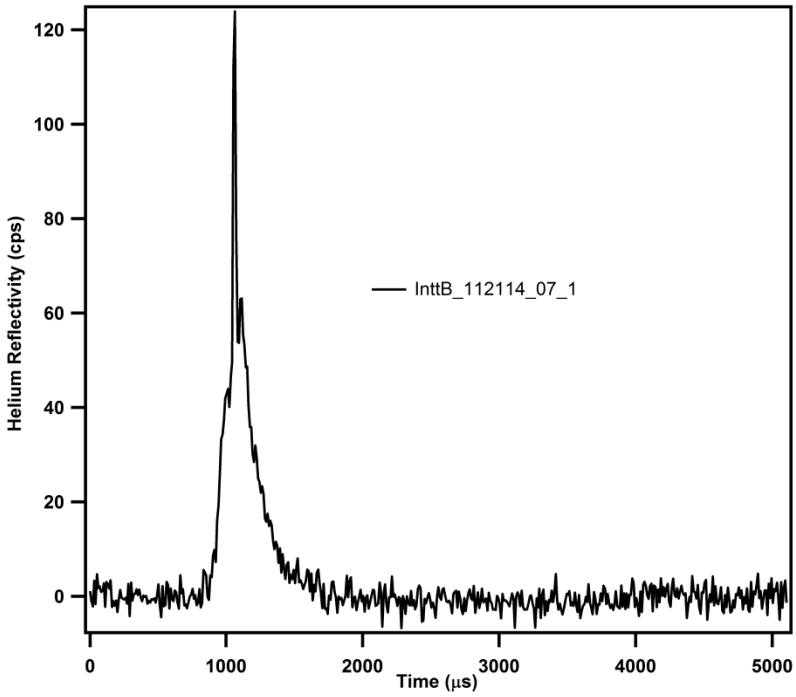

Raw He/CH_3-Ge(111) inelastic time-of-flight spectrum which contributes an experimental phonon point to the final dispersion curves in **Figure 4-6**. *Cross-correlation spectrum taken in long mode with a 200 K beam, 140 K surface temperature, Γ–M alignment, 32.2° incident angle, and 23.2° final angle.*

Experiment file: Figure 4-6.pxp

Raw data file: 112114.007

Figure A4-19

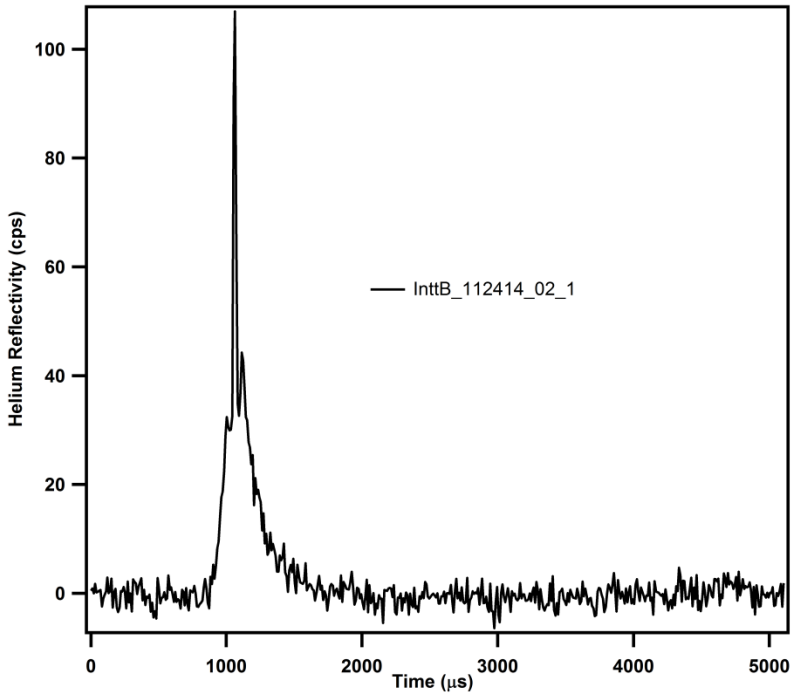

Raw He/CH_3-Ge(111) inelastic time-of-flight spectrum which contributes an experimental phonon point to the final dispersion curves in **Figure 4-6**. *Cross-correlation spectrum taken in long mode with a 200 K beam, 140 K surface temperature, Γ–M alignment, 32.2° incident angle, and 24.2° final angle.*

Experiment file: Figure 4-6.pxp

Raw data file: 112414.002

Figure A4-20

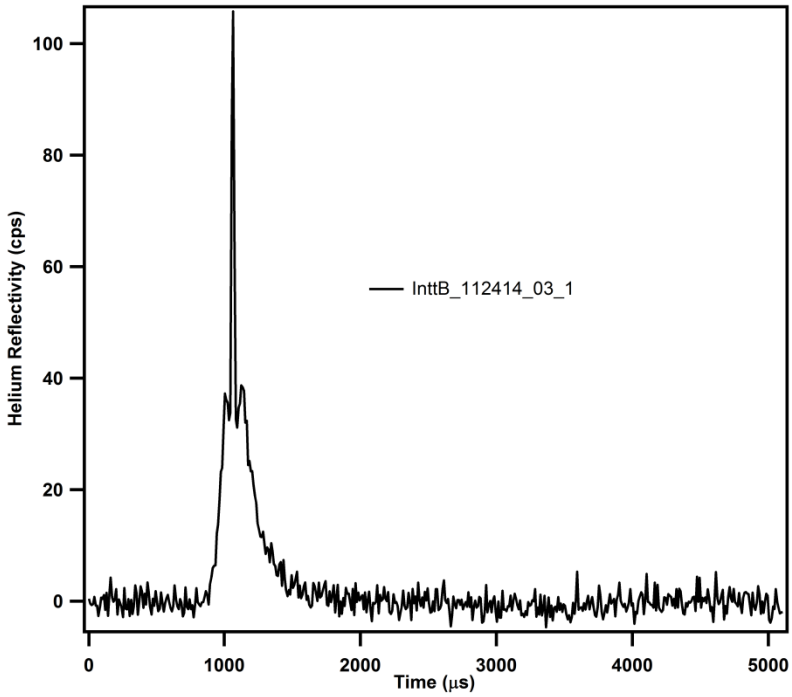

Raw He/CH_3-Ge(111) inelastic time-of-flight spectrum which contributes an experimental phonon point to the final dispersion curves in **Figure 4-6**. *Cross-correlation spectrum taken in long mode with a 200 K beam, 140 K surface temperature, Γ–M alignment, 32.2° incident angle, and 25.7° final angle.*

Experiment file: Figure 4-6.pxp

Raw data file: 112414.003

Figure A4-21

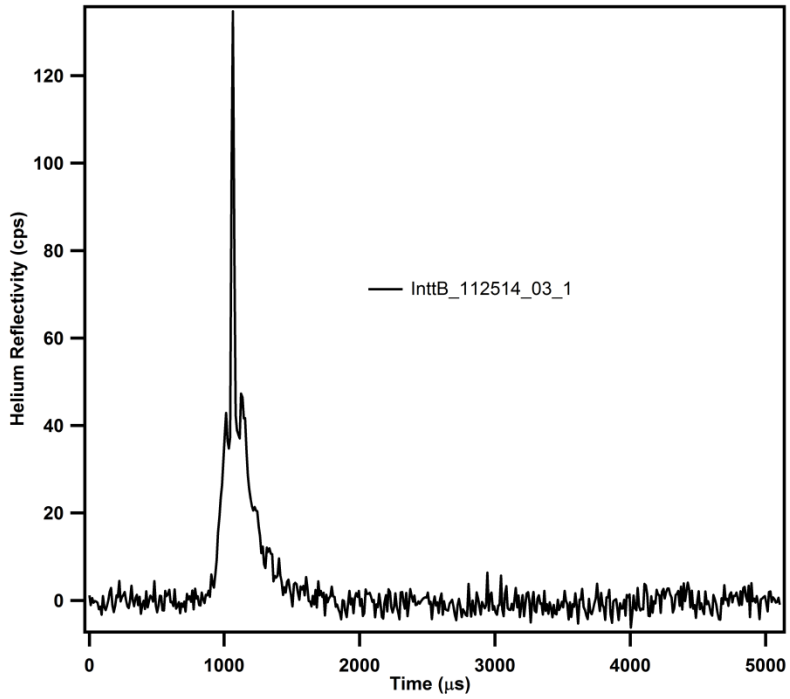

Raw He/CH_3-Ge(111) inelastic time-of-flight spectrum which contributes an experimental phonon point to the final dispersion curves in **Figure 4-6**. *Cross-correlation spectrum taken in long mode with a 200 K beam, 140 K surface temperature, Γ–M alignment, 32.2° incident angle, and 33.7° final angle.*

Experiment file: Figure 4-6.pxp

Raw data file: 112514.003

Figure A4-22

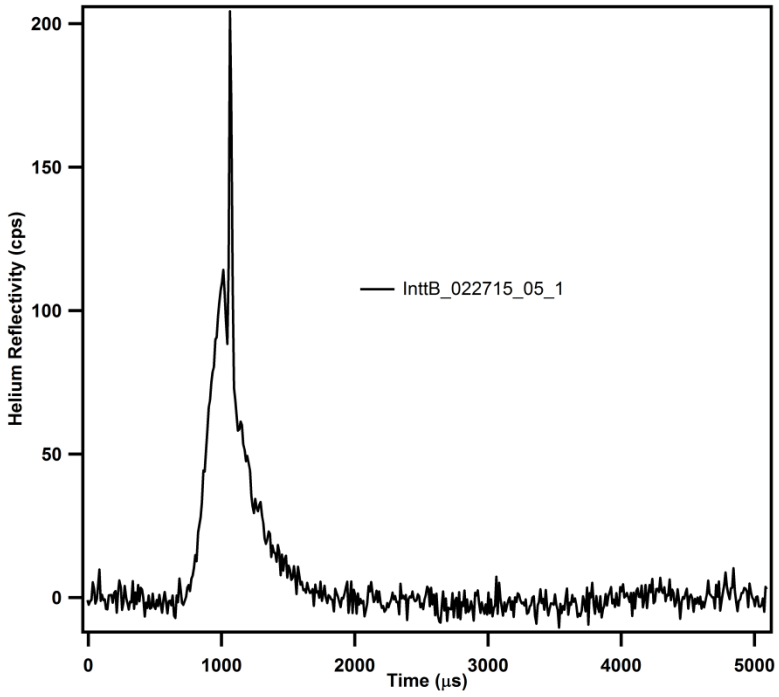

Raw He/CH_3-Ge(111) inelastic time-of-flight spectrum which contributes an experimental phonon point to the final dispersion curves in **Figure 4-6**. *Cross-correlation spectrum taken in short mode with a 100 K beam, 300 K surface temperature, Γ–M alignment, 32.2° incident angle, and 10.7° final angle.*

Experiment file: Figure 4-6.pxp

Raw data file: 022715.005

Figure A4-23

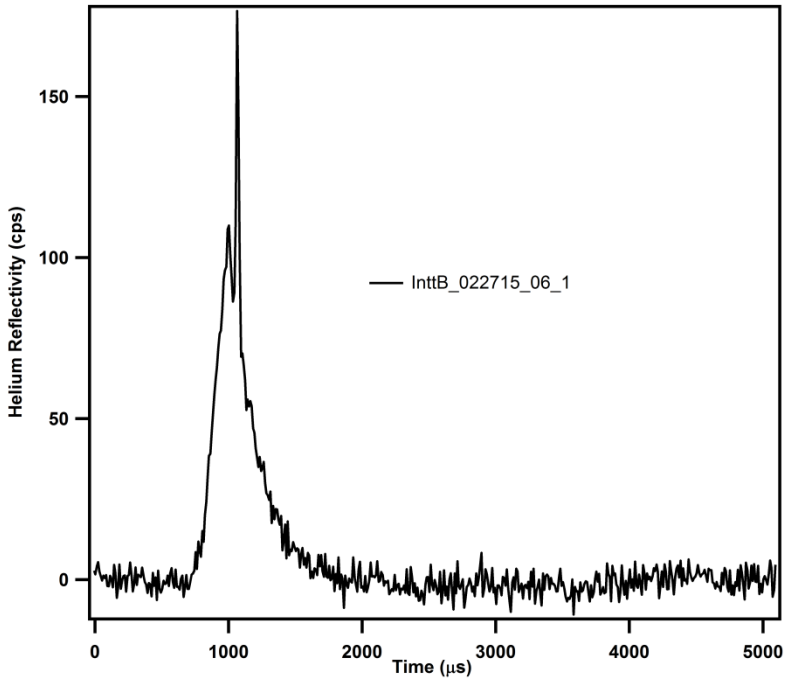

Raw He/CH_3-Ge(111) inelastic time-of-flight spectrum which contributes an experimental phonon point to the final dispersion curves in **Figure 4-6**. *Cross-correlation spectrum taken in short mode with a 100 K beam, 300 K surface temperature, Γ–M alignment, 32.2° incident angle, and 9.7° final angle.*

Experiment file: Figure 4-6.pxp

Raw data file: 022715.006

Figure A4-24

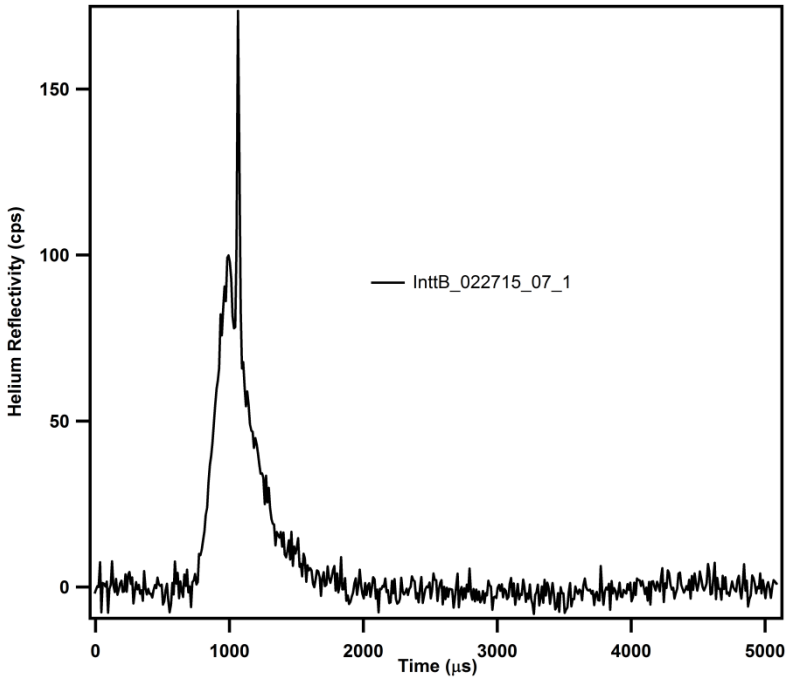

Raw He/CH_3-Ge(111) inelastic time-of-flight spectrum which contributes an experimental phonon point to the final dispersion curves in **Figure 4-6**. *Cross-correlation spectrum taken in short mode with a 100 K beam, 300 K surface temperature, Γ–M alignment, 32.2° incident angle, and 8.7° final angle.*

Experiment file: Figure 4-6.pxp

Raw data file: 022715.007

Figure A4-25

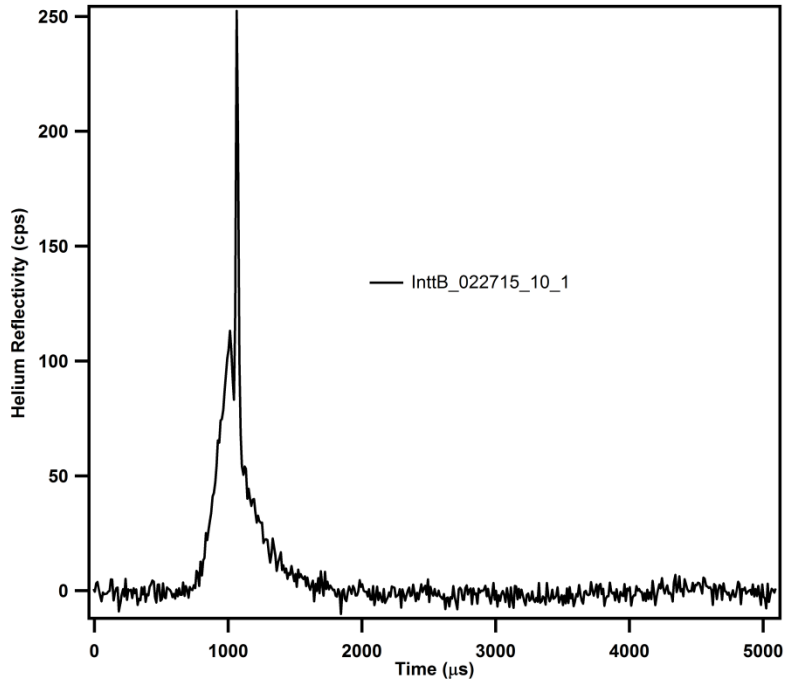

Raw He/CH_3-Ge(111) inelastic time-of-flight spectrum which contributes an experimental phonon point to the final dispersion curves in **Figure 4-6**. *Cross-correlation spectrum taken in short mode with a 100 K beam, 300 K surface temperature, Γ–M alignment, 32.2° incident angle, and 27.2° final angle.*

Experiment file: Figure 4-6.pxp

Raw data file: 022715.010

Figure A4-26

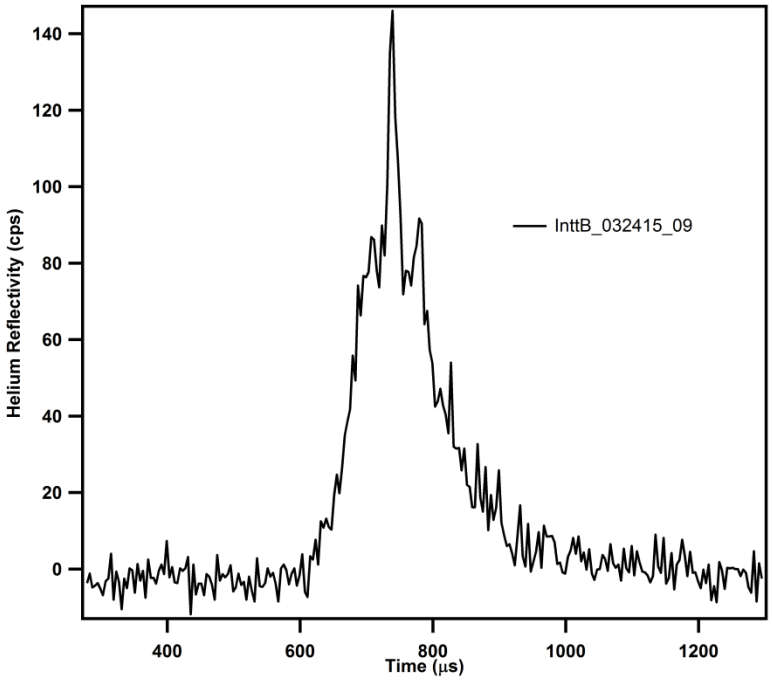

Raw He/CH_3-Ge(111) inelastic time-of-flight spectrum which contributes an experimental phonon point to the final dispersion curves in **Figure 4-6**. *Cross-correlation spectrum taken in short mode with a 200 K beam, 140 K surface temperature, Γ–M alignment, 32.2° incident angle, and 24.2° final angle.*

Experiment file: Figure 4-6.pxp

Raw data file: 032415.009

Figure A4-27

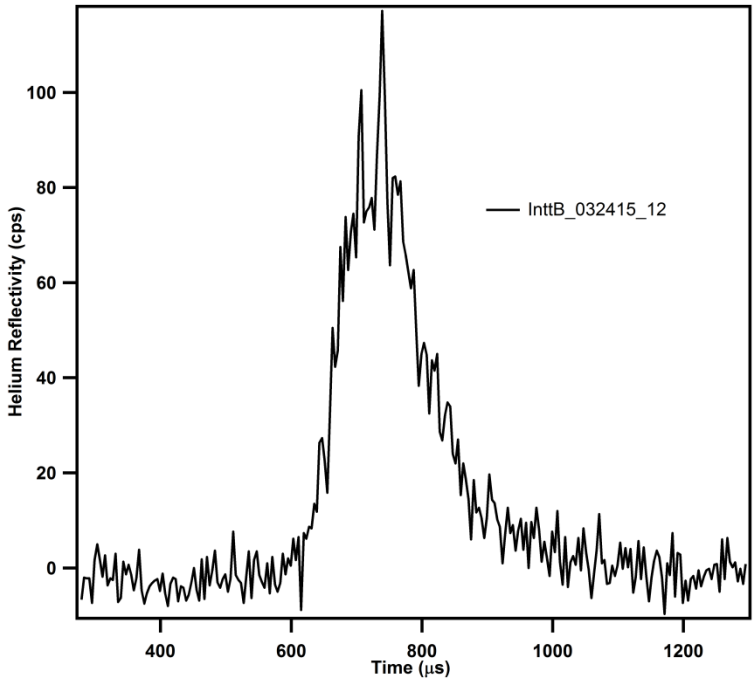

Raw He/CH_3-Ge(111) inelastic time-of-flight spectrum which contributes an experimental phonon point to the final dispersion curves in **Figure 4-6**. *Cross-correlation spectrum taken in short mode with a 200 K beam, 300 K surface temperature, Γ–M alignment, 32.2° incident angle, and 24.2° final angle.*

Experiment file: Figure 4-6.pxp

Raw data file: 032415.012

Figure A4-28

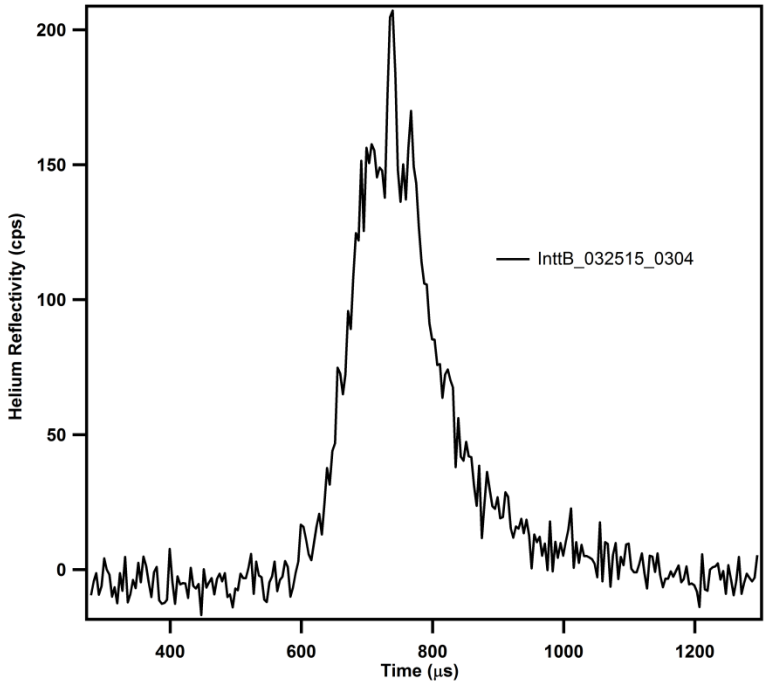

Raw He/CH_3-Ge(111) inelastic time-of-flight spectrum which contributes an experimental phonon point to the final dispersion curves in **Figure 4-6**. *Cross-correlation spectrum taken in short mode with a 200 K beam, 300 K surface temperature, Γ–M alignment, 32.2° incident angle, and 23.2° final angle.*

Experiment file: Figure 4-6.pxp

Raw data file: 032515.003; 032515.004

Figure A4-29

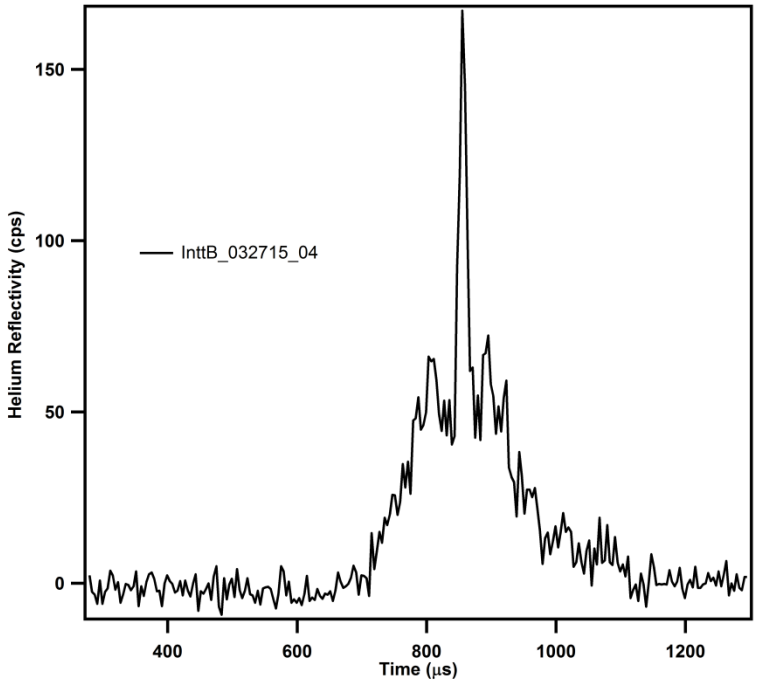

Raw He/CH_3-Ge(111) inelastic time-of-flight spectrum which contributes an experimental phonon point to the final dispersion curves in **Figure 4-6**. *Cross-correlation spectrum taken in short mode with a 150 K beam, 250 K surface temperature, Γ–M alignment, 36.2° incident angle, and 25.7° final angle.*

Experiment file: Figure 4-6.pxp

Raw data file: 032715.004

Figure A4-30

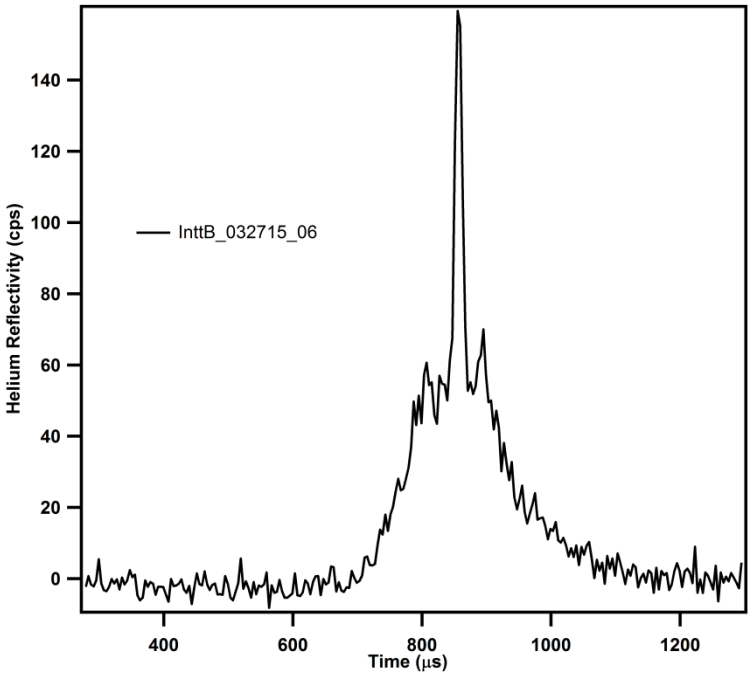

Raw He/CH_3-Ge(111) inelastic time-of-flight spectrum which contributes an experimental phonon point to the final dispersion curves in **Figure 4-6**. *Cross-correlation spectrum taken in short mode with a 150 K beam, 250 K surface temperature, Γ–M alignment, 36.2° incident angle, and 25.2° final angle.*

Experiment file: Figure 4-6.pxp

Raw data file: 032715.006

Figure A4-31

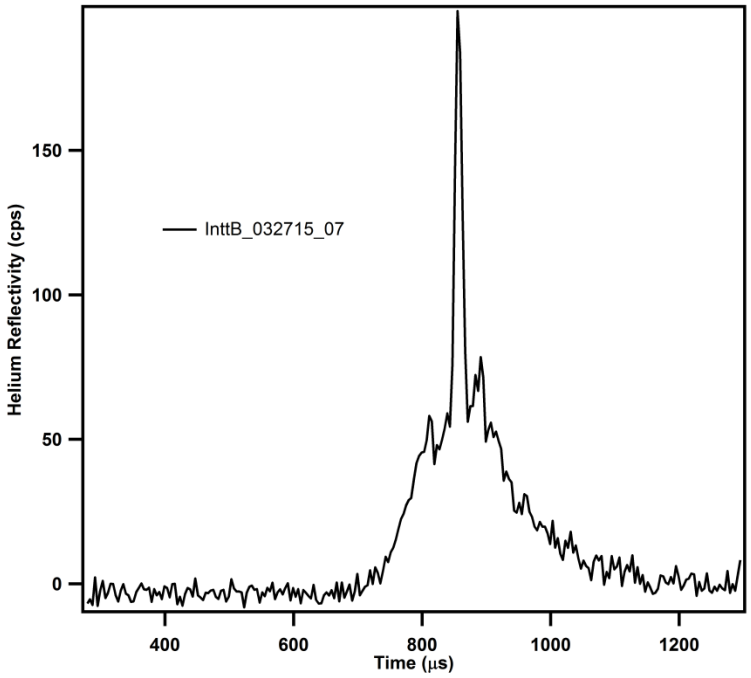

Raw He/CH_3-Ge(111) inelastic time-of-flight spectrum which contributes an experimental phonon point to the final dispersion curves in **Figure 4-6**. *Cross-correlation spectrum taken in short mode with a 150 K beam, 200 K surface temperature, Γ–M alignment, 36.2° incident angle, and 25.2° final angle.*

Experiment file: Figure 4-6.pxp

Raw data file: 032715.007

Figure A4-32

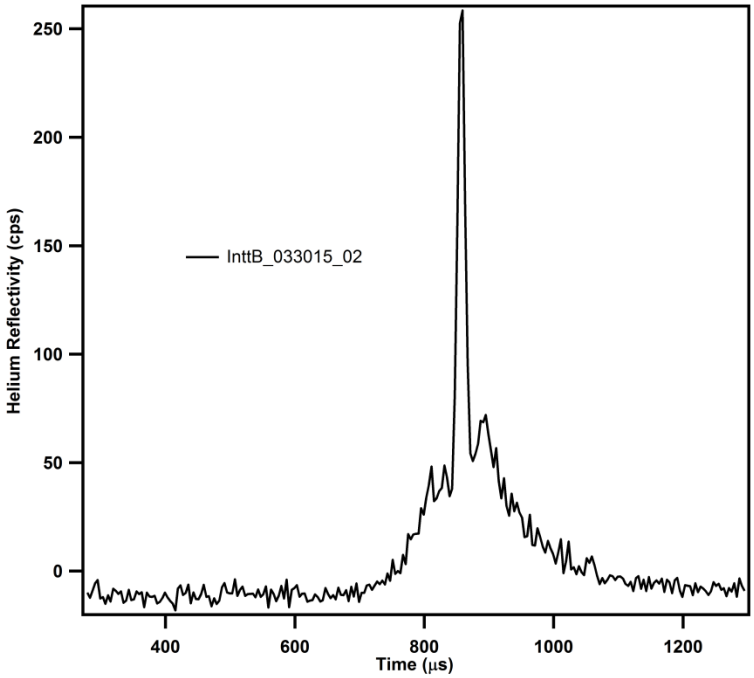

Raw He/CH_3-Ge(111) inelastic time-of-flight spectrum which contributes an experimental phonon point to the final dispersion curves in **Figure 4-6**. *Cross-correlation spectrum taken in short mode with a 150 K beam, 160 K surface temperature, Γ–M alignment, 36.2° incident angle, and 25.2° final angle.*

Experiment file: Figure 4-6.pxp

Raw data file: 033015.002

Figure A4-33

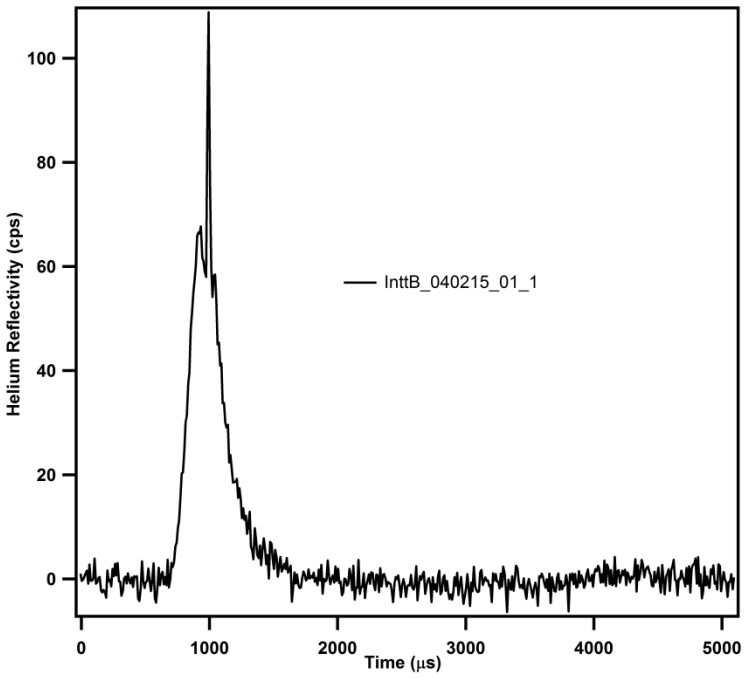

Raw He/CH_3-Ge(111) inelastic time-of-flight spectrum which contributes an experimental phonon point to the final dispersion curves in **Figure 4-6**. *Cross-correlation spectrum taken in short mode with a 115 K beam, 350 K surface temperature, Γ–M alignment, 36.2° incident angle, and 23.7° final angle.*

Experiment file: Figure 4-6.pxp

Raw data file: 040215.001

Figure A4-34

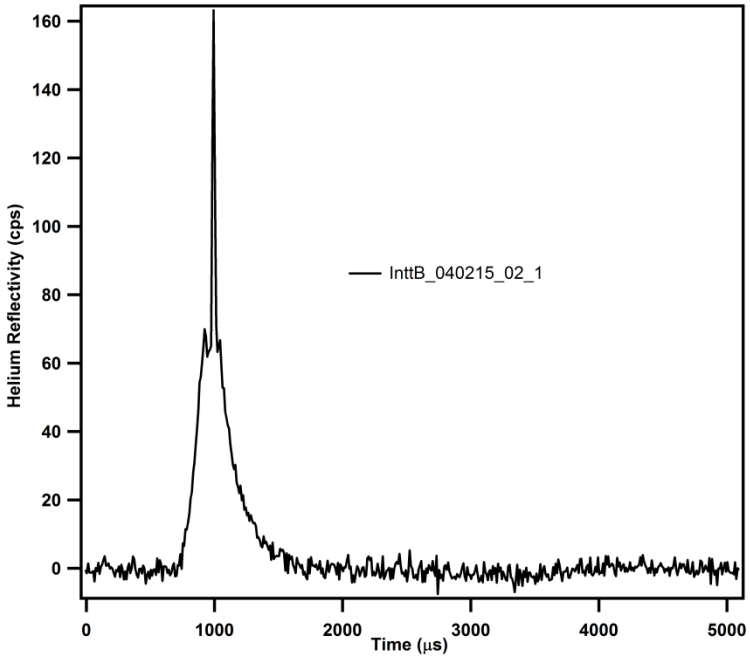

Raw He/CH_3-Ge(111) inelastic time-of-flight spectrum which contributes an experimental phonon point to the final dispersion curves in **Figure 4-6**. *Cross-correlation spectrum taken in short mode with a 115 K beam, 250 K surface temperature, Γ–M alignment, 36.2° incident angle, and 23.7° final angle.*

Experiment file: Figure 4-6.pxp

Raw data file: 040215.002

Figure A4-35

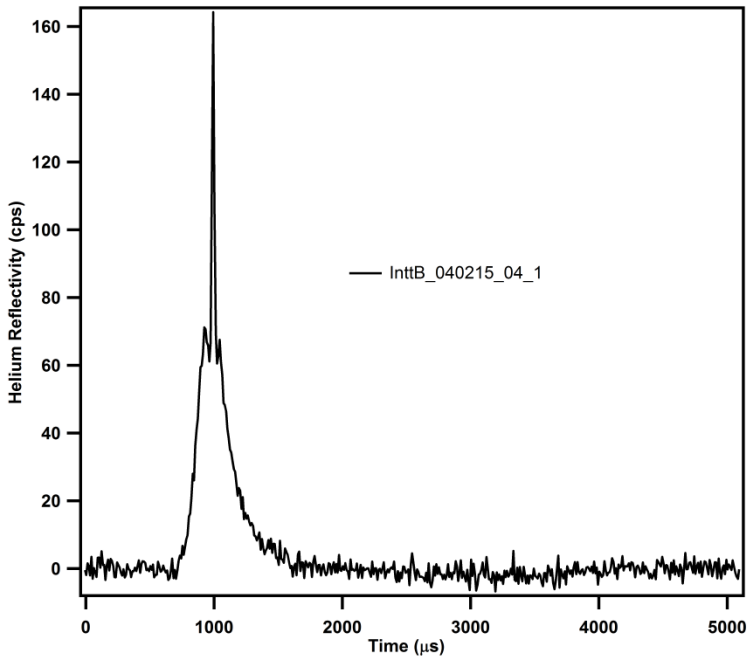

Raw He/CH_3-Ge(111) inelastic time-of-flight spectrum which contributes an experimental phonon point to the final dispersion curves in **Figure 4-6**. *Cross-correlation spectrum taken in short mode with a 115 K beam, 250 K surface temperature, Γ–M alignment, 36.2° incident angle, and 23.7° final angle.*

Experiment file: Figure 4-6.pxp

Raw data file: 040215.004

Figure A4-36

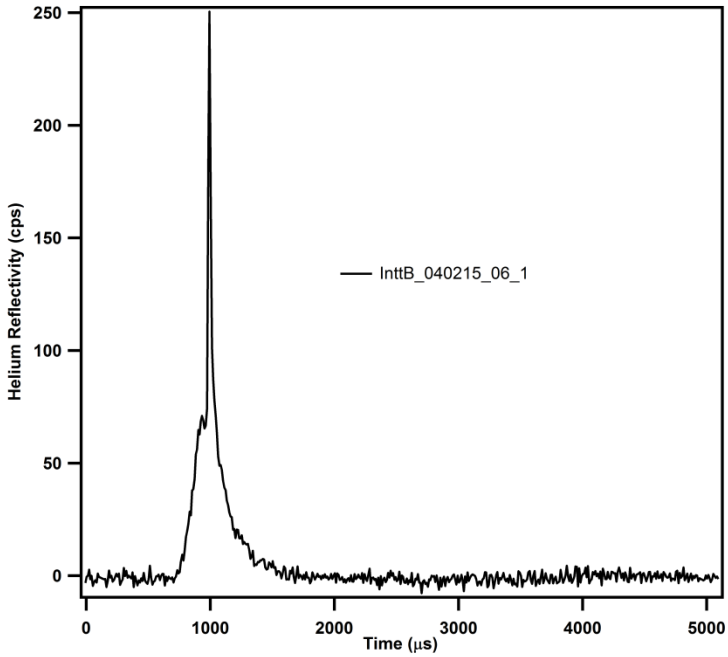

Raw He/CH_3-Ge(111) inelastic time-of-flight spectrum which contributes an experimental phonon point to the final dispersion curves in **Figure 4-6**. *Cross-correlation spectrum taken in short mode with a 115 K beam, 250 K surface temperature, Γ–M alignment, 36.2° incident angle, and 21.7° final angle.*

Experiment file: Figure 4-6.pxp

Raw data file: 040215.006

Figure A4-37

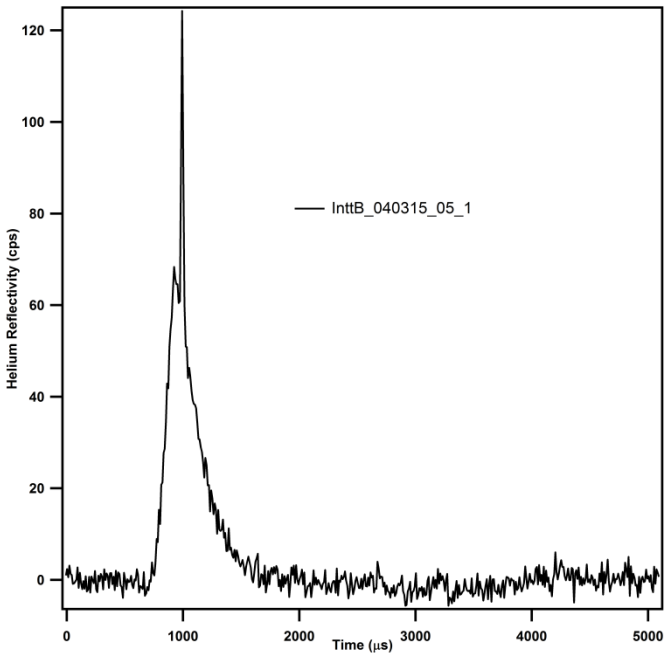

Raw He/CH_3-Ge(111) inelastic time-of-flight spectrum which contributes an experimental phonon point to the final dispersion curves in **Figure 4-6**. *Cross-correlation spectrum taken in short mode with a 115 K beam, 250 K surface temperature, Γ–K alignment, 36.2° incident angle, and 18.2° final angle.*

Experiment file: Figure 4-6.pxp

Raw data file: 040315.005

Figure A4-38

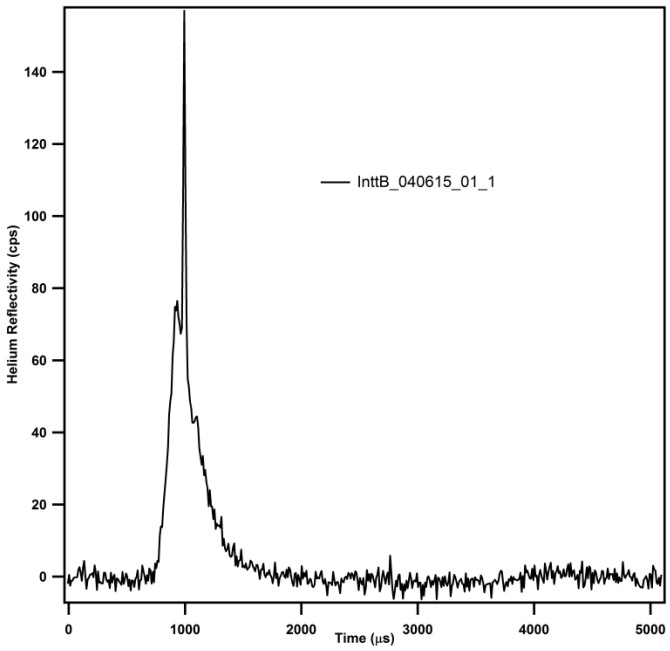

Raw He/CH_3-Ge(111) inelastic time-of-flight spectrum which contributes an experimental phonon point to the final dispersion curves in **Figure 4-6**. *Cross-correlation spectrum taken in short mode with a 115 K beam, 250 K surface temperature, Γ–K alignment, 36.2° incident angle, and 27.2° final angle.*

Experiment file: Figure 4-6.pxp

Raw data file: 040615.001

Figure A4-39

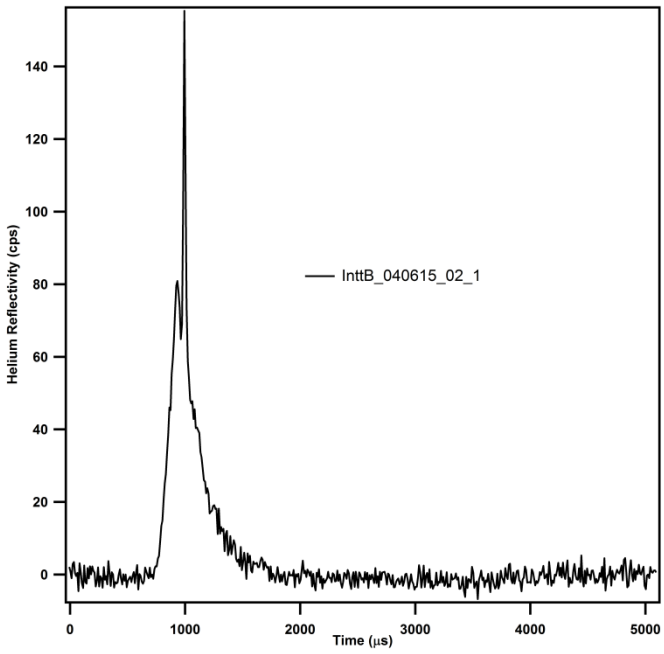

Raw He/CH_3-Ge(111) inelastic time-of-flight spectrum which contributes an experimental phonon point to the final dispersion curves in **Figure 4-6**. *Cross-correlation spectrum taken in short mode with a 115 K beam, 250 K surface temperature, Γ–K alignment, 36.2° incident angle, and 28.2° final angle.*

Experiment file: Figure 4-6.pxp

Raw data file: 040615.002

Figure A4-40

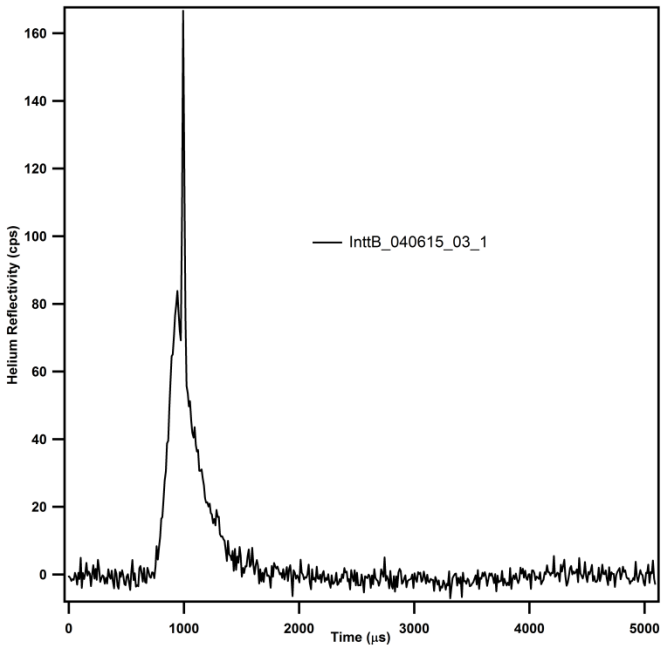

Raw He/CH_3-Ge(111) inelastic time-of-flight spectrum which contributes an experimental phonon point to the final dispersion curves in **Figure 4-6**. *Cross-correlation spectrum taken in short mode with a 115 K beam, 250 K surface temperature, Γ–K alignment, 36.2° incident angle, and 29.2° final angle.*

Experiment file: Figure 4-6.pxp

Raw data file: 040615.003

Figure A4-41

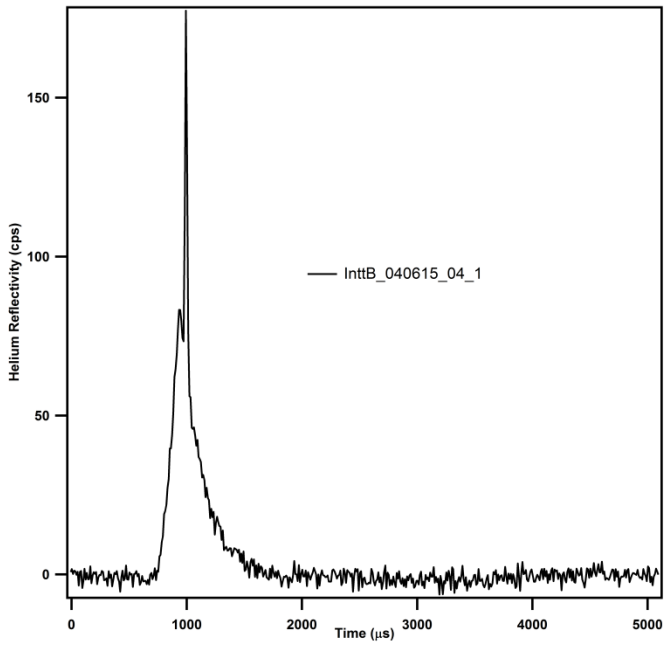

Raw He/CH_3-Ge(111) inelastic time-of-flight spectrum which contributes an experimental phonon point to the final dispersion curves in **Figure 4-6**. *Cross-correlation spectrum taken in short mode with a 115 K beam, 250 K surface temperature, Γ–K alignment, 36.2° incident angle, and 30.2° final angle.*

Experiment file: Figure 4-6.pxp

Raw data file: 040615.004

Figure A4-42

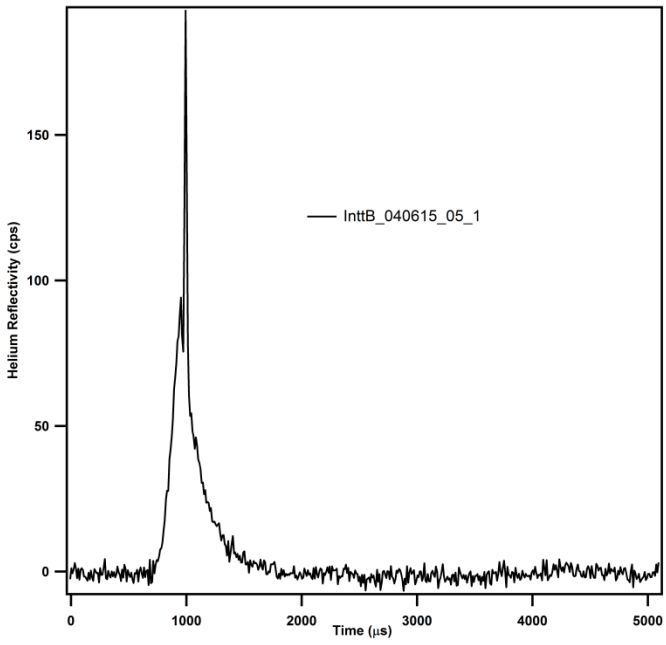

Raw He/CH_3-Ge(111) inelastic time-of-flight spectrum which contributes an experimental phonon point to the final dispersion curves in **Figure 4-6**. *Cross-correlation spectrum taken in short mode with a 115 K beam, 250 K surface temperature, Γ–K alignment, 36.2° incident angle, and 31.2° final angle.*

Experiment file: Figure 4-6.pxp

Raw data file: 040615.005

Figure A4-43

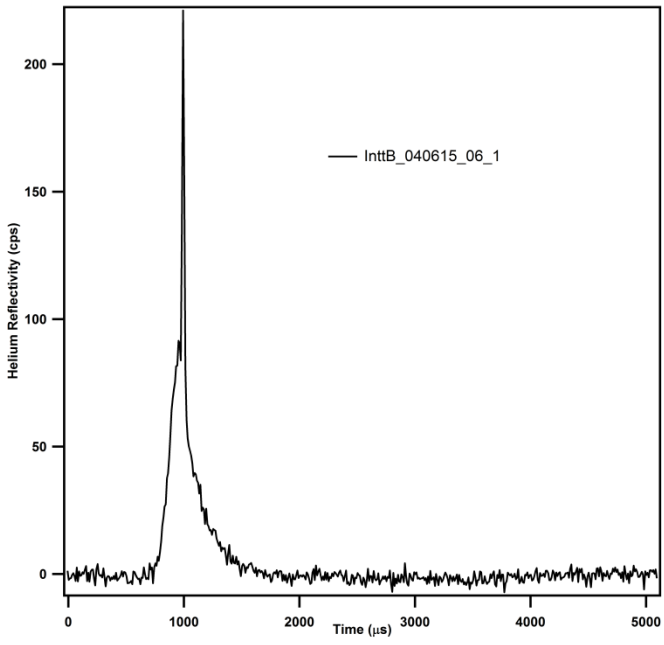

Raw He/CH_3-Ge(111) inelastic time-of-flight spectrum which contributes an experimental phonon point to the final dispersion curves in **Figure 4-6**. *Cross-correlation spectrum taken in short mode with a 115 K beam, 250 K surface temperature, Γ–K alignment, 36.2° incident angle, and 32.2° final angle.*

Experiment file: Figure 4-6.pxp

Raw data file: 040615.006

Figure A4-44

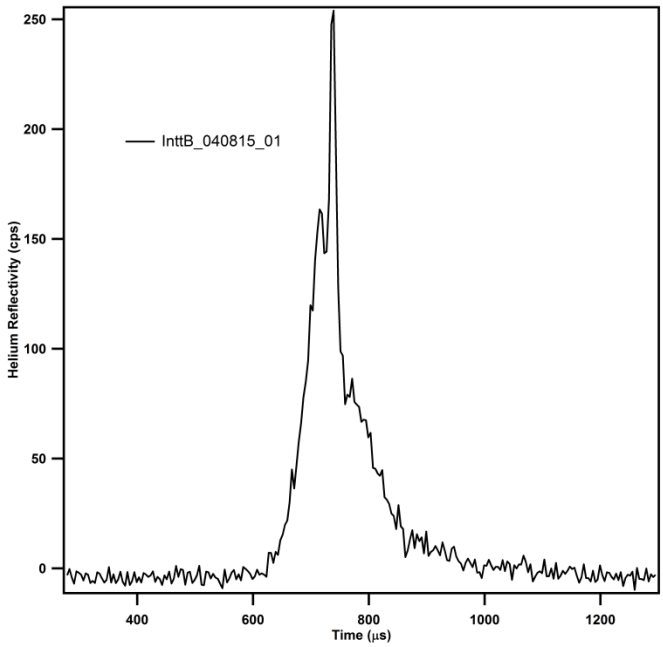

Raw He/CH_3-Ge(111) inelastic time-of-flight spectrum which contributes an experimental phonon point to the final dispersion curves in **Figure 4-6**. *Cross-correlation spectrum taken in short mode with a 200 K beam, 250 K surface temperature, Γ–K alignment, 36.2° incident angle, and 32.2° final angle.*

Experiment file: Figure 4-6.pxp

Raw data file: 040815.001

Figure A4-45

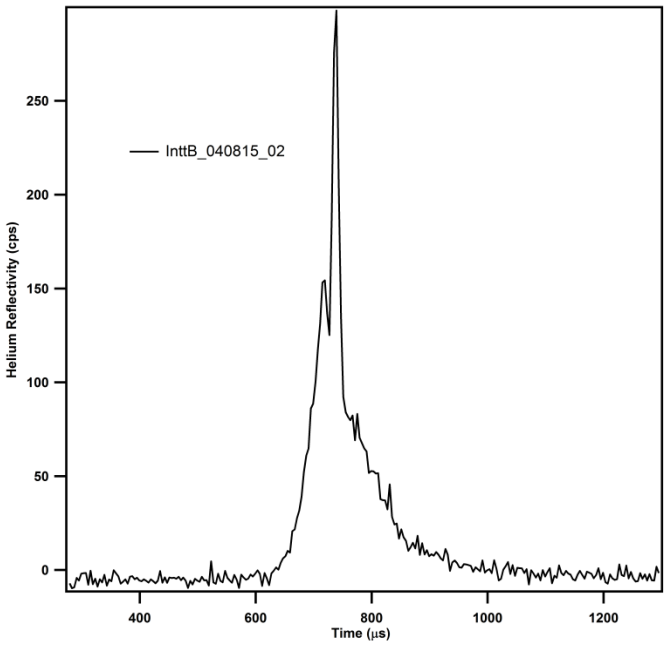

Raw He/CH_3-Ge(111) inelastic time-of-flight spectrum which contributes an experimental phonon point to the final dispersion curves in **Figure 4-6**. *Cross-correlation spectrum taken in short mode with a 200 K beam, 200 K surface temperature, Γ–K alignment, 36.2° incident angle, and 32.2° final angle.*

Experiment file: Figure 4-6.pxp

Raw data file: 040815.002

Figure A4-46

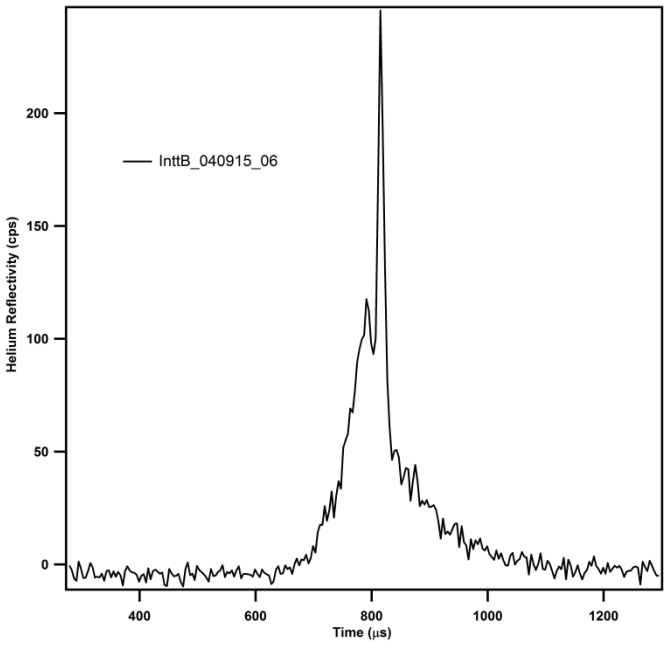

Raw He/CH_3-Ge(111) inelastic time-of-flight spectrum which contributes an experimental phonon point to the final dispersion curves in **Figure 4-6**. *Cross-correlation spectrum taken in short mode with a 165 K beam, 250 K surface temperature, Γ–K alignment, 36.2° incident angle, and 32.2° final angle.*

Experiment file: Figure 4-6.pxp

Raw data file: 040915.006

Figure A4-47

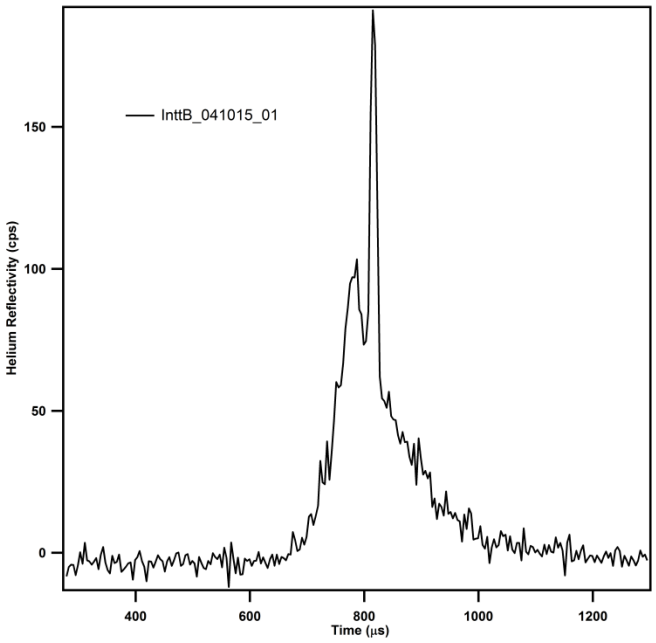

Raw He/CH_3-Ge(111) inelastic time-of-flight spectrum which contributes an experimental phonon point to the final dispersion curves in **Figure 4-6**. *Cross-correlation spectrum taken in short mode with a 165 K beam, 250 K surface temperature, Γ–K alignment, 36.2° incident angle, and 30.2° final angle.*

Experiment file: Figure 4-6.pxp

Raw data file: 041015.001

Figure A4-48

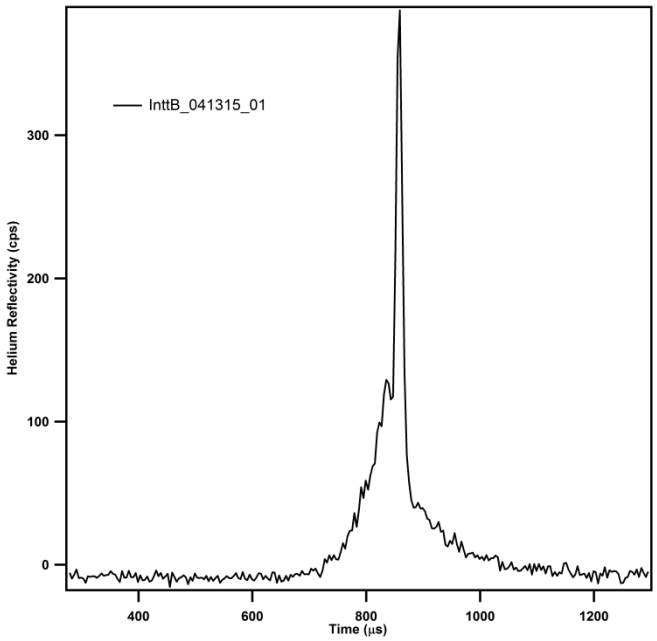

Raw He/CH_3-Ge(111) inelastic time-of-flight spectrum which contributes an experimental phonon point to the final dispersion curves in **Figure 4-6**. *Cross-correlation spectrum taken in short mode with a 150 K beam, 250 K surface temperature, Γ–K alignment, 36.2° incident angle, and 33.2° final angle.*

Experiment file: Figure 4-6.pxp

Raw data file: 041315.001

Figure A4-49

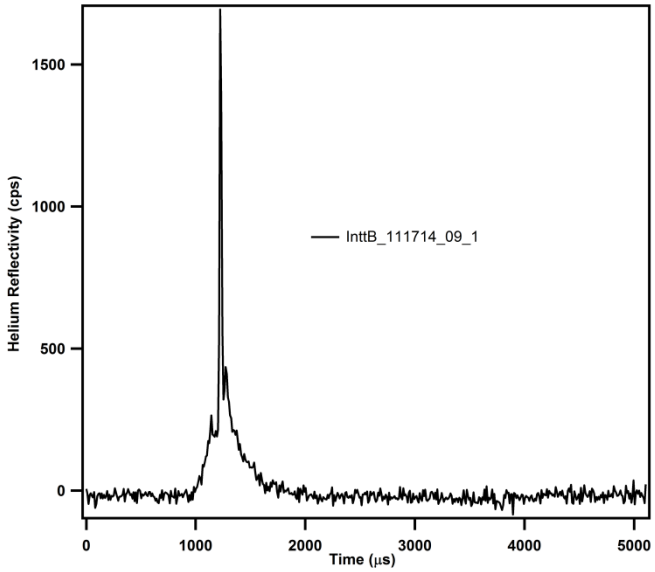

Raw He/CH_3-Ge(111) inelastic time-of-flight spectrum which contributes an experimental phonon point to the final dispersion curves in **Figure 4-6**. *Cross-correlation spectrum taken in long mode with a 150 K beam, 140 K surface temperature, Γ–M alignment, 35.2° incident angle, and 23.2° final angle.*

Experiment file: Figure 4-6.pxp

Raw data file: 111714.009

Figure A4-50

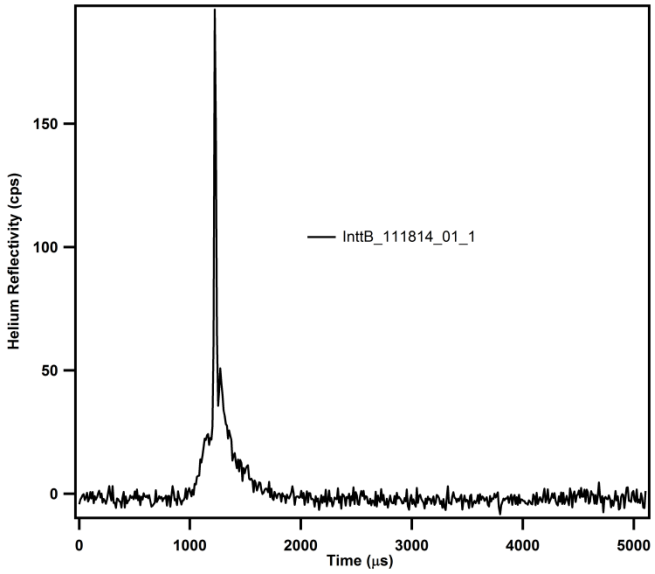

Raw He/CH_3-Ge(111) inelastic time-of-flight spectrum which contributes an experimental phonon point to the final dispersion curves in **Figure 4-6**. *Cross-correlation spectrum taken in long mode with a 150 K beam, 140 K surface temperature, Γ–M alignment, 35.2° incident angle, and 23.2° final angle.*

Experiment file: Figure 4-6.pxp

Raw data file: 111814.001

Figure A5-1

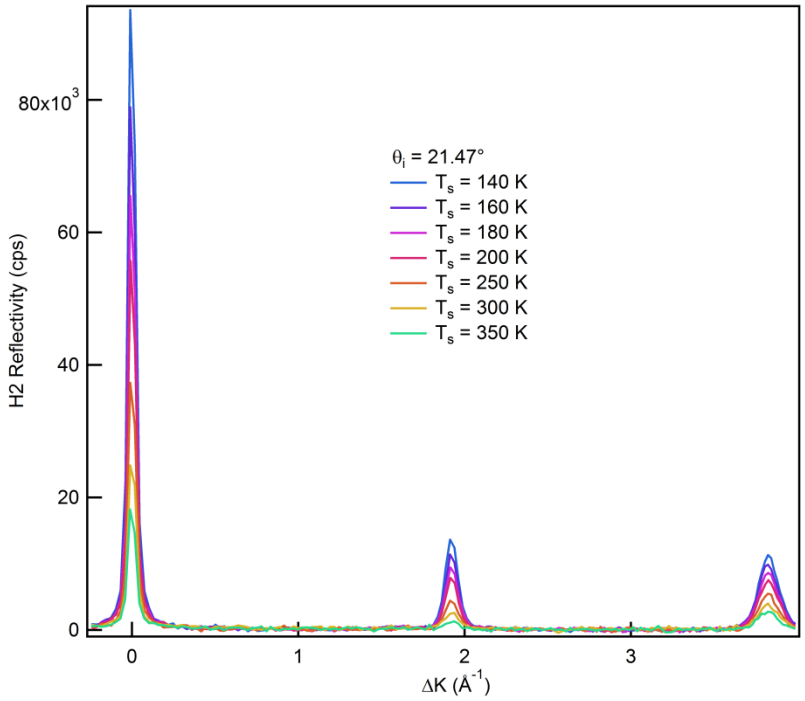

Raw H_2/CH_3-Si(111) diffraction spectra at different surface temperatures and incident angle θ_i=21.47°; fitted peak areas for each temperature correspond to a point used in **Figure 5-6(b).**

Experiment file: 071113_D08-D14.pxp

Raw data file: 071113.D08; 071113.D09; 071113.D10; 071113.D11; 071113.D12; 071113.D13; 071113.D14

Figure A5-2

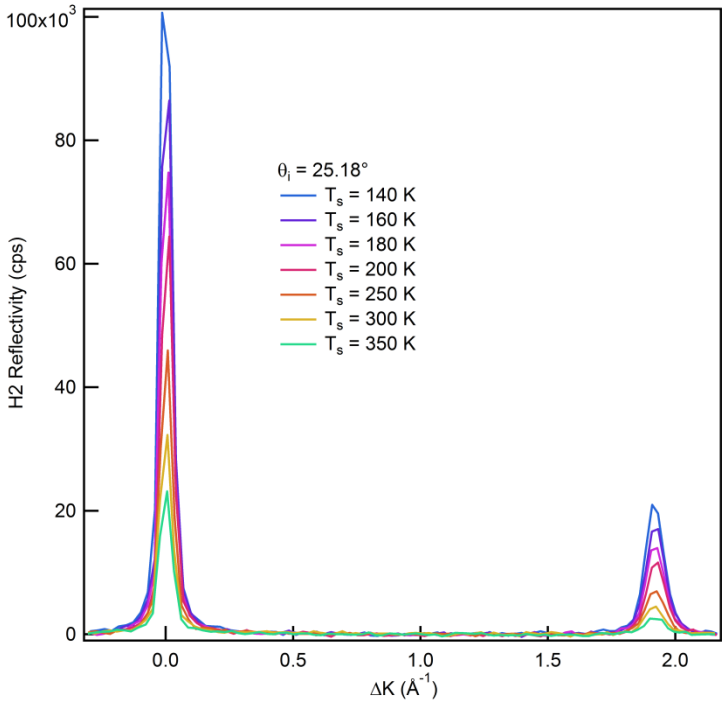

Raw H_2/CH_3-Si(111) diffraction spectra at different surface temperatures and incident angle θ_i=25.18°; fitted peak areas for each temperature correspond to a point used in **Figure 5-6(b).**

Experiment file: 071113_D01-D07.pxp

Raw data file: 071113.D01; 071113.D02; 071113.D03; 071113.D04; 071113.D05; 071113.D06; 071113.D07

Figure A5-3

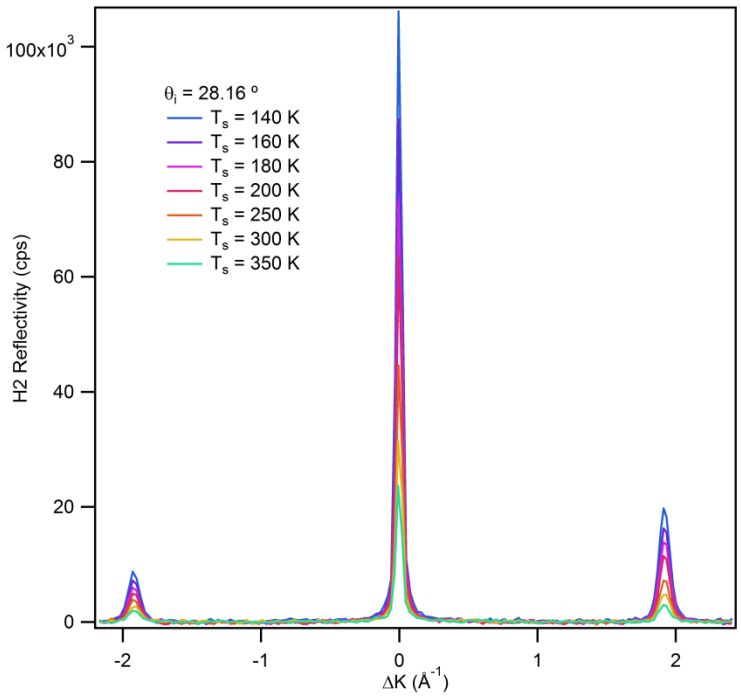

Raw H_2/CH_3-Si(111) diffraction spectra at different surface temperatures and incident angle θ_i=28.16°; fitted peak areas for each temperature correspond to a point used in **Figure 5-6(b).**

Experiment file: 071713_D01-D07.pxp

Raw data file: 071713.D01; 071713.D02; 071713.D03; 071713.D04; 071713.D05; 071713.D06; 071713.D07

Figure A5-4

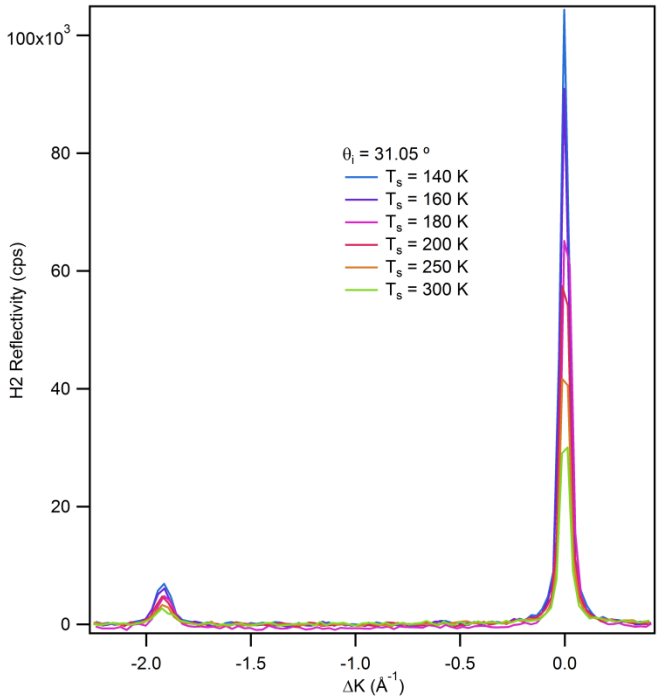

Raw H_2/CH_3-Si(111) diffraction spectra at different surface temperatures and incident angle θ_i=31.05°; fitted peak areas for each temperature correspond to a point used in **Figure 5-6(b).**

Experiment file: 071613_D08-D14.pxp

Raw data file: 071613.D08; 071613.D09; 071613.D10; 071613.D11; 071613.D12; 071613.D13; 071613.D14

Figure A5-5

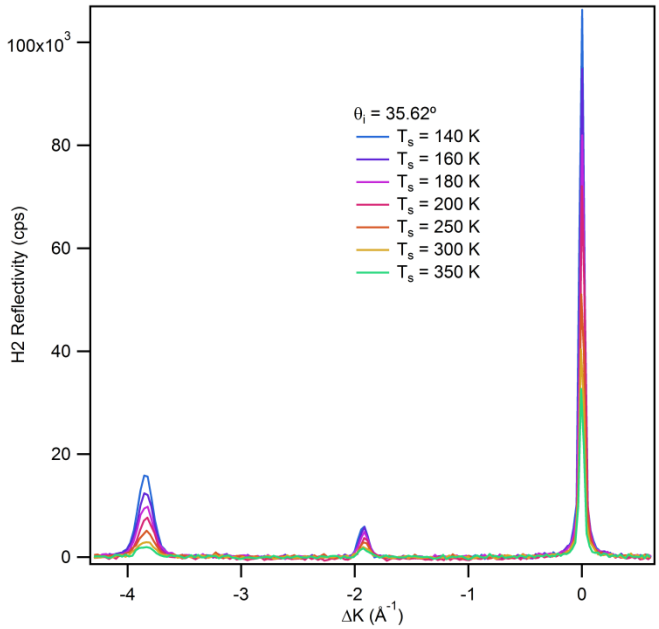

Raw H_2/CH_3-Si(111) diffraction spectra at different surface temperatures and incident angle θ_i=35.62°; fitted peak areas for each temperature correspond to a point used in **Figure 5-6(b).**

Experiment file: 071613_D01-D07.pxp

Raw data file: 071613.D01; 071613.D02; 071613.D03; 071613.D04; 071613.D05; 071613.D06; 071613.D07

Figure A5-6

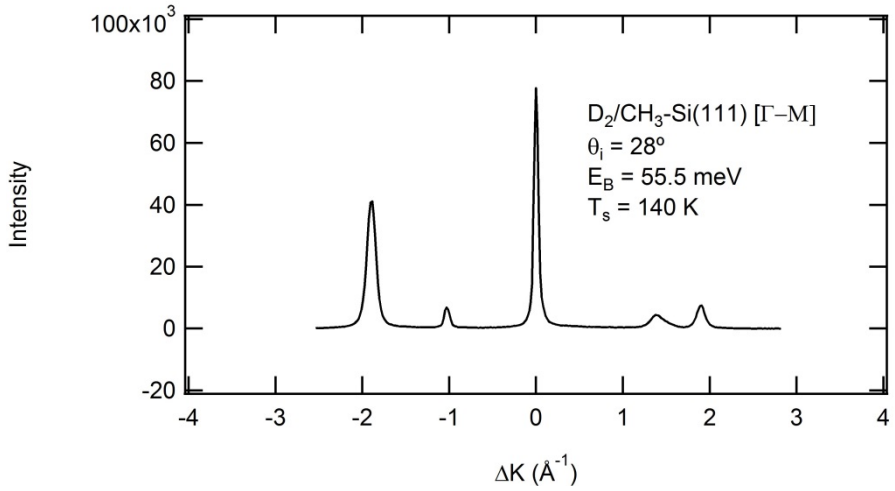

Raw D_2/CH_3-Si(111) diffraction spectrum; fitted peak areas for elastic and rotationally inelastic diffraction peaks input into equation (5-10) to compute a rotational excitation probability ratio, as displayed in **Figure 5-7**.

Experiment file: Figure A5-6 (031914_D01).pxp.

Raw data file: 031914.D01

Figure A5-7

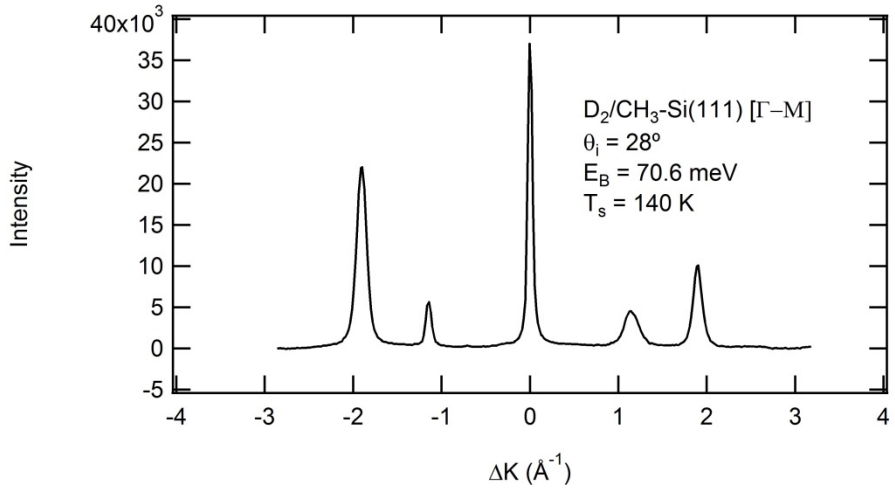

Raw D_2/CH_3-Si(111) diffraction spectrum; fitted peak areas for elastic and rotationally inelastic diffraction peaks input into equation (5-10) to compute a rotational excitation probability ratio, as displayed in **Figure 5-7**.

Experiment file: Figure A5-7 (031914_D02).pxp.

Raw data file: 031914.D02

Figure A5-8

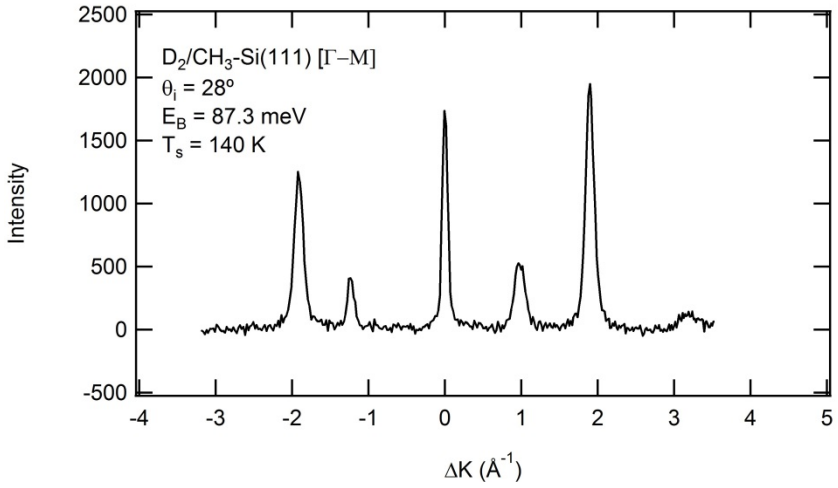

Raw D_2/CH_3-Si(111) diffraction spectrum; fitted peak areas for elastic and rotationally inelastic diffraction peaks input into equation (5-10) to compute a rotational excitation probability ratio, as displayed in **Figure 5-7**.

Experiment file: Figure A5-8 (061813_D02).pxp.

Raw data file: 061813.D02

Figure A5-9

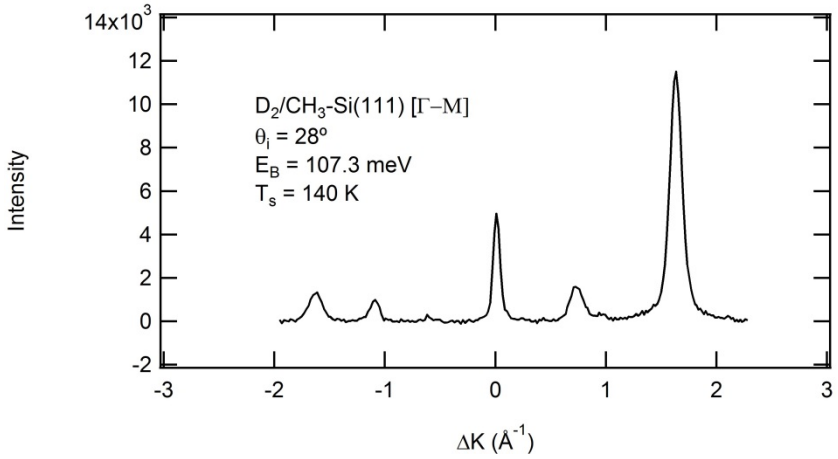

Raw D_2/CH_3-Si(111) diffraction spectrum; fitted peak areas for elastic and rotationally inelastic diffraction peaks input into equation (5-10) to compute a rotational excitation probability ratio, as displayed in **Figure 5-7**.

Experiment file: Figure A5-9 (031914_D06).pxp.

Raw data file: 031914.D06

Figure A5-10

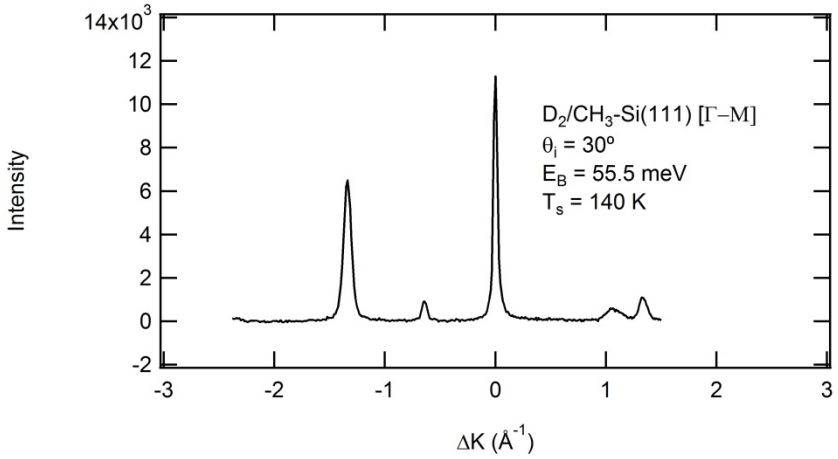

Raw D_2/CH_3-Si(111) diffraction spectrum; fitted peak areas for elastic and rotationally inelastic diffraction peaks input into equation (5-10) to compute a rotational excitation probability ratio, as displayed in **Figure 5-7**.

Experiment file: Figure A5-10 (062413_D02).pxp.

Raw data file: 062413.D02

Figure A5-11

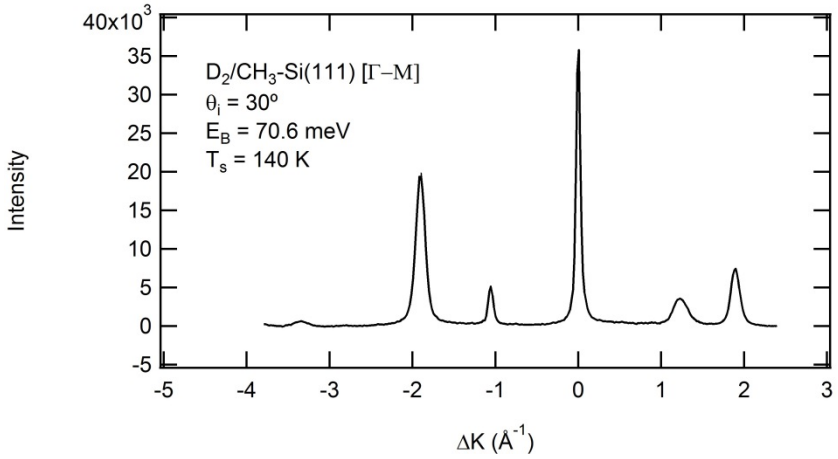

Raw D_2/CH_3-Si(111) diffraction spectrum; fitted peak areas for elastic and rotationally inelastic diffraction peaks input into equation (5-10) to compute a rotational excitation probability ratio, as displayed in **Figure 5-7**.

Experiment file: Figure A5-11 (031914_D03).pxp.

Raw data file: 031914.D03

Figure A5-12

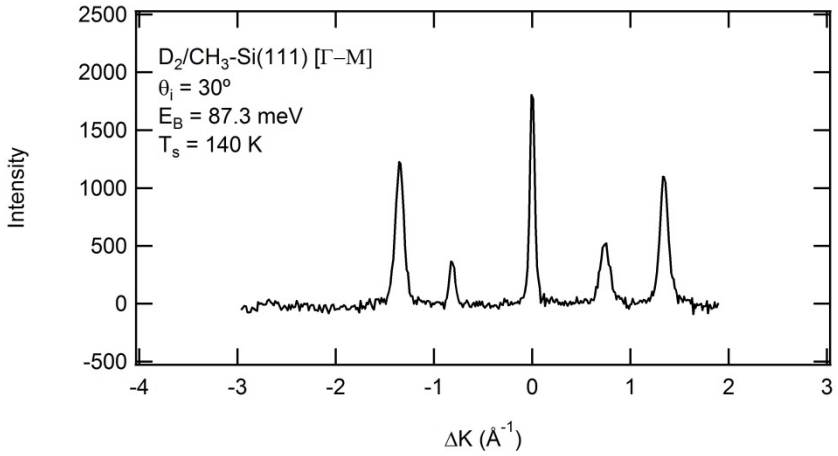

Raw D_2/CH_3-Si(111) diffraction spectrum; fitted peak areas for elastic and rotationally inelastic diffraction peaks input into equation (5-10) to compute a rotational excitation probability ratio, as displayed in **Figure 5-7**.

Experiment file: Figure A5-12 (061813_D03).pxp.

Raw data file: 061813.D03

Figure A5-13

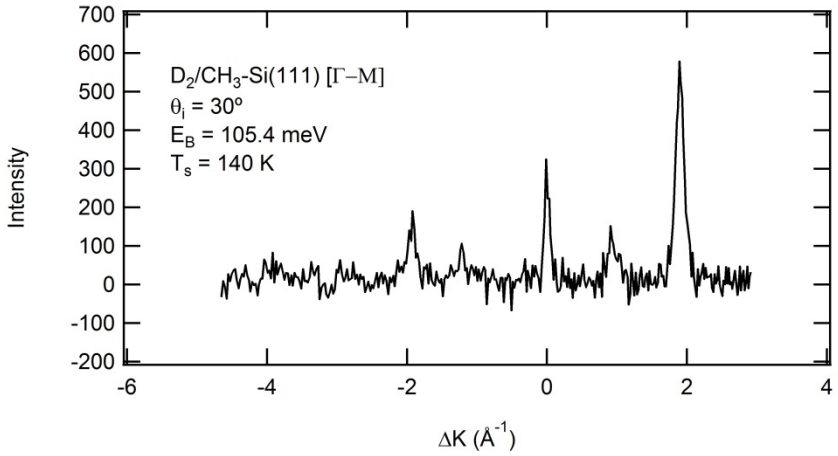

Raw D_2/CH_3-Si(111) diffraction spectrum; fitted peak areas for elastic and rotationally inelastic diffraction peaks input into equation (5-10) to compute a rotational excitation probability ratio, as displayed in **Figure 5-7**.

Experiment file: Figure A5-13 (070313_D02).pxp.

Raw data file: 070313.D02

Figure A5-14

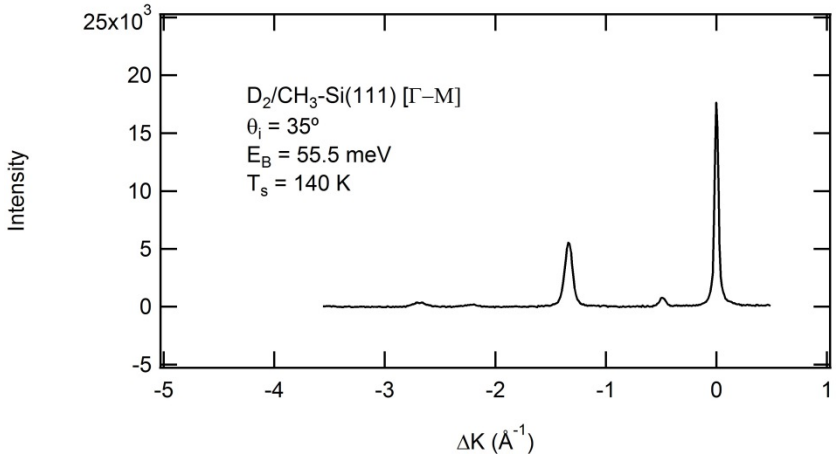

Raw D_2/CH_3-Si(111) diffraction spectrum; fitted peak areas for elastic and rotationally inelastic diffraction peaks input into equation (5-10) to compute a rotational excitation probability ratio, as displayed in **Figure 5-7**.

Experiment file: Figure A5-14 (062413_D03).pxp.

Raw data file: 062413.D03

Figure A5-15

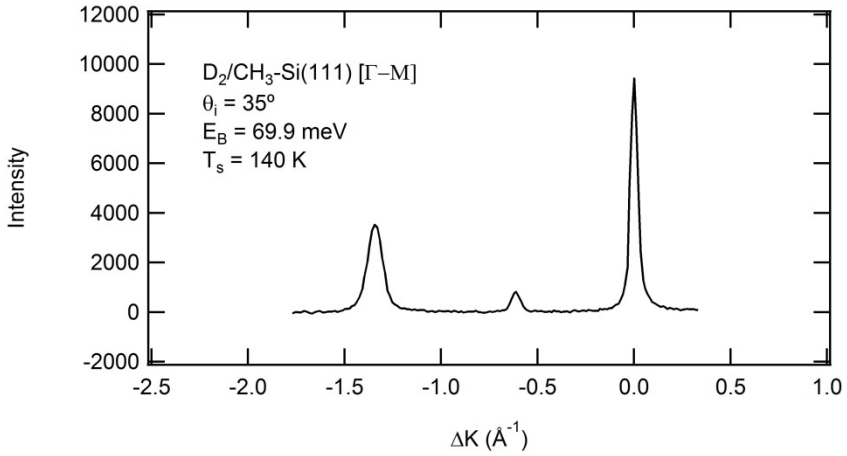

Raw D_2/CH_3-Si(111) diffraction spectrum; fitted peak areas for elastic and rotationally inelastic diffraction peaks input into equation (5-10) to compute a rotational excitation probability ratio, as displayed in **Figure 5-7**.

Experiment file: Figure A5-15 (062513_D01).pxp.

Raw data file: 062513.D01

Figure A5-16

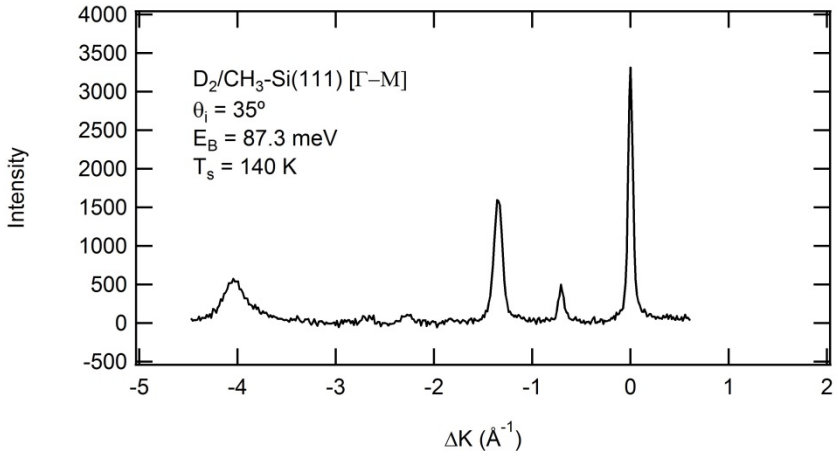

Raw D_2/CH_3-Si(111) diffraction spectrum; fitted peak areas for elastic and rotationally inelastic diffraction peaks input into equation (5-10) to compute a rotational excitation probability ratio, as displayed in **Figure 5-7**.

Experiment file: Figure A5-16 (061813_D05).pxp.

Raw data file: 061813.D05

Figure A5-17

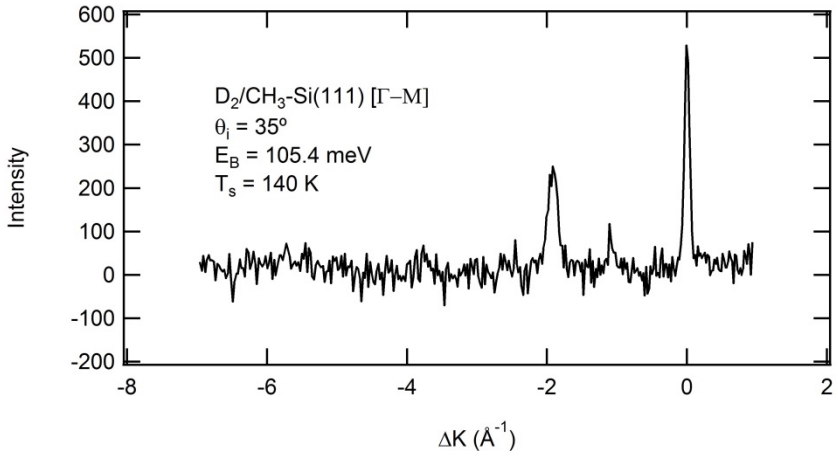

Raw D_2/CH_3-Si(111) diffraction spectrum; fitted peak areas for elastic and rotationally inelastic diffraction peaks input into equation (5-10) to compute a rotational excitation probability ratio, as displayed in **Figure 5-7**.

Experiment file: Figure A5-17 (070313_D03).pxp.

Raw data file: 070313.D03

Figure A7-1

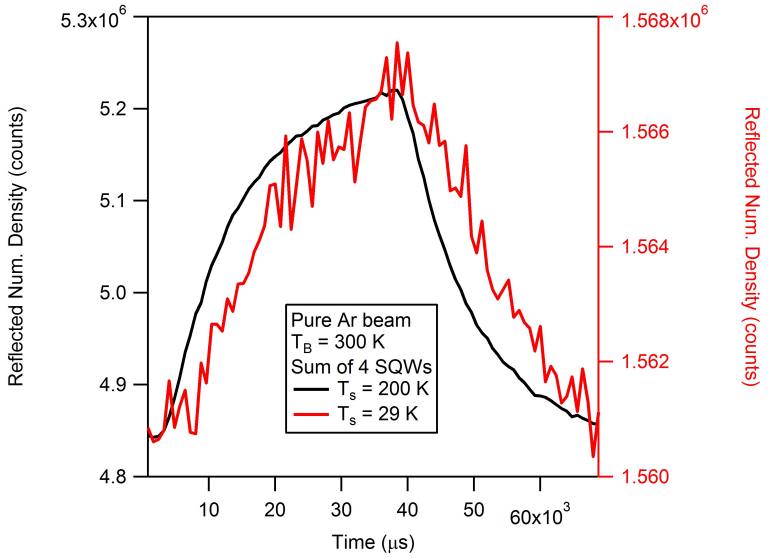

Square wave collected by residual gas analyzer, looking at reflectivity of ^{40}Ar from pure Ar beam (T_B = 300 K) above and below the condensation temperature. The ratio of modulated signal for these two spectra is used to calculate the sticking coefficient in **Figure 7-3**.

Experiment file: Figure A7-1.pxp.

Raw data files: 103117_01, 103117_03, 103117_04, 103117_06, 103117_07, 103117_08, 103117_09, 103117_10

Figure A7-2

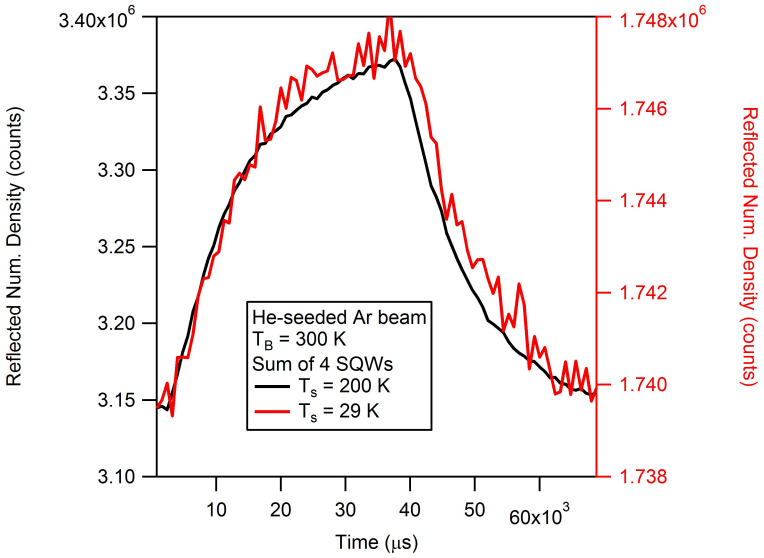

Square wave collected by residual gas analyzer, looking at reflectivity of ^{40}Ar from helium-seeded Ar beam (T_B = 300 K) above and below the condensation temperature. The ratio of modulated signal for these two spectra is used to calculate the sticking coefficient in **Figure 7-3**.

Experiment file: Figure A7-2.pxp.

Raw data files: 103117_11, 103117_12, 103117_13, 103117_14, 103117_15, 103117_16, 103117_17, 103117_18

Figure A7-3

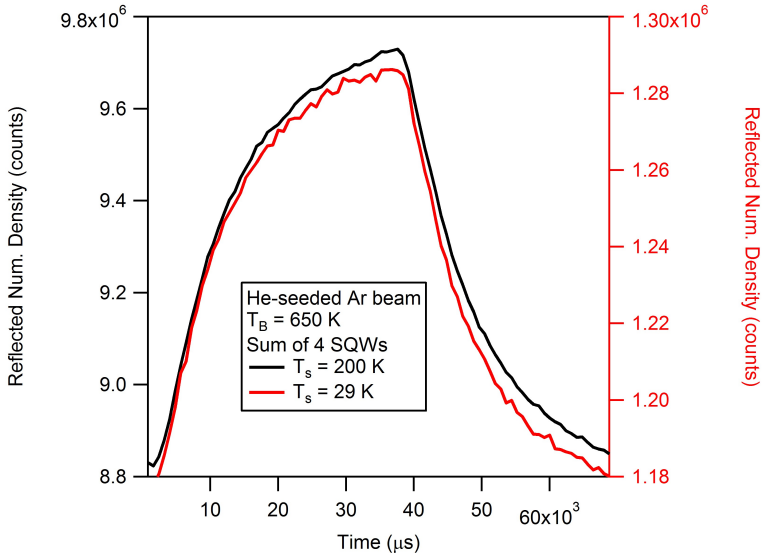

Square wave collected by residual gas analyzer, looking at reflectivity of ^{40}Ar from helium-seeded Ar beam (T_B = 650 K) above and below the condensation temperature. The ratio of modulated signal for these two spectra is used to calculate the sticking coefficient in **Figure 7-3**.

Experiment file: Figure A7-3.pxp.

Raw data files: 110317_15, 110317_16, 110317_17, 110317_18, 110317_19, 110317_20, 110317_21, 110317_22

Figure A7-4

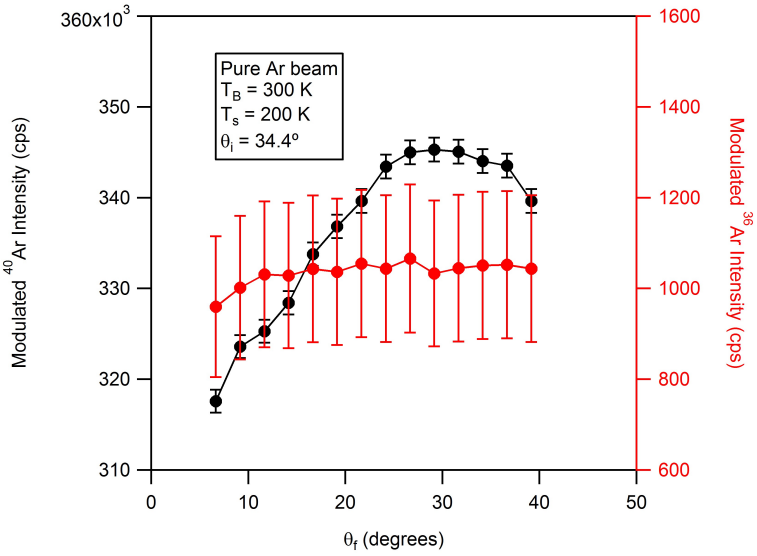

Modulated intensity of ^{40}Ar and ^{36}Ar over a range of scattered angles for a fixed set of incident conditions. The ratio of these spectra is used in **Figure 7-4.**

Experiment file: Figure A7-4.pxp.

Raw data files: 030917.D04, 030917.D05

Figure A7-5

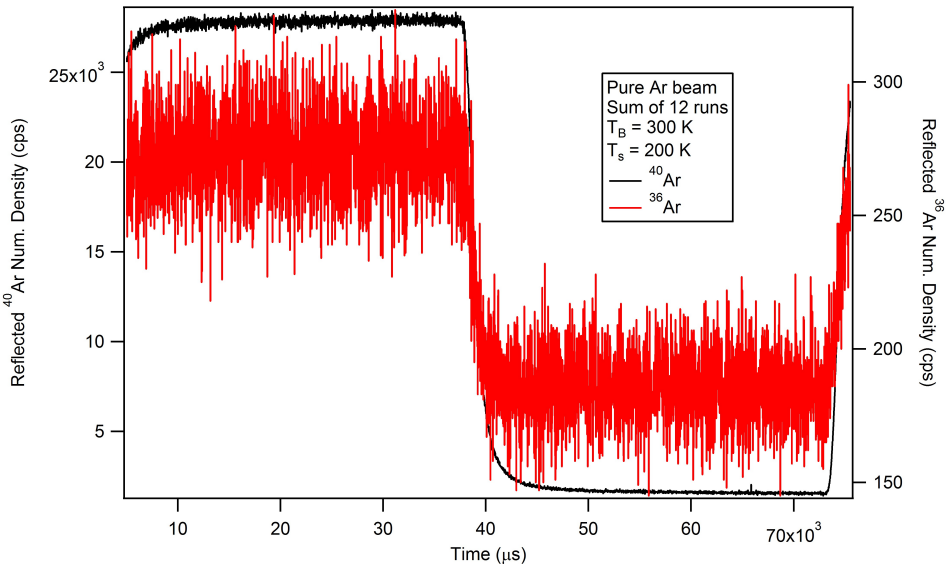

Composite square wave of reflectivity of ^{40}Ar and ^{36}Ar from 200 K surface for pure Ar beam (T_B = 300 K). The ratio of modulated signal for these two spectra is used to calculate the incident beam composition in **Figure 7-6**.

Experiment file: Figure A7-5.pxp.

Raw data files: 100917_22, 101017_02, 101017_03, 101017_04, 101017_05, 101017_06, 101217_02, 101217_03, 101217_09, 101317_02, 101417_02, 101417_03

Figure A7-6

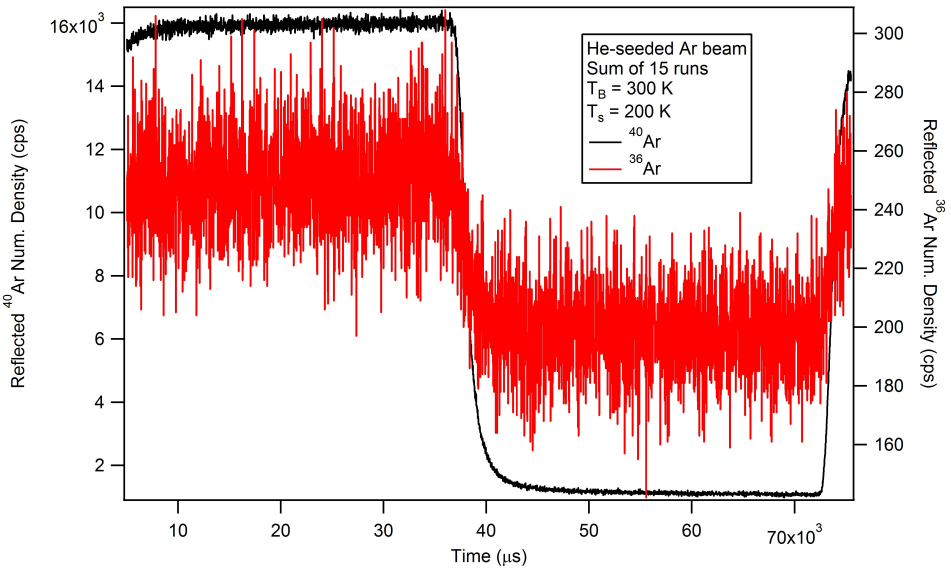

Composite square wave of reflectivity of ^{40}Ar and ^{36}Ar from 200 K surface for He-seeded Ar beam (T_B = 300 K). The ratio of modulated signal for these two spectra is used to calculate the incident beam composition in **Figure 7-6**.

Experiment file: Figure A7-6.pxp.

Raw data files: 101317_08, 101317_09, 101317_10, 101317_11, 101417_05, 101417_06, 101617_02, 101617_03, 101617_04, 101617_05, 102417_03, 102417_04, 102517_02, 102517_03, 102617_02

Figure A7-7

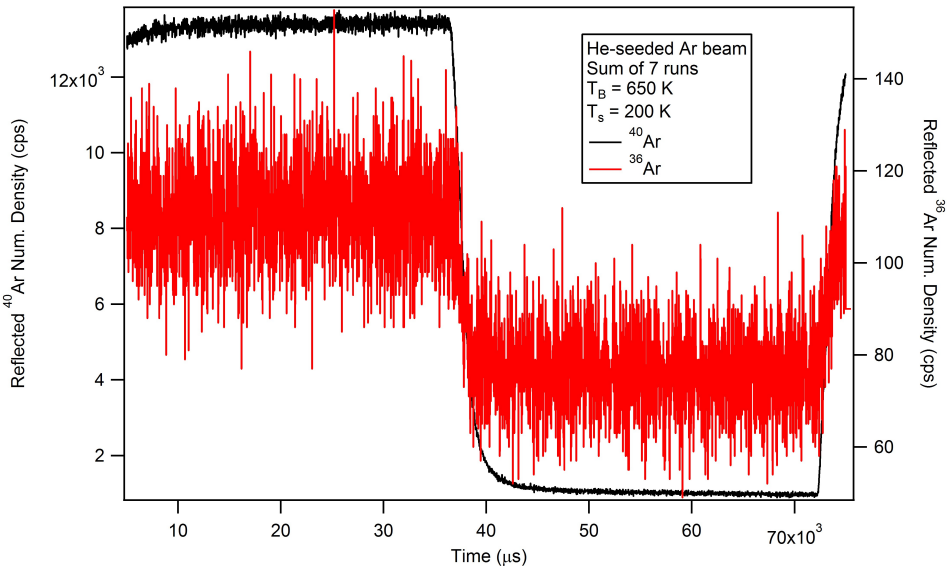

Composite square wave of reflectivity of ^{40}Ar and ^{36}Ar from 200 K surface for He-seeded Ar beam (T_B = 650 K). The ratio of modulated signal for these two spectra is used to calculate the incident beam composition in **Figure 7-6**.

Experiment file: Figure A7-7.pxp.

Raw data files: 110317_24, 110617_04, 110617_05, 110717_02, 110717_03, 110717_04, 110717_05

Figure A7-8

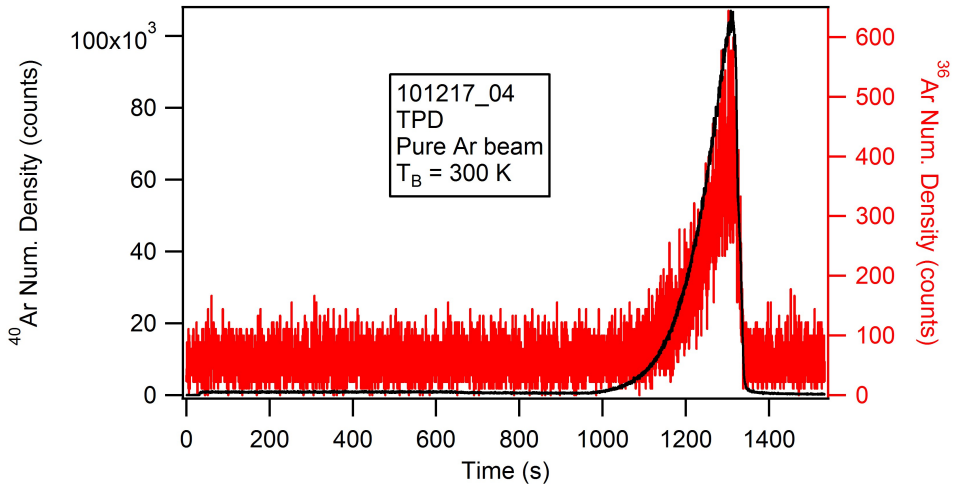

TPD of ^{40}Ar and ^{36}Ar dosed using pure Ar beam (T_B = 300 K). The ratio of integrated number density for these two spectra is used to calculate the condensate composition in **Figure 7-6**.

Experiment file: TPD_PureAr_300K.pxp.

Raw data files: 101217_04

Figure A7-9

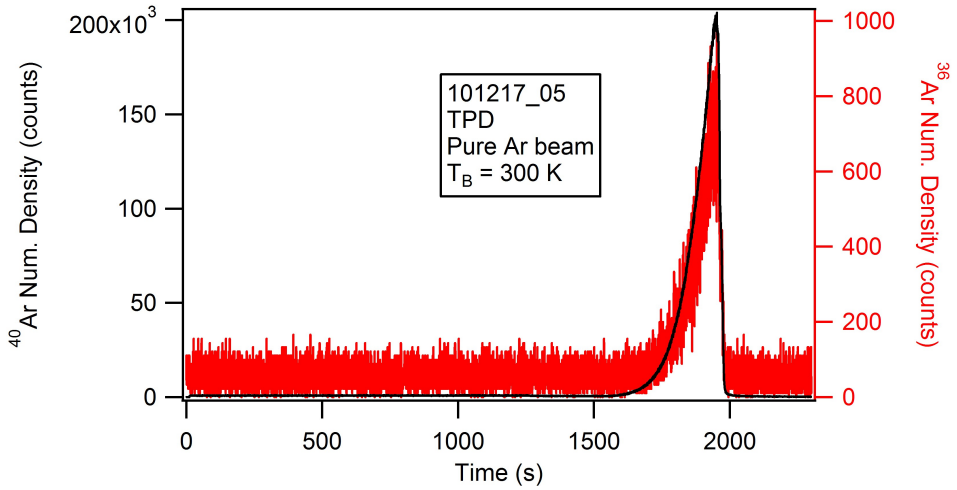

TPD of ^{40}Ar and ^{36}Ar dosed using pure Ar beam (T_B = 300 K). The ratio of integrated number density for these two spectra is used to calculate the condensate composition in **Figure 7-6**.

Experiment file: TPD_PureAr_300K.pxp.

Raw data files: 101217_05

Figure A7-10

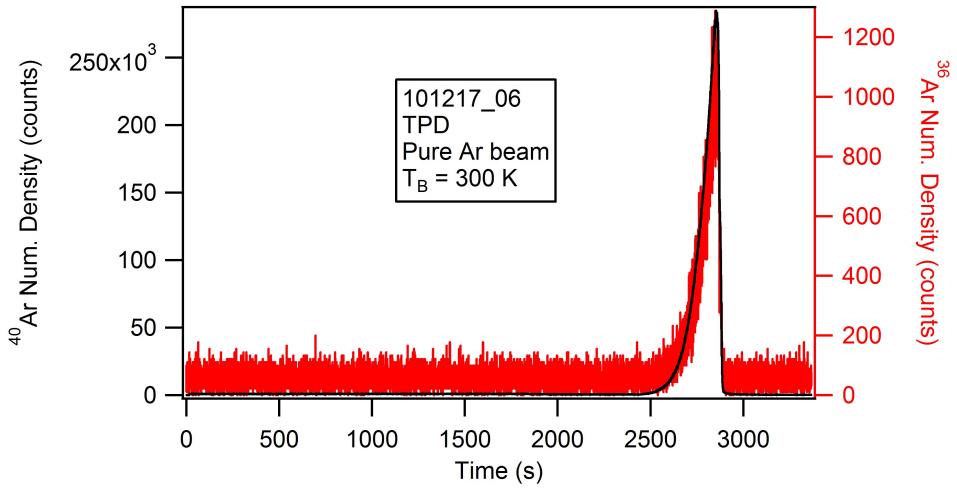

TPD of ^{40}Ar and ^{36}Ar dosed using pure Ar beam (T_B = 300 K). The ratio of integrated number density for these two spectra is used to calculate the condensate composition in **Figure 7-6**.

Experiment file: TPD_PureAr_300K.pxp.

Raw data files: 101217_06

Figure A7-11

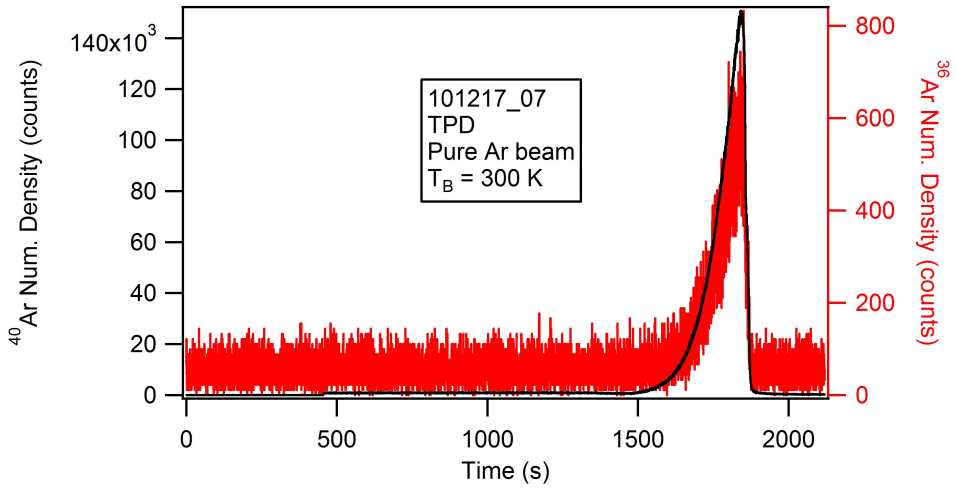

TPD of ^{40}Ar and ^{36}Ar dosed using pure Ar beam (T_B = 300 K). The ratio of integrated number density for these two spectra is used to calculate the condensate composition in **Figure 7-6**.

Experiment file: TPD_PureAr_300K.pxp.

Raw data files: 101217_07

Figure A7-12

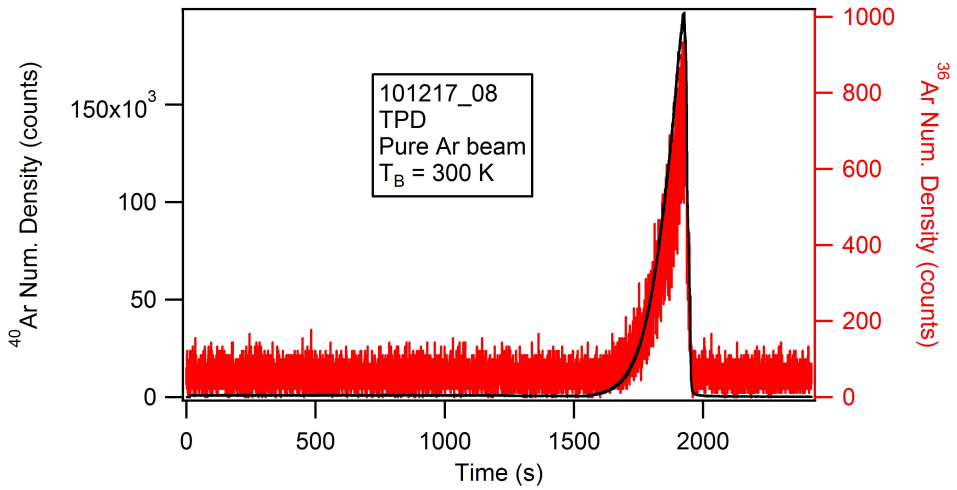

TPD of ^{40}Ar and ^{36}Ar dosed using pure Ar beam (T_B = 300 K). The ratio of integrated number density for these two spectra is used to calculate the condensate composition in **Figure 7-6**.

Experiment file: TPD_PureAr_300K.pxp.

Raw data files: 101217_08

Figure A7-13

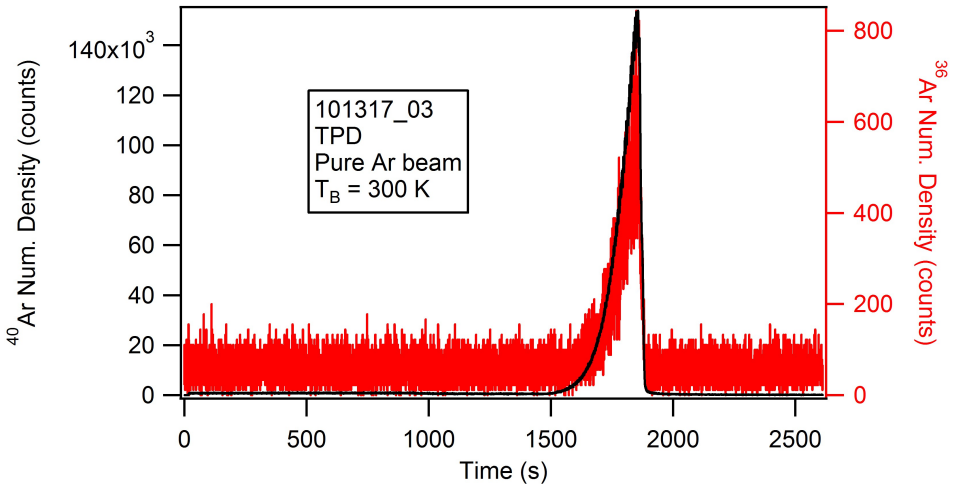

TPD of ^{40}Ar and ^{36}Ar dosed using pure Ar beam (T_B = 300 K). The ratio of integrated number density for these two spectra is used to calculate the condensate composition in **Figure 7-6**.

Experiment file: TPD_PureAr_300K.pxp.

Raw data files: 101317_03

Figure A7-14

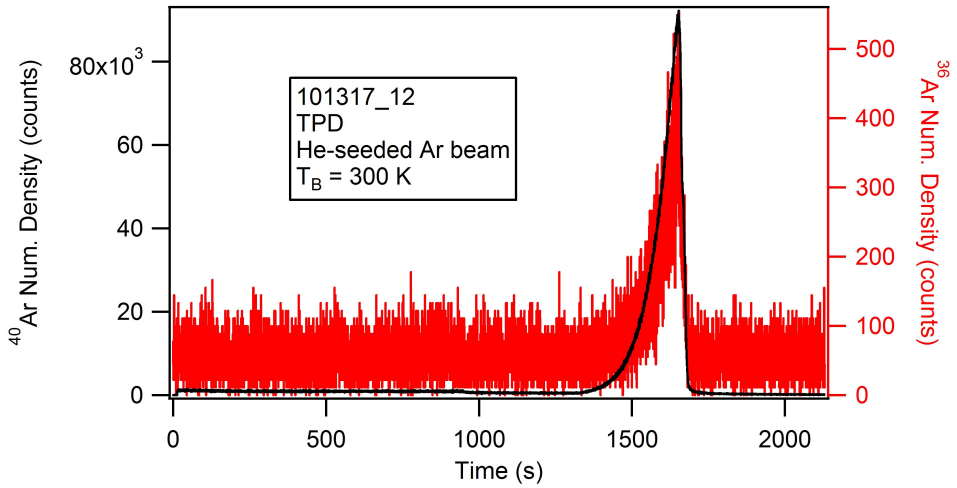

TPD of ^{40}Ar and ^{36}Ar dosed using He-seeded Ar beam (T_B = 300 K). The ratio of integrated number density for these two spectra is used to calculate the condensate composition in **Figure 7-6**.

Experiment file: TPD_HeAr_300K.pxp.

Raw data files: 101317_12

Figure A7-15

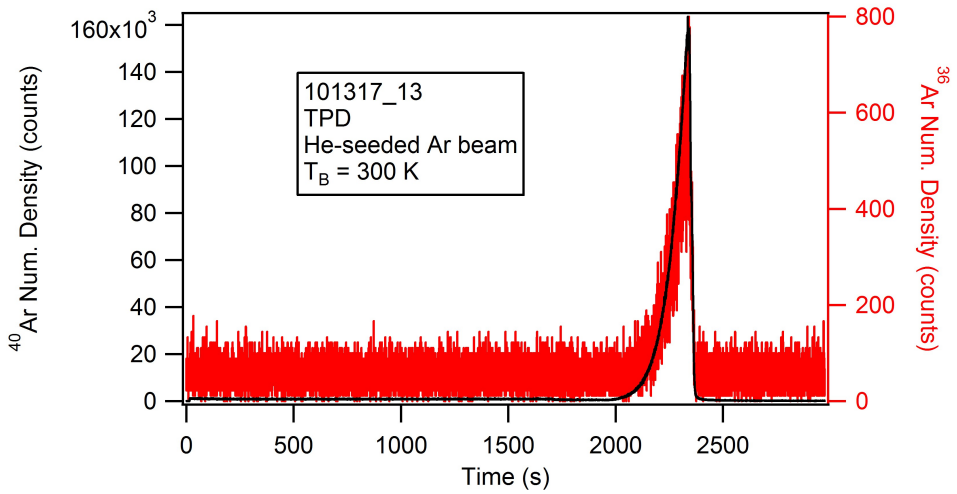

TPD of ^{40}Ar and ^{36}Ar dosed using He-seeded Ar beam (T_B = 300 K). The ratio of integrated number density for these two spectra is used to calculate the condensate composition in **Figure 7-6**.

Experiment file: TPD_HeAr_300K.pxp.

Raw data files: 101317_13

Figure A7-16

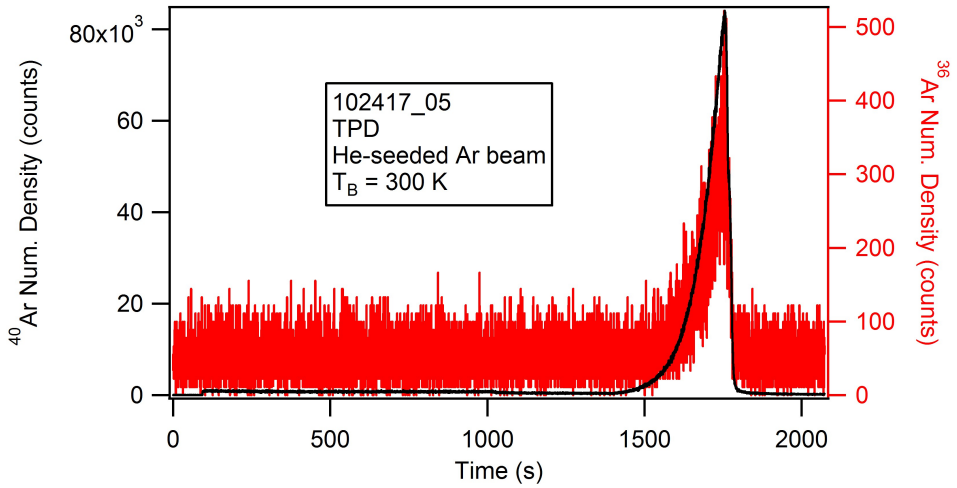

TPD of ^{40}Ar and ^{36}Ar dosed using He-seeded Ar beam (T_B = 300 K). The ratio of integrated number density for these two spectra is used to calculate the condensate composition in **Figure 7-6**.

Experiment file: TPD_HeAr_300K.pxp.

Raw data files: 102417_05

Figure A7-17

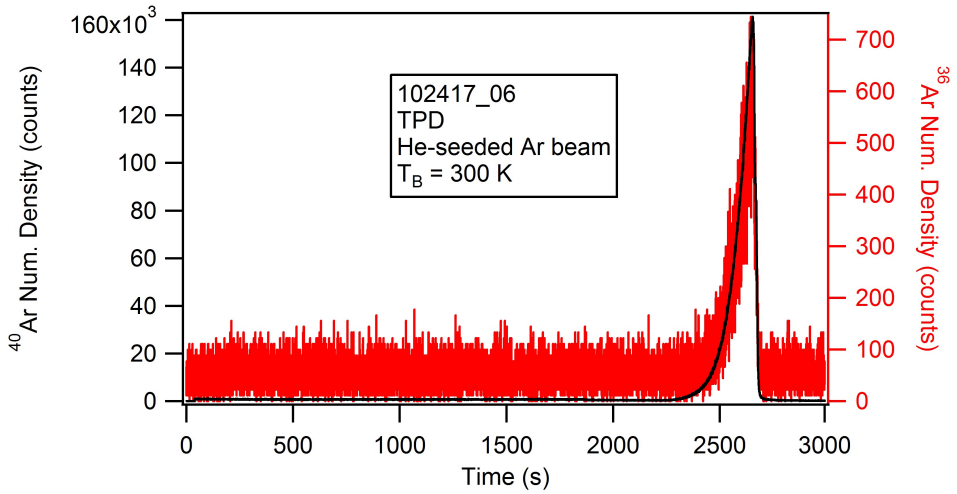

TPD of ^{40}Ar and ^{36}Ar dosed using He-seeded Ar beam (T_B = 300 K). The ratio of integrated number density for these two spectra is used to calculate the condensate composition in **Figure 7-6**.

Experiment file: TPD_HeAr_300K.pxp.

Raw data files: 102417_06

Figure A7-18

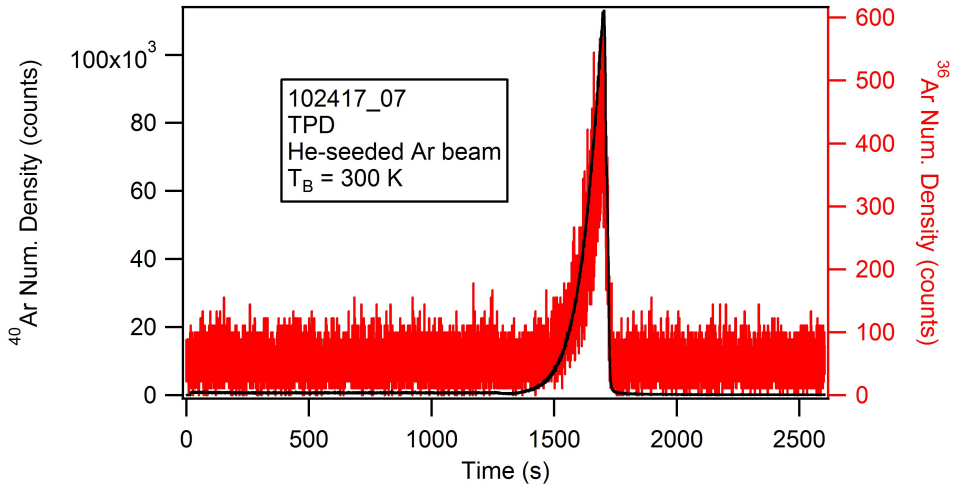

TPD of ^{40}Ar and ^{36}Ar dosed using He-seeded Ar beam (T_B = 300 K). The ratio of integrated number density for these two spectra is used to calculate the condensate composition in **Figure 7-6**.

Experiment file: TPD_HeAr_300K.pxp.

Raw data files: 102417_07

Figure A7-19

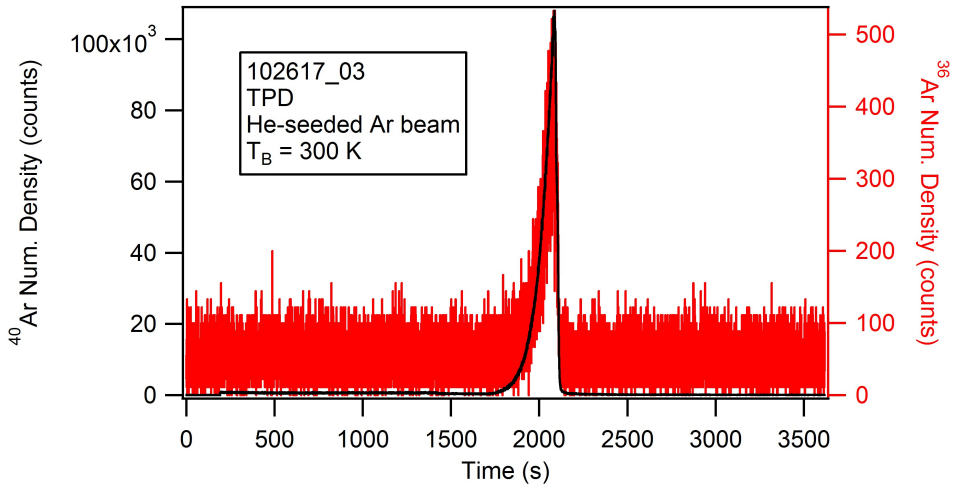

TPD of ^{40}Ar and ^{36}Ar dosed using He-seeded Ar beam (T_B = 300 K). The ratio of integrated number density for these two spectra is used to calculate the condensate composition in **Figure 7-6**.

Experiment file: TPD_HeAr_300K.pxp.

Raw data files: 102617_03

Figure A7-20

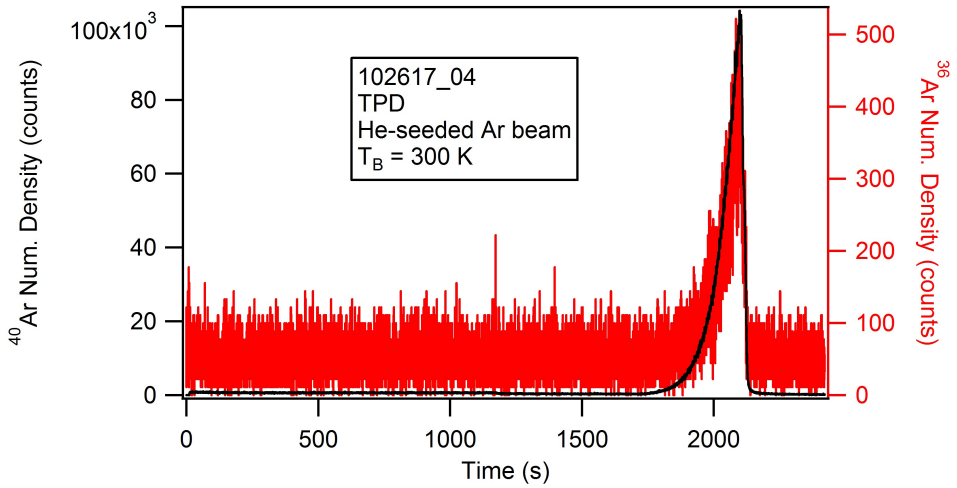

TPD of ^{40}Ar and ^{36}Ar dosed using He-seeded Ar beam (T_B = 300 K). The ratio of integrated number density for these two spectra is used to calculate the condensate composition in **Figure 7-6**.

Experiment file: TPD_HeAr_300K.pxp.

Raw data files: 102617_04

Figure A7-21

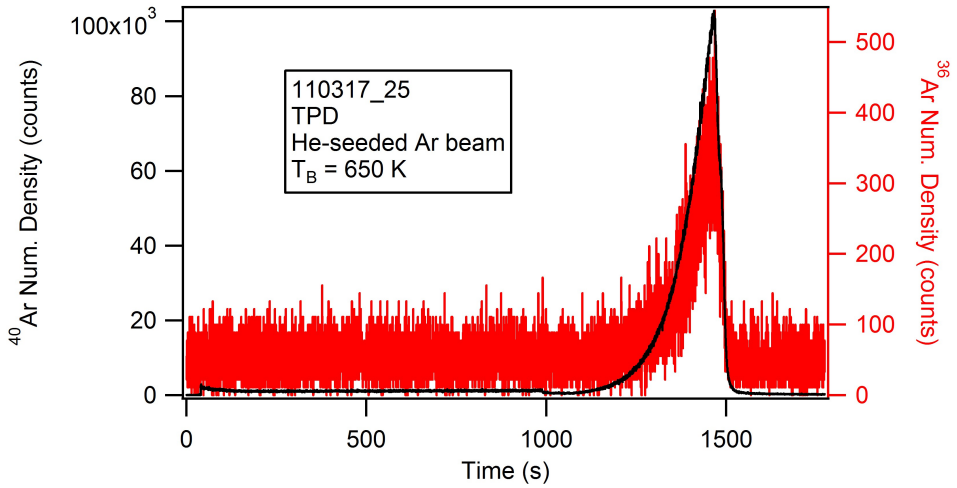

TPD of ^{40}Ar and ^{36}Ar dosed using He-seeded Ar beam (T_B = 650 K). The ratio of integrated number density for these two spectra is used to calculate the condensate composition in **Figure 7-6**.

Experiment file: TPD_HeAr_650K.pxp.

Raw data files: 110317_25

Figure A7-22

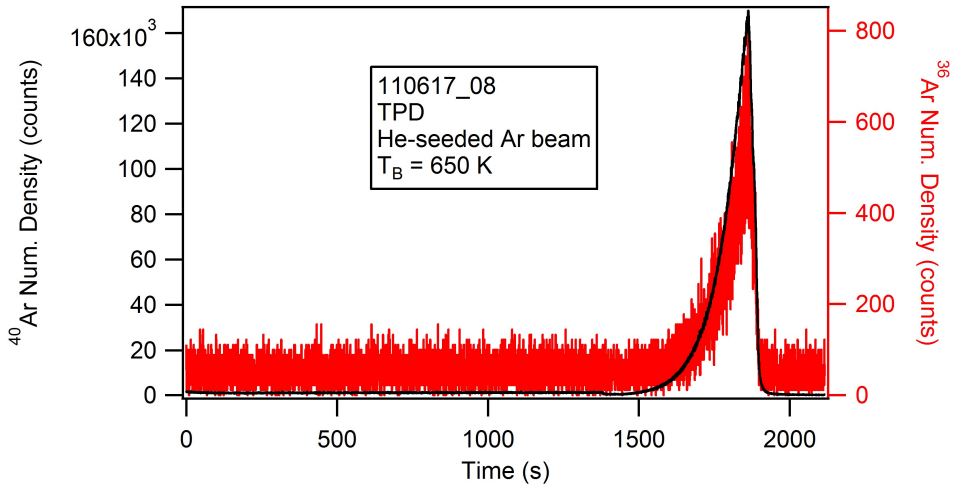

TPD of ^{40}Ar and ^{36}Ar dosed using He-seeded Ar beam (T_B = 650 K). The ratio of integrated number density for these two spectra is used to calculate the condensate composition in **Figure 7-6**.

Experiment file: TPD_HeAr_650K.pxp.

Raw data files: 110617_08

Figure A7-23

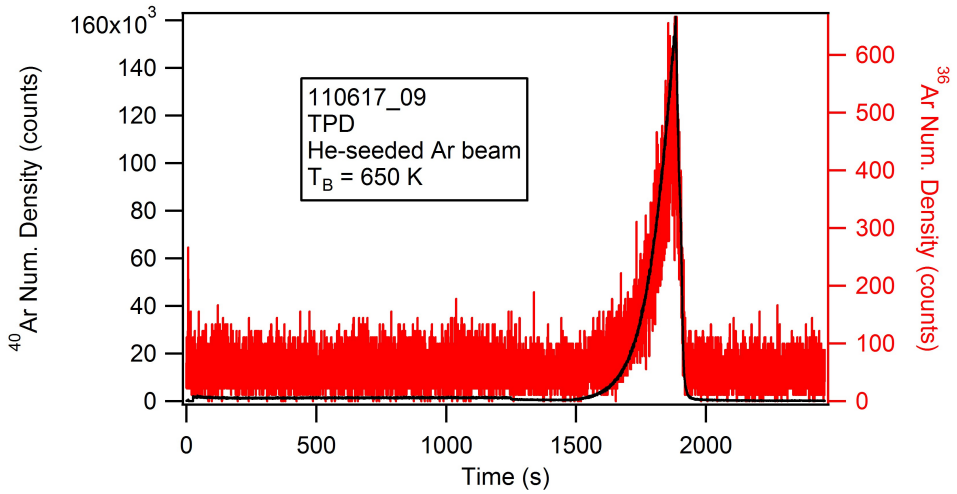

TPD of ^{40}Ar and ^{36}Ar dosed using He-seeded Ar beam (T_B = 650 K). The ratio of integrated number density for these two spectra is used to calculate the condensate composition in **Figure 7-6**.

Experiment file: TPD_HeAr_650K.pxp.

Raw data files: 110617_09

Figure A7-24

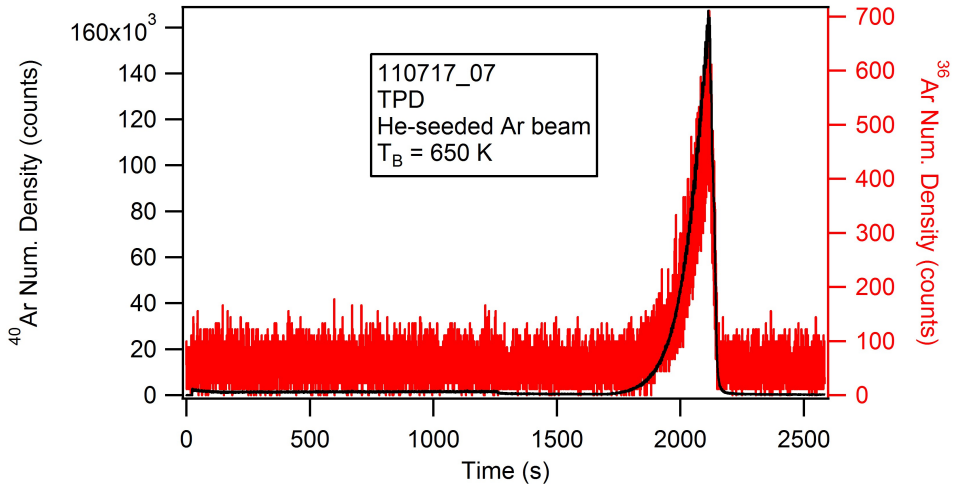

TPD of ^{40}Ar and ^{36}Ar dosed using He-seeded Ar beam (T_B = 650 K). The ratio of integrated number density for these two spectra is used to calculate the condensate composition in **Figure 7-6**.

Experiment file: TPD_HeAr_650K.pxp.

Raw data files: 110717_07

References

(1) Estermann, I.; Stern, O. Beugung von Molekularstrahlen. *Zeitschrift für Phys.* **1930**, *61* (1–2), 95–125.

(2) Ramsey, N. F. Molecular Beams: Our Legacy from Otto Stern. *Zeitschrift für Phys. D Atoms Mol. Clust.* **1988**, *10*, 121–125.

(3) Kantrowitz, A.; Grey, J. A High Intensity Source for the Molecular Beam. Part I. Theoretical. *Rev. Sci. Instrum.* **1951**, *22* (5), 328–332.

(4) Scoles, G. *Atomic and Molecular Beam Methods Volume I*; Oxford University Press: New York, 1988.

(5) Koleske, D. D.; Sibener, S. J. Generation of Pseudorandom Sequences for Use in Cross-Correlation Modulation. *Rev. Sci. Instrum.* **1992**, *63* (8), 3852.

(6) Hund, Z. M.; Nihill, K. J.; Campi, D.; Wong, K. T.; Lewis, N. S.; Bernasconi, M.; Benedek, G.; Sibener, S. J. Atomic Surface Structure of CH_3-Ge(111) Characterized by Helium Atom Diffraction and Density Functional Theory. *J. Phys. Chem. C* **2015**, *119* (32), 18458–18466.

(7) Frank, M. M.; Koester, S. J.; Copel, M.; Ott, J. A.; Paruchuri, V. K.; Shang, H.; Loesing, R. Hafnium Oxide Gate Dielectrics on Sulfur-Passivated Germanium. *Appl. Phys. Lett.* **2006**, *89* (11), 112905.

(8) Brunco, D. P.; De Jaeger, B.; Eneman, G.; Mitard, J.; Hellings, G.; Satta, A.; Terzieva, V.; Souriau, L.; Leys, F. E.; Pourtois, G.; Houssa, M.; Winderickx, E.; Vranken, E.; Sioncke, S.; Opsomer, K.; Nicholas, G.; Caymax, M.; Stesmans, A.; Van Steenbergen, J.; Mertens, P. W.; Meuris, M.; Heyns, M. M. Germanium MOSFET Devices: Advances in Materials Understanding, Process Development, and Electrical Performance. *J. Electrochem. Soc.* **2008**, *155* (7), H552.

(9) Guter, W.; Schöne, J.; Philipps, S. P.; Steiner, M.; Siefer, G.; Wekkeli, A.; Welser, E.; Oliva, E.; Bett, A. W.; Dimroth, F. Current-Matched Triple-Junction Solar Cell Reaching 41.1% Conversion Efficiency under Concentrated Sunlight. *Appl. Phys. Lett.* **2009**, *94* (22), 223504.

(10) King, R. R.; Law, D. C.; Edmondson, K. M.; Fetzer, C. M.; Kinsey, G. S.; Yoon, H.; Sherif, R. A.; Karam, N. H. 40% Efficient Metamorphic GaInP/GaInAs/Ge Multijunction Solar Cells. *Appl. Phys. Lett.* **2007**, *90* (18), 183516.

(11) Montgomery, H. C.; Brown, W. L. Field-Induced Conductivity Changes in Germanium. *Phys. Rev.* **1956**, *103* (4), 865–870.

(12) Kingston, R. H. Water-Vapor-Induced N-Type Surface Conductivity on P-Type Germanium. *Phys. Rev.* **1955**, *98* (6), 1766–1775.

(13) Jona, F.; Thompson, W. A.; Marcus, P. M. Experimental Determination of the Atomic Structure of a H-Terminated Si(111) Surface. *Phys. Rev. B* **1995**, *52* (11), 8226–8230.

(14) Cargnoni, F.; Gatti, C.; May, E.; Narducci, D. Geometrical Reconstructions and Electronic Relaxations of Silicon Surfaces. I. An Electron Density Topological Study of H-Covered and Clean Si(111)(1×1) Surfaces. *J. Chem. Phys.* **2000**, *112* (2), 887–899.

(15) Kaxiras, E.; Joannopoulos, J. D. Hydrogenation of Semiconductor Surfaces: Si and Ge (111). *Phys. Rev. B* **1988**, *37* (15), 8842–8848.

(16) Li, X.-P.; Vanderbilt, D.; King-Smith, R. D. First-Principles Study of Steps on the Si(111):H Surface. *Phys. Rev. B* **1994**, *50* (7), 4637–4641.

(17) Stumpf, R.; Marcus, P. M. Relaxation of the Clean and H-Covered C(111) and the Clean Si(111)-1x1 Surfaces. *Phys. Rev. B* **1993**, *47* (23), 16016–16019.

(18) Imbihl, R.; Demuth, J. E.; Himpsel, F. J.; Marcus, P. M.; Thompson, W. A. Structure Analysis of Ge(111)1x1-H by Low-Energy Electron Diffraction. *Phys. Rev. B* **1987**, *36* (9), 5037–5040.

(19) Ong, C. K. The Relaxation of the H-Terminated Diamond (C), Si and Ge (111) Surfaces. *Solid State Commun.* **1989**, *70* (2), 225–227.

(20) Copel, M.; Culbertson, R. J.; Tromp, R. M. Relaxation and H Coverage of Ammonium Fluoride Treated Si(111). *Appl. Phys. Lett.* **1994**, *65* (18), 2344–2346.

(21) Loscutoff, P. W.; Bent, S. F. Reactivity of the Germanium Surface: Chemical Passivation and Functionalization. *Annu. Rev. Phys. Chem.* **2006**, *57*, 467–495.

(22) Rivillon, S.; Chabal, Y. J.; Amy, F.; Kahn, A. Hydrogen Passivation of Germanium (100) Surface Using Wet Chemical Preparation. *Appl. Phys. Lett.* **2005**, *87* (25), 253101.

(23) Linford, M. R.; Fenter, P.; Eisenberger, P. M.; Chidsey, C. E. D. Alkyl Monolayers on Silicon Prepared from 1-Alkenes and Hydrogen-Terminated Silicon. *J. Am. Chem. Soc.* **1995**, *117* (11), 3145–3155.

(24) Buriak, J. M. Organometallic Chemistry on Silicon and Germanium Surfaces. *Chem. Rev.* **2002**, *102* (5), 1271–1308.

(25) Sharp, I. D.; Schoell, S. J.; Hoeb, M.; Brandt, M. S.; Stutzmann, M. Electronic Properties of Self-Assembled Alkyl Monolayers on Ge Surfaces. *Appl. Phys. Lett.* **2008**, *92* (22), 223306.

(26) Gorostiza, P.; de Villeneuve, C. H.; Sun, Q. Y.; Sanz, F.; Wallart, X.; Boukherroub, R.; Allongue, P. Water Exclusion at the Nanometer Scale Provides Long-Term Passivation of

Silicon (111) Grafted with Alkyl Monolayers. *J. Phys. Chem. B* **2006**, *110*, 5576–5585.

(27) Choi, K.; Buriak, J. M. Hydrogermylation of Alkenes and Alkynes on Hydride-Terminated Ge(100) Surfaces. *Langmuir* **2000**, *16*, 7737–7741.

(28) Bodlaki, D.; Yamamoto, H.; Waldeck, D. H.; Borguet, E. Ambient Stability of Chemically Passivated Germanium Interfaces. *Surf. Sci.* **2003**, *543*, 63–74.

(29) He, J.; Lu, Z.-H.; Mitchell, S. A.; Wayner, D. D. M. Self-Assembly of Alkyl Monolayers on Ge(111). *J. Am. Chem. Soc.* **1998**, *120*, 2660–2661.

(30) Gerlich, D.; Cullen, G. W.; Amick, J. A. The Stabilization of Germanium Surfaces by Ethylation. *J. Electrochem. Soc.* **1962**, *109* (3), 133.

(31) Royea, W. J.; Juang, A.; Lewis, N. S. Preparation of Air-Stable, Low Recombination Velocity Si(111) Surfaces through Alkyl Termination. *Appl. Phys. Lett.* **2000**, *77* (13), 1988.

(32) Yu, H.; Webb, L. J.; Heath, J. R.; Lewis, N. S. Scanning Tunneling Spectroscopy of Methyl- and Ethyl-Terminated Si(111) Surfaces. *Appl. Phys. Lett.* **2006**, *88* (25), 252111.

(33) Bansal, A.; Li, X.; Lauermann, I.; Lewis, N. S.; Yi, S. I.; Weinberg, W. H. Alkylation of Si Surfaces Using a Two-Step Halogenation/Grignard Route. *J. Am. Chem. Soc.* **1996**, *118* (30), 7225–7226.

(34) Bansal, A.; Lewis, N. S. Stabilization of Si Photoanodes in Aqueous Electrolytes through Surface Alkylation. *J. Phys. Chem. B* **1998**, *102* (21), 4058–4060.

(35) Knapp, D.; Brunschwig, B. S.; Lewis, N. S. Chemical, Electronic, and Electrical Properties of Alkylated Ge(111) Surfaces. *J. Phys. Chem. C* **2010**, *114* (111), 12300–12307.

(36) Knapp, D.; Brunschwig, B.S.; Lewis, N. S. Transmission Infrared Spectra of CH_3–, CD_3–, and $C_{10}H_{21}$–Ge (111) Surfaces. *J. Phys. Chem. C* **2011**, *115*, 16389–16397.

(37) Becker, J. S.; Brown, R. D.; Johansson, E.; Lewis, N. S.; Sibener, S. J. Helium Atom Diffraction Measurements of the Surface Structure and Vibrational Dynamics of CH_3-Si(111) and CD_3-Si(111) Surfaces. *J. Chem. Phys.* **2010**, *133* (10), 104705.

(38) Brown, R. D.; Tong, Q.; Becker, J. S.; Freedman, M. A.; Yufa, N. A.; Sibener, S. J. Dynamics of Molecular and Polymeric Interfaces Probed with Atomic Beam Scattering and Scanning Probe Imaging. *Faraday Discuss.* **2012**, *157*, 307.

(39) Brown, R. D.; Hund, Z. M.; Campi, D.; O'Leary, L.; Lewis, N.; Bernasconi, M.; Benedek, G.; Sibener, S. J. Hybridization of Surface Waves with Organic Adlayer Librations: A Helium Atom Scattering and Density Functional Perturbation Theory Study of Methyl-Si(111). *Phys. Rev. Lett.* **2013**, *110* (15), 156102.

(40) Brown, R. D.; Hund, Z. M.; Campi, D.; O'Leary, L. E.; Lewis, N. S.; Bernasconi, M.; Benedek, G.; Sibener, S. J. The Interaction of Organic Adsorbate Vibrations with Substrate Lattice Waves in Methyl-Si(111)-(1x1). *J. Chem. Phys.* **2014**, *141* (2).

(41) Gans, B.; Knipp, P. A.; Koleske, D. D.; Sibener, S. J. Surface Dynamics of Ordered $Cu_3Au(001)$ Studied by Elastic and Inelastic Helium Atom Scattering. *Surf. Sci.* **1992**, *264*, 81–94.

(42) Giannozzi, P.; Baroni, S.; Bonini, N.; Calandra, M.; Car, R.; Cavazzoni, C.; Ceresoli, D.; Chiarotti, G. L.; Cococcioni, M.; Dabo, I.; Dal Corso, A.; de Gironcoli, S.; Fabris, S.; Fratesi, G.; Gebauer, R.; Gerstmann, U.; Gougoussis, C.; Kokalj, A.; Lazzeri, M.; Martin-Samos, L.; Marzari, N.; Mauri, F.; Mazzarello, R.; Paolini, S.; Pasquarello, A.; Paulatto, L.; Sbraccia, C.; Scandolo, S.; Sclauzero, G.; Seitsonen, A. P.; Smogunov, A.; Umari, P.; Wentzcovitch, R. M. QUANTUM ESPRESSO: A Modular and Open-Source Software Project for Quantum Simulations of Materials. *J. Phys. Condens. Matter* **2009**, *21* (39), 395502.

(43) Vanderbilt, D. Soft Self-Consistent Pseudopotentials in a Generalized Eigenvalue Formalism. *Phys. Rev. B* **1990**, *41* (11), 7892.

(44) Perdew, J. P.; Zunger, A. Self-Interaction Correction to Density-Functional Approximations for Many-Electron Systems. *Phys. Rev. B* **1981**, *23* (10), 5048–5079.

(45) Perdew, J. P.; Burke, K.; Ernzerhof, M. Generalized Gradient Approximation Made Simple. *Phys. Rev. Lett.* **1996**, *77* (18), 3865–3868.

(46) Monkhorst, H. J.; Pack, J. D. Special Points for Brillouin-Zone Integrations. *Phys. Rev. B* **1976**, *13* (12), 5188–5192.

(47) Hom, T.; Kiszenik, W.; Post, B. Accurate Lattice Constants from Multiple Reflection Measurements II. Lattice Constants of Germanium, Silicon and Diamond. *J. Appl. Cryst.* **1975**, *8*, 457–458.

(48) Baroni, S.; Gironcoli, S. De; Dal Corso, A.; Giannozzi, P. Phonons and Related Crystal Properties from Density-Functional Perturbation Theory. *Rev. Mod. Phys.* **2001**, *73*, 515–557.

(49) Vandevondele, J.; Krack, M.; Mohamed, F.; Parrinello, M.; Chassaing, T.; Hutter, J. QUICKSTEP: Fast and Accurate Density Functional Calculations Using a Mixed Gaussian and Plane Waves Approach. *Comput. Phys. Commun.* **2005**, *167* (2), 103–128.

(50) Goedecker, S.; Teter, M.; Hutter, J. Separable Dual-Space Gaussian Pseudopotentials. *Phys. Rev. B* **1996**, *54* (3), 1703–1710.

(51) Krack, M. Pseudopotentials for H to Kr Optimized for Gradient-Corrected Exchange-Correlation Functionals. *Theor. Chem. Acc.* **2005**, *114*, 145–152.

(52) Cao, S.; Tang, J.-C.; Shen, S.-L. Multiple-Scattering and DV-Xa Analyses of a Cl-

Passivated Ge(111) Surface. *J. Phys. Condens. Matter* **2003**, *15*, 5261–5268.

(53) Lapujoulade, J.; Lejay, Y.; Armand, G. The Thermal Attentuation of Coherent Elastic Scattering of Noble Gas from Metal Surfaces. *Surf. Sci.* **1980**, *95*, 107–130.

(54) Esbjerg, N.; Norskov, J. K. Dependence of the He-Scattering Potential at Surfaces on the Surface-Electron-Density Profile. *Phys. Rev. Lett.* **1980**, *459* (10), 807–810.

(55) Henzler, M. Measurement of Surface Defects by Low-Energy Electron Diffraction. *Appl. Phys. A* **1984**, *34*, 205–214.

(56) Hund, Z. M.; Nihill, K. J.; Campi, D.; Wong, K. T.; Lewis, N. S.; Bernasconi, M.; Benedek, G.; Sibener, S. J. Vibrational Dynamics and Band Structure of Methyl-Terminated Ge(111). *J. Chem. Phys.* **2015**, *143* (12).

(57) Zielasek, V.; Büssenschütt, A.; Henzler, M. Low-Energy Electron Thermal Diffuse Scattering from Al(111) Individually Resolved in Energy and Momentum. *Phys. Rev. B* **1997**, *55* (8), 5398–5403.

(58) Barnes, R. F.; Lagally, M. G.; Webb, M. B. Multiphonon Scattering of Low-Energy Electrons. *Phys. Rev.* **1968**, *171* (3), 627–633.

(59) Henzler, M. LEED Studies of Surface Imperfections. *Appl. Surf. Sci.* **1982**, *11–12*, 450–469.

(60) Henzler, M. Quantitative Evaluation of Random Distributed Steps at Interfaces and Surfaces. *Surf. Sci.* **1978**, *73*, 240–251.

(61) Niu, L.; Gaspar, D. J.; Sibener, S. J. Phonons Localized at Step Edges: A Route to Understanding Forces at Extended Surface Defects. *Science.* **1995**, *268*, 847–850.

(62) Solares, S. D.; Yu, H.; Webb, L. J.; Lewis, N. S.; Heath, J. R.; Goddard, W. A. Chlorination-Methylation of the Hydrogen-Terminated Silicon(111) Surface Can Induce a Stacking Fault in the Presence of Etch Pits. *J. Am. Chem. Soc.* **2006**, *128* (12), 3850–3851.

(63) Wong, K. T.; Kim, Y. G.; Soriaga, M. P.; Brunschwig, B. S.; Lewis, N. S. Synthesis and Characterization of Atomically Flat Methyl-Terminated Ge(111) Surfaces. *J. Am. Chem. Soc.* **2015**, *137* (28), 9006–9014.

(64) Malyk, S.; Shalhout, F. Y.; O'Leary, L. E.; Lewis, N. S.; Benderskii, A. V. Vibrational Sum Frequency Spectroscopic Investigation of the Azimuthal Anisotropy and Rotational Dynamics of Methyl-Terminated Silicon(111) Surfaces. *J. Phys. Chem. C* **2013**, *117* (2), 935–944.

(65) Riordan, M.; Hoddeson, L.; Herring, C. The Invention of the Transistor. *Rev. Mod. Phys.* **1999**, *71* (2), S336–S345.

(66) Delabie, A.; Bellenger, F.; Houssa, M.; Conard, T.; Van Elshocht, S.; Caymax, M.; Heyns,

M.; Meuris, M. Effective Electrical Passivation of Ge(100) for High- K Gate Dielectric Layers Using Germanium Oxide. *Appl. Phys. Lett.* **2007**, *91* (8), 82904.

(67) Kita, K.; Suzuki, S.; Nomura, H.; Takahashi, T.; Nishimura, T.; Toriumi, A. Direct Evidence of GeO Volatilization from GeO_2/Ge and Impact of Its Suppression on GeO_2/Ge Metal-Insulator-Semiconductor Characteristics. *Jpn. J. Appl. Phys.* **2008**, *47* (4), 2349–2353.

(68) Farías, D.; Lange, G.; Rieder, K. H.; Toennies, J. P. Helium Scattering Structure Analyses of the c(2x8) Reconstruction and the High-Temperature (1x1) Structure of Ge(111). *Phys. Rev. B* **1997**, *55* (11).

(69) Bringans, R. D.; Höchst, H. Angular Resolved Photoemission Measurements on Clean and Hydrogen Covered Ge(111) Surfaces. *Appl. Surf. Sci.* **1982**, *11/12*, 368–374.

(70) Sun, S.; Sun, Y.; Liu, Z.; Lee, D.-I.; Pianetta, P. Roles of Oxygen and Water Vapor in the Oxidation of Halogen Terminated Ge(111) Surfaces. *Appl. Phys. Lett.* **2006**, *89* (23), 231925,1-3.

(71) Knapp, D.; Brunschwig, B. S.; Lewis, N. S. Chemical, Electronic, and Electrical Properties of Alkylated Ge(111) Surfaces. *J. Phys. Chem. C* **2010**, *114* (28), 12300–12307.

(72) Jiang, S.; Butler, S.; Bianco, E.; Restrepo, O. D.; Windl, W.; Goldberger, J. E. Improving the Stability and Optical Properties of Germanane via One-Step Covalent Methyl-Termination. *Nat. Commun.* **2014**, *5*, 3389.

(73) Webb, L. J.; Rivillon, S.; Michalak, D. J.; Chabal, Y. J.; Lewis, N. S. Transmission Infrared Spectroscopy of Methyl- and Ethyl-Terminated Silicon(111) Surfaces. *J. Phys. Chem. B* **2006**, *110* (14), 7349–7356.

(74) Becker, J. S.; Brown, R. D.; Johansson, E.; Lewis, N. S.; Sibener, S. J. Helium Atom Diffraction Measurements of the Surface Structure and Vibrational Dynamics of CH_3-Si(111) and CD_3-Si(111) Surfaces. *J. Chem. Phys.* **2010**, *133* (10), 104705.

(75) Brown, R. D.; Hund, Z. M.; Campi, D.; O'Leary, L. E.; Lewis, N. S.; Bernasconi, M.; Benedek, G.; Sibener, S. J. Hybridization of Surface Waves with Organic Adlayer Librations: A Helium Atom Scattering and Density Functional Perturbation Theory Study of Methyl-Si(111). *Phys. Rev. Lett.* **2013**, *110* (15), 156102.

(76) Ferguson, G. A.; Raghavachari, K. The Emergence of Collective Vibrations in Cluster Models: Quantum Chemical Study of the Methyl-Terminated Si(111) Surface. *J. Chem. Phys.* **2006**, *125* (15), 154708.

(77) Kress, W.; de Wette, F. W. *Surface Phonons*; Springer-Verlag: New York, 1991.

(78) Gans, B.; King, S. K.; Knipp, P. A.; Koleske, D. D.; Sibener, S. J. Structure and Dynamics of Cu_3Au(001) Studied by Elastic and Inelastic Helium Atom Scattering. *J. Electron*

Spectros. Relat. Phenomena **1990**, *54/55*, 333–341.

(79) Farías, D.; Rieder, K.-H. Atomic Beam Diffraction from Solid Surfaces. *Reports Prog. Phys.* **1998**, *61* (98), 1575–1664.

(80) Beeby, J. L. The Scattering of Helium Atoms from Surfaces. *J. Phys. C* **1971**, *4*, L359.

(81) Ha, J. S.; Greene, E. F. He Diffraction Study of the Structural Phase Transition on the Ge(111) Surface at 550 K. *J. Chem. Phys.* **1989**, *91* (12), 7957–7963.

(82) Ohkuma, K.; Nakamura, K. Reconstruction-Induced Mean-Square Displacements on the (001)-(2×1) Surface of Diamond-Structure Crystals. *J. Phys. C Solid State Phys.* **1979**, *12*, L835–L839.

(83) Buckland, J. R.; Allison, W. Determination of the Helium/Si(111)-(1×1)H Potential. *J. Chem. Phys.* **2000**, *112* (2), 970–978.

(84) Camillone, N.; Chidsey, C. E. D.; Liu, G.; Putvinski, T. M.; Scoles, G. Surface Structure and Thermal Motion of n-Alkane Thiols Self-Assembled on Au(111) Studied by Low Energy Helium Diffraction. *J. Chem. Phys.* **1991**, *94* (12), 8493.

(85) Kittel, C. *Introduction to Solid State Physics*, 8th ed.; Wiley: Hoboken, 2004.

(86) Nilsson, G.; Nelin, G. Phonon Dispersion Relations in Ge at 80 K. *Phys. Rev. B* **1971**, *3* (2), 364–369.

(87) Zeng, X.; Elsayed-Ali, H. E. Surface Thermal Expansion of Ge(111). *Surf. Sci.* **1999**, *442*, L977–L982.

(88) Griffiths, J. E. Infrared Spectra of Methylgermane, Methyl-d_3-Germane, and Methylgermane-d_3. *J. Chem. Phys.* **1963**, *38* (12), 2879.

(89) Toennies, J. P. Phonon Inelastic Scattering of He Atoms from Single Crystal Surfaces. *J. Vac. Sci. Technol. A* **1984**, *2* (2), 1055–1065.

(90) Gibson, K. D.; Sibener, S. J. Determination of the Surface Phonon Dispersion Relations for Monolayer, Bilayer, Trilayer, and Thick Kr (111) Films Physisorbed on Ag (111) by Inelastic He Scattering. *Phys. Rev. Lett.* **1985**, *55* (14), 1514–1517.

(91) Tamtögl, A.; Kraus, P.; Mayrhofer-Reinhartshuber, M.; Campi, D.; Bernasconi, M.; Benedek, G.; Ernst, W. E. Surface and Subsurface Phonons of Bi(111) Measured with Helium Atom Scattering. *Phys. Rev. B* **2013**, *87* (3), 35410.

(92) Weare, J. H. Helium Scattering from Solid Surfaces. *J. Chem. Phys.* **1974**, *61* (7), 2900.

(93) Wei, S.; Chou, M. Y. Phonon Dispersions of Silicon and Germanium from First-Principle Calculations. *Phys. Rev. B* **1994**, *50* (4), 2221–2226.

(94) Han, X.; Balgar, T.; Hasselbrink, E. Vibrational Dynamics of Hydrogen on Ge Surfaces.

J. Chem. Phys. **2009**, *130* (13), 134701.

(95) Lobo, J.; Farías, D.; Hulpke, E.; Toennies, J.; Michel, E. Phonon Dispersion Curves of the Ge(111)-c(2×8) Surface Determined by He Atom Scattering. *Phys. Rev. B* **2006**, *74* (3), 35303.

(96) Glebov, A. L.; Toennies, J. P.; Vollmer, S.; Benedek, G. Acoustic Phonons of the Ge(111) Surface above 1000 K. *Europhys. Lett.* **1999**, *46* (3), 369–375.

(97) Santini, P.; Miglio, L.; Benedek, G.; Ruggerone, P. Surface Phonon Dispersion Curves in GaAs(110) and Ge(111)2x1: A Critical Comparison. *Surf. Sci.* **1991**, *241*, 346–352.

(98) Santini, P.; Ruggerone, P.; Miglio, L.; Doak, R. B. Intrinsic and Extrinsic Effects in Surfaces: Acoustic-Phonon Softening of Capped Si(111) Surfaces. *Phys. Rev. B* **1992**, *46* (15), 9865–9868.

(99) Nihill, K. J.; Hund, Z. M.; Muzas, A.; Diaz, C.; del Cueto, M.; Frankcombe, T.; Plymale, N. T.; Lewis, N. S.; Martin, F.; Sibener, S. J. Experimental and Theoretical Study of Rotationally Inelastic Diffraction of $H_2(D_2)$ from Methyl-Terminated Si(111). *J. Chem. Phys.* **2016**, *145*, 84705.

(100) Bansal, A.; Lewis, N. S. Stabilization of Si Photoanodes in Aqueous Electrolytes through Surface Alkylation. *J. Phys. Chem. B* **1998**, *102* (21), 4058–4060.

(101) Bansal, A.; Li, X.; Lauermann, I.; Lewis, N. S. Alkylation of Si Surfaces Using a Two-Step Halogenation/Grignard Route. *J. Am. Chem. Soc.* **1996**, *118* (11), 7225–7226.

(102) Maldonado, S.; Plass, K. E.; Knapp, D.; Lewis, N. S. Electrical Properties of Junctions between Hg and Si(111) Surfaces Functionalized with Short-Chain Alkyls. *J. Phys. Chem. C* **2007**, *111* (48), 17690–17699.

(103) Maldonado, S.; Lewis, N. S. Behavior of Electrodeposited Cd and Pb Schottky Junctions on CH_3-Terminated n-Si(111) Surfaces. *J. Electrochem. Soc.* **2009**, *156* (May 2012), H123.

(104) Plass, K. E.; Liu, X.; Brunschwig, B. S.; Lewis, N. S. Passivation and Secondary Functionalization of Allyl-Terminated Si(111) Surfaces. *Chem. Mater.* **2008**, *20*, 2228–2233.

(105) Webb, L. J.; Lewis, N. S. Comparison of the Electrical Properties and Chemical Stability of Crystalline Silicon(111) Surfaces Alkylated Using Grignard Reagents or Olefins with Lewis Acid Catalysts. *J. Phys. Chem. B* **2003**, *107* (23), 5404–5412.

(106) Wong, K. T.; Lewis, N. S. What a Difference a Bond Makes: The Structural, Chemical, and Physical Properties of Methyl-Terminated Si(111) Surfaces. *Acc. Chem. Res.* **2014**, No. 111.

(107) Ekinci, Y.; Toennies, J. P. Elastic and Rotationally Inelastic Diffraction of D_2 Molecules

from the LiF(001) Surface. *J. Chem. Phys.* **2002**, *72* (20), 205430.

(108) King, D. A.; Wells, M. G. Molecular Beam Investigation of Adsorption Kinetics on Bulk Metal Targets: Nitrogen on Tungsten. *Surf. Sci.* **1972**, *29*, 454–482.

(109) Farías, D.; Miranda, R. Diffraction of Molecular Hydrogen from Metal Surfaces. *Prog. Surf. Sci.* **2011**, *86* (9–10), 222–254.

(110) Farías, D.; Busnengo, H. F.; Martín, F. Probing Reaction Dynamics at Metal Surfaces with H_2 Diffraction. *J. Phys. Condens. Matter* **2007**, *19* (30), 305003.

(111) Barredo, D.; Laurent, G.; Nieto, P.; Farías, D.; Miranda, R. High-Resolution Elastic and Rotationally Inelastic Diffraction of D_2 from NiAl(110). *J. Chem. Phys.* **2010**, *133* (12).

(112) Yu, H.; Webb, L. J.; Ries, R. S.; Solares, S. D.; Goddard, W. A.; Heath, J. R.; Lewis, N. S. Low-Temperature STM Images of Methyl-Terminated Si(111) Surfaces. *J. Phys. Chem. B* **2005**, *109* (2), 671–674.

(113) Hunger, R.; Fritsche, R.; Jaeckel, B.; Jaegermann, W.; Webb, L. J.; Lewis, N. S. Chemical and Electronic Characterization of Methyl-Terminated Si(111) Surfaces by High-Resolution Synchrotron Photoelectron Spectroscopy. *Phys. Rev. B* **2005**, *72* (4), 45317.

(114) Bansal, A.; Li, X.; Yi, S. I.; Weinberg, W. H.; Lewis, N. S. Spectroscopic Studies of the Modification of Crystalline Si(111) Surfaces with Covalently-Attached Alkyl Chains Using a Chlorination/Alkylation Method. *J. Phys. Chem. B* **2001**, *105* (42), 10266–10277.

(115) O'Leary, L. E.; Johansson, E.; Brunschwig, B. S.; Lewis, N. S. Synthesis and Characterization of Mixed Methyl/Allyl Monolayers on Si(111). *J. Phys. Chem. B* **2010**, *114* (45), 14298–14302.

(116) Laurent, G.; Barredo, D.; Farías, D.; Miranda, R.; Díaz, C.; Rivière, P.; Somers, M. F.; Martín, F. Experimental and Theoretical Study of Rotationally Inelastic Diffraction of D_2 from NiAl(110). *Phys. Chem. Chem. Phys.* **2010**, *12* (43), 14501–14507.

(117) Valero, R.; Kroes, G. J.; Ekinci, Y.; Toennies, J. P. Rotational Transitions and Diffraction in D_2 Scattering from the LiF(001) Surface: Theory and Experiment. *J. Chem. Phys.* **2006**, *124* (23).

(118) Farías, D.; Miranda, R.; Rieder, K. H.; Diño, W. A.; Fukutani, K.; Okano, T.; Kasai, H.; Okiji, A. On the Influence of Incident Angle in the Scattering Dynamics of D_2 from NiAl(110). *Chem. Phys. Lett.* **2002**, *359* (1–2), 127–134.

(119) Bertino, M. F.; Hofmann, F.; Toennies, J. P. The Effect of Dissociative Chemisorption on the Diffraction of D_2 from Ni(110). *J. Chem. Phys.* **1997**, *106* (10), 4327–4338.

(120) Bertino, M. F.; Graham, A. P.; Rusin, L. Y.; Toennies, J. P. Diffraction and Rotational Transitions in the Scattering of D_2 from Cu(001) at Energies up to 250 meV. *J. Chem. Phys.* **1998**, *109* (18), 8036–8044.

(121) Yu, C.; Whaley, K. B.; Hogg, C. S.; Sibener, S. J. Investigation of the Spatially Isotropic Component of the Laterally Averaged Molecular Hydrogen/Ag(111) Physisorption Potential. *J. Chem. Phys.* **1985**, *83* (8), 4217.

(122) Ekinci, Y.; Toennies, J. Elastic and Rotationally Inelastic Diffraction of D_2 Molecules from the LiF(001) Surface. *Phys. Rev. B* **2005**, *72* (20), 205430.

(123) Cvetko, D.; Morgante, A.; Santaniello, A.; Tommasini, F. Deuterium Scattering from Rh(110) Surface. *J. Chem. Phys.* **1996**, *104* (19), 7778–7783.

(124) Rivière, P.; Busnengo, H. F.; Martín, F. Adsorption and Scattering of H_2 and D_2 by NiAl(110). *J. Chem. Phys.* **2005**, *123* (7), 74705.

(125) Rivière, P.; Somers, M. F.; Kroes, G. J.; Martín, F. Quantum Dynamical Study of the H_2 and D_2 Dissociative Adsorption and Diffraction from the NiAl (110) Alloy Surface. *Phys. Rev. B - Condens. Matter Mater. Phys.* **2006**, *73* (20), 205417.

(126) Nieto, P.; Pijper, E.; Barredo, D.; Laurent, G.; Olsen, R. A.; Baerends, E.-J.; Kroes, G.-J.; Farías, D. Reactive and Nonreactive Scattering of H_2 from a Metal Surface Is Electronically Adiabatic. *Science.* **2006**, *312*, 86–89.

(127) Nieto, P.; Farías, D.; Miranda, R.; Luppi, M.; Baerends, E. J.; Somers, M. F.; van der Niet, M. J. T. C.; Olsen, R. A.; Kroes, G.-J. Diffractive and Reactive Scattering of H_2 from Ru(0001): Experimental and Theoretical Study. *Phys. Chem. Chem. Phys.* **2011**, *13* (18), 8583–8597.

(128) Díaz, C.; Martín, F.; Kroes, G.-J.; Minniti, M.; Farías, D.; Miranda, R. H_2 Diffraction from a Strained Pseudomorphic Monolayer of Cu Deposited on Ru(0001). *J. Phys. Chem. C* **2012**, *116* (25), 13671–13678.

(129) Díaz, C.; Busnengo, H. F.; Rivìre, P.; Farías, D.; Nieto, P.; Somers, M. F.; Kroes, G. J.; Salin, A.; Martín, F. A Classical Dynamics Method for H_2 Diffraction from Metal Surfaces. *J. Chem. Phys.* **2005**, *122* (15).

(130) Kroes, G.-J.; Somers, M. F. Six-Dimensional Dynamics of Dissociative Chemisorption of H_2 on Metal Surfaces. *J. Theor. Comput. Chem.* **2005**, *4* (2), 493–581.

(131) Kroes, G.-J.; Díaz, C. Quantum and Classical Dynamics of Reactive Scattering of H_2 from Metal Surfaces. *Chem. Soc. Rev.* **2015**.

(132) Plymale, N. T.; Kim, Y. G.; Soriaga, M. P.; Brunschwig, B. S.; Lewis, N. S. Synthesis, Characterization, and Reactivity of Ethynyl- and Propynyl-Terminated Si(111) Surfaces. *J. Phys. Chem. C* **2015**, *119* (34), 19847–19862.

(133) Higashi, G. S.; Chabal, Y. J.; Trucks, G. W.; Raghavachari, K. Ideal Hydrogen Termination of the Si(111) Surface. *Appl. Phys. Lett.* **1990**, *56* (7), 656.

(134) Scoles, G. *Atomic and Molecular Beam Methods Volume II*; Oxford University Press:

New York, 1992.

(135) Faubel, M.; Gianturco, F. A.; Ragnetti, F.; Rusin, L. Y.; Sondermann, F.; Tappe, U.; Toennies, J. P. The H_2–Ne Interaction. *J. Chem. Phys.* **1994**, *101* (10), 8800.

(136) Bishop, D. M.; Wetmore, R. W. Vibrational Spacings for H_2^+, D_2^+ and H_2. *Mol. Phys.* **1973**, *26*, 145–157.

(137) Kresse, G.; Hafner, J. Ab Initio Molecular Dynamics for Liquid Metals. *Phys. Rev. B* **1993**, *47* (1), 558–561.

(138) Kresse, G.; Furthmuller, J. Efficient Iterative Schemes for Ab Initio Total-Energy Calculations Using a Plane-Wave Basis Set. *Phys. Rev. B* **1996**, *54* (16), 11169–11186.

(139) Blöchl, P. E. Projector Augmented-Wave Method. *Phys. Rev. B* **1994**, *50* (24), 17953–17979.

(140) Ischtwan, J.; Collins, M. A. Molecular Potential Energy Surfaces by Interpolation. *J. Chem. Phys.* **1994**, *100*, 8080–8088.

(141) Bettens, R. P. A.; Collins, M. A. Learning to Interpolate Molecular Potential Energy Surfaces with Confidence: A Bayesian Approach. *J. Chem. Phys.* **1999**, *111*, 816–826.

(142) Crespos, C.; Collins, M. A.; Pijper, E.; Kroes, G.-J. Application of the Modified Shepard Interpolation Method to the Determination of the Potential Energy Surface for a Molecule-Surface Reaction: H_2 + Pt(111). *J. Chem. Phys.* **2004**, *120* (5), 2392–2404.

(143) Díaz, C.; Vincent, J. K.; Krishnamohan, G. P.; Olsen, R. A.; Kroes, G.-J.; Honkala, K.; Nørskov, J. K. Multidimensional Effects on Dissociation of N_2 on Ru(0001). *Phys. Rev. Lett.* **2006**, *96*, 1–4.

(144) Díaz, C.; Vincent, J. K.; Krishnamohan, G. P.; Olsen, R. A.; Kroes, G.-J.; Honkala, K.; Nørskov, J. K. Reactive and Nonreactive Scattering of N_2 from Ru(0001): A Six-Dimensional Adiabatic Study. *J. Chem. Phys.* **2006**, *125*, 1–13.

(145) Díaz, C.; Olsen, R. A.; Busnengo, H. F.; Kroes, G.-J. Dynamics on Six-Dimensional Potential Energy Surfaces for H_2/Cu(111): Corrugation Reducing Procedure versus Modified Shepard Interpolation Method and PW91 versus RPBE. *J. Phys. Chem. C* **2010**, *114*, 11192–11201.

(146) Frankcombe, T. J.; Collins, M. A.; Zhang, D. H. Modified Shepard Interpolation of Gas-Surface Potential Energy Surfaces with Strict Plane Group Symmetry and Translational Periodicity. *J. Chem. Phys.* **2012**, *137*, 1–10.

(147) Collins, M. A. Molecular Potential-Energy Surfaces for Chemical Reaction Dynamics. *Theor. Chem. Acc.* **2002**, *108*, 313–324.

(148) Swope, W. C.; Andersen, H. C.; Berens, P. H.; Wilson, K. R. A Computer Simulation

Method for the Calculation of Equilibrium Constants for the Formation of Physical Clusters of Molecules: Application to Small Water Clusters. *J. Chem. Phys.* **1982**, *76* (1), 637–649.

(149) Busnengo, H. F.; Dong, W.; Sautet, P.; Salin, A. Surface Temperature Dependence of Rotational Excitation of H_2 Scattered from Pd(111). *Phys. Rev. Lett.* **2001**, *87*, 127601–1.

(150) Díaz, C.; Busnengo, H. F.; Martin, F.; Salin, A. Angular Distribution of H_2 Molecules Scattered from the Pd(111) Surface. *J. Chem. Phys.* **2003**, *118*, 2886–2892.

(151) Beck, M. H.; Jäckle, A.; Worth, G. A.; Meyer, H.-D. The Multiconfiguration Time-Dependent Hartree (MCTDH) Method: A Highly Efficient Algorithm for Propagating Wavepackets. *Phys. Rep.* **2000**, *324* (1), 1–105.

(152) Worth, G. A.; Beck, M. H.; Jackle, A.; Meyer, H.-D. The MCTDH Package, 2007.

(153) del Cueto, M.; Muzas, A. S.; Füchsel, G.; Gatti, F.; Martín, F.; Díaz, C. Role of van Der Waals Forces in the Diffraction of Noble Gases from Metal Surfaces. *Phys. Rev. B* **2016**, *93* (6), 60301.

(154) Van Harrevelt, R.; Manthe, U. Multiconfigurational Time-Dependent Hartree Calculations for Dissociative Adsorption of H_2 on Cu(100). *J. Chem. Phys.* **2004**, *121* (8), 3829–3835.

(155) Crespos, C.; Meyer, H. D.; Mowrey, R. C.; Kroes, G.-J. Multiconfiguration Time-Dependent Hartree Method Applied to Molecular Dissociation on Surfaces: H_2+Pt(111). *J. Chem. Phys.* **2006**, *124* (7).

(156) Krishnamohan, G. P.; Olsen, R. A.; Kroes, G.-J.; Gatti, F.; Woittequand, S. Quantum Dynamics of Dissociative Chemisorption of CH_4 on Ni(111): Influence of the Bending Vibration. *J. Chem. Phys.* **2010**, *133* (14).

(157) Kroes, G.-J. Six-Dimensional Quantum Dynamics of Dissociative Chemisorption of H_2 on Metal Surfaces. *Prog. Surf. Sci.* **1999**, *60*, 1–85.

(158) Neuhauser, D. Reactive Scattering with Absorbing Potentials in General Coordinate Systems. *Chem. Phys. Lett.* **1992**, *200* (1–2), 173–178.

(159) Jäckle, A.; Meyer, H.-D. Product Representation of Potential Energy Surfaces. *J. Chem. Phys.* **1996**, *104* (20), 7974–7984.

(160) Gumhalter, B. Single- and Multiphonon Atom–Surface Scattering in the Quantum Regime. *Phys. Rep.* **2001**, *351*, 1–159.

(161) Yamada, T.; Kawai, M.; Wawro, A.; Suto, S.; Kasuya, A. HREELS, STM, and STS Study of CH_3-Terminated Si(111)-(1x1) Surface. *J. Chem. Phys.* **2004**, *121* (21), 10660–10667.

(162) Graham, J. D.; Nihill, K. J.; Sibener, S. J. Separation of Isotopes in Space and Time by Gas-Surface Atomic Diffraction. *In Preparation* **2017**.

(163) Lindemann, F. A.; Aston, F. W. XLVIII. The Possibility of Separating Isotopes. *Philos. Mag. Ser. 6* **1919**, *37* (221), 523–534.

(164) Love, L. O. Electromagnetic Separation of Isotopes at Oak Ridge: An Informal Account of History, Techniques, and Accomplishments. *Science.* **1973**, *182* (4110), 343–352.

(165) Yergey, A. L.; Yergey, A. K. Preparative Scale Mass Spectrometry: A Brief History of the Calutron. *J. Am. Soc. Mass Spectrom.* **1997**, *8* (9), 943–953.

(166) Ruf, T.; Henn, R. W.; Asen-Palmer, M.; Gmelin, E.; Cardona, M.; Pohl, H.-J.; Devyatych, G. G.; Sennikov, P. G. Thermal Conductivity of Isotopically Enriched Silicon. *Solid State Commun.* **2000**, *115*, 243–247.

(167) Li, J.-Y.; Huang, C.-T.; Rokhinson, L. P.; Sturm, J. C. Extremely High Electron Mobility in Isotopically-Enriched ^{28}Si Two-Dimensional Electron Gases Grown by Chemical Vapor Deposition. *Appl. Phys. Lett.* **2013**, *103* (16), 162105.

(168) Makarov, G. N. Low Energy Methods of Molecular Laser Isotope Separation. *Phys. Uspekhi* **2015**, *58* (7), 670–700.

(169) Mazur, T. R.; Klappauf, B.; Raizen, M. G. Demonstration of Magnetically Activated and Guided Isotope Separation. *Nat. Phys.* **2014**, *10* (8), 601–605.

(170) Bokhan, P. A.; Buchanov, V. V.; Fateev, N. V.; Kalugin, M. M.; Kazaryan, M. A.; Prokhorov, A. M.; Zakrevskĭi, D. E. *Laser Isotope Separation in Atomic Vapor*; 2006.

(171) Anderson, J. B.; Andres, R. P.; Fenn, J. B. Supersonic Nozzle Beams. *Adv. Chem. Phys.* **1966**, *10*, 275–317.

(172) Boato, G.; Cantini, P.; Mattera, L. A Study of the (001)LiF Surface at 80 K by Means of Diffractive Scattering of He and Ne Atoms at Thermal Energies. *Surf. Sci.* **1976**, *55* (1), 141–178.

(173) Isa, N.; Gibson, K. D.; Yan, T.; Hase, W.; Sibener, S. J. Experimental and Simulation Study of Neon Collision Dynamics with a 1-Decanethiol Monolayer. *J. Chem. Phys.* **2004**, *120* (5), 2417–2433.

(174) Szewc, C.; Collier, J. D.; Ulbricht, H. Note: A Helical Velocity Selector for Continuous Molecular Beams. *Rev. Sci. Instrum.* **2010**, *81* (106107), 10–13.

(175) Politano, A.; Borca, B.; Minniti, M.; Hinarejos, J. J.; Vázquez de Parga, A. L.; Farías, D.; Miranda, R. Helium Reflectivity and Debye Temperature of Graphene Grown Epitaxially on Ru(0001). *Phys. Rev. B* **2011**, *84* (3), 35450.

(176) Rieder, K.-H.; Stocker, W. Observation of Pronounced Neon Diffraction from Low-Index Metal Surfaces. *Phys. Rev. Lett.* **1984**, *52* (5), 352–355.

(177) Cole, M. W.; Frankl, D. R. Atomic and Molecular Beam Scattering from Crystal Surfaces

in the Quantum Regime. *Surf. Sci.* **1978**, *70*, 585–616.

(178) Schweizer, E. K.; Rettner, C. T. Quantum Effects in the Scattering of Argon from 2H-W(100). *Phys. Rev. Lett.* **1989**, *62* (26), 3085–3088.

(179) Althoff, F.; Andersson, T.; Andersson, S. Quantum Scattering of Heavy Particles from a 10 K Cu(111) Surface. *Phys. Rev. Lett.* **1997**, *79* (22), 4429–4432.

(180) Levi, A. C.; Huang, C.; Allison, W.; Maclaren, D. A. Quantum Scattering of Neon from a Nanotextured Surface. *J. Phys. Condens. Matter* **2009**, *21* (22), 225009.

(181) Minniti, M.; Diaz, C.; Fernandez Cunado, J. L.; Politano, A.; Maccariello, D.; Martin, F.; Farias, D.; Miranda, R. Helium, Neon and Argon Diffraction from Ru(0001). *J. Phys. Condens. Matter* **2012**, *24*.

(182) NSAC-ISOTOPES Subcommittee. *Meeting Isotope Needs and Capturing Opportunities for the Future: The 2015 Long Range Plan for the DOE-NP Isotope Program*; 2015.

(183) Rivard, M. J.; Bobek, L. M.; Butler, R. A.; Garland, M. A.; Hill, D. J.; Krieger, J. K.; Muckerheide, J. B.; Patton, B. D.; Silberstein, E. B. The US National Isotope Program: Current Status and Strategy for Future Success. *Appl. Radiat. Isot.* **2005**, *63* (2), 157–178.

(184) Sibener, S. J.; Lee, Y. T. The Internal and Translational Energy Dependence of Molecular Condensation Coefficients: SF_6 and CCl_4. *J. Chem. Phys.* **1994**, *101* (2), 1693–1703.

(185) Goodman, F. O.; Wachman, H. Y. *Dynamics of Gas-Surface Scattering*; Academic Press: New York, 1976.

(186) Bunermann, O.; Jiang, H.; Dorenkamp, Y.; Kandratsenka, A.; Janke, S. M.; Auerbach, D. J.; Wodtke, A. M. Electron-Hole Pair Excitation Determines the Mechanism of Hydrogen Atom Adsorption. *Science.* **2015**, *350* (6266), 1346–1349.